Resistive switching in mixed orthorhombic/hexagonal $RMnO_3$ (R = Y, Er) polycrystalline thin films

Inaugural-Dissertation
to obtain the academic degree
Doctor rerum naturalium (Dr. rer. nat.)

submitted to the Department of Biology, Chemistry, Pharmacy
of Freie Universität Berlin

by

RONG WU

Berlin

May 2024

The research of this thesis was carried out under the supervision of Prof. Dr. Catherine Dubourdieu at the Institute of Chemistry and Biochemistry between January 2020 and May 2024.

1st reviewer: Prof. Dr. Catherine Dubourdieu

2nd reviewer: Prof. Dr. Ilia Valov

Date of defense: 17.09.2024

Acknowledgement

I would like to thank my doctoral advisor, Prof. Dr. Catherine Dubourdieu, for giving me this great opportunity to work in the QM-IFOX group. I really appreciate her constant support, insightful guidance and valuable feedback throughout my research. I am also grateful for her patience and time invested in editing all my papers and manuscript.

I wish to express appreciation to Prof. Dr. Ilia Valov for being my second reviewer.

I would like to acknowledge the funding of this work by the BMBF in the framework of the ForMikro project ERMI.

I am also grateful to Dr. Veeresh Despande, Dr. Dong Jik Kim, Dr. Sebastian Schmitt, and Dr. Thanh Luan Phan for their daily supervision and support. From Veeresh, I learned electrical characterization and analytical thinking; from DJ, I learned thin film characterization; and from Sebastian, I learned Raman spectroscopy.

I want to thank Dr. Florian Maudet for his patience, encouragement, and support both as my colleague and friend. I learned spectroscopic ellipsometry, data analysis and presentation skills from him.

I appreciate the help from Dr. Wassim Hamouda for the XPS measurements and fruitful discussions, and from Sven Wiesner and Jürgen Albert for their technical support in the lab. My thanks also go to the secretaries in the group: Dr. Nikoline Hansen for her patient support, and Alisa Ognef for her positive energy.

Thanks to Valentin Hevelke for checking the Zusammenfassung of this thesis.

I am grateful to the academic partners from the ERMI project, Prof. Dr. Bernhard Wicht, Ferdinand Pieper, and Prof. Dr. Heidemarie Schmidt, for the fruitful collaboration.

I thank Dr. Thomas Cornelius and Dr. Matthias Rössle for the collaboration on time-resolved XRD measurements.

I thank Dr. Richard Schrödter, Dr. Ahmet Demirkol, and Prof. Dr. Ronald Tetzlaff for the collaboration on neuristor applications.

Thanks to all the responsible people from the clean room at TU Berlin.

Thanks to Karsten Harbauer for depositing Pt and Ti, to Sascha Petz for the technical support on the AJA sputtering tool, to Michael Kirsch for depositing Al.

I also appreciate the collaboration with Maximilian Winkler for the low-temperature PUND measurements, and Moritz Engl for the temperature-dependent I-V measurements.

I am very glad to have the chance to work with amazing people in the QM-IFOX group: Ibukun Olaniyan, Charlotte Van Dijck, Keerthana S Nair, Marco Holzer (the first coolest guy I met in Berlin), Valentin Hevelke (my best German teacher), Onur Toprak (introduced Çiğ köfte to my foodie life), Deborah Kern (another Schnatterntante), Hamid Raza, Sandip Lashkare, Arnab De, and all members with whom I worked together. Thank you for bringing laughter and joy to the lab and making research life much more fun.

Particular thanks to Ibukun for cheering me up like a brother when I was down and sharing all the achievements, no matter how small; to Charlotte for being my gym and food buddy, motivating me to stay physical active and mentally healthy; to Keerthana for cheering me up whenever I needed her support, showing patience even when I broke her 'Puttu' again and again; and to Adriana for sharing interesting stories and providing mental support both in research and life.

I want to thank Chang Yu, Binbin Zhou, Jian'an Yi, Rekikua Alemayehu and all my friends for their support and encouragement. Playing tennis with Chang has been one of the best moments during every weekend.

Special thanks to Markus Lübeck for his support and sometimes failed 'sandwiched' comments.

Lastly, I want to thank my parents and sister for their endless support, unconditional love, and trust.

Thank you all for being part of this journey.

Declaration of authorship

I hereby declare that I alone am responsible for the content of my doctoral dissertation and that I have only used the sources or references cited in the dissertation.

Date: 29.05.2024 Signature: Rong Wu

Table of Contents

Acknowledgement I

Declaration of authorship III

Abbreviations IX

Abstract 1

Zusammenfassung 3

Introduction 5

1 Scientific background 10

1.1 Multiferroic materials 11

1.2 Introduction to rare earth manganites 13

1.2.1 Hexagonal $RMnO_3$ 14

1.2.2 Orthorhombic $RMnO_3$ 17

1.2.3 Electrical conductivity in $RMnO_3$ 18

1.2.4 Literature review on synthesis of $RMnO_3$ thin films 23

1.3 Emergent memory devices 24

1.4 Resistive switching devices 25

1.4.1 Neuromorphic applications 25

1.4.2 Classification of resistive switching behavior 27

1.4.3 Physical mechanisms of resistive switching 29

1.4.4 Literature review on resistive switching in $RMnO_3$ thin films 36

1.5 Objectives of this work 38

2 Experimental methods 42

2.1 Film preparation 43

2.1.1 Sputtering 43

2.1.2 Evaporation 45

2.2 Device fabrication 47

2.3 Characterization methods 51

2.3.1 Grazing incidence X-ray diffraction 51

2.3.2 Spectroscopic ellipsometry 52

2.3.3 Atomic force microscopy 55

2.3.4 Scanning electron microscopy 59

2.3.5 Raman spectroscopy 60

2.3.6 X-ray photoelectron spectroscopy 62

2.3.7 Electrical characterization 64

2.3.8 Operando time-resolved X-ray diffraction during PUND measurement 68

3 Investigation of the impedance (*R*, *L*, *C*) of metal/$RMnO_3$/metal stacks 72

3.1 Device architecture and electrical measurement configurations 74

3.2 Package-based measurement 76

3.2.1 Parasitic calibration 76

3.2.2 Reference inductor 77

3.2.3 $YMnO_3$-based device characterization 78

3.3 Probe station-based measurement 79

3.3.1 Parasitic calibration 79

3.3.2 $RMnO_3$-based device characterization 83

3.4 Summary 86

4 $YMnO_3$ thin film-based electrochemical metallization (ECM) devices 88

4.1 Polycrystalline $YMnO_3$ thin film optimization 90

4.1.1 Sputtering conditions 91

4.1.2 Annealing conditions 94

4.2 Identification and quantification of the crystalline phases 101

4.3 Ferroelectric properties 104

4.4 Resistive switching in Pt/$YMnO_3$/Al devices 107

4.4.1 Device fabrication 108

4.4.2 Bipolar resistive switching of Pt/$YMnO_3$/Al devices 108

4.4.3 Thickness effect 112

4.4.4 Discussion on the filamentary mechanism 113

4.5 Reconfigurability between capacitive and resistive states 121

4.6 Summary 125

5 $ErMnO_3$ thin film-based valence change memory (VCM) devices 128

5.1 Polycrystalline $ErMnO_3$ thin film optimization 129

5.1.1 Deposition on polycrystalline Pt coated Si substrates 129

5.1.2 Deposition on textured (111) Pt coated Si substrates 138

5.2 Identification and quantification of the crystalline phases 140

5.3 Ferroelectric properties 144

5.3.1 Polarization-voltage measurement 144

5.3.2 Piezoelectric response 148

5.4 Valence change memory (VCM)-type Pt/$ErMnO_3$/Ti/Au devices 150

5.4.1 Device fabrication 150

5.4.2 Electrical characterization of Pt/$ErMnO_3$/Ti/Au devices with minor o-$ErMnO_3$ content 151

5.5 Impact of the crystalline phases 156

5.6 Role of top electrodes 162

5.7 Summary 164

6 $ErMnO_3$ thin film-based threshold switching devices 166

6.1 Device fabrication and sample information 168

6.2 Threshold switching in Pt/$ErMnO_3$/Pt devices 176

6.2.1 Effect of the second thermal annealing on resistive switching 176

6.2.2 Volatile threshold switching characterization 176

6.2.3 Physical model of the threshold switching in Pt/$ErMnO_3$/Pt devices 179

6.2.4 On the roles of the orthorhombic and hexagonal phases 185

6.3 Applications (implementation of the NDR devices into circuits) 188

6.3.1 Reconfigurability between resistive and inductive states 188

6.3.2 NDR devices as artificial neurons 190
6.4 Summary 192
Summary and outlook 193
Summary 193
Outlook 194
References 197
List of publications 227

Abbreviations

AC	Alternative current
AFM	Atomic force microscopy
ALD	Atomic layer deposition
Ar	Argon
APT	Atomic probe tomography
BSE	Backscattered electron
c-AFM	Conductive atomic force microscopy
DC	Direct current
DFT	Density functional theory
DHM	Dynamic hysteresis measurement
DI	Deionized
DRAM	Dynamic random-access memory
DUT	Device under test
ECM	Electrochemical metallization
EDX	Energy-dispersive X-ray spectroscopy
ERMI	Erforschung rekonfigurierbarer, passiver Mikroelektronikbauelemente für Energieeffizienz und Flexibilität
FRAM	Ferroelectric random-access memory
FWHM	Full width at half maximum
LCMO	$La_{0.7}Ca_{0.3}MnO_3$
LIF	Leaky integrate-and-fire
GIXRD	Grazing incidence X-ray diffraction
h-$YMnO_3$	Hexagonal $YMnO_3$
h-$ErMnO_3$	Hexagonal $ErMnO_3$
HRS	High resistance state

IMT	Insulator-metal transition
IoT	Internet-of-Things
IQR	Interquartile range
LRS	Low resistance state
MBE	Molecular beam epitaxial
MIM	Metal insulator metal
MOCVD	Metal-organic chemical vapor deposition
MRAM	Magnetic random-access memory
NDR	Negative differential resistance
o-$YMnO_3$	Orthorhombic $YMnO_3$
o-$ErMnO_3$	Orthorhombic $ErMnO_3$
OTS	Ovonic threshold switch
PCB	Printed circuit board
PCM	Phase change memory
PFM	Piezoresponse force microscopy
PF	Poole Frenkel
PLD	Pulsed laser deposition
PUND	Positive Up Negative Down
RAM	Random-access memory
RF	Radio frequency
RIE	Reactive ion etching
RMS	Root-mean-square
RRAM	Resistive random-access memory
RTP	Rapid thermal processing
SE	Secondary electron
SEM	Scanning electron microscopy
TC	Curie temperature

TEM	Transmission electron microscopy
VCM	Valence change memory
XPS	X-ray photoelectron spectroscopy
3D	Three dimensions

Abstract

Resistive random-access memory (RRAM), one of the next-generation non-volatile memory technologies, offers scalability, enhanced performance, and lower power consumption compared to traditional memories, making it a promising solution for future memory architectures. In this work, we study different types of polycrystalline $RMnO_3$ (R = Y, Er) thin films-based RRAM devices.

This research starts with the synthesis and characterization of polycrystalline $YMnO_3$ and $ErMnO_3$ thin films with mixed hexagonal and orthorhombic phases. Films are prepared with radio frequency sputtering at room temperature and post-deposition annealing. The orthorhombic phase cannot always be discriminated by X-ray diffraction, as there is an overlap with the peaks of the hexagonal phase and its low volume fraction and the nano-sized grains lead to undetectable peaks. Employing a set of correlative spectroscopy and microscopy techniques, we develop a method to unambiguously identify the presence of the orthorhombic phase, locate it, and quantify it.

Subsequently, we investigate different types of memristive devices using polycrystalline thin films with the presence of both hexagonal and orthorhombic phases.

First, electrochemical metallization (ECM) memristive devices based on $YMnO_3$ with Al active electrode are studied. These devices exhibit bipolar resistive switching with high R_{OFF}/R_{ON} ratios (~ 10^4), low Set/Reset voltages (V_{Set} ~ 1.7 V and V_{Reset} ~ -0.36 V), and good retention. The resistive switching mechanism is ascribed to the formation and rupture of an Al filament along oxygen-deficient boundaries between hexagonal and orthorhombic phases. These localized nanochannels for Al^{3+} migration effectively remove the randomness of the Al filament formation in the electrolyte.

Second, we investigate bipolar resistive switching in Pt/$ErMnO_3$/Ti/Au devices. They exhibit high R_{OFF}/R_{ON} ratios (~ 10^5) and ultra-low resistances (~ 10 Ω) in the low resistance state (R_{ON}). The resistive switching is the result of the formation and rupture of an oxygen-vacancy-based conductive filament, which likely occurs either in the orthorhombic phase or at the boundary between the two polymorphs. An increased fraction of the orthorhombic phase strongly reduces the operating voltage in devices (down to V_{Set} ~ -2.07 V) and the variability of V_{Set}. The presence of hexagonal phase prevents large leakage currents in the devices, which otherwise would not show switching behavior.

Finally, we present the first demonstration of electroforming-free threshold switching devices with $ErMnO_3$. Pt/$ErMnO_3$/Pt devices exhibit repeatable unipolar threshold switching with a memory window of 0.7 V, characterized by a S-shape current-controlled negative differential resistance (NDR). The devices show a high endurance up to 10^4 sweeps. We successfully model the threshold switching using Joule-heating-enhanced 3D Poole-Frenkel conduction mechanism. The conducting orthorhombic phase plays a key role

in enabling the self-heating mechanism while the hexagonal phase prevents too large electrical and thermal conductivities. Adjusting the conductivity of o-$ErMnO_3$ and engineering the two crystalline phase fractions are key knobs for tuning the threshold switching characteristics. The oscillatory behavior of the NDR devices is demonstrated. This new type of NDR devices based on two polymorphs with different electronic and thermal properties present advantages for tunability of the memory window compared to known NDR devices such as those based on an insulator-to-metal transition (e.g. VO_2) or based on the formation of a filament (e.g. NbO_x).

In all studied devices, the coexistence of the hexagonal and orthorhombic phases of $RMnO_3$ (R = Y, Er) provides unique functionalities. The possibility to engineer these two phases both in conductivity and content through synthesis, provide original routes to design new memristive devices and optimize their properties.

Zusammenfassung

Resistiver Direktzugriffsspeicher (RRAM), eine der nichtflüchtigen Speichertechnologien der nächsten Generation, bietet Skalierbarkeit, verbesserte Leistung und geringeren Stromverbrauch im Vergleich zu herkömmlichen Speichern, was ihn zu einer vielversprechenden Lösung für zukünftige Speicherarchitekturen macht. In dieser Abhandlung untersuchen wir verschiedene Arten von polykristallinen $RMnO_3$ (R = Y, Er) Dünnschichten-basierten RRAM-Bauteilen.

Diese Studie beginnt mit der Synthese und Charakterisierung von polykristallinen $YMnO_3$- und $ErMnO_3$-Dünnschichten mit gemischten hexagonalen und orthorhombischen Phasen. Die Schichten werden durch Hochfrequenzsputtern bei Raumtemperatur mit anschließendem Glühen hergestellt. Die orthorhombische Phase kann durch Röntgenbeugung nicht immer eindeutig von anderen Phasen unterschieden werden, da es einen Überlapp mit den Peaks der hexagonalen Phase gibt und ihr geringer Volumenanteil und die nanogroßen Körner zu nicht nachweisbaren Peaks führen. Mit Hilfe einer Reihe korrelativer Spektroskopie- und Mikroskopietechniken entwickeln wir eine Methode, um die orthorhombische Phase eindeutig zu identifizieren, zu lokalisieren und zu quantifizieren.

Anschließend untersuchen wir verschiedene Arten von memristiven Bauelementen unter Verwendung von polykristallinen Dünnschichten, die sowohl hexagonale als auch orthorhombische Phasen aufweisen.

Zunächst werden elektrochemisch metallisierte (ECM) memristive Bauelemente auf der Basis von $YMnO_3$ mit aktiver Al-Elektrode untersucht. Diese Bauelemente zeigen bipolare Widerstandsschaltung mit hohen R_{OFF}/R_{ON} -Verhältnissen (~ 10^4), niedrigen Set/Reset-Spannungen (V_{Set} ~ 1.7 V und V_{Reset} ~ -0.36 V) und guter Retention. Der Widerstandsschaltmechanismus wird auf die Bildung und den Bruch eines Al-Filaments entlang sauerstoffarmer Grenzen zwischen hexagonalen und orthorhombischen Phasen zurückgeführt. Diese lokalisierten Nanokanäle für die Al^{3+}-Migration beseitigen wirksam die Zufälligkeit der Al-Filamentbildung im Elektrolyten.

Zweitens untersuchen wir die bipolare Widerstandsschaltung in Pt/$ErMnO_3$/Ti/Au-Bauelementen. Sie weisen hohe R_{OFF}/R_{ON} -Verhältnisse (~ 10^5) und extrem niedrige Widerstände (~ 10 Ω) im niederohmigen Zustand (R_{ON}) auf. Die Widerstandsschaltung ist das Ergebnis der Bildung und des Bruchs eines leitfähigen Filaments auf der Basis von Sauerstoff-Fehlstellen, das wahrscheinlich entweder in der orthorhombischen Phase oder an der Grenze zwischen den beiden Polymorphen auftritt. Ein erhöhter Anteil der orthorhombischen Phase verringert die Betriebsspannung in den Geräten (bis zu V_{Set} ~ -2.07 V) und die Variabilität von V_{Set} stark. Das Vorhandensein der hexagonalen Phase verhindert große Leckströme in den Bauelementen, die sonst keinem Schaltverhalten zeigen würden.

Schließlich präsentieren wir erstmalig elektroformungsfreie Schwellenwert-Schaltvorrichtungen mit $ErMnO_3$. Pt/$ErMnO_3$/Pt-Bauelemente zeigen wiederholbare unipolare Schwellenwertschaltungen mit

einem Speicherfenster von 0.7 V, das durch einen S-förmigen stromgesteuerten negativen Differenzialwiderstand (NDR) gekennzeichnet ist. Die Bauelemente weisen eine hohe Ausdauer von bis zu 10^4 Durchläufen auf. Wir modellieren die Schwellenwertumschaltung erfolgreich mit einem durch Joule-Wärme verstärkten 3D-Poole-Frenkel-Leitungsmechanismus. Die leitende orthorhombische Phase spielt eine Schlüsselrolle bei der Ermöglichung des Selbsterwärmungsmechanismus, während die hexagonale Phase zu große elektrische und thermische Leitfähigkeiten verhindert. Die Einstellung der Leitfähigkeit von o-$ErMnO_3$ und die Entwicklung der beiden kristallinen Phasenanteile sind wichtige Stellschrauben für die Abstimmung der Schwellenwerteigenschaften. Das oszillierende Verhalten der NDR-Bauelemente wird demonstriert. Diese neue Art von NDR-Bauelementen, die auf zwei Polymorphen mit unterschiedlichen elektronischen und thermischen Eigenschaften basieren, bietet Vorteile für die Abstimmbarkeit des Speicherfensters im Vergleich zu bekannten NDR-Bauelementen, die auf einem Isolator-Metall-Übergang (z. B. VO_2) oder auf der Bildung eines Filaments (z. B. NbO_x) basieren.

In allen untersuchten Bauelementen bietet die Koexistenz der hexagonalen und orthorhombischen Phasen von $RMnO_3$ (R = Y, Er) einzigartige Funktionalitäten. Die Möglichkeit, diese beiden Phasen durch Synthese sowohl in ihrer Leitfähigkeit als auch in ihrem Gehalt zu verändern, bietet originelle Wege, um neue memristive Bauelemente zu entwickeln und ihre Eigenschaften zu optimieren.

Introduction

In the era of big data, rapid advancement of information technology and breakthroughs in fields such as the Internet-of-Things (IoT), deep learning, edge computing, cloud computing, and autonomous vehicles demand higher computational power while simultaneously aiming for energy efficiency.[1, 2] However, in traditional computing systems, like the von Neumann architecture, the separation of processing and memory units lead to significant time and energy costs when transferring large data between them.[3, 4] This inefficiency poses particular challenges in data-centric applications such as artificial intelligence, where rapid access to large amounts of data is crucial.

To address the von Neumann bottleneck, neuromorphic computing systems aim at emulating the brain's structure, function and energy efficiency in hardware. These systems integrate processing and memory units, mimicking the parallel, distributed, and event-driven nature of neural networks. By doing so, neuromorphic systems aim to enhance computational efficiency and performance, especially for tasks requiring extensive data handling.

Key components of neuromorphic computing include artificial synapses and spiking neurons. Synapses transmit signals (electrical events) from one neuron to another one. The strength of the connection between two neurons is the synaptic weight. Emerging memories like resistive random-access memory (RRAM),[5–7] which exhibit a resistive switching phenomenon and can be programmed in an analog fashion, hold promise as artificial synapses.[8, 9] Neurons transmit electrical signals along their axon and communicate with other neurons. Most neurons communicate primarily through spikes (or action potentials). Traditional artificial neuron circuits, which use transistors and capacitors, are limited by complex configurations and integration density. To improve area efficiency, emerging devices such as volatile threshold switching devices, a type of RRAM, are proposed to build spiking neurons. These devices can undergo abrupt changes in current or voltage in response to input signals, generating spike responses to emulate the firing of neurons.[10–12]

Hexagonal $RMnO_3$ (where R represents rare earths) compounds are multiferroic ternary oxides, which are ferroelectric at room temperature. The combination of resistive switching properties and multiferroicity in $RMnO_3$ could introduce new functionalities for device applications. For instance, integrating resistive switching with ferroelectricity could enable multilevel analog resistive switching for neuromorphic applications.[13, 14] Additionally, H. Schmidt *et al.* proposed that topological vortex states in the hexagonal phase could couple with different resistance states.[15–17] In their interpretation, the nanosized ferroelectric vortices not only serve as the conducting path responsible for transitioning to the low resistance state (LRS) but also function as inductors due to their winding structures. Hence, they suggested that the reconfigurability between capacitive and inductive states could be achieved.

Building on this concept, the research project “Erforschung rekonfigurierbarer, passiver Mikroelektronikbauelemente für Energieeffizienz und Flexibilität” (ERMI), funded by BMBF under the ForMikro program, aimed to use $RMnO_3$ (R = Y, Er) thin films with reconfigurability between capacitive and inductive states, to develop energy-efficient voltage transformers for local power supply.[18–20] My doctoral work has been funded and performed within this project. In this context, I explored not only *L*-*C* but also *R*-*C* reconfigurability.

Few groups have explored non-volatile resistive switching performances in hexagonal polycrystalline $YMnO_3$ thin films,[17, 21–25] and none have addressed the potential presence and role of the orthorhombic phase, although the metastable $YMnO_3$ phase forms easily together with the hexagonal one in thin films, since strain acts as “high pressure”. The hexagonal and orthorhombic phases exhibit distinct electronic properties. Incorporating conductive orthorhombic $RMnO_3$ into a hexagonal $RMnO_3$ matrix has the potential to allow tuning of the device conductivity and of the resistive switching properties (ON/OFF ratio, operation voltage…). Additionally, boundaries between the two crystalline phases may be privileged locations for filament nucleation or diffusion paths.

In this thesis, we investigate non-volatile and volatile resistive switching in mixed hexagonal/orthorhombic $YMnO_3$ and $ErMnO_3$ polycrystalline thin films. It involves developing methods for identifying and quantifying mixed crystalline phases, understanding the resistive switching mechanisms at play with different electrodes, and optimizing the device properties (via processing conditions, film thickness, crystalline phase fractions, and conductivity engineering of the two polymorphs). Through these efforts, the thesis aims to advance the fundamental understanding of resistive switching in these compounds and demonstrate an original approach to design devices by leveraging the properties of polymorphs of the same compound.

The dissertation is structured in six chapters.

Chapter 1 provides an overview of the scientific background essential for understanding the material properties and resistive switching phenomena observed in rare earth manganite ($RMnO_3$) thin films.

Chapter 2 introduces the experimental methodology and characterization techniques employed in this work.

In Chapter 3, we explore capacitive and inductive behaviors in manganite thin films using two-terminal devices.

In Chapter 4, we investigate the electrochemical metallization resistive switching and its origin in $Pt/YMnO_3/Al$ memristive devices with polycrystalline $YMnO_3$ films containing a mixture of o-$YMnO_3$ and h-$YMnO_3$ phases.

In Chapter 5, we study the bipolar resistive switching behavior in valence change memory Pt/$ErMnO_3$/Ti/Au devices and explore the impact of the hexagonal and orthorhombic phases and their relative content on the resistive switching.

In Chapter 6, we demonstrate, for the first time, electroforming-free threshold switching behavior in Pt/$ErMnO_3$/Pt devices, taking advantage of the mixture of hexagonal and orthorhombic phases. We propose a physical model of threshold switching to address the underlying physical mechanism and investigate the roles of hexagonal and orthorhombic phases on triggering the threshold switching.

Finally, we summarize the results and provide an outlook on resistive switching in $RMnO_3$-based devices.

Chapter 1: Scientific background

1 Scientific background 10
1.1 Multiferroic materials 11
1.2 Introduction to rare earth manganites 13
1.2.1 Hexagonal $RMnO_3$ 14
1.2.2 Orthorhombic $RMnO_3$ 17
1.2.3 Electrical conductivity in $RMnO_3$ 18
1.2.4 Literature review on synthesis of $RMnO_3$ thin films 23
1.3 Emergent memory devices 24
1.4 Resistive switching devices 25
1.4.1 Neuromorphic applications 25
1.4.2 Classification of resistive switching behavior 27
1.4.3 Physical mechanisms of resistive switching 29
1.4.3.1 Electrochemical metallization memory (ECM) switching 31
1.4.3.2 Valence change memory (VCM) switching 32
1.4.3.3 Threshold switching 33
1.4.4 Literature review on resistive switching in $RMnO_3$ thin films 36
1.5 Objectives of this work 38

This chapter provides an overview of the scientific background essential for understanding and investigating the material properties and resistive switching phenomena observed in rare earth manganite ($RMnO_3$) thin films. We introduce multiferroic materials in Section 1.1. In Section 1.2, we present $RMnO_3$ compounds, including their multiferroic properties (ferroelectricity in particular), and conduction mechanisms. We report the synthesis methods employed for $RMnO_3$ thin film growth. In Section 1.3, we introduce emergent memory devices. In Section 1.4, we provide a detailed explanation of the principles and mechanisms underlying resistive switching, along with a brief review of studies on resistive switching behavior in $RMnO_3$. Finally, we present the objectives of this work in Section 1.5.

1.1 Multiferroic materials

Multiferroic materials represent a class of materials that exhibit more than one primary ferroic order simultaneously. The term *multiferroic* was introduced by Hans Schmid in 1993.[26] There are four types of primary ferroic orders: ferroelectricity (spontaneous polarization P induced by an electric field E), ferromagnetism (spontaneous magnetization M induced by a magnetic field H), ferroelasticity (strain ε induced by a stress σ), and ferrotorodicity (spontaneous toroidal moment T induced by a toroidal field G), as seen in Figure 1.1a.[27, 28]

The presence of multiple ferroic orders within the same phase is of particular interest if there is a coupling between them, such as the magnetoelectric effect (Figure 1.1b). This effect arises from the coupling between electric and magnetic properties, for instance, changing the magnetization by an electric field or modifying the electric polarization with a magnetic field.[29] If magnetism can be efficiently manipulated by an electric field rather than a magnetic field, it potentially reduces the energy consumption by several orders of magnitude. Moreover, while the applied magnetic field remains the same, the applied electric field scales with the dimension of the objects, emphasizing the versatility of the magnetoelectric effect.[30] As a result, the magnetoelectric effect has attracted significant attention.[30–32]

D. Khomskii proposed two types of multiferroics (type I and type II).[33] Type II multiferroics are magnetism-driven, as ferroelectricity arises from magnetic ordering, whereas all others lacking a magnetic origin are categorized as type I.

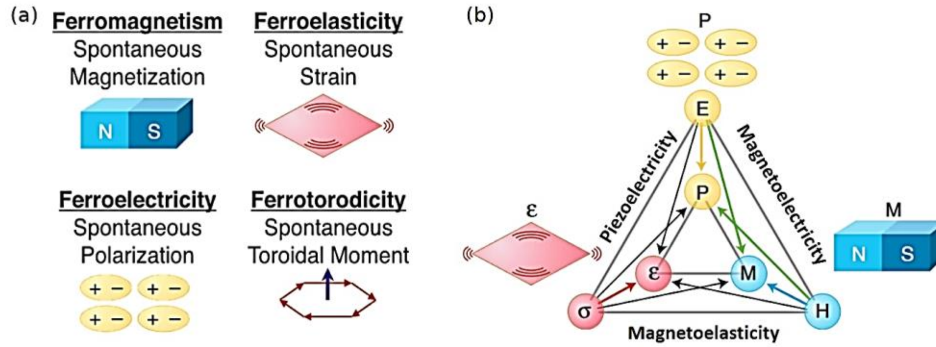

Figure 1.1: (a) A schematic of four primary symmetry-based ferroic orders. This figure is adapted from ref.[30, 34] (b) Schematic illustrating different types of coupling present in materials. This figure is from ref.[34]

Now let us discuss ferroelectrics. They exhibit a spontaneous electric polarization that can be reversed under an external electric field (Figure 1.2a).[35] The first documented observation of ferroelectricity occurred in Rochelle salt ($KNaC_4H_4O_6{\bullet}4H_2O$) in 1920 by Joseph Valasek.[36] However, it was not until two decades later that ferroelectricity gained significant attention with its discovery in materials such as $BaTiO_3$ and $PbTiO_3$.[37] Since then, the study of ferroelectricity has continued to evolve, with ongoing advancements in understanding its fundamental properties and applications.[38]

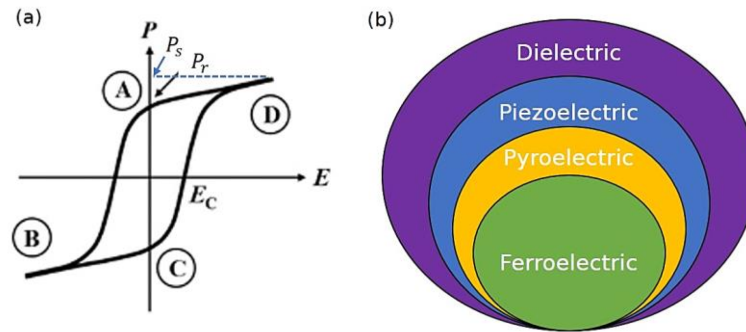

Figure 1.2: (a) Polarization *P* vs electric field *E* (*P*-*E*) hysteresis loop displayed in ferroelectric materials. This figure is from ref.[39] (b) The relationship between the ferroelectric, pyroelectric, piezoelectric and dielectric properties.

All ferroelectrics are pyroelectric (polarization induced by a change in temperature), piezoelectric (polarization induced by a stress), and dielectric, as illustrated in Figure 1.2b.

Ferroelectric phase transition (ferroelectric to paraelectric phase) occurs at the Curie temperature (T_C). Within a ferroelectric material, there exist regions with uniform polarization named as ferroelectric domains.[35] The boundaries separating these domains are referred to as domain walls. By applying an electric field, the polarizations all align along the field (single domain) through the movement of domain walls. The polarization can be reversed by applying an electric field of opposite direction.[35] This process

of polarization reversal under an electric field is represented by a hysteresis curve, as shown in Figure 1.2a. As the electric field increases, the domains align in the positive direction, eventually reaching its saturated value (P_s). When the external field is removed, some domains retain alignment in the positive direction, referring to a remanent polarization of the ferroelectric material (P_r). When a negative electric field is applied, the ferroelectric material undergoes polarization switching at the coercive field ($-E_C$). Subsequently, the polarization direction flips further with increasing negative electric field. Hence, variables such as coercive field (E_C), remanent polarization (P_r) and saturated polarization (P_s) are crucial factors for the potential applications of ferroelectric materials.

1.2 Introduction to rare earth manganites

Rare earth manganites ($RMnO_3$), first discovered in the early 1960s, represent one of the most investigated multiferroic compounds today.[40] $RMnO_3$ crystallize at room temperature in an orthorhombic or in a hexagonal structure (o-$RMnO_3$, h-$RMnO_3$), depending on the ionic size of rare earth elements, as depicted in Figure 1.3a. According to the tolerance factor defined by Goldschmidt (see Equation 1.1),[41] $RMnO_3$ with large rare earth elements (R = La-Dy) crystalize in an orthorhombic perovskite-type structure with space group *Pnma* (Figure 1.4a). $RMnO_3$ with small rare earth elements (R = Y-Lu) adopt the layered hexagonal phase with space group $P6_3cm$ (Figure 1.4b).[42, 43]

$$t = \frac{r_A + r_0}{\sqrt{2}(r_B + r_O)} \qquad \text{Equation 1.1}$$

where t is tolerance factor, r_A, r_B, r_O are the ionic radii of the A-site cation, B-site cation and oxygen anion, respectively.

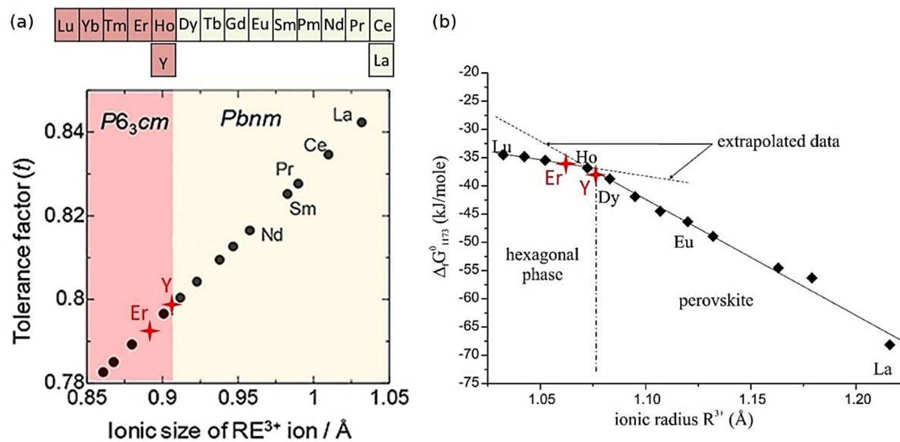

Figure 1.3: (a) Tolerance factor and stable crystal structure as a function of ionic size of rare earth in $RMnO_3$. This graphic is reproduced from ref.[44] (b) Free energy of $RMnO_3$ formation from R_2O_3 and Mn_2O_3 at 900 ºC and ambient pressure, which is calculated with oxygen dissociation pressure data.[43] We have highlighted the two compounds studied in this work with red stars. This graphic is reproduced from ref.[45]

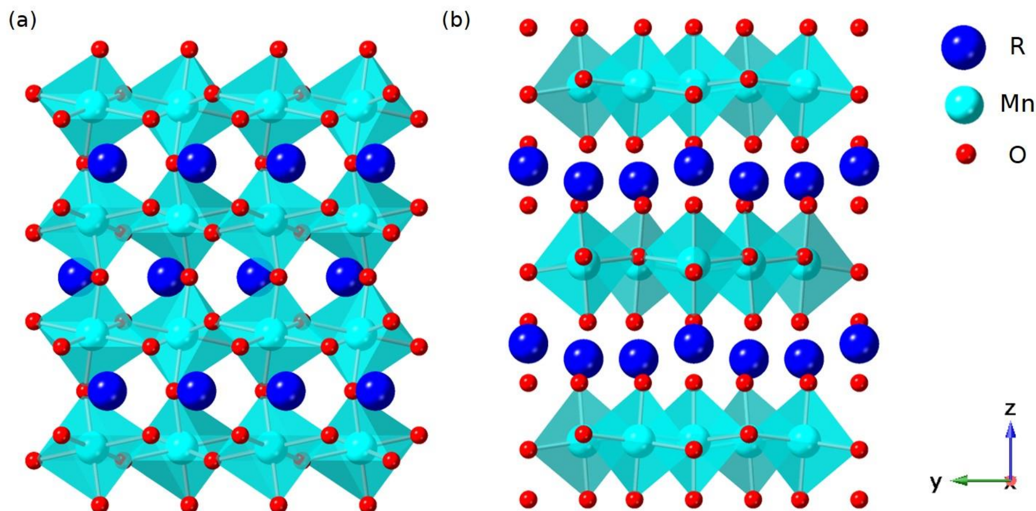

Figure 1.4: Crystal structure of $RMnO_3$ in (a) orthorhombic phase and (b) hexagonal phase, respectively. These figures are generated by CrystalMaker.

The Goldschmidt tolerance factor indicates the stability and distortion of perovskite crystal structures,[41] establishing the boundary between hexagonal and orthorhombic phases. Additionally, we can consider the phases from a thermodynamic point of view, as demonstrated by A. A. Bosak *et al.*[45, 46] They reported the Gibbs free energy of $RMnO_3$ formation from R_2O_3 and Mn_2O_3 at 900 ℃ and ambient pressure (Figure 1.3b).[45, 46] It aligns well with the results based on the Goldschmidt tolerance factor. The thermodynamically stable phase of $RMnO_3$ with smaller rare earth elements (R = Y-Lu) is the hexagonal phase. They also discussed that the metastable orthorhombic phase can be stabilized if the difference between the Gibbs energies of these two polymorphs is below 10-15 kJ mol^{-1}.[45] Therefore, orthorhombic $RMnO_3$ (R = Y-Lu) can be stabilized under certain conditions, such as high-pressure synthesis,[47–52] soft chemistry synthesis[53–55] and as thin films, through epitaxial strain.[56–59] Vice versa, the hexagonal $RMnO_3$ (R = Dy, Gd, Eu, Sm) can be stabilized by epitaxial strain using a ZrO_2 (Y_2O_3) substrate.[45, 46, 60]

$YMnO_3$ and $ErMnO_3$, the two manganites to be studied in this work, are situated close to the stability boundary (marked as red stars in Figure 1.3). In other words, their Gibbs free energies of $RMnO_3$ formation are similar for the hexagonal and orthorhombic phases. One can therefore expect that the metastable orthorhombic phase may form.

1.2.1 Hexagonal $RMnO_3$

Hexagonal $RMnO_3$ compounds are type-I multiferroics which are ferroelectrics at room temperature. Their ferroelectricity is induced by a geometrically driven mechanism.[61] The ferroelectricity is called improper

ferroelectricity, as the polarization is not the primary order parameter.[62] In h-$RMnO_3$, corner-shared MnO_5 polyhedra alternate with layers of rare earth R^{3+} ions (Figure 1.4b). Above the Curie temperature T_C, the hexagonal phase is in a centrosymmetric paraelectric phase (Figure 1.5a). Below T_C, the MnO_5 polyhedra start to buckle and tilt, inducing the trimerization of Mn^{3+} ions, while R^{3+} ions shift up and down (up-down-down pattern), as illustrated in Figure 1.5b. This imbalanced shift of R^{3+} results in a non-centrosymmetric structure with spontaneous polarization along the *c*-axis. Table 1.1 lists Curie temperatures and polarization values of h-$RMnO_3$ single crystals.

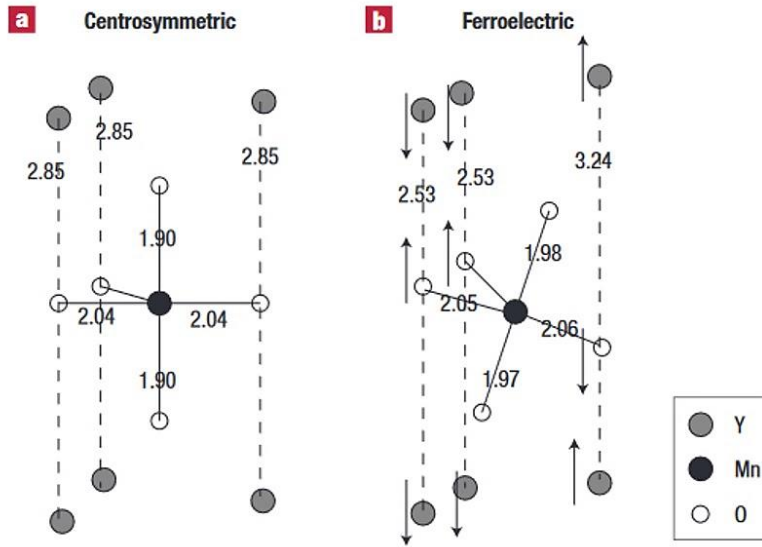

Figure 1.5: Schematic of a MnO_5 polyhedron with Y layers in (a) the centrosymmetric and (b) the ferroelectric structures. The bond lengths (Å) are indicated by the numbers, and the arrows depict atomic displacements relative to the centrosymmetric structure. These figures are from ref.[61]

Table 1.1: Curie temperatures (T_C) and polarization (from experiments and theoretical calculations) for hexagonal $RMnO_3$ single crystals. The low polarization values of $TmMnO_3$ and $LuMnO_3$ are due to the leakage current.

Compound	$YMnO_3$	$HoMnO_3$	$ErMnO_3$	$TmMnO_3$	$YbMnO_3$	$LuMnO_3$
T_C (K)	920[63]	873[64]	833[64]	621[65]	993[63]	750[66]
$P_{exp.}$ (μC cm^{-2})	5.5[67]	5.6[67]	5.6[67]	0.1[65]	5.6[67]	0.096[66]
$P_{theory.}$ (μC cm^{-2})	6.2[68]	8.0[69]	8.1[69]	8.3[69]	-	8.5[69]

Furthermore, h-$RMnO_3$ exhibit an intriguing polarization domain structure. The domains assemble in a "cloverleaf-like" pattern, where six domains merge at one line (vortex line) (Figure 1.6). Three types of antiphase domains (± α, ± ß, ± γ) arise from different trimerization, indicated by different tilting angles.[70] Here, ± refers to the polarization direction, either pointing up (+) or down (-). As sketched in Figure 1.6a, b, six domains can grow in a sequence of $[\alpha^+, \beta^-, \gamma^+, \alpha^-, \beta^+, \gamma^-]$ or in the reversed order, forming vortex or anti-Vortex structures. The distribution of vortices is shown in three dimensions (3D) in Figure 1.6c.[71] External stimuli such as electric fields,[15] pressure,[72] and thermal annealing (temperature, cooling rate)[73, 74] can change the density of vortices.

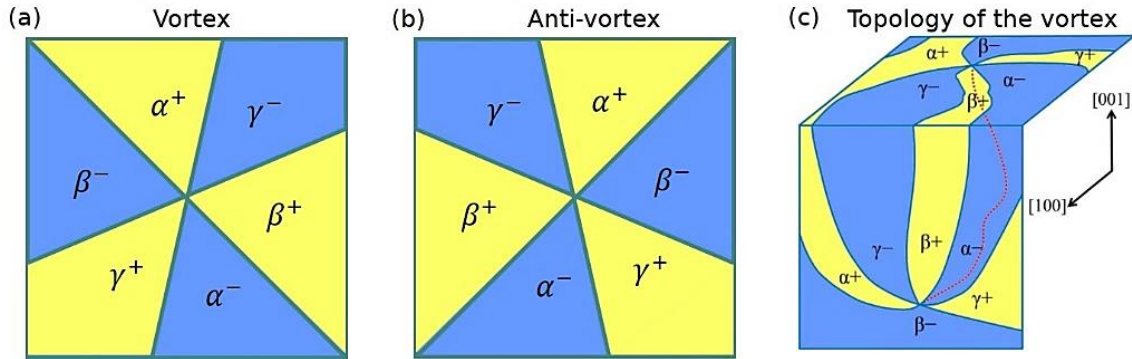

Figure 1.6: Schematics of six domains showing (a) a vortex $[\alpha^+, \beta^-, \gamma^+, \alpha^-, \beta^+, \gamma^-]$ structure, (b) an anti-vortex $[\alpha^+, \beta^-, \gamma^+, \alpha^-, \beta^+, \gamma^-]$ structure, and (c) the distribution of the vortex in three dimensions. Yellow and blue regions refer to upward and downward polarization domains, respectively. The red dotted line indicates the vortex line. This figure is from ref.[71]

Choi *et al.* first reported conductive atomic force microscopy (c-AFM) of the six-domain patterns, indicating different conductance of domains and domain walls.[70] Recently, both charged and neutral domain walls have caught great attention,[75–79] due to their wide range of functional electric properties. Piezoresponse force microscopy (PFM), showing domains with in-plane polarization (Figure 1.7a), together with the c-AFM study (Figure 1.7b), could provide information on positively charged head-to-head domain walls, negatively charged tail-to-tail domain walls, and neutral 180 ° domain walls. However, scientific and technological advantages of domain walls are limited in single crystals by the difficulty of measuring and accessing individual domain walls, as well as low scalability for integrating devices towards potential applications.

To the best of our knowledge, there is only one report of "cloverleaf-like" domains in thin films.[80] In this report, the polarization pattern was investigated in epitaxial hexagonal $YMnO_3$ thin films, which exhibits a domain size of ~ 20 nm (see Figure 1.7c).[80] Additionally, there are no reports on polarization hysteresis

loop measurements at room temperature for thin films, due to the presence of large leakage currents in the metal/p-type $RMnO_3$/metal stacks. Such measurements can be carried out at low temperatures.

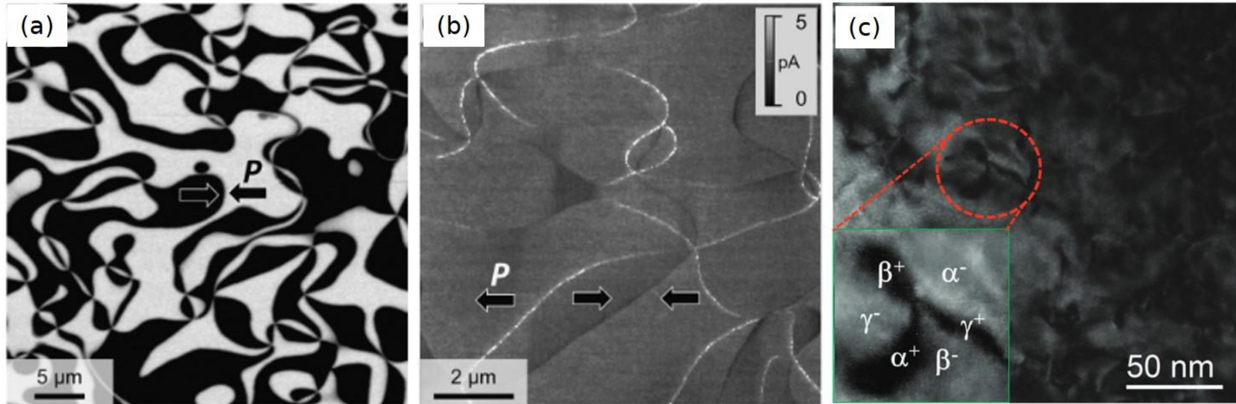

Figure 1.7: (a) Piezoresponse force microscopy (PFM) and (b) conductive atomic force microscopy (c-AFM) of (110)-oriented $ErMnO_3$ single crystal. Both figures are from ref.[81] (c) The dark-field transmission electron microscopy (TEM) image of an epitaxial $YMnO_3$ film in the [001] zone axis. The inset shows the enlarged single vortex domain structure. This figure is from ref.[80]

1.2.2 Orthorhombic $RMnO_3$

Orthorhombic $RMnO_3$ compounds are type-II multiferroics and their ferroelectricity is induced by a mechanism known as symmetric-exchange striction.[82, 83] This process involves the gain of magnetic exchange energy, which minimizes the total nearest-neighbor exchange energy through local ferromagnetic double-exchange interactions. Consequently, changes occur in the bond angles of Mn-O-Mn bonds between different phases, as illustrated in Figure 1.8. At 50 K, there exists one type of Mn-O-Mn bond with a specific angle, whereas at 21 K in the ferroelectric phase, two inequivalent Mn-O-Mn bonds emerge, leading to alternating bond structures along the *b*-axis. This alteration in bond structure corresponds to changes in the spin arrangement of Mn ions (ferromagnetic or antiferromagnetic), which in turn influence the Mn-O-Mn bond angles. The resulting atomic displacements of Mn and oxygen ions, particularly along the *a*-axis, contribute to the development of ferroelectric polarization.

However, achieving ferroelectricity typically requires temperatures below 40 K for bulk materials and 100 K for thin films,[84] which is not suitable for practical applications. Additionally, their electric polarization (P) is relatively small ($P < 0.5$ μC/cm^2),[82–86] compared to that observed in hexagonal $RMnO_3$ ($P \sim 5$ μC/cm^2, Table 1.1).

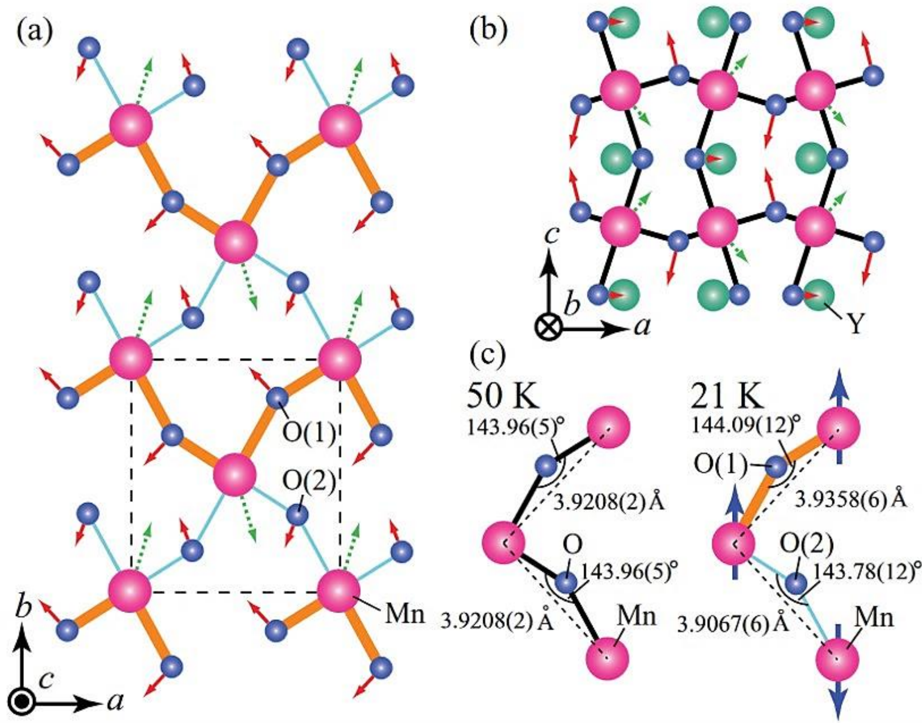

Figure 1.8: Schematics of the ferroelectric atomic displacements projected onto (a) the *ab* plane and (b) the *ac* plane in the ferroelectric E-type phase. Dotted and solid arrows indicate the directions and the relative atomic displacements of Mn and O, respectively. For clarity, the displacements of O ions are magnified. A unit cell is indicated by a broken line. (c) Changes in the Mn-O-Mn bond angles and the distance between the neighboring Mn ions in the *ab* plane. In the ferroelectric phase (21 K), the E-type spin configuration is represented by large arrows. Here we assumed the ferromagnetic (antiferromagnetic) spin arrangement for Mn-O-Mn bond with larger (smaller) bond angles. These figures are from ref.[83]

1.2.3 Electrical conductivity in $RMnO_3$

As $YMnO_3$ and $ErMnO_3$ are p-type semiconductors,[69, 87, 88] we provide a brief overview of the electronic conduction mechanisms involved in semiconductor thin films sandwiched by two metals. These mechanisms can be categorized as interface- and bulk-limited conductions.

The ideal barrier height between a p-type semiconductor and a metal can be described by the equation:

$$\emptyset_B = E_g + \chi - \phi_m \qquad \text{Equation 1.2}$$

where E_g represents the band gap energy, χ is the electron affinity of semiconductor, and ϕ_m is the metal work function.

Two types of contacts can form at the semiconductor and metal interface: ohmic (when $E_g + \chi < \emptyset_B$), or Schottky contacts (when $E_g + \chi > \emptyset_B$), as illustrated in Figure 1.9. The electronic conduction is governed by the bulk-limited conduction for ohmic contacts and dominated by interface-limited conduction for Schottky contacts.

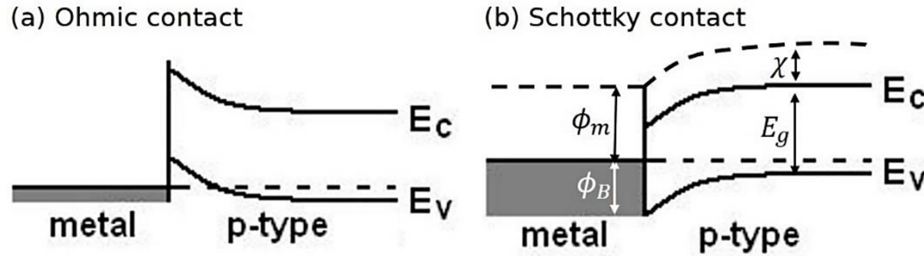

Figure 1.9: Band diagram showing formation of metal/p-type semiconductor as (a) Ohmic contact and (b) Schottky contact. These figures are adapted from ref.[89]

One typical interface-limited mechanism is Schottky or thermionic emission, wherein thermally activated electrons can overcome the energy barrier and be injected into the conduction band of the semiconductor.[90] This model allows us to express the current's dependence on applied voltage as:

$$\ln\left(\frac{I}{T^2}\right) = \frac{q\sqrt{q/4\pi\varepsilon_i d}}{kT}\sqrt{V} - \frac{q\phi_B}{kT} \qquad \text{Equation 1.3}$$

where I is the current, V is the external applied voltage, ϕ_B is the Schottky barrier height, ε_i is the permittivity of the switching layer, k is the Boltzmann's constant, T is the absolute temperature, and d is the Schottky distance.

There are other types of bulk-limited conduction mechanisms such as Poole-Frenkel, hopping, space-charge-limited conductions. Here, we describe the Poole-Frenkel model in detail. It involves thermally activated charge carriers being emitted from traps into the valence band of the p-type semiconductor.[90] This phenomenon can be mathematically described as:

$$\ln\left(\frac{I}{V}\right) = \frac{q\sqrt{q/\pi\varepsilon_i di}}{kT}\sqrt{V} - \frac{q\phi_T}{kT} + \ln\left(q\mu N_c\right) \qquad \text{Equation 1.4}$$

where ϕ_T is the trap energy barrier height, di is the dielectric distance, μ, and N_c are mobility and density of carriers, respectively.

Both hexagonal and orthorhombic $YMnO_3$ and $ErMnO_3$ are p-type semiconductors. The hexagonal phase has a band gap of ~1.5 – 1.6 V[87, 88] and the orthorhombic form has a band gap lower than that of the hexagonal phase.[69]

Bulk conductivity can be effectively modified by doping with different types and concentrations of impurities (donors and acceptors), which alters the charge density and potential trap barrier within the semiconductor.[91] In both the hexagonal and orthorhombic phases, R and Mn are typically trivalent in their ideal configuration. While R remains in its stable 3+ configuration, Mn can adopt other oxidation states (Mn^{2+} and Mn^{4+}) through the introduction of donors or acceptors, as illustrated in Figure 1.10.[92, 93]

The electronic structure of Mn^{3+} is represented by $[Ar]3d^4$ configuration. In the undoped case, the Mn $3d^4$ bands exhibit differences between the two phases due to their distinct crystal structures. In the hexagonal phase, a Mn^{3+} ion surrounded by five oxygen ions in a MnO_5 polyhedron configuration undergoes crystal field splitting of *d* electronic orbitals into three sets.[92, 94] Conversely, in the orthorhombic phase, a Mn^{3+} ion with six oxygen ions in an octahedron configuration experiences a different splitting of *d* bands attributed to the Jahn-Teller effect.[93, 95]

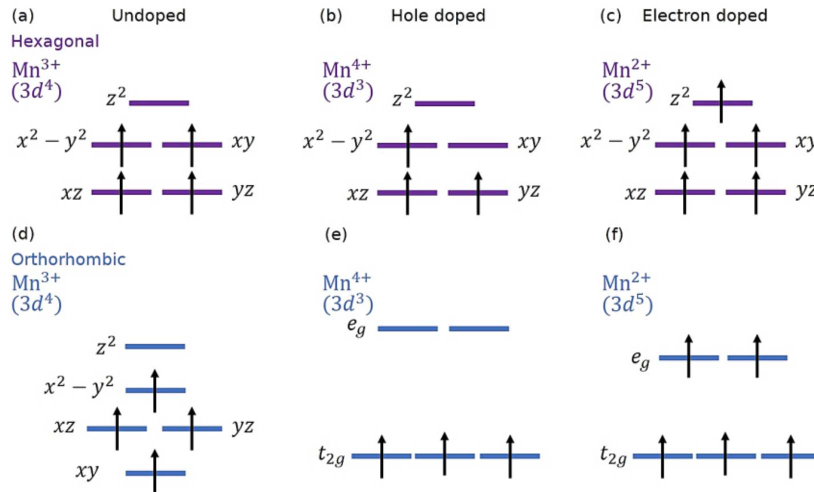

Figure 1.10: Illustration of the Mn *d* bands in undoped and doped (a-c) hexagonal $RMnO_3$ (polyhedron) and (d-f) orthorhombic $RMnO_3$ (octahedron). The Jahn-Teller effect occurs in undoped octahedron. Figure (a) is adapted from ref.[92] and figure (b) is adapted from ref.[93]

Hole and electron introduction into the Mn sites can be described by Equations 1.5 and 1.6, respectively. In the hexagonal phase, hole doping induces a transition from d^4 to d^3 by creating a hole in the $d_{x^2-y^2}/d_{xy}$ bands, and electron doping leads to a transition from d^4 to d^5 by introducing an electron into d_{z^2} band (Figure 1.10b, c).[94] For the case of orthorhombic phase, after holes and electrons are introduced, the Jahn-Teller distortion no longer exists, resulting in no splitting of the d bands (Figure 1.10e, f).[93, 95]

$$\mathrm{Mn}_{\mathrm{Mn}}^{x} + h^{\cdot} \longrightarrow \mathrm{Mn}_{\mathrm{Mn}}^{\cdot} \qquad \text{Equation 1.5}$$

$$\mathrm{Mn}_{\mathrm{Mn}}^{x} + e' \longrightarrow \mathrm{Mn}_{\mathrm{Mn}}' \qquad \text{Equation 1.6}$$

where $\mathrm{Mn}_{\mathrm{Mn}}^{x}$, $\mathrm{Mn}_{\mathrm{Mn}}^{\cdot}$, and $\mathrm{Mn}_{\mathrm{Mn}}'$ refer to Mn^{3+} (neutral), Mn^{4+} (p-type doped, positive) and Mn^{2+} (n-type doped, negative) on Mn lattice sites, respectively.

The conductance properties of $RMnO_3$ can be effectively modified by substituting the A-site (rare earth elements) with other elements such as Ca^{2+} (p-type doping) and Zr^{4+} (n-type doping),[94, 96] or by substituting the B-site (Mn) with other elements such as Cu^{2+} (p-type doping) and Ti^{4+} (n-type doping).[97, 98]

In this study, our primary focus is on oxygen doping to modify the oxygen content in $RMnO_3$, as described by the following equations. The oxygen content is significantly influenced by the atmospheres, whether oxygen-excess or -deficient, during the growth and annealing process.[99–103] Excessive levels of oxygen can lead to the formation of secondary oxidized phases.[104, 105] Despite that oxygen doping offers less precise control compared to element doping, it enables flexible tuning of the electrical conductance after synthesis.

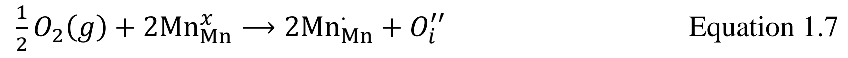

$$\frac{1}{2}O_2(g) + 2\mathrm{Mn}_{\mathrm{Mn}}^{x} \longrightarrow 2\mathrm{Mn}_{\mathrm{Mn}}^{\cdot} + O_i'' \qquad \text{Equation 1.7}$$

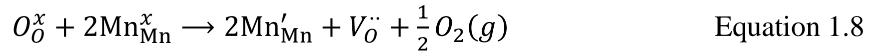

$$O_O^x + 2\mathrm{Mn}_{\mathrm{Mn}}^{x} \longrightarrow 2\mathrm{Mn}_{\mathrm{Mn}}' + V_O^{\cdot\cdot} + \frac{1}{2}O_2(g) \qquad \text{Equation 1.8}$$

where O_i'', O_O^x and $V_O^{\cdot\cdot}$ refer to oxygen interstitials (p-type doped), oxygen ions (neutral) and oxygen vacancies (n-type doped), respectively.

Now, we consider the oxygen defects in both crystalline phases. Prior research indicates that o-$RMnO_3$ is easily produced and stabilized in oxygen-rich environments, while reducing conditions favor the hexagonal structure (with oxygen vacancies).[54]

For the oxygen-deficient case, both hexagonal and orthorhombic structures have the formula $\mathrm{RMnO}_{3-\delta}$.

Let us consider now the oxygen-rich case. It has been extensively studied in the perovskite $LaMnO_3$, formulated as $\mathrm{LaMnO}_{3+\delta}$. The perovskite structure cannot accommodate excess oxygen in interstitial sites. The nonstoichiometry δ is instead accommodated by cation vacancies, as has been shown by several studies on the defect chemistry of that material either by thermogravimetric analysis measurements[106–108] or diffraction experiments.[109–111] Accordingly, the composition of $\mathrm{LaMnO}_{3+\delta}$ is better expressed as $\mathrm{La}_{1-x}\mathrm{Mn}_{1-x}\mathrm{O}_3$ with cation vacancies.[106–111]

Hence, in the close-packed perovskite structure of o-$RMnO_3$, the excess oxygen is accommodated via cation (R, Mn) vacancies ($\mathrm{R}_{1-x}\mathrm{Mn}_{1-x}\mathrm{O}_3$). This excess oxygen can enhance the perovskite's geometric stability

(larger tolerance factor) by reducing the ionic radius of Mn ions through the oxidation of Mn^{3+} to Mn^{4+} (see Equation 1.7).[112, 113] This aligns well with the density functional theory (DFT) based calculations by P. K. Todd *et al*.,[114] who evaluated the thermodynamic stability of $Y_{1-x}Mn_{1-x}O_3$ polymorphs (Figure 1.11). According to their findings, the defect-free hexagonal phase is thermodynamically stable at all temperatures ($T \leq 1400$ K), while the orthorhombic phase is predicted to be stable when the cation defect concentration exceeds 2.2% at $T = 0$ K, decreasing further with temperature. This observation is supported by significantly lower cation vacancy formation energies in the orthorhombic phase (compared to the hexagonal phase) as reported by Bergum *et al*.[112] Since cation vacancies are linked to an increased oxidation state of Mn, Mn^{4+} paired with cation vacancies is expected to be present in the orthorhombic phase.

In cases where cation vacancies in $R_{1-x}Mn_{1-y}O_3$ are not in equal proportions, more complex scenarios can arise. For instance, this situation may involve Mn^{4+} along with oxygen vacancies to compensate for more deficient R on the A-site.[115]

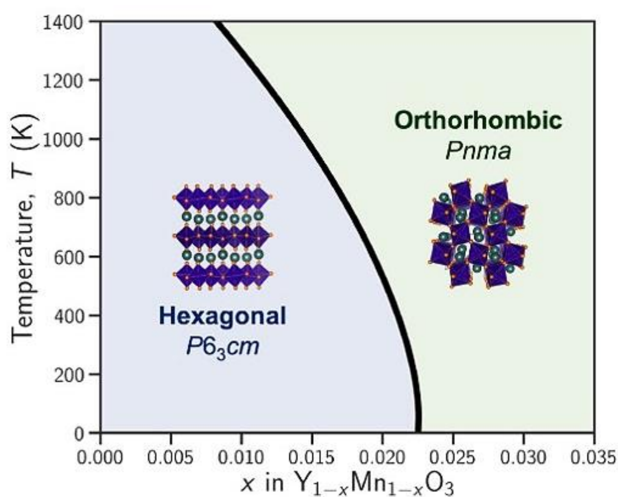

Figure 1.11: DFT-calculated phase diagram of cation-deficient $YMnO_3$ polymorphs with respect to temperatures and the concentration of cation (Y, Mn) vacancies, x, in $Y_{1-x}Mn_{1-x}O_3$. Note that all structures are initialized with antiferromagnetic orderings, and the Fermi energy of electrons is fixed at $E_F = 1.0$ eV. The figure is from ref.[114]

The defect mechanisms between the two crystalline structures differ significantly. Hexagonal $RMnO_{3+\delta}$ accommodates excess oxygen through oxygen interstitials paired with Mn^{4+}, as the layered hexagonal structure is ~11% less dense than the orthorhombic structure.[116] Additionally, the degree of excess oxygen accommodation varies between the phases,[117] with the orthorhombic phase potentially able to accommodate a higher degree of excess oxygen, leading to a higher amount of Mn^{4+}. The number of defects is heavily influenced by the synthesis process.

One of the most commonly reported conduction mechanisms in o-$RMnO_3$ is small polaron hopping conduction.[118–120] This process involves hopping between Mn^{3+}/Mn^{4+} states (p-type doped), as illustrated in Figure 1.12. Specifically, an electron with higher energy in Mn^{3+} transitions into the empty e_g-orbital of Mn^{4+}, along with double hopping conduction, where electron transitions on an O 2p-orbital connecting Mn^{3+} and Mn^{4+}.[121] Electron hopping between Mn^{2+}/Mn^{3+} states (n-type doped) is less commonly observed, primarily due to the longer bond length between Mn ions resulting from the larger size of Mn^{2+}, which increases the hopping energy.[122]

Furthermore, Poole-Frenkel conduction has been reported in both hexagonal[97, 123, 124] and orthorhombic $RMnO_3$.[125] These behaviors may originate from small polaron hopping.[126, 127]

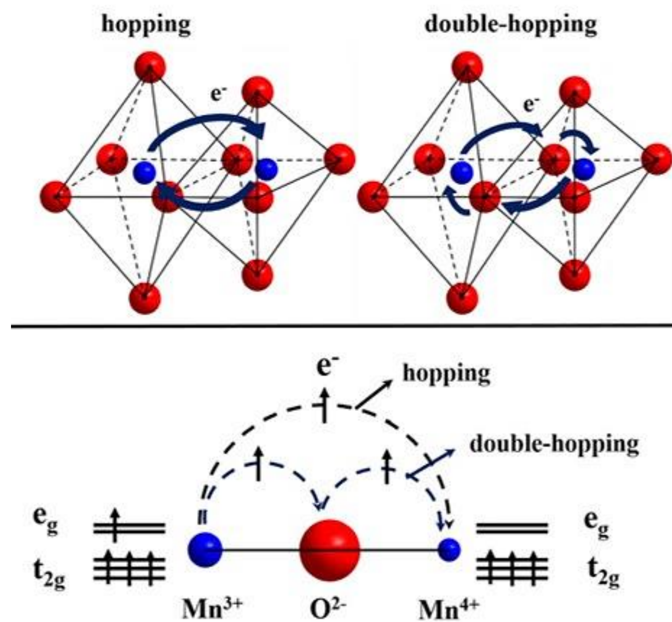

Figure 1.12: Mn^{3+}–Mn^{4+} hopping and Mn^{3+}–O–Mn^{4+} double hopping conduction model. This figure is from ref.[121]

1.2.4 Literature review on synthesis of $RMnO_3$ thin films

One of the pioneering studies on hexagonal $RMnO_3$ thin film growth was conducted by N. Fujimura *et al.* in 1996, who proposed such thin films as potential candidates for non-volatile memory devices.[128] They achieved epitaxial h-$YMnO_3$ films on MgO (111) and ZnO (0001)/sapphire (0001), as well as polycrystalline h-$YMnO_3$ films on Pt (111)/MgO (111) substrates using radio frequency (RF) magnetron sputtering at substrate temperatures ranging from 700 to 800 ºC.[128] P. A. Salvador *et al.* reported the successful growth of epitaxial o-$YMnO_3$ thin films on $SrTiO_3$ (001) and $NdGaO_3$ (101) substrates via pulsed laser deposition (PLD). They proposed that this metastable orthorhombic phase can be stabilized using epitaxial strain,[56] providing an alternative route to obtain the metastable phase without the need for high pressures and temperatures typically associated with traditional bulk synthesis techniques.[47–51, 53, 54] Shortly

after, J. P. Sénateur and C. Dubourdieu in collaboration with A. Kaul and O. Gorbenko demonstrated the growth of several normally non-stable phases by epitaxial phase stabilization.[45, 46, 57, 60, 129–132] $HoMnO_3$, $YMnO_3$, $TmMnO_3$ and $LuMnO_3$, which normally crystallize in a hexagonal structure, were stabilized in the perovskite orthorhombic phase using $LaAlO_3$ substrate.[57] Conversely, $DyMnO_3$, $GdMnO_3$, $EuMnO_3$ and $SmMnO_3$, which normally crystallize in an orthorhombic perovskite phase, were stabilized in the hexagonal form using ZrO_2 (Y_2O_3) substrate.[45, 46, 60]

$RMnO_3$ (R = Y, Er) thin films have been grown on various substrates including Si (111),[133–136] Si (100),[137–139] Si/Y_2O_3,[140–143] ZrO_2 (Y_2O_3) substrate,[45, 46, 60] Al_2O_3 (0001)/Pt (111),[80, 140, 142, 144, 145] Si/SiO_2/TiO_x/Pt,[144] Si/SiO_2/Ti/Pt.[22, 136, 146–150] Deposition techniques employed include sol-gel process,[134, 137, 140, 144, 147, 150, 151], molecular beam epitaxy (MBE),[142] atomic layer deposition (ALD),[152, 153] metal-organic chemical vapor deposition (MOCVD),[45, 46, 149, 154, 57, 60, 129–132, 136, 143] RF sputtering,[67, 128, 138, 139, 141] and PLD.[17, 21, 143, 145, 148, 155–157, 22–25, 56, 80, 133, 135] Among these techniques, PLD stands out as the most commonly used method at the moment, both for high-quality epitaxial h-$RMnO_3$ thin film growth for exploring multiferroic property [80, 145, 155] and for polycrystalline $RMnO_3$ thin film growth for device applications (later shown in Section 1.4.4).[17, 21–25, 156, 157] In this study, we use RF sputtering with post-deposition annealing to prepare polycrystalline $RMnO_3$ ($YMnO_3$ and $ErMnO_3$) thin films on Pt-coated Si substrates.

1.3 Emergent memory devices

As the demand for memory storage and computing technology continues to escalate, navigating the complexities of future memory technologies has emerged as a significant challenge.[158–161] Figure 1.13 illustrates key milestones in the history of non-volatile memory.[161] It began with Dr. Masuoka's invention of NAND flash in 1984,[162] which Toshiba commercialized in 1989.[161] Subsequent advancements included the introduction of multilevel cell NAND in 2001,[163] followed by the development of 3D NAND by Toshiba in 2007[164] and Samsung's 3D NAND in 2012. By 2010, embedded memories had progressed to the 28-nm node, revealing limitations with traditional concepts.[165] In 2015, Intel and Micron introduced 3D XPoint Technology based on phase change memory, which bridged the performance gap between dynamic random access memory (DRAM) and Flash, revolutionizing system memory architectures.[161]

Today, emergent memory technologies such as resistive random-access memory (RRAM), magnetic random-access memory (MRAM), phase-change memory (PCM) and ferroelectric random-access memory (FRAM), attract attention for next-generation memory architectures. These technologies offer not only scalability and enhanced performance, but also lower power consumption compared to the traditional memory solutions, making them promising candidates for addressing the evolving demands of future memory technologies.[160]

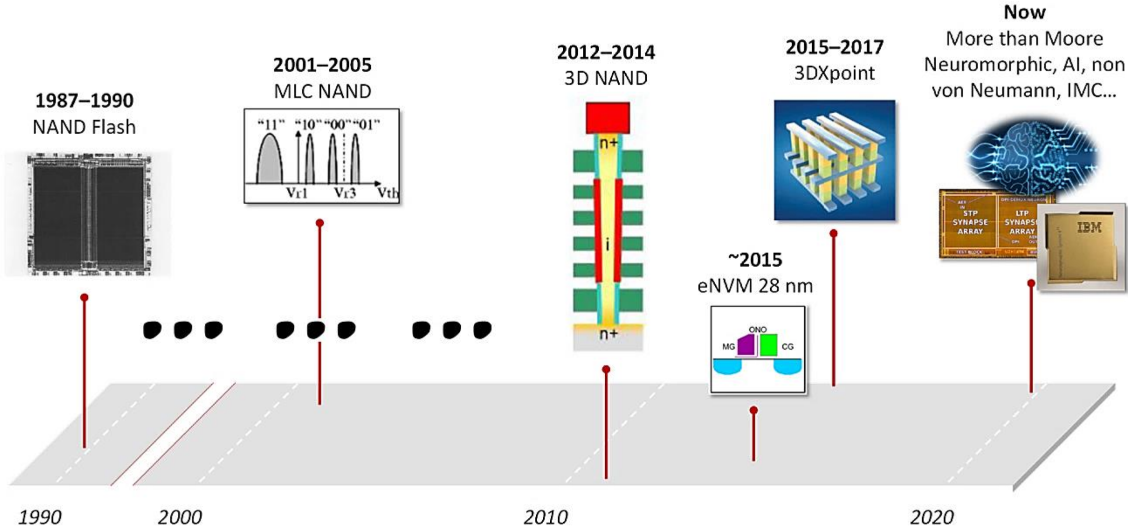

Figure 1.13: Main milestones in the history of non-volatile memories. This figure is from ref.[161]

1.4 Resistive switching devices

1.4.1 Neuromorphic applications

In traditional von Neumann computing systems, separate processing and memory units lead to significant costs in time and energy when moving large data between them (as shown in Figure 1.14a).[3, 4] This inefficiency poses challenges, especially for highly data-centric applications like artificial intelligence, where rapid access to large amounts of data is crucial. To overcome the von-Neumann bottleneck, neuromorphic computing systems offer a promising solution by emulating the structure and function of biological nervous systems in hardware. These systems integrate processing and memory units together, mirroring the parallel, distributed, and event-driven nature of the brain's neural networks (Figure 1.14b).

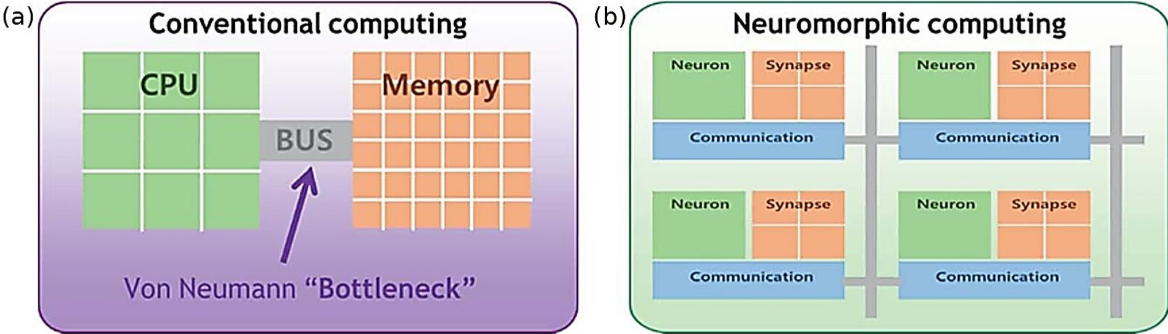

Figure 1.14: Comparison between (a) conventional computing and (b) neuromorphic computing. The figures are from ref.[166]

This concept is inspired by the remarkable efficiency of the human brain, which has approximately 10^{11} neurons, each forming around 10^{4} connections to other neurons, resulting in a huge network of approximately 10^{15} synaptic nodes.[167] Neurons comprise three main components: the soma, dendrites, and an axon (Figure 1.15a). The soma collects signals from dendrites and transmits them to other neurons via an axon, enabling rapid and accurate signal transmission within the nervous system. Synapses act as nano-gaps between neurons, linking the axon terminal of one neuron to the dendrite of another (Figure 1.15b). Signals passing through synapses are integrated in the soma to generate action potentials, determining the outputs to the post-synaptic neuron. The strength of this connection, referred to as synaptic weight, depends on ion concentrations and governs the interaction between neurons.[167] Through the modulation of ions and the release of neurotransmitters, synaptic weight regulates neural network behavior. This connectivity enables the brain to function as an efficient information-processing system.

In the context of neuromorphic computing, plasticity refers to the capability of artificial synapses to adjust their properties (such as synaptic weight) in an adaptable manner, similar to biological synapses. Emerging memories such as RRAM devices exhibit a resistive switching phenomenon and can be programmed in an analog fashion, making them suitable as plastic synaptic devices.[5–7] The adjustment of resistance levels in RRAM devices closely resembles the modulation of synaptic weight in biological systems, which efficiently store and process information. By dynamically altering their resistance levels in response to input stimulus, RRAM devices emulate plasticity in biological synapses, enabling the implementation of learning and memory functions within hardware.

Volatile threshold switching devices also hold promise in mimicking the spiking neuron behavior in computational models, such as the leaky integrate-and-fire model.[10–12] When equipped with additional capacitors and resistors, these devices can undergo abrupt changes in current or voltage in response to input signals, resulting in self-sustained oscillations. This characteristic effectively generates spike responses, which emulates the firing of neurons.[10–12] One significant advantage of these neuron circuits is that they do not require inductors, leading to low power consumption and enhanced scalability. This feature is vital for the development of large-scale neuromorphic systems, enabling efficient implementation of complex neural networks in hardware.

Artificial neuron networks have been developed to mimic the function of biological nervous system. The simple neural networks consist of input, hidden and output layers of neurons connected by artificial synapses (Figure 1.15c, d).[7] Synaptic devices like RRAM, arranged in a crossbar structure (Figure 1.15e), enable the construction of these networks for neuromorphic computing.[8, 9] This architecture allows for efficient, parallel processing of information, mimicking the highly interconnected nature of the human brain and offering significant potential for advancements in machine learning and artificial intelligence.

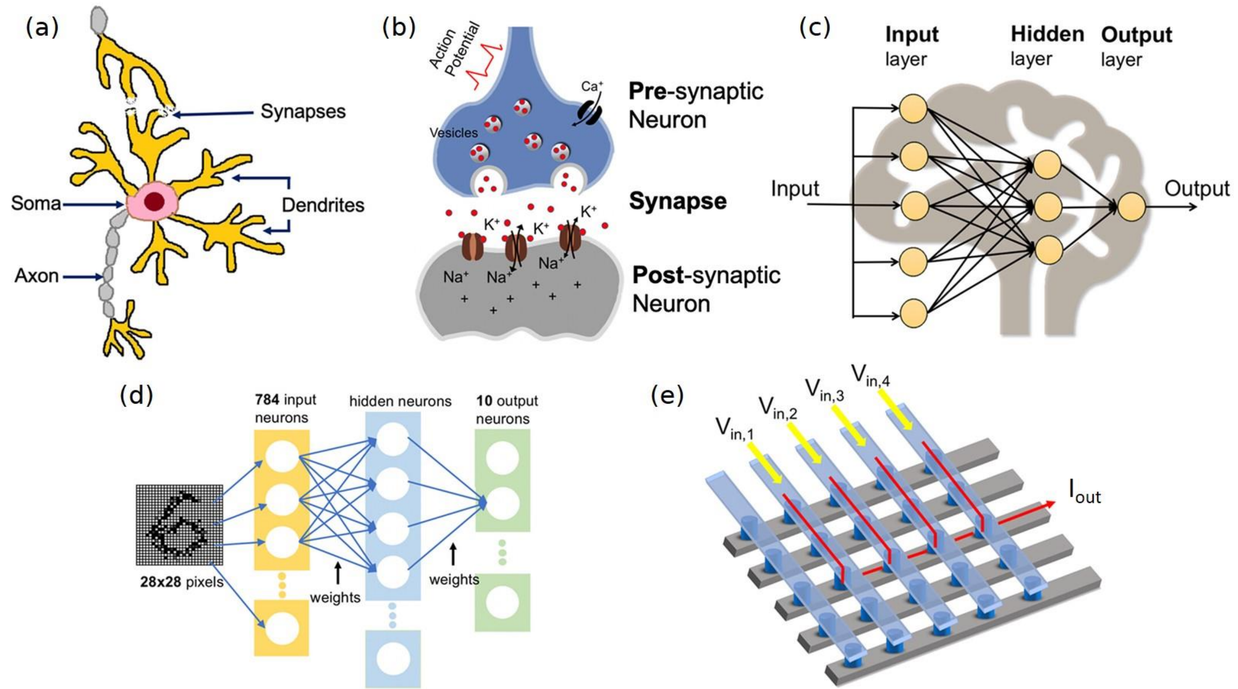

Figure 1.15: Schematics of (a) a biological neuron, (b) a synapse, (c) an artificial neural network, (d) a three-layer neural network for handwritten digit recognition, (e) a crossbar structure. The figures are from ref.[7]

1.4.2 Classification of resistive switching behavior

The RRAM memory cell features a capacitor-like structure, with insulating or semiconducting materials sandwiched between two metal electrodes (Figure 1.16).[160, 168] It exhibits resistive switching phenomena, wherein the resistance of the memory cell changes in response to an applied electrical stimulus (voltage or current). This property enables the storage of information based on distinct resistance states. Figure 1.16a illustrates a hysteresis current-voltage (*I*-*V*) curve of a resistive switching device. The device can be switched (write) between high resistance state (HRS) and low resistance state (LRS), which can be interpreted as a switch between logical “0” and “1”. These logical states can be subsequently read at a small voltage. Multistate resistive switching refers to a phenomenon when the resistances of memory cells can be altered to multiple discrete levels, rather than being confined to binary “0” and “1” states. This enhances storage densities and space efficiency in memory devices. Moreover, the ability to achieve multistate resistive switching is the key for these devices to mimic synapses in neuromorphic computing, facilitating the emulation of synaptic plasticity.

By implementing the crossbar array configuration (Figure 1.16b), where RRAM cells can be integrated at the intersections of perpendicular nanowires (word lines and bit lines), we can achieve the smallest theoretical size of $4F^2$ (cell size under the word line and bit line) and maximize area efficiency.[169]

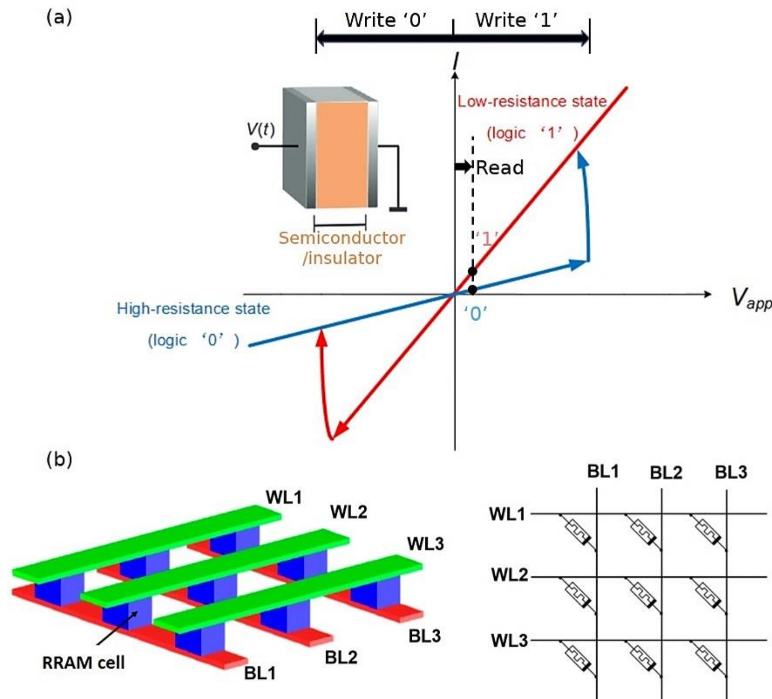

Figure 1.16: (a) Sketch of a resistive switching device and its hysteresis *I-V* curve. The figure is adapted from ref.[168, 170] (b) Sketch of the structure of crossbar arrays and its circuit diagram. WL and BL refer to word line and bit line, respectively. The figure is from ref.[169]

Resistive switching behaviors can be classified into unipolar and bipolar, based on *I-V* characteristics, as shown in Figure 1.17a, b.[171] In unipolar switching, the Set process – switching from the high resistance state (HRS, OFF state) to low resistance state (LRS, ON state), and the Reset process – switching from LRS to HRS, occur while applying the same polarity. In bipolar resistive switching, the Set and Reset processes take place depending on the polarity of the applied voltage. For both types of resistive switching behaviors, a compliance current of the control system (source) is applied, or a series resistor is added during the Set process, to avoid device hard breakdown.

Additionally, resistive switching can also be categorized into abrupt switching (Figure 1.17a, b), analogue switching (Figure 1.17c), and threshold switching (Figure 1.17d), based on their Set and Reset transitions. Both abrupt switching and analogue switching are non-volatile switching; the difference between them is characterized by either a discontinuous or continuous change when the applied voltage is ramped during the Set and Reset processes. The threshold switching is a volatile switching (Figure 1.17d).

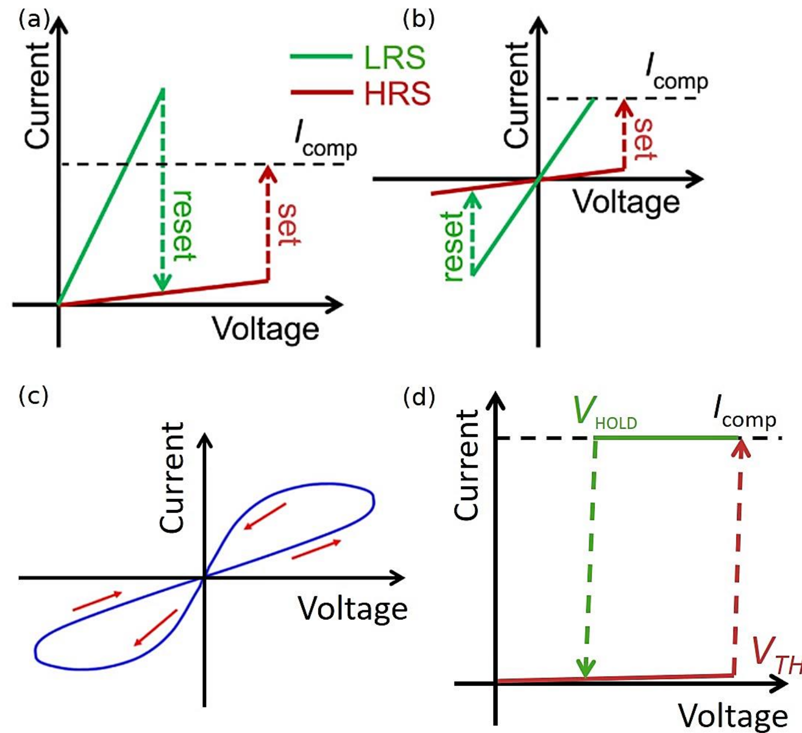

Figure 1.17: Different *I-V* characteristics in resistive switches. In figures the red solid lines show the high resistance state (HRS) and the green solid lines show the low resistance state (LRS). The red dotted lines refer to the Set process – transition from HRS to LRS and the green dotted lines refer to the Reset process – transition from LRS to HRS. Compliance current I_{comp} is applied during the set process to avoid device hard break down. (a) Abrupt unipolar switching, (b) abrupt bipolar switching, (c) analogue switching, (d) threshold switching (V_{TH} refers to threshold voltage and V_{Hold} refers to holding voltage). Note that threshold switching is volatile switching. Figures (a) and (b) are from ref.[171] Figure (c) is from ref.[172]

1.4.3 Physical mechanisms of resistive switching

In addition to classification based on the *I-V* characteristics, physical mechanisms can also be used to categorize resistive switching devices (Figure 1.18). Phase change, magnetic effect, or ferroelectric effect-based resistive switching are normally separated from the term "RRAM", and they will not be discussed.

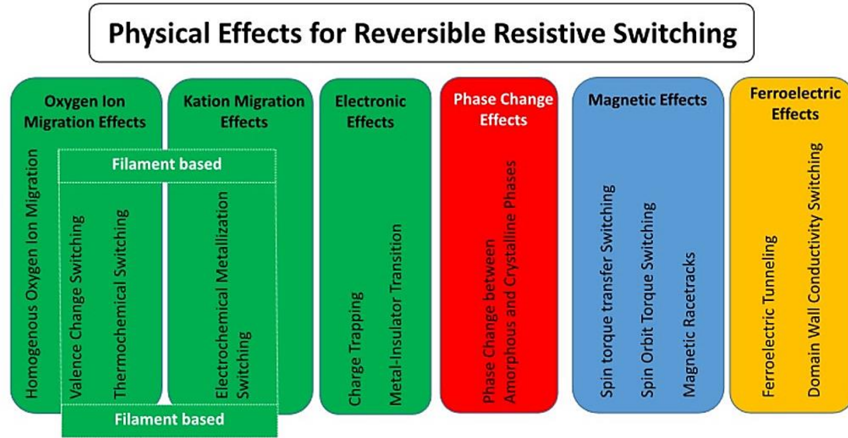

Figure 1.18: Possible physical mechanisms of resistive switching behaviors. The mechanisms marked in green are summarized under RRAM. Other mechanisms are classified as phase change, magnetic and ferroelectric effects-based memories. The figure is from ref.[173]

Besides all the possible physical mechanisms involved in RRAM devices (marked in green in Figure 1.18), the types of conducting path can be used to categorize the resistive switching.[160] One type of conducting path can be a localized filament. The switching behavior originates from the formation and rupture of one or several conductive filament(s), as illustrated in Figure 1.19a. Filamentary-type resistive switching is associated with abrupt switching. Studies have shown that filamentary conducting paths form easily in grain boundaries when the active material is polycrystalline.[174–176] The other type of conducting path is an interface, where the switching happens over the entire device area. This switching mechanism is often related to analogue and bipolar switching.

In this work, we will investigate electrochemical metallization (ECM) switching in Chapter 4, valence change memory (VCM) switching in Chapter 5, and threshold switching in Chapter 6. We will now explain the detailed mechanisms underlying these switching processes.

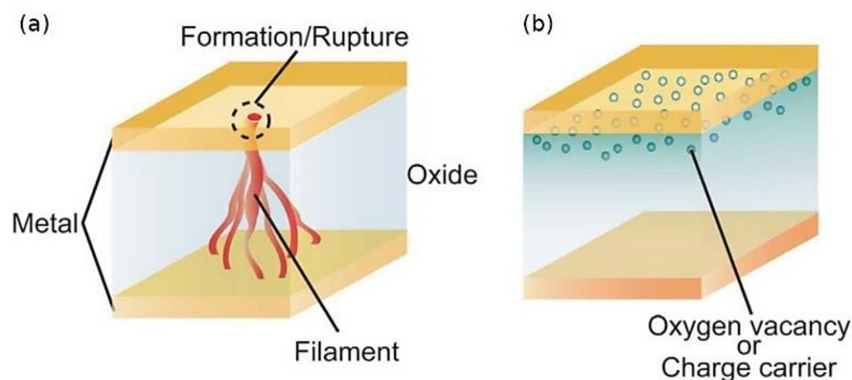

Figure 1.19: Proposed models for resistive switching under RRAM based on (a) a filamentary conducting path, or (b) an interface-type conducting path. The figures are from ref.[160]

1.4.3.1 Electrochemical metallization memory (ECM) switching

Electrochemical metallization memory (ECM), also known as conductive bridge RAM, relies on the formation and dissolution of a metallic filament (electrochemical dissolution and deposition of an active electrode metal).[177–179] The basic operation and the corresponding *I*-*V* characteristic are illustrated in Figure 1.20. The device consists of an active electrode metal such as Ag[180–184] or Cu,[185–189] a semiconductor/insulator solid state electrolyte such as SiO_2[184, 187–192] or Ge chalcogenides[182, 183], and an inert electrode such as W,[180, 185, 187] or Pt.[181, 186]

The device in its pristine state exhibits high resistance (Figure 1.20a). During the Set process, a positive bias is applied to the active electrode (Ag in this case) until it reaches the threshold voltage (V_{TH}). This process involves several steps: anodic oxidation and dissolution of the active electrode (Equation 1.9, Figure 1.20b), drift of metal cations towards the inert electrode under the electric field (Figure 1.20c), and reduction and electro-crystallization of metal on the surface of the inert electrode to form a metal filament (Figure 1.20d). Once the metal filament bridges the two electrodes (or when the gap is small enough to allow tunneling), the device switches from HRS to LRS. The Reset process takes place when an opposite polarity is applied, causing the electrochemical dissolution of the metal filament and the switching of the device back to HRS (Figure 1.20e).

$$M \leftrightarrow M^{n+} + ne^{-} \qquad \text{Equation 1.9}$$

where M^{n+} is metal cation.

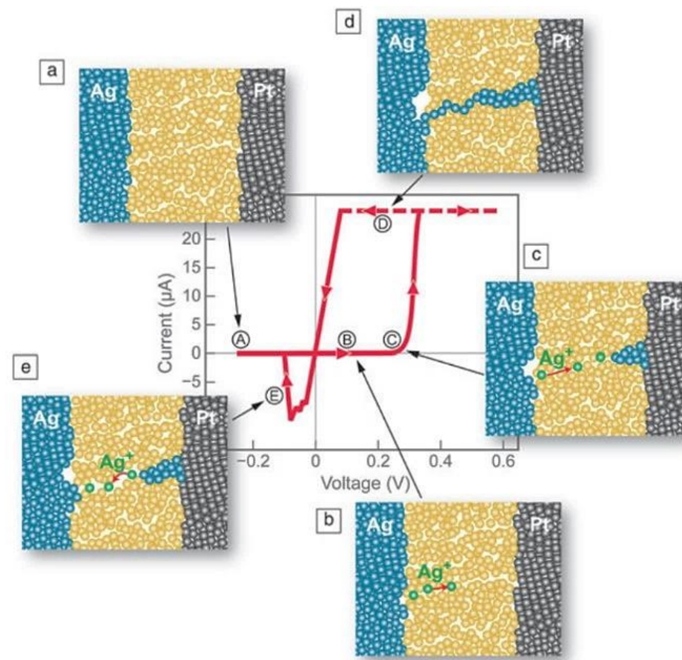

Figure 1.20: Electrochemical metallization switching (ECM). Schematic of the switching mechanism and an *I*-*V* characteristic for a typical ECM based switching cycle. The figure is from ref.[179]

ECM devices offer high scalability as the ON-state current is area independent. The current is determined by the size of the filament, which is at the nanometer scale. This promotes devices scaling down to footprints of 15 nm[193] and potentially atomic level in crossbar cells.[194] Additionally, ECM devices hold the advantages of fast operation (~20 ns),[183] low power consumption, and easy fabrication.[179] Voltage operation as low as 250 mV has been shown.[192] Quantized conductance has been shown in this type of devices, hence, offering the potential of multilevel resistance states.[187, 192]

1.4.3.2 Valence change memory (VCM) switching

Valence change memory (VCM) device typically consists of transition metal oxides with point defects as the active layer sandwiched by two metal electrodes. The origin of this switching is attributed to the migration of anions, typically oxygen ions related defects such as oxygen vacancies, leading to a subsequent valence change of the metals in metal oxides.[168, 195] There are fundamentally two different switching types based on the VCM mechanism: filamentary- or interface-type. Here, we focus on the filamentary-type mechanism.

In the filamentary-type VCM cell with asymmetric inert electrodes, proposed by R. Waser *et al*., the oxide layer exhibits different potential barriers with different electrodes which result in Schottky or ohmic contacts.[196, 197] The basic operation and the corresponding *I-V* characteristic are illustrated in Figure 1.21. During the Set process, a negative voltage is applied to the electrode A with the larger barrier potential at the interface. This leads to the occurrence of oxygen evolution reaction, generating oxygen vacancies (see Equation 1.10). The electric field drives the oxygen vacancies through the metal oxide towards the anode (electrode A, Figure 1.21B). The oxygen vacancy migration results in the formation of an oxygen vacancy-based nanoscale filament bridging both electrodes, causing the device to switch from HRS to LRS. During the Reset process, a positive bias is applied to electrode A. This positive voltage repels the oxygen vacancies away from electrode A, leading to local reoxidation (Figure 1.21C). Subsequently, the device turns back to HRS (Figure 1.21D).

$$O_O^x \leftrightarrow \frac{1}{2} O_2(g) + V_O^{\cdot\cdot} + 2e' \qquad \text{Equation 1.10}$$

To enable VCM switching, creating an asymmetry in the device structure is crucial. This can be achieved through various methods. Asymmetric inert electrodes can be used to create an oxygen gradient by forming different oxide/electrodes interfaces (Figure 1.21). A reactive electrode can be used, which will be oxidized at the interface with the oxide, and will act as an oxygen exchange layer at the interface.[198, 199] Additionally, changing the stoichiometry of the oxide during the deposition or post-deposition treatments can also create an oxygen gradient within the device.[200, 201] Note that the forming voltages in VCM cells can be modulated

by tuning the oxygen vacancy concentration in the pristine devices.[200, 201] This control over forming voltages provides flexibility in device optimization and performance tuning.

Filamentary-type VCM devices exhibit high scalability, multilevel switching capability[202] (by controlling the operation voltage[203] and compliance current[203, 204]), and high switching speed (~100 ps reported in Ta_2O_5[205]).

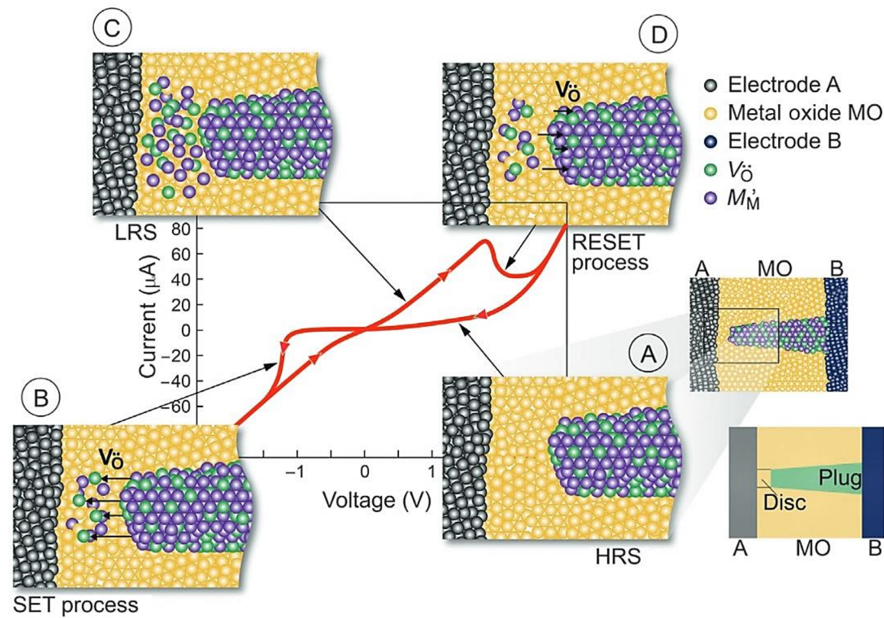

Figure 1.21: Valence change memory (VCM) switching. Schematic of the switching mechanism and an *I-V* characteristic for a typical valence change switching cycle. This figure is from ref.[197]

1.4.3.3 Threshold switching

Threshold switching is a type of volatile switching, which can be divided into three groups based on the active material: chalcogenide glasses, known as ovonic threshold switches (OTS) (Figure 1.22a),[206] fast-diffusing metal ions such as Cu and Ag (Figure 1.22b),[207] and metal oxides such as NbO_x,[208–214] VO_2,[215] TiO_2,[216] TaO_x,[217] $PrMnO_3$.[218]

We will concentrate on the mechanisms involved in metal oxides-based threshold switching. Some metal oxide threshold switches exhibit an S-type negative differential resistance (NDR) region, which can be stabilized with current-controlled sweeps, as shown in Figure 1.23b (the voltage-controlled *I-V* shown in Figure 1.23a). Most of these mechanisms can be explained by self-heating-triggered mechanisms (Figure 1.23c).[210, 212, 216–221]

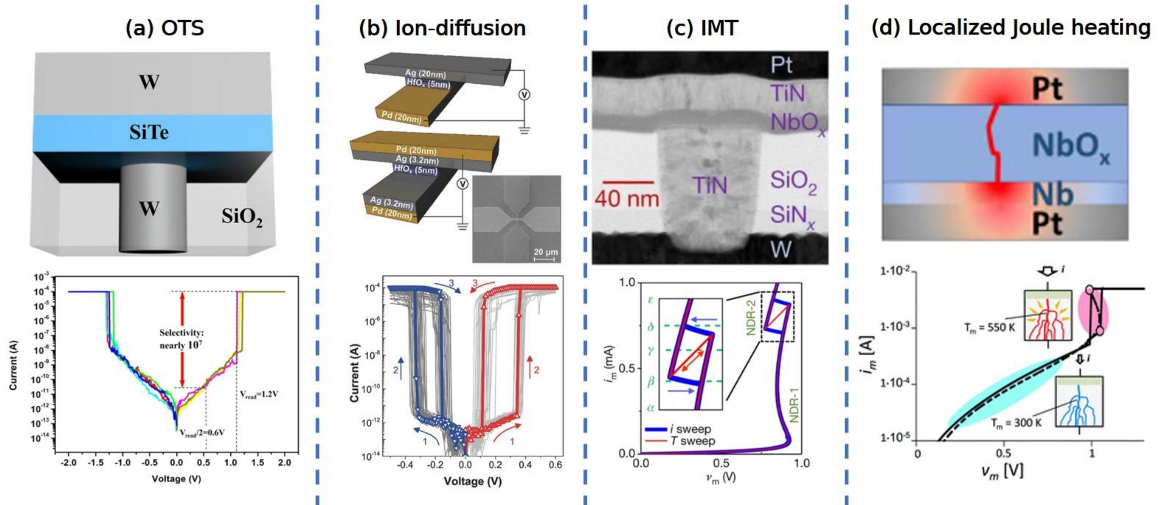

Figure 1.22: Various threshold switching devices. (a) Ovonic threshold switching (OTS). This figure is from ref.[206] (b) Ion-diffusion threshold switching. This figure is from ref.[207] (c) Insulator-metal transition (IMT). This figure is from ref.[222] (d) Self-heating triggered threshold switching. This figure is from ref.[219]

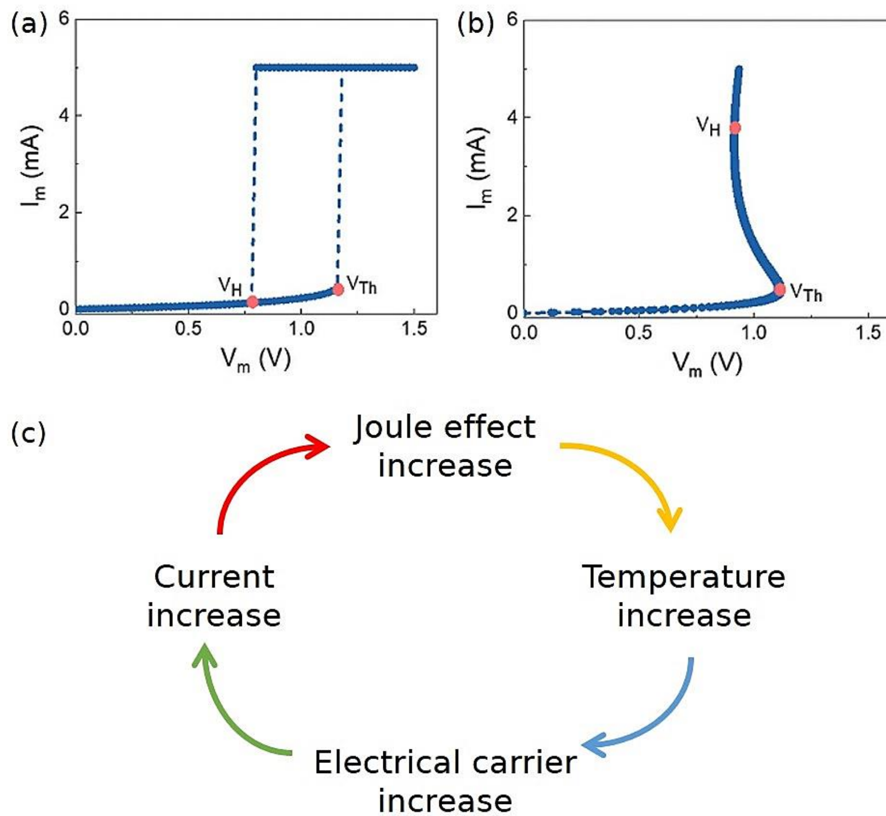

Figure 1.23: *I-V* characteristics of Pt/NbO_x/Pt devices under (a) voltage-controlled operation. (b) current-controlled operation. These figures are from ref.[223] (c) Schematic of self-heating-triggered mechanism: thermal runaway. The figure is from ref.[224]

Thermal runaway mainly occurs within two types of localized conduction paths: either a metal phase that has formed upon an insulator to metal phase transition (IMT) (Figure 1.22c),[222] or a conducting filament (Figure 1.22d).[219] When a filament is involved, the self-heating-triggered devices typically need to be electroformed to obtain a small-diameter conductive filament,[225] where localized Joule heating occurs. The threshold switching involving a filament in oxide such as NbO_x,[212, 213, 221] and TaO_x[217] has been successfully modelled using thermal feedback-based 3D Poole-Frenkel conduction. This model effectively combines electronic conduction with thermal feedback to explain the S-shape NDR. The conduction mechanism dominates the current flow below the threshold voltage, while self-heating of the filament dominates above the threshold voltage (higher current).

In this model, the conductivity is written as follow:

$$\sigma(F,\ T) = \sigma_p e^{-\frac{E_a}{k_B T}} \left\{ \left(\frac{k_B T}{\beta\sqrt{F}} \right)^2 \left[1 + \left(\frac{\beta\sqrt{F}}{2k_B T} - 1 \right) e^{\frac{\beta\sqrt{F}}{2k_B T}} \right] + \frac{1}{2} \right\} \qquad \text{Equation 1.11}$$

where $\beta = (\frac{q^3}{\pi\varepsilon_0\varepsilon_r})^{\frac{1}{2}}$, ε_r is the high frequency dielectric constant, E_a is the activation energy, $\sigma_p = \frac{L}{R_p A}$ is a prefactor constant, L is the film thickness, A is the active region area, R_p is the resistance, F is the electric field, and T is the internal temperature of the active region.

The internal temperature is supposed to be spatially uniform within the active region of the device and the heat transfer occurs at the quasi-static limit,[212] which can be described by the following equation:

$$C_{th}\frac{dT_N}{dt} = (T - T_{stage})\tau_{th} + IV_{dev}, \frac{dT_N}{dt} \sim 0 \qquad \text{Equation 1.12}$$

$$T = T_{stage} + IV_{dev}/\tau_{th} \qquad \text{Equation 1.13}$$

where C_{th} is the thermal capacitance, T_{stage} is the stage temperature, V_{dev} is the voltage drop over the device, and τ_{th} is the thermal conductance. Here we assume that τ_{th} is temperature independent in the investigated temperature range.

Self-heating-triggered threshold switching devices are closely linked to the leakage current of the devices; thus, their performances are significantly impacted by the intrinsic material properties.[221] Though this type of devices exhibits limitations in leakage current (normally larger than OTS), the devices hold advantages in endurance (10^{12} cycles).[226] They demonstrate good integration compatibility with metal oxide-based RRAM when employed as selectors, as they share the similar fabrication processes.[173, 221]

1.4.4 Literature review on resistive switching in $RMnO_3$ thin films

Few groups have explored non-volatile resistive switching performances in hexagonal polycrystalline $YMnO_3$ thin films[17, 21–25]. To the best of our knowledge, there is no study on $ErMnO_3$-based devices. As this work focuses on exploring switching behaviors in $YMnO_3$ and $ErMnO_3$ devices, a literature review on resistive switching in $YMnO_3$ is presented in this section. Note that there are currently no reports on ECM as well as threshold switching in devices based on $YMnO_3$ or $ErMnO_3$.

Studies on different electrode configurations, $YMnO_3$ composition variations, and microstructural aspects to explore the underlying mechanisms have been reported. Yan *et al.* investigated Pt/$YMn_{1-\delta}O_3$/Pt stacks, revealing unipolar resistive switching attributed to the formation and rupture of conductive filaments induced by Mn vacancies.[21] Bogusz *et al.* studied unipolar resistive switching in h-$YMnO_3$ films with Au or Al top and Pt bottom electrodes, identifying oxygen vacancies as key to filament formation along grain boundaries and charged domain walls.[17, 22] Wei *et al.* observed multilevel bipolar resistive switching in In/$YMnO_3$/Nb:$SrTiO_3$ devices, linking this behavior to modifications in the depletion region at the pn junction interface between h-$YMnO_3$ and Nb:$SrTiO_3$ upon polarization reversal.[23] Recent work by Rayapati *et al.* and by K. N. Rathod *et al.* studied cations doped h-$YMnO_3$ for electroforming-free filamentary unipolar resistive switching in Al/h-$YMnO_3$/Pt stacks,[24] and interface-type bipolar resistive switching in Ag/h-$YMnO_3$/Si.[25]

In Table 1.2, we summarize the reports on the polycrystalline $YMnO_3$-based resistive switching devices. Studies have been so far only focused on polycrystalline hexagonal $YMnO_3$ thin films (stoichiometric and off-stoichiometric). All these devices were prepared using pulsed laser deposition for $YMnO_3$ growth. None of the studies address the possible presence of the o-$YMnO_3$ in the polycrystalline h-$YMnO_3$ films and its potential role on the resistive switching properties.

Table 1.2: Literatures of resistive switching performances and parameters of polycrystalline $YMnO_3$-based resistive switching devices

System	Switching mode	Film thickness	Film preparation	V_{Form} (V)	V_{Set} (V)	V_{Reset} (V)	R_{OFF}/ R_{ON}	Retention (s)	Mechanism	Ref.
$Pt/YMn_{1-δ}O_3/Pt$	Unipolar	150	PLD at 800 °C	~ ± 10	~ ± (2.2 – 10)	~ ± (0.6 – 1.3)	> 10^4	> 10^5	Red/Ox metallic filament formation (Mn vacancy)	[21]
$Au/YMnO_3/Pt/Ti$	Unipolar	150	PLD at 800 °C	Free	~ ± 15	~ ± 2	> 10^3	> 5 × 10^4	Red/Ox metallic filament formation (oxygen vacancy)	[22]
$Pt/YMnO_3/Al/Ti$	Unipolar	153	PLD at 800 °C	Free	~ ± (3 – 20)	~ ± (0.7 – 5)	> 10^4	> 8 × 10^4	Red/Ox metallic filament formation (oxygen vacancy)	[17]
$Pt/YMnO_3/Al$		189		Free (-), +20 (+)	~ - (3 – 20), + (3 – 10)					
$Al/Y_{0.95}Mn_{1.05}/Pt$	Unipolar	200	PLD at 800 °C	~ ± 30	~ ± 10	~ ± 2	5.5 ×10^5	> 8 × 10^4	Red/Ox metallic filament formation (oxygen vacancy)	[24]
$Al/Y_1Mn_{0.99}Ti_{0.01}/Pt$				~ ± 30	~ ± 20		5.0 ×10^5			
$Al/Y_{0.94}Mn_{1.05}Ti_{0.01}/Pt$				Free	~ ± 25		6.0 ×10^5			
$In/YMnO_3/NSTO$	Bipolar	350	PLD at 800 °C	Free	+3.5	-3.5	> 10^3	> 5 × 10^4	Polarization reversal-induced modification of the width of the	[23]
$Ag/Y_{0.95}Sr_{0.05}MnO_3$ /Si	Bipolar	100	PLD at 700 °C	Free	+6	-6	3	–	Oxygen vacancy migration	[25]
$Ag/Y_{0.95}Ca_{0.05}MnO_3$ /Si	Bipolar	100	PLD at 700 °C	Free	+5	-5	> 10^2	–	Red/Ox metallic filament formation (oxygen vacancy)	[156]
Ag/ $Y_{0.95}Ca_{0.05}MnO_3$/N	Unipolar	100	PLD at 700 °C	Free	±10	±10	~10	> 10^5	Defects such as oxygen vacancy migration and charge	[157]

1.5 Objectives of this work

Compact and energy-efficient power supplies are essential for high-performance microelectronic systems, particularly in growing sectors such as mobility, industrial applications and energy.[227, 228] Addressing this need, the research project "Erforschung rekonfigurierbarer, passiver Mikroelektronikbauelemente für Energieeffizienz und Flexibilität" (ERMI) was funded by BMBF as part of the ForMikro program. This project aims to use novel passive components (inductors *L* and capacitors *C*) to develop energy-efficient voltage transformers for local power supply.[18–20]

In a study reported by H. Schmidt *et al.,* the vortex density in $YMnO_3$ thin films-based devices was linked to changes in resistances (HRS and LRS), as illustrated in Figure 1.24.[15] They found that a low vortex density corresponded to the HRS, attributed to fewer conductive vortices. Conversely, a high vortex density was associated with the LRS. In their interpretation, the nanosized vortices not only serve as the conducting path responsible for transitioning to the LRS, but also function as inductors due to their winding structures. They suggested that reconfigurability between capacitive state (HRS) and inductive state (LRS) could be achieved.

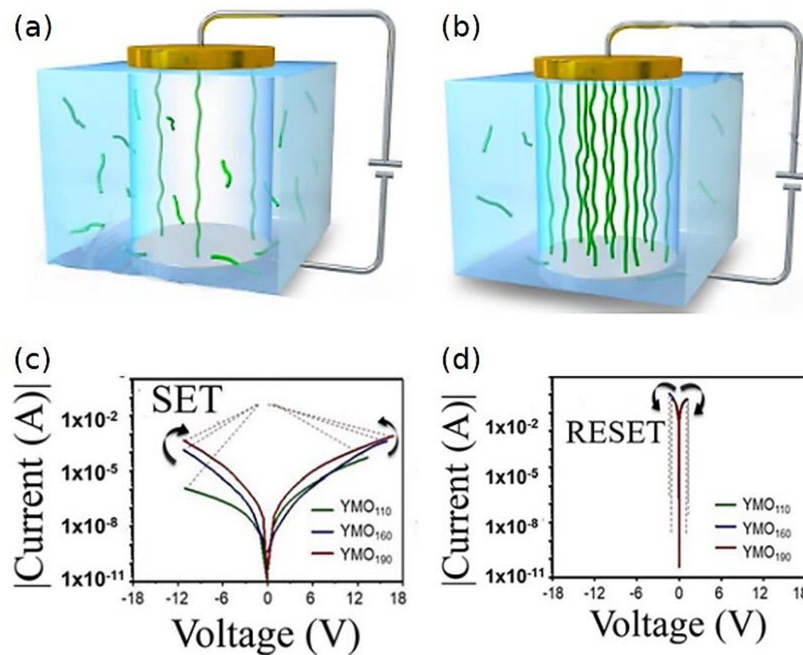

Figure 1.24: Sketches of reconfigurable devices based on ferroelectric manganite thin films ($RMnO_3$) (a) in the OFF state with a small vortex density and large resistance, (b) in the ON state with a large vortex density and small resistance. These figures were made by Heidemarie Schmidt from the ForMikro kickoff meeting. (c) and (d) Current-voltage (*I*-*V*) characteristics of the devices in OFF and ON states. These figures are from ref.[15]

One of the objectives of our study was to explore this concept further, investigating the reconfigurability between capacitive (OFF) and inductive (ON) states in devices. However, our investigation revealed that *L-C* reconfigurability is not possible due to actually negligible inductive behavior, as detailed in Chapter 3.

We shifted our focus to exploring *R-C* reconfigurability, as these compounds ($YMnO_3$, $ErMnO_3$) offered promising routes to tune the resistive switching based not only on the types of electrodes used but also on the possibility to leverage the properties of both the hexagonal and orthorhombic phases. Furthermore, combing resistive switching and ferroelectricity, if feasible, would offer an additional path to achieve multilevel analog resistive switching states for neuromorphic applications.[13, 14]

The objectives of this work are outlined below.

- Synthesizing of polycrystalline hexagonal $YMnO_3$ and $ErMnO_3$ films and of mixed hexagonal/orthorhombic films.
- Characterizing and quantifying the mixed crystalline phases: Develop a method to clearly identify and locate the orthorhombic phase within the hexagonal matrix. Subsequently, quantitatively estimate the fraction of the two crystalline phases (orthorhombic and hexagonal) in polycrystalline $YMnO_3$ and $ErMnO_3$ thin films.
- Studying ferroelectric properties of $YMnO_3$ and $ErMnO_3$ thin films.
- Studying and understanding resistive switching mechanisms: Investigate the mechanisms underlying resistive switching in $YMnO_3$ and $ErMnO_3$-based devices with different top electrodes.
- Optimizing device performance: Investigate the impact of film thickness and crystalline phase fractions on the performance of the memristive devices. Optimize device parameters to achieve desired characteristics such as ultra-low R_{ON} (required by ERMI project), low operating voltages, large memory window, and high endurance. Explore the possibilities offered by the coexistence of two polymorphs (hexagonal and orthorhombic) to design new devices. Engineering the amount and conductivity of the orthorhombic phase to modify the switching and to optimize the device performance.
- Integration into functional circuit (frequency compensation circuit): Investigate how the reconfigurability between capacitive and resistive states can be utilized to modulate the frequency response of the circuits.

The dissertation is structured in six chapters.

Chapter 1 provides an overview of the scientific background essential for understanding the material properties and resistive switching phenomena observed in rare earth manganite ($RMnO_3$) thin films.

Chapter 2 introduces the experimental methodology and characterization techniques employed in this work.

In Chapter 3, we explore capacitive and inductive behaviors in manganite thin films using two-terminal devices.

In Chapter 4, we investigate the electrochemical metallization resistive switching and its origin in Pt/$YMnO_3$/Al memristive devices with polycrystalline $YMnO_3$ films containing a mixture of o-$YMnO_3$ and h-$YMnO_3$ phases.

In Chapter 5, we study the bipolar resistive switching behavior in valence change memory Pt/$ErMnO_3$/Ti/Au devices and explore the impact of the hexagonal and orthorhombic phases and their relative content on the resistive switching.

In Chapter 6, we demonstrate, for the first time, electroforming-free threshold switching behavior in Pt/$ErMnO_3$/Pt devices, taking advantage of the mixture of hexagonal and orthorhombic phases. We propose a physical model of threshold switching to address the underlying physical mechanism and investigate the roles of hexagonal and orthorhombic phases on triggering the threshold switching.

Finally, we summarize the results and provide an outlook on resistive switching in $RMnO_3$-based devices.

Chapter 2: Experimental methods

2 Experimental methods 42
2.1 Film preparation 43
2.1.1 Sputtering 43
2.1.1.1 RF sputtering 43
2.1.1.2 DC sputtering 44
2.1.2 Evaporation 45
2.2 Device fabrication 47
2.3 Characterization methods 51
2.3.1 Grazing incidence X-ray diffraction 51
2.3.2 Spectroscopic ellipsometry 52
2.3.3 Atomic force microscopy 55
2.3.3.1 Basic principle 55
2.3.3.2 Conductive atomic force microscopy 57
2.3.3.3 Piezoresponse force microscopy 58
2.3.4 Scanning electron microscopy 59
2.3.5 Raman spectroscopy 60
2.3.6 X-ray photoelectron spectroscopy 62
2.3.7 Electrical characterization 64
2.3.7.1 Impedance measurement 65
2.3.7.2 Ferroelectric characterization 65
2.3.7.3 Current-voltage characteristic 67
2.3.7.4 Kelvin (4-wire) resistance measurement 67
2.3.7.5 Retention measurement 68
2.3.8 Operando time-resolved X-ray diffraction during PUND measurement 68

In this chapter, the experimental methodology and characterization techniques employed for the studies in the subsequent chapters are introduced. First of all, we describe the film preparation methods in Section 2.1. The detailed device fabrication process by photolithography is explained in Section 2.2. Finally, in Section 2.3 we summarize the principles of the characterization methods used: grazing incidence X-ray diffraction (GIXRD), spectroscopic ellipsometry, atomic force microscopy (AFM), scanning electron microscopy (SEM), Raman spectroscopy, synchrotron time-resolved XRD and electrical characterizations.

2.1 Film preparation

Manganite thin films were deposited by radio frequency (RF) sputtering. Different metal thin films were prepared by direct current (DC) sputtering and evaporation.

2.1.1 Sputtering

Sputtering deposition is a physical process, whereby a solid target surface is bombarded with high energy ions, resulting in backward scattered sputtered atoms, as illustrated in Figure 2.1.[229] In this work, RF and DC sputtering systems were used for oxide and metal depositions, respectively.

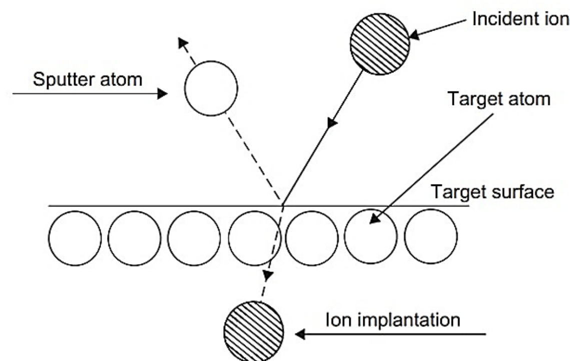

Figure 2.1: Physical sputtering processes. The figure is from ref.[229]

2.1.1.1 RF sputtering

RF sputtering supports a wide range of target materials, which can be conducting and non-conducting materials. RF sputtering provides more uniform and reproducible thin films during the deposition process (compared to DC sputtering), because charges built up on surface of the target can be eliminated by alternating currents (AC).

A typical sputtering system is sketched in Figure 2.2. Argon (Ar) as an inert gas is inserted and ionized in the vacuum chamber, through AC power source at radio frequencies. The manganite target material is bombarded by high energy Ar^+ ions and the backward scattered atoms are ejected from the target. These

sputtered atoms then travel through the vacuum chamber and reach the substrate, forming a thin film on the substrate.

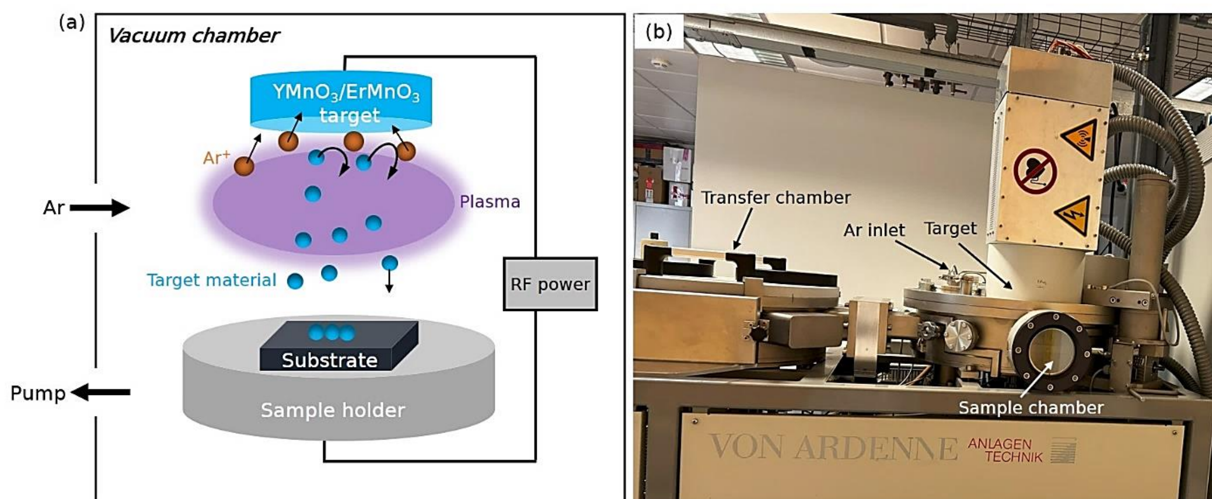

Figure 2.2: (a) Schematic of a RF sputtering chamber. (b) RF sputter system (Von Ardenne).

Von Ardenne RF sputter system was employed for the deposition of both $YMnO_3$ and $ErMnO_3$ thin films. The film thickness can be defined by changing the deposition time with a constant deposition rate. Note that a pre-sputtering process, with the same deposition parameters, was carried out for 5 min to clean up the impurity and contaminants on the surface of the target, and help to stabilize the sputtering process. The optimization process of the films will be discussed in Chapters 4 and 5.

2.1.1.2 DC sputtering

A DC sputtering system is illustrated in Figure 2.3. In DC sputtering, one electrode is the cathode with the metal Pt target and another electrode is the anode connected with the substrate. Ar gas is inserted and ionized in the vacuum chamber under DC power. The generated Ar^+ ions are accelerated towards the cathode and collide with the surface atoms of the target material, resulting in sputtered atoms ejected from the target. These atoms then travel through the vacuum chamber and hit the substrate, forming a thin film. The system utilized in this work has off-axis target-substrate configuration, whereby lower energy emitted sputtered atoms can be captured on the rotating substrate. Therefore, the energetic bombardment on the substrate can be largely minimized, leading to a more controllable process with better film quality.

The AJA International off-axis sputter system (Figure 2.3b), capable of operating in both DC and RF sputtering modes, was employed for the deposition of Pt and Ta layers. Note that Ta was deposited using RF sputtering. Table 2.1 lists the deposition parameters of Pt and Ta. These parameters were optimized by Sascha Petz from the Young Investigator Group MaXray at HZB.

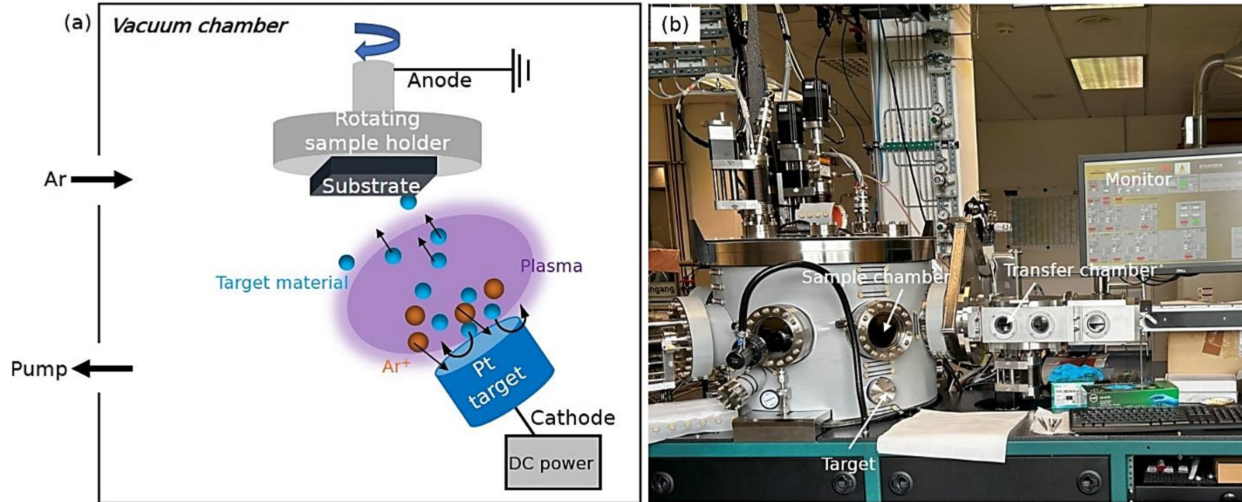

Figure 2.3: (a) Schematic of off-axis DC sputter chamber. (b) DC sputter system (AJA International).

Table 2.1: Deposition parameters of Pt and Ta.

Metal	Ar pressure (μbar)	DC power (W)	Temperature	Growth rate (nm/s)
Pt	4	400	Room temperature	0.102
Ta	4	300	Room temperature	0.025

2.1.2 Evaporation

Another deposition technique employed in this work for metallic electrodes is thermal or electron (E)-beam evaporation. A metal is evaporated in vacuum and then atoms condense on the substrate.[230]

Figure 2.4a shows a schematic of the thermal evaporation system. In this setup, the source material is placed on a tungsten boat functioning as a resistant heater. Upon supplying power to the boat, the target material is heated, causing the evaporation of atoms which then condense on the substrate to form a thin film.

Veeco thermal evaporator system (Figure 2.4b) in clean room at the Technical University of Berlin (TU Berlin) was employed for deposition of Al, Au, and Ti. The power applied to the boat is increased until a stable deposition rate is reached, which is on average at around 1 Å/s and kept lower than 3.5 Å/s.

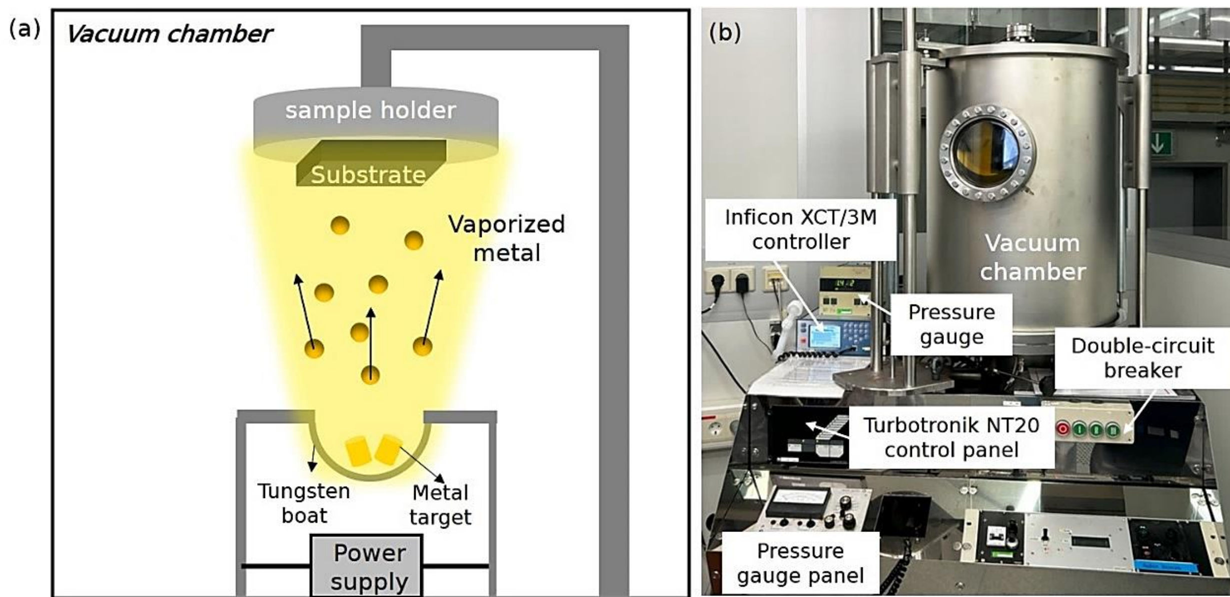

Figure 2.4: (a) Schematic of thermal evaporation. (b) Veeco thermal evaporator system in clean room at TU Berlin.

In Figure 2.5a, an evaporation system with another heat source – electron beam – is illustrated. In this configuration, a highly-charged electron beam possessing considerable energy is employed to melt the target material. Subsequently, the evaporated atoms are deposited onto the substrate positioned above the target. The E-beam evaporation technique is particularly suitable for materials with high melting temperatures, such as Pt, Ti and some oxides.

Telemark evaporator with a customized high vacuum system (Figure 2.5b) was applied for deposition of Pt and Ti. The electron beam typically works at 10 kV acceleration voltage with an emission current up to 200 mA. The deposition rates are at the range of 0.5 – 10 Å/s, which are monitored by a quartz crystal microbalance during deposition. All depositions were performed by Karsten Harbauer from the Institue of Solar Fuels at HZB.

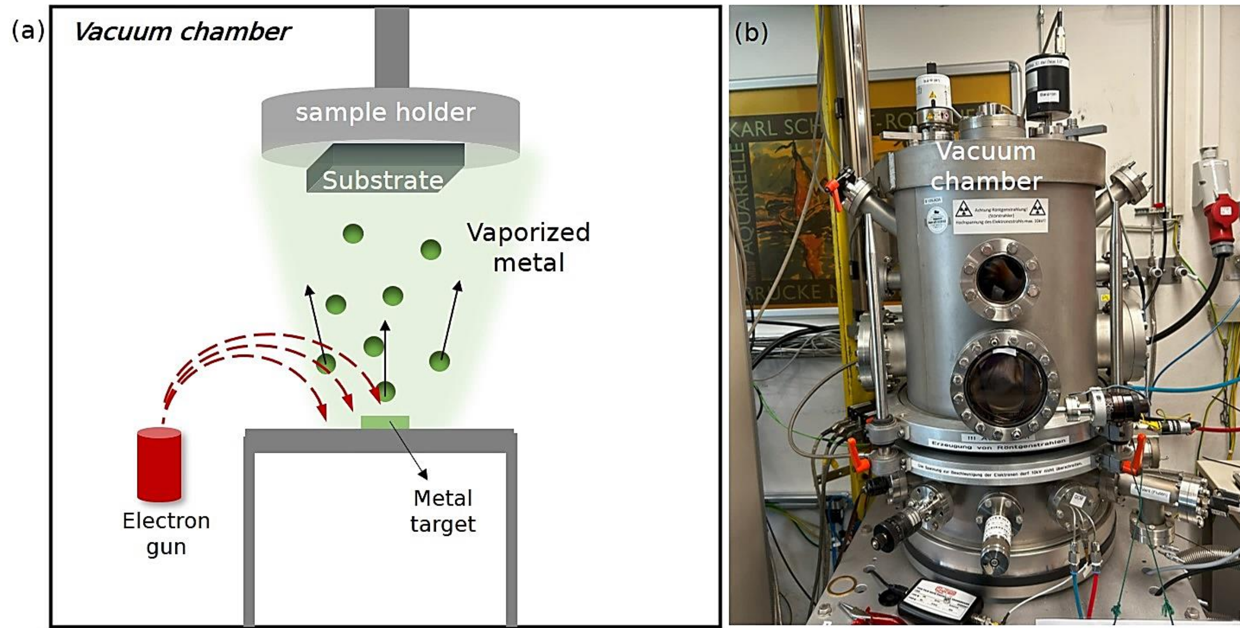

Figure 2.5: (a) Schematic of electron-beam evaporation. (b) E-beam evaporator system.

2.2 Device fabrication

Traditional photolithography requires the fabrication of a photomask and the use of a mask aligner to transfer the pattern onto a resist-coated sample. Direct laser writing lithography does not require a physical mask, since the pattern is exposed directly onto the sample using a focused laser beam.[231] It offers flexibility and superior resolution (~ 500 nm) but may be slower and more expensive than photolithography for large-scale production. We have used photolithography at the TU Berlin clean room and direct laser writing lithography at HZB.

Figure 2.6 depicts the micro-structuring process using a positive photoresist and its process parameters. Initially, a substrate or sample is uniformly coated with a ~1.6 µm-thick photoresist (AZ5412E) via spin coating at 4000 rpm for 30 s, followed by a pre-baking step (on hotplate at 90 °C for 3 min) to eliminate solvent residues from the resist. Subsequently, to transfer the desired pattern from a mask to the resist-covered substrate, the mask is precisely aligned with a dedicated mask aligner, and a 350 nm UV light is applied and expose the resist at dedicated locations for 24 s, as depicted in Figure 2.6 i). Alternatively, another method of pattern transfer, outlined in Figure 2.6 ii), involves direct laser writing lithography. Here, the pattern is directly exposed onto the photoresist using a 375 nm laser coupled with a light modulator to generate the desired features. Following exposure, the resist forms an indene carboxylic acid and can be soluble in alkaline solutions. The sample undergoes immersion in a developer solution (AZ726MIF) for ~40 s (exposed by mask aligner) or 60 s (exposed by direct laser writing), which selectively dissolves the exposed resist and leaves the unexposed areas in positive resist mode. Note that the developing time varies

slightly due to the humidity change in the clean room. After the developing, it is crucial to immerse the sample into the running deionized (DI) water and dry it with nitrogen, to remove the developer and stop the development step.

Subsequent steps involve the deposition of thin films such as manganites or metals onto the patterned resist. A lift-off process is then performed by immersing the substrate in acetone to eliminate the photoresist, leaving only the thin films in the patterned regions. Lift-off process of metal thin films is carried out at room temperature with ultrasonic cleaning in acetone for 5 min. Lift-off process of manganite thin films requires ultrasonic cleaning in acetone at 50 °C for 1 hour and 40 min followed with rinsing by DMSO for 10 s.

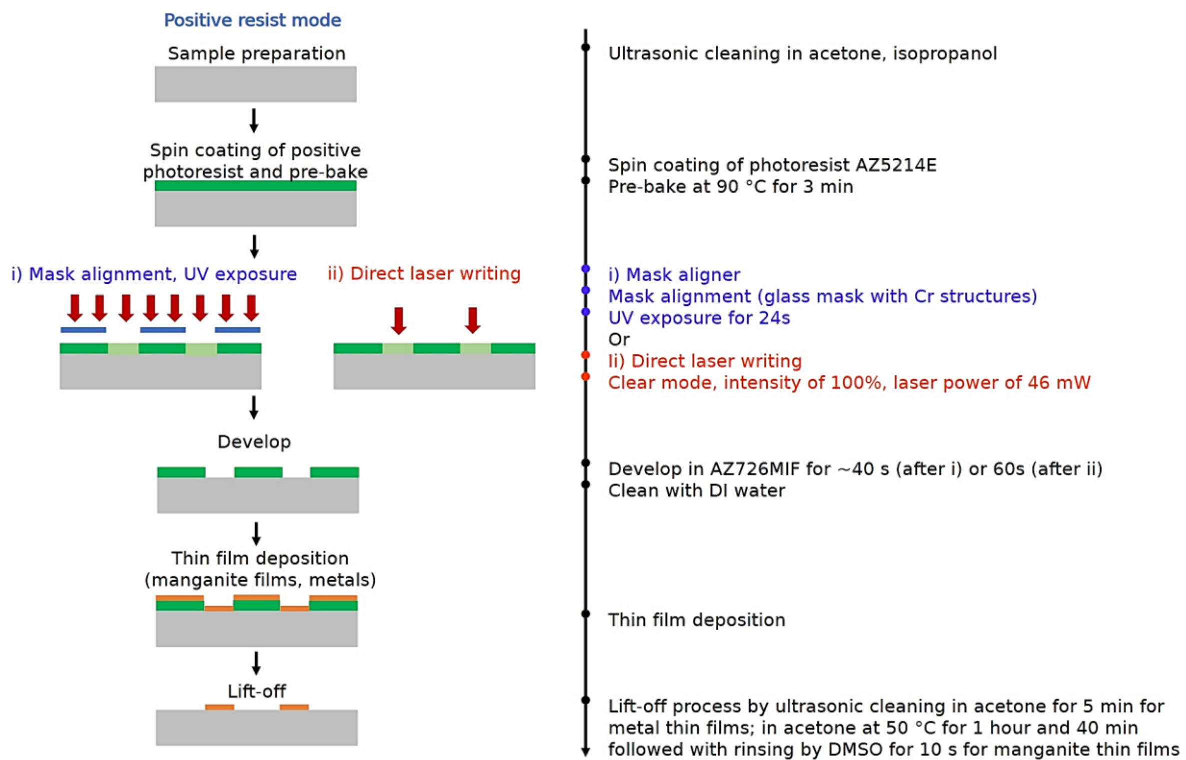

Figure 2.6: Micro-structuring by lithography processes in positive resist mode.

A bi-layer resist is applied for patterning and depositing thick films (larger than 200 nm in this work), as LOR develops isotopically, creating a bi-layer sidewall profile (Figure 2.7). Hence, lift-off works well with thicker film in this case. To obtain a bi-layer resist, a substrate is preheated at 170 °C for 2 min, which allows the spin coated LOR to adhere better to the surface. Then the LOR-coated substrate is pre-baked at 170 °C for 5 min to remove the solvent. All the following steps remain the same as shown in Figure 2.6; only the lift-off process is carried out by immersing the sample in NMP or DMSO for 5 min, followed by acetone for 5 min.

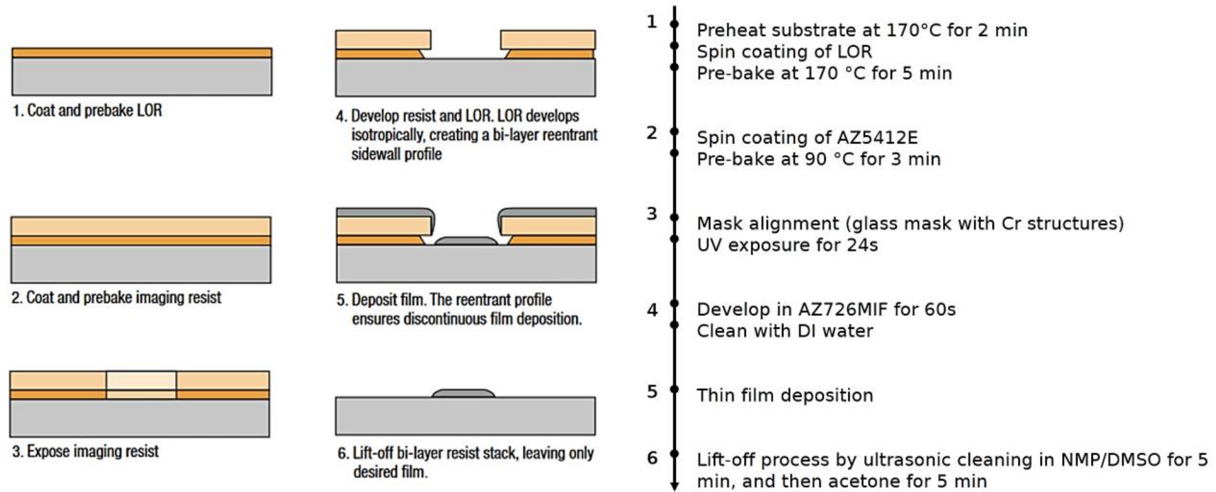

Figure 2.7: Micro-structuring by lithography processes with a bi-layer resist. The figure is adapted from ref.[232]

Additionally, during the device fabrication process, certain amorphous thin film layers, such as Al_2O_3, can be etched away during the development of the resist (Figure 2.6). To address this issue, an alternative micro-structing process is presented here, employing image reversal mode with positive resist, as depicted in Figure 2.8. Initially, a thin film layer such as tungsten, which needs to be patterned later, is deposited onto the sample with the Al_2O_3 layer. Subsequently, the resist is uniformly spin-coated onto the sample, followed by a pre-baking step (on a hotplate at 90 °C for 3 min). The resist is exposed to 350 nm UV at dedicated locations for 24 s after the mask alignment. Then a post-bake at 120 °C for 2 min is performed to the sample. Afterwards, the exposed areas of resist lose their capability to develop, whereas the unexposed areas remain photoactive, which is soluble in the developer after a flood exposure without a mask for 70 s. A patterned resist is then generated by immersion of the sample in the developer solution. Reactive ion etching (RIE) is performed to selectively etch away the metal layer and the resist is subsequently stripped away by immersing the sample in acetone, resulting in the formation of patterned metal structures.

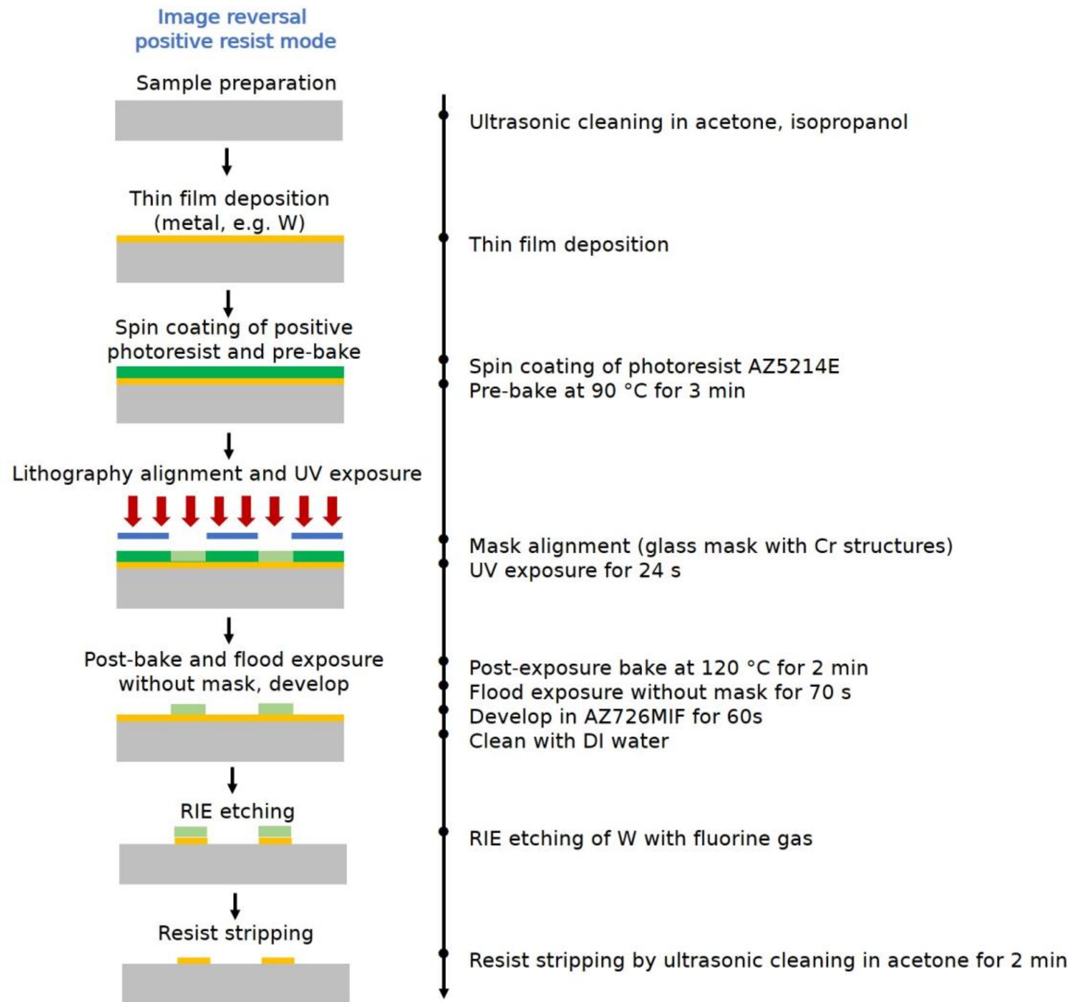

Figure 2.8: Micro-structuring by lithography processes in image reversal positive resist mode.

All the photolithographic processes involving the photolithography mask aligner (Karl Suss MA6 with a mercury short-arc lamp HBO 350 W from OSRAM, see Figure 2.9a) were carried out in the clean room at TU Berlin. All the processes involving the direct laser writing lithography (DLW66+ Heidelberg, see Figure 2.9b) were conducted at HZB. The device fabrication processes regarding detailed information on structures and materials will be described later in the Chapters 4, 5 and 6.

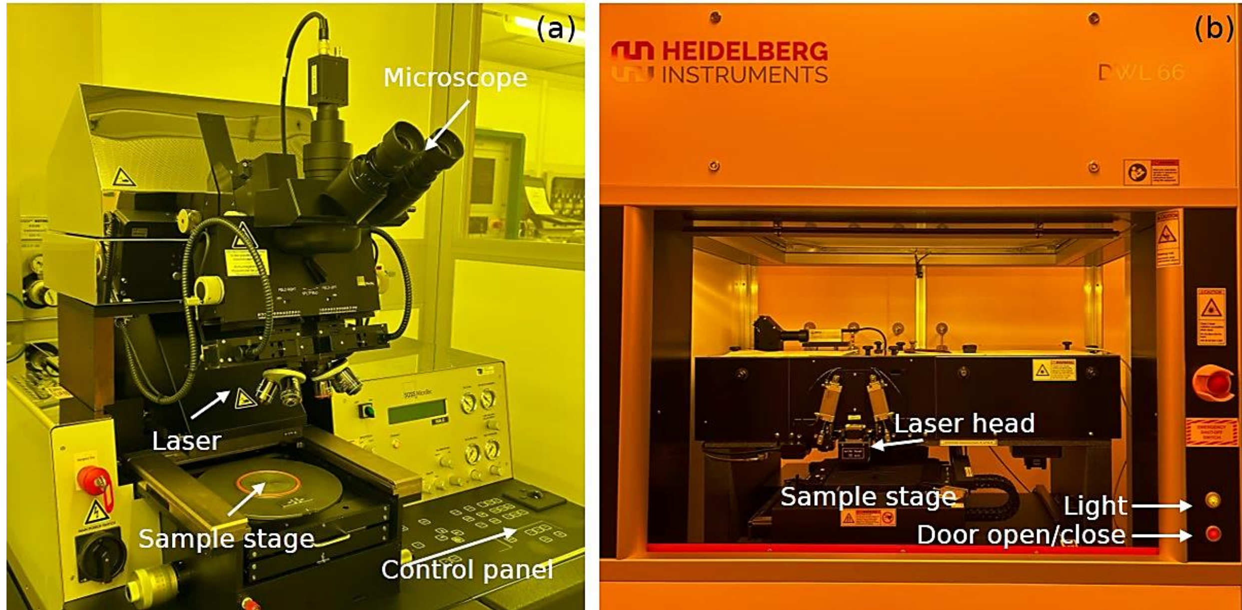

Figure 2.9: (a) Photolithography mask aligner (Karl Suss MA6) used during exposure process in clean room at TU Berlin. (b) Direct laser writing lithography (DLW66+ Heidelberg) in clean room at HZB.

2.3 Characterization methods

2.3.1 Grazing incidence X-ray diffraction

X-ray diffraction (XRD) is a non-destructive analytical method, which is based on the constructive interference of X-rays. By measuring the intensity of X-rays scattered at different angles from a sample, XRD provides valuable insights into the crystalline structure of materials.[233]

Grazing incidence XRD (GIXRD), characterized by a fixed small incident angle (ω), is a common characterization technique for polycrystalline thin films. A low angle of incidence increases the volume that will diffract in the thin films.[234] The setup of GIXRD is shown in Figure 2.10. The X-ray beam, generated by a cathode X-ray tube and filtered for monochromatic radiation, is subsequently collimated and directed at the sample at a fixed incident angle ω. The interaction between the incident X-rays (wave vector k_i) and the sample produces constructive interferences and diffracted X-rays (wave vector k_f) when Bragg's law (see Equation 2.1) is fulfilled. The X-ray detector is rotated around the sample to capture the diffracted pattern over 2θ range. Subsequently, data analysis follows for defining the d-spacings of the sample crystalline structure, identifying the compound, and determining its lattice parameters and crystalline orientations.

$$n\lambda = 2d \sin\theta \qquad \text{Equation 2.1}$$

where n is the diffraction order, λ is the X-ray wavelength, d is the inter-planar spacing and θ is the diffraction angle.

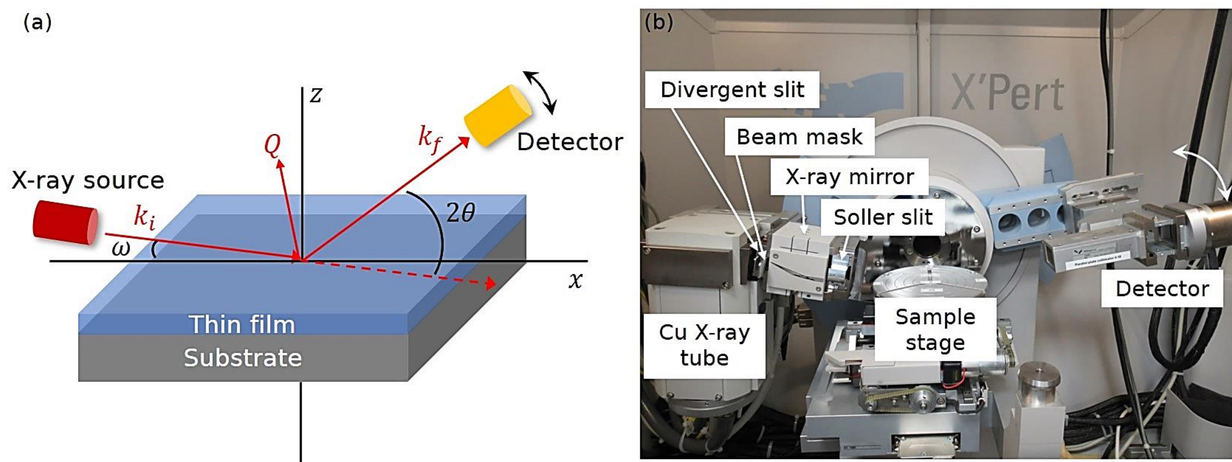

Figure 2.10: (a) Schematic of grazing incidence X-ray diffraction (GIXRD) measurement. ω is the fixed incident angle, 2θ is the diffracted angle, and $Q = k_f - k_i$ is the scattering vector. (b) PANalytical MPD diffractometer.

A PANalytical MPD diffractometer with Cu K_α ($\lambda = 1.5406$ Å) parallel beam was used for GIXRD measurements (Figure 2.10b). The setup configurations and scanning parameters are listed in Table 2.2.

Table 2.2: The setup configurations and scanning parameters employed for all GIXRD measurements.

Divergent slit	1/16°
Beam mask	2 mm
Detector	Xe point detector with parallel plate collimator
Incident angle	1°
Scan range	10 – 80°
Step size	0.1°
Scan time per step	10 s

2.3.2 Spectroscopic ellipsometry

Ellipsometry is a non-destructive optical technique, which provides the optical constants (refractive index n and extinction coefficient k) and layer thickness.[235]

The fundamental principle of ellipsometry is illustrated in Figure 2.11a, where linearly polarized light changes in its polarized state upon reflection from the sample surface at an incident angle θ (relative to the normal). The change in both amplitude and phase of the polarized wave depends on the optical constants (n, k) and film thickness of the sample layer. These changes are recorded by the detector as ellipsometry parameters (ψ, Δ),[236, 237] which can be described by the fundamental equation of ellipsometry.

$$\frac{R_{\mathrm{p}}}{R_{\mathrm{s}}} = \tan(\Psi) e^{i \cdot \Delta} \qquad \text{Equation 2.2}$$

where R_{p} and R_{s} are reflectances for the p- and s-polarizations, $\tan(\psi)$ and Δ represent the magnitude of the reflectivity ratio, and the phase difference between the reflected p- and s-polarizations.

A standard procedure of film analysis is presented in Figure 2.11b. First, the ellipsometry parameters (ψ, Δ) around the Brewster angle (where Equation 2.2 is maximal, 60°, 65°, 70° in this work) are recorded. Subsequently, a suitable optical model comprising a stack of multilayers with corresponding optical constants and thicknesses on an infinitely thick substrate is constructed. Different functional models are adopted depending on the material type: Cauchy model for transparent materials, Lorentz model for semiconductors with a transparent spectra region or metals, and Drude model for metals or heavily-doped semiconductors.[238] For $YMnO_3$ and $ErMnO_3$ thin films in this research, Tauc-Lorentz model is used, particularly suitable for semiconductors in their amorphous and polycrystalline forms.[238] Following the construction of the optical model stack (thickness, dielectric constants…), the (ψ, Δ) spectra can be analytically calculated. The parameters of the model are then adjusted to fit the experimental data. The determination of the optical constants and thin film characteristics such as thickness and roughness can then be extracted once the model converge to a solution closely matching the data. Additionally, film uniformity can be assessed by making a measurement at various position of the sample.

In this study, spectroscopic ellipsometry measurements were conducted using a Woollam M2000 Ellipsometer coupled with CompleteEASE software, as shown in Figure 2.12. During the measurements, different incident angles (60°, 65°, 70°) and a wavelength range of 192-1690 nm were used. A Tauc-Lorentz model was used to construct the optical model for a $YMnO_3$ or $ErMnO_3$ thin film on Pt-coated Si substrates.

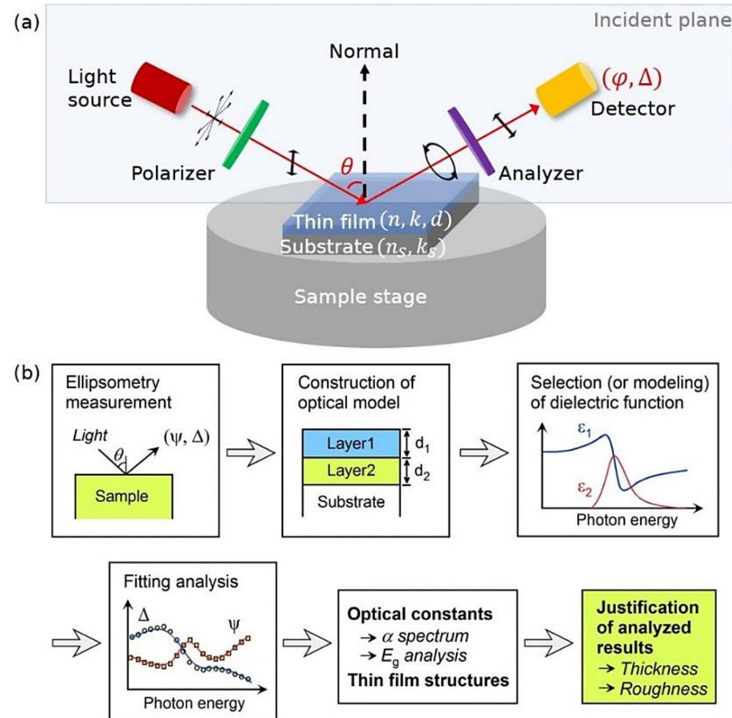

Figure 2.11: (a) Schematic of ellipsometry setup. n and k are the refractive index and extinction coefficient of the sample, respectively. θ indicates the incident angle. ψ and Δ are the ellipsometry parameters defined by the amplitude reflection coefficients for polarization. (b) A standard procedure for spectroscopic ellipsometry measurements. This figure is from ref.[235]

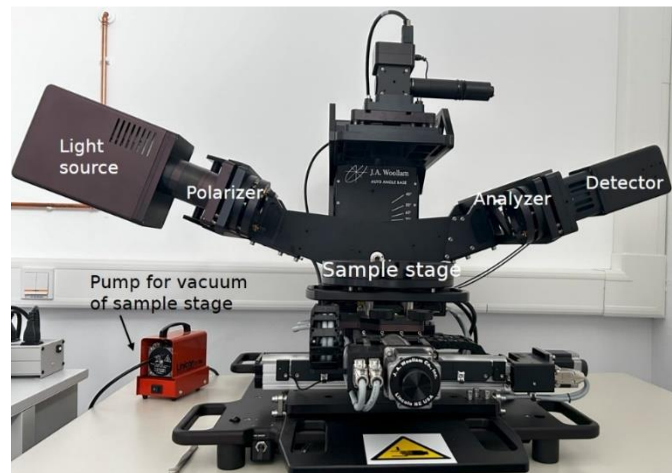

Figure 2.12: J.A. Woollam M-2000 Ellipsometer system.

2.3.3 Atomic force microscopy

Atomic force microscopy (AFM) is one of the most powerful surface characterization techniques to study the topography and some physical properties at sub-nanometer scale resolution, including mechanical, electrical or electromechanical properties. In this study, standard imaging and advanced modes, such as conductive AFM (c-AFM) and piezoresponse force microscopy (PFM), are employed with a Park Systems NX10 microscope (Figure 2.13). Table 2.3 provides an overview of the tips used in the experiments.

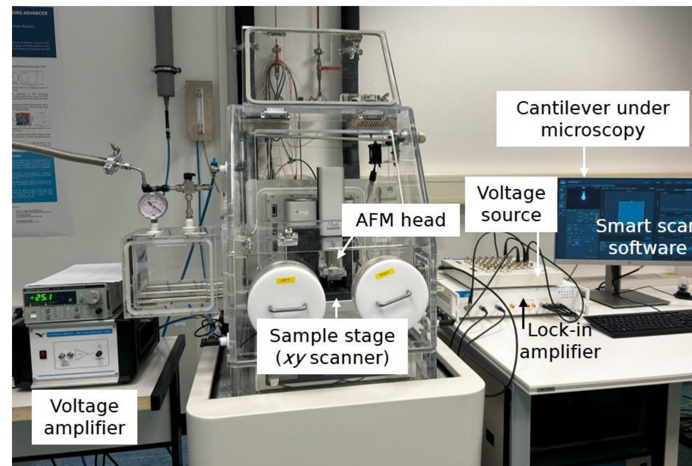

Figure 2.13: Park Systems NX10 AFM setup.

Table 2.3: Cantilevers and their parameters used in the experiments.

Probe name	Multi75-G[239]	Nano sensors PPP-EFM[240]	HQ:NSC14/Pt[241]
Resonance frequency (kHz)	75	75	160
Force constant (Nm^{-1})	3	2.8	5
Tip radius (nm)	10	< 7	< 30
Coating	None	Pt/Ir (95% Pt, 5% Ir)	Pt
Appropriate mode	Standard imaging	c-AFM, PFM	c-AFM, PFM

2.3.3.1 Basic principle

Figure 2.14 is the schematic illustration for the AFM operation where the tip scans the surface of the sample to acquire topographic information.[242, 243] The bending of the cantilever indicates the local height change on the sample surface by monitoring the laser spot reflected from the backside of the bent cantilever on a

split four-sector photodiode. The lateral torsion as well as the vertical bending of the cantilever, can be detected from the laser spot position on the quadrant photodiode, as depicted in Figure 2.14b.

For a precise topographic map of the surface, the sample usually undergoes a precise controlled movement in three directions (*x, y, z*) by the piezo scanner and a feedback controller.[242] The feedback loop is employed to keep the cantilever bending constant by controlling the height of the sample and the electronics records the height information for the topography as a function of the *x, y* location. Our NX10 microscopy has separate *xy*-scanner and *z*-scanner to minimize any mechanical crosstalk between *x*, *y* and *z* movements.

Depending on the distance between the tip apex and the sample surface, the operating modes are classified into contact, non-contact and taping modes (Figure 2.14c). The repulsive and attractive forces refer to short-range (Pauli, < 1 nm) and long-range forces (van-der-Waals), respectively.[244, 245] As a tip approaches the sample surface, it initially gets pulled towards the surface by the attractive force while the short-range repulsive force dominates the interaction with a further decrease of the distance between the tip and the surface. In the contact mode, the tip scans the sample surface while exerting a constant force onto the surface, which is set by the predefined setpoint. During the scanning, the cantilever gets bent in response to surface height variations and the feedback loop immediately adjusts the *z* scanner to maintain the constant cantilever bending or applied tip force, giving information on the surface topography.[242] Our study focuses on the contact mode and its advanced derivatives such as c-AFM and PFM.

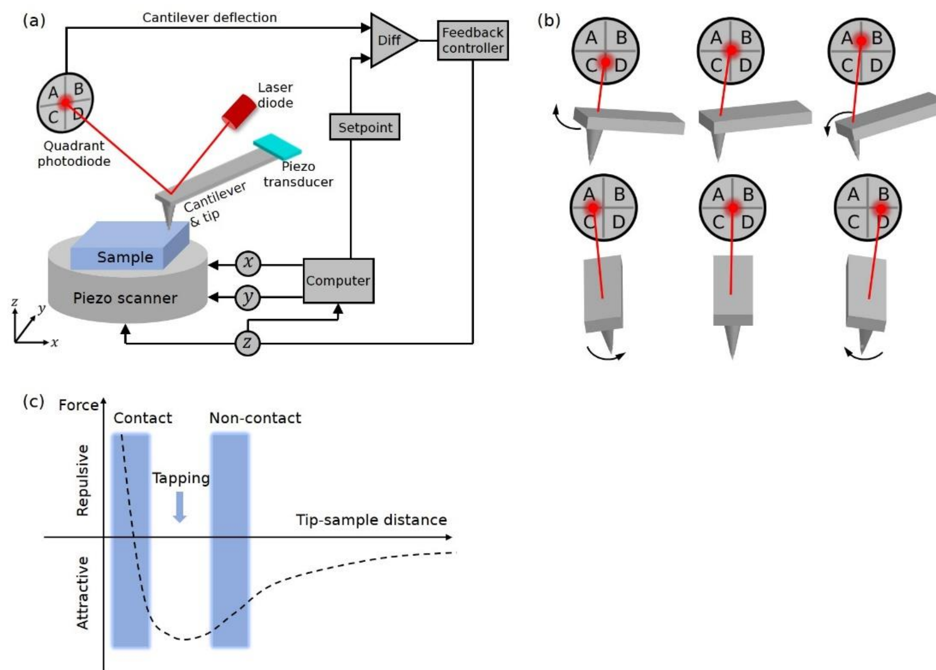

Figure 2.14: Principle of atomic force microscopy (AFM). (a) Schematic of AFM setup. (b) Different beam spot positions on the quadrant photodiode due to cantilever deflection in vertical and lateral directions. (c) Interatomic force as a function of the distance between the tip and the sample surface, different modes of the AFM operation are indicated along the tip-sample distance. Graph (a) partially adapted from ref.[242]

2.3.3.2 Conductive atomic force microscopy

Conductive atomic force microscopy (c-AFM) has emerged as a valuable tool to investigate the local conductance characteristics of samples by surface scanning in contact mode. As depicted in the c-AFM setup illustrated in Figure 2.15, a voltage source applies a certain voltage to the bottom electrode of the sample and the current flow between the conductive tip and the electrically biased bottom electrode is measured through an integrated current amplifier. Consequently, both the topography and the current maps of the sample are simultaneously obtained. In addition to imaging the current distribution at a given DC bias, the conduction behavior of the sample at a specific location can be investigated by *I-V* spectroscopy, whereby the voltage is systematically swept forward and backward at a given rate, which enables comprehensive assessment of sample conductance characteristics.[246]

Nevertheless, it is imperative to acknowledge a primary limitation inherent to c-AFM: the accuracy of the sample's conductivity characteristics is significantly influenced by the tip-sample contact.[247, 248] Factors such as sample surface roughness, contamination, tip geometry, applied tip force, and tip degradation throughout the measurements collectively influence the current flow between the tip and the sample. Thus, the findings obtained through c-AFM should be considered more qualitative in nature rather than strictly quantitative, reflecting the challenges associated with achieving precise and reproducible measurements under varying experimental conditions.

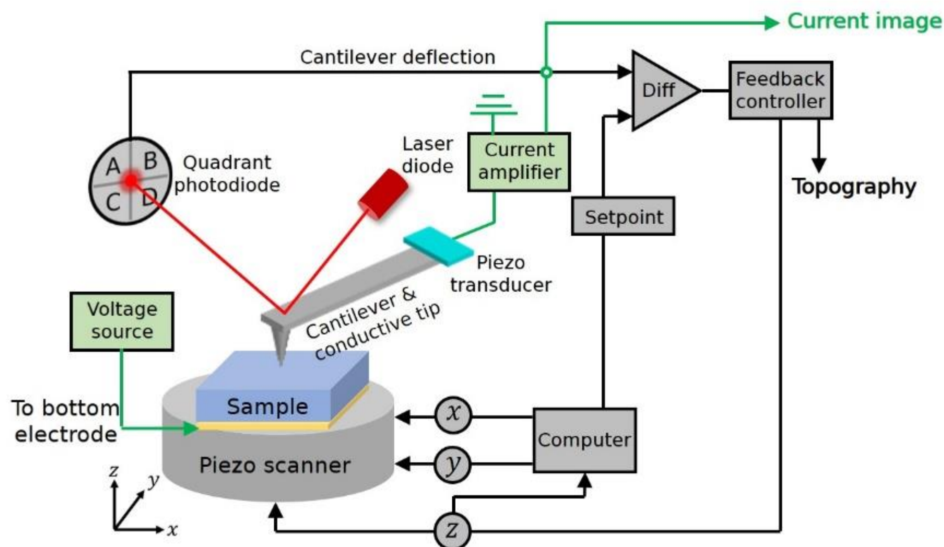

Figure 2.15: Principle of conductive atomic force microscopy (c-AFM).

During the c-AFM measurements, the conductive Pt-coated cantilever tip (Nano sensors PPP-EFM, HQ:NSC14/Pt) was grounded, and a DC bias was applied to the sample bottom electrode. A voltage magnifier (× 20) was employed when the applied voltage exceeds the maximum value of 10 V.

2.3.3.3 Piezoresponse force microscopy

Ferroelectric materials display a spontaneous polarization which can be switched by an external electric field or a mechanical inhomogeneous force. Piezoresponse force microscopy (PFM) is a powerful tool to image and manipulate ferroelectric domain structures of ferroelectric thin films at the nanoscale.[249–251]

The experimental setup of PFM is schematically presented in Figure 2.16. To image the ferroelectric domains, a conductive tip scans the sample surface in the contact mode while an AC voltage is applied to the bottom electrode of the sample, which brings piezoelectric vibration and, therefore, cantilever vibration. This vibration is detected by the laser spot vibration on the photodiode and the external lock-in amplifier demodulates the vibration signal, yielding the piezoelectric signal which is effectively separated from the topographic cantilever deflection. The phase signal from the lock-in amplifier corresponds to the vertical component of the local polarization. The piezoresponse signal is in phase or 180° out-of-phase with the applied field, if the polarization below the tip is parallel or antiparallel to the applied field, respectively (see Figure 2.16b). The amplitude signal reflects the amplitude of the polarization but also mechanical prospects of the surface and potential electrostatic interaction with the tip. The amplitude is zero at the domain wall between two 180 ° domains. In addition, manipulation of ferroelectric domain structures can be achieved through application of a DC voltage to the sample.

We used UHF lock-in amplifier from Zurich Instruments and conductive Pt-coated cantilevers (Nano sensors PPP-EFM) for PFM measurements. An AC voltage of 1.5 V peak-to-peak was used.

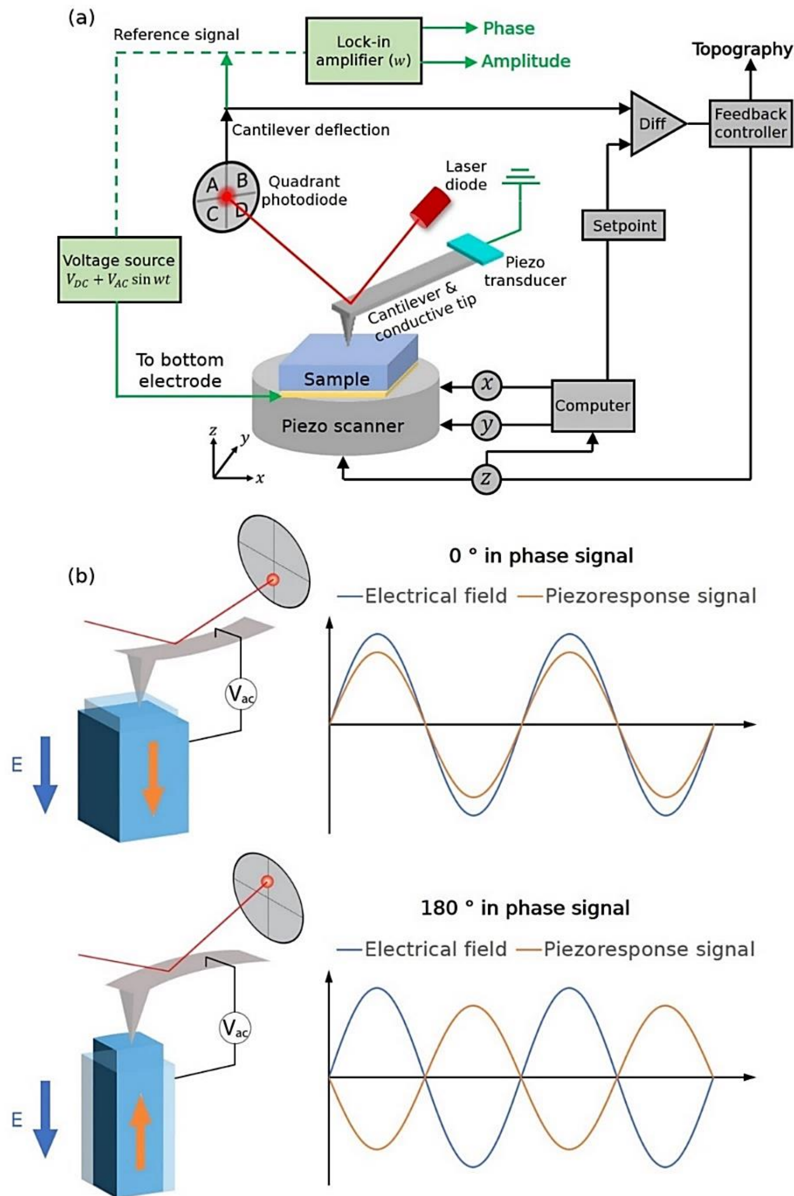

Figure 2.16: Principle of piezoresponse force microscopy (PFM). (a) Schematic of PFM setup. This figure is partially adapted from ref.[250] (b) Schematic of PFM working principle.

2.3.4 Scanning electron microscopy

Scanning electron microscopy (SEM) is a highly versatile technique for high-resolution images which provides surface information of the materials, such as topography, morphology, composition, and crystallography.[252]

The underlying principle of SEM is presented in Figure 2.17a. A focused electron beam with highly energetic primary electrons is released from the source and the electron wavelength can be varied by the applied accelerating voltage to the electron gun. The electron beam scans over and strikes the sample

surface, generating various signals including secondary electrons (SEs), backscattered electrons (BSEs), characteristic X-rays, and Auger electrons. These signals are subsequently collected by electron detectors. The SE detector positioned off to the side of the vacuum chamber gives information of topographic contrast. The in-lens detector placed in the beam path of the microscopy, detects the SEs and/or BSEs with high collection efficiency.[253] The signal provides topographic and compositional information.

Energy-dispersive X-ray spectroscopy (EDX) can be coupled with SEM to analyze the characteristic X-rays emitted. Each element emits X-rays at specific energy levels, which allows the identification and quantification of the elements in the sample.

In this work, thin films were characterized by SEM utilizing an in-lens detector at acceleration voltages of 10.0 kV (ZEISS-Gemini) and 1.0 kV (ZEISS-Merlin). Additionally, EDX from ZEISS-Gemini system was employed at acceleration voltages of 20.0 kV for elemental analysis.

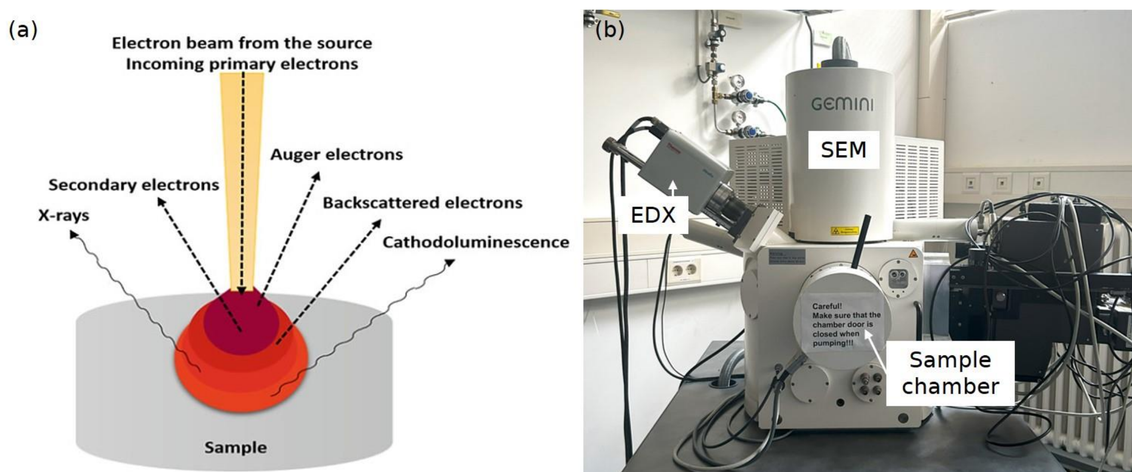

Figure 2.17: (a) Principle of scanning electron microscopy (SEM). The interaction of electron beam with sample and the signal emitted from the sample.[252] (b) ZEISS-Gemini SEM system.

2.3.5 Raman spectroscopy

Raman spectroscopy is a non-destructive analysis technique, which allows the determination of the chemical composition, crystalline structure and bonds in the sample. This technique is based on the Raman scattering – the interaction between light and chemical bonds within the samples under examination.[254, 255] An incoming light with a specific wavelength λ_{laser}, undergoes processes including light absorption, transmission, reflection, and various scatterings upon interaction with the sample, as presented in Figure 2.18a. The predominant portion of the scattered light retains the same wavelength as the laser source ($\lambda_{laser} = \lambda_{scatter}$), which is named as Rayleigh scattering and only provides limited information. A small amount of light is scattered at different wavelengths depending on the nature and crystalline structure of

the sample, which corresponds to Stokes Raman scattering ($\lambda_{laser} < \lambda_{scatter}$) and anti-Stokes Raman scattering ($\lambda_{laser} > \lambda_{scatter}$). Both scatterings are inelastic, however, Stokes Raman scattering (molecule gains energy from the scattering of photons) is more common to be used in Raman spectroscopy measurements, since the anti-Stokes Raman requires that the molecule is at an excited vibrational state and lose energy. Hence, Raman shift, denoting the energy difference between the incident light and the scattered one is the representative of the vibration modes of the atomic or molecular bonds.

Figure 2.18b illustrates the principle of the Raman spectroscopy setup. During the measurement, a sample is excited by a focused monochromatic light through the integrated optics system. The scattered light is subsequently directed and focused onto the detector for signal collection. Computer processing extracts the Raman signal as signal intensity plotted against Raman shift, yielding a Raman spectrum. Spatial mapping involves sequential acquisition of spectra across an area of interest by moving the stage in (*x, y*) directions in a point-by-point manner.

The Raman measurements of the thin films were performed using Horiba HR-evolution LabRam spectrometer. LabSpec6 software was used for viewing the Raman spectra. A continuous laser of 325 nm wavelength was used as the excitation source with a line grating of 1800 l/mm. The excitation source was focused unto the thin film through a ~1 μm diameter microscope having a magnification of ×40 and numerical aperture of 0.49. Additionally, a neutral density (ND) filter status of 3.2% and a confocal hole size of 150 μm were applied during the measurements. Raman spectroscopy mapping was performed by moving the XY stage with a spatial resolution of ~1 μm.

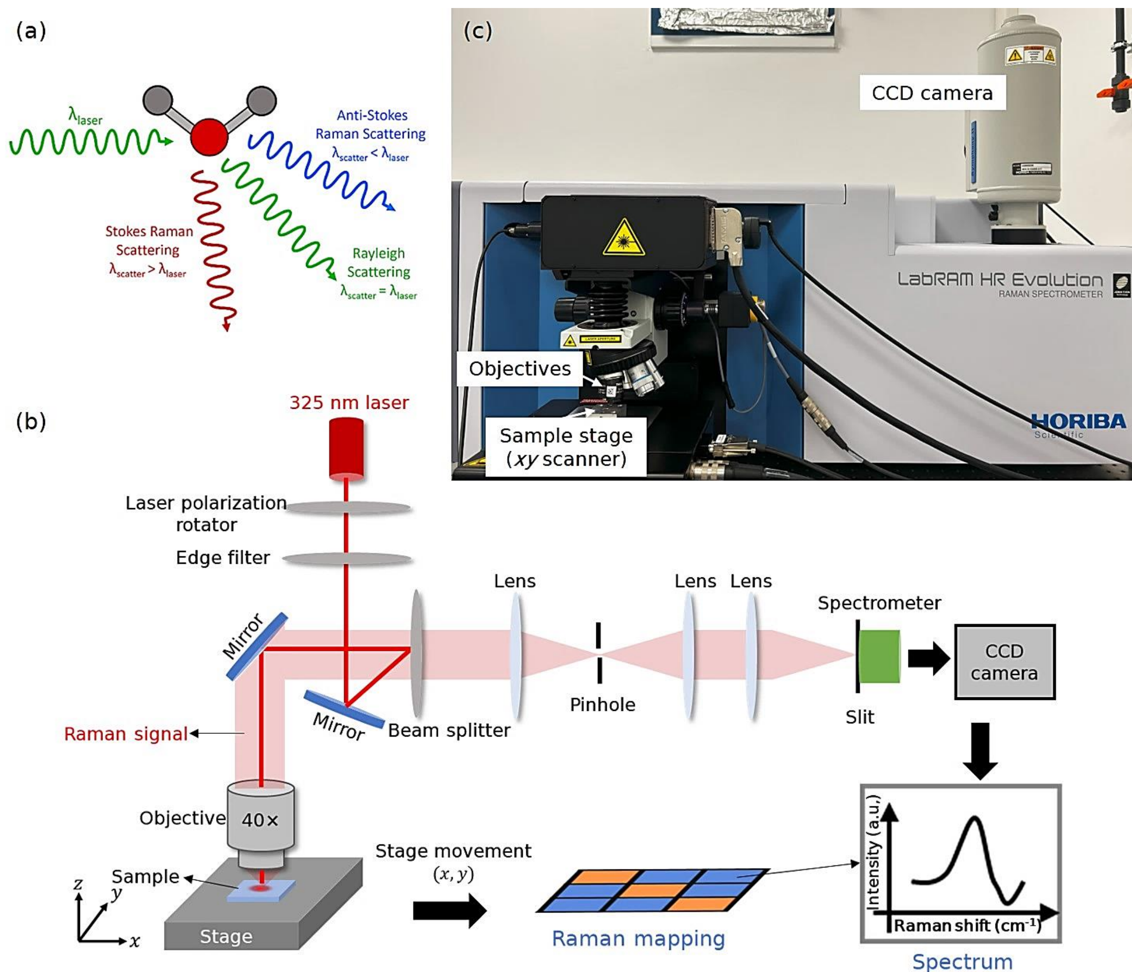

Figure 2.18: (a) Three different scatterings with a given input wavelength and the comparison to the scattered wavelengths. This image is from ref.[255] (b) Principle of Raman spectroscopy system. The graph (b) is partially adapted from ref.[256] (c) Horiba LabRam Raman spectrometer.

2.3.6 X-ray photoelectron spectroscopy

X-ray photoelectron spectroscopy (XPS) is a non-destructive, surface sensitive quantitative technique based on the photoelectric effect, which reveals chemical bond and electronic information on the elements and their environments in a sample.[257]

The sample is irradiated with X-rays leading to the emission of electrons (called photoelectrons) as a result of transfer of the X-ray energy to electrons occupying core levels, as illustrated in Figure 2.19a. The photoelectric effect can be described by the mathematic equation (Equation 2.3) and states that the minimum energy of photons to be used must be higher than the electron binding energy and the sample work function. As the binding energy (E_B) of the electron determines how tightly it is bound to the orbital, it is a material property independent of other factors such as X-rays. Hence, according to Equation 2.3, the

binding energy of electrons can be analyzed through the kinetic energy (E_K) of the escaped photoelectrons.[258] The binding energies are characteristic of specific electron orbitals in atoms.

$$E_B = hv - \phi_S - E_K \qquad \text{Equation 2.3}$$

where h is Planck's constant and v is the photon frequency, E_B is the binding energy and E_K is the kinetic energy of the emitted electron, ϕ_S is the work function of the sample.

E_K and sample work function (ϕ_S) in Equation 2.3 can be replaced by the measured kinetic energy (E'_k) from the spectrometer and its work function ($\phi_{spectro}$), when the Fermi levels of the sample and spectrometer are well aligned with a good ohmic contact (see Figure 2.19a and Equation 2.4). Hence, calibration of the spectrometer Fermi level (E_F) with a metallic reference is mandatory to allow in turn the direct access to E_B from the measured kinetic energy (E'_K) independently from the sample work function (ϕ_S).

$$E_B = hv - \phi_{spectro} - E'_K \qquad \text{Equation 2.4}$$

XPS system is schematically illustrated in Figure 2.19b. After X-ray excitation, the emitted electrons are directed and focused towards the entrance slit of a hemispherical energy analyzer with electrostatic lenses. Ultra-high vacuum environment (~10^{-10} mbar) is used to ensure no kinetic energy loss of the ejected electrons before reaching the analyzer. Afterwards, the electrons travel into the hemispherical analyzer thanks to a radial field and only electrons with a specified energy (called pass energy) will be able to travel through the analyzer and reach the exit slit.[257] They will be subsequently collected by the electron multiplier detector.

In this study, the chemical compositions and bonding environments of $ErMnO_3$ polycrystalline films were evaluated by an XPS system from Specs GmbH (Figure 2.19c), with a monochromatic Al Kα source ($hv = 1486.7$ eV). Photoelectrons were collected using a hemispherical energy analyzer (PHOIBOS 150) with 1D delay line detector at a fixed pass energy of 20 eV, giving an overall experimental energy resolution of ~ 300 meV. The energy resolution is determined by the experimental resolution (full width at half maximum (FWHM) of the X-ray source and thermal broadening), which has a gaussian shape and by the intrinsic energy resolution of the photoionized state, which has a Lorentzian shape. The take-off angle (i.e angle between the sample surface and the electron analyzer) was set to 90 º, giving a probing depth of ~ 3λ, where λ stands for the inelastic mean free path of the electrons before leaving the sample. With Al Kα, $\lambda_{\mathrm{Mn}\ 2p}$ through $ErMnO_3$ is calculated to be 2 ± 0.5 nm using the TT2PM software, giving a probing depth of ~ 6 nm. The binding energies were referenced to the Fermi edge of metallic Mo in electrical contact with the sample. CasaXPS software was used to subtract the secondary electron background and to model the

Mn $2p_{3/2}$ core level spectra using Pseudo-Voight functions (convolution of Gaussian and Lorentzian) in order to evaluate the Mn oxidation state.

The XPS measurements were performed by Dr. Wassim Hamouda. I treated and analyzed the data.

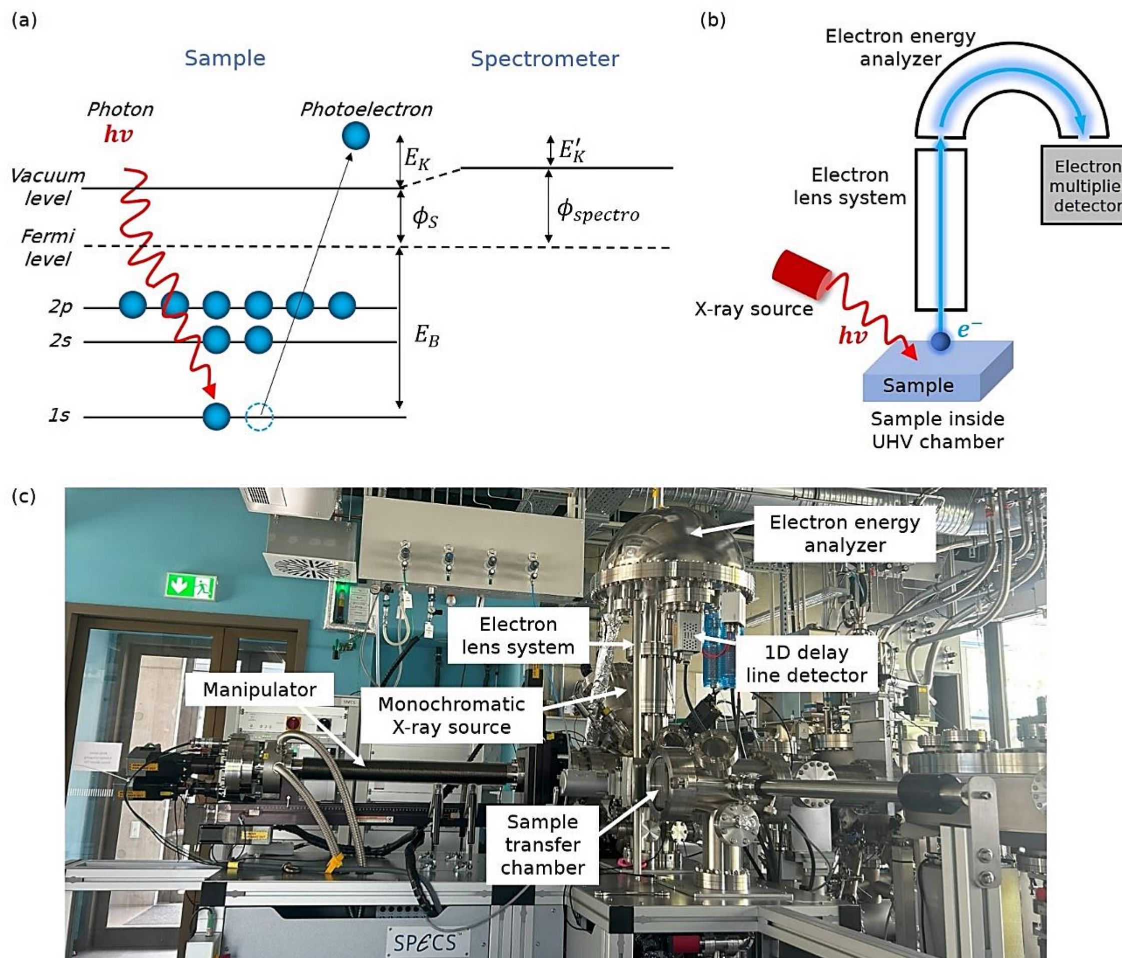

Figure 2.19: (a) Energy level diagram of the sample aligned with the spectrometer in a photoemission experiment, including the x-ray source energy ($h\nu$), the binding energy of the electron (E_B), the work function of the sample (ϕ_S) and spectrometer ($\phi_{spectro}$), the kinetic energy of sample (E_K) and measured kinetic energy (E'_K). (b) Schematic of X-ray photoelectron spectroscopy system. (c) Photo of the employed XPS system from Specs GmbH.

2.3.7 Electrical characterization

Impedance measurements, ferroelectric measurements, and resistive switching measurements, including *I-V* measurements with quasi-static DC sweeps, Kelvin (4-wire) resistance measurements, endurance and retention measurements, were carried out on capacitive structures. These measurements were performed at room temperature using a Keysight B1500 semiconductor device parameter analyzer with an MPI TS2000-

SE probe station, as presented in Figure 2.20. Additionally, ferroelectric measurements were conducted using the Radiant Precision Multiferroic II ferroelectric test system together with Vision software.

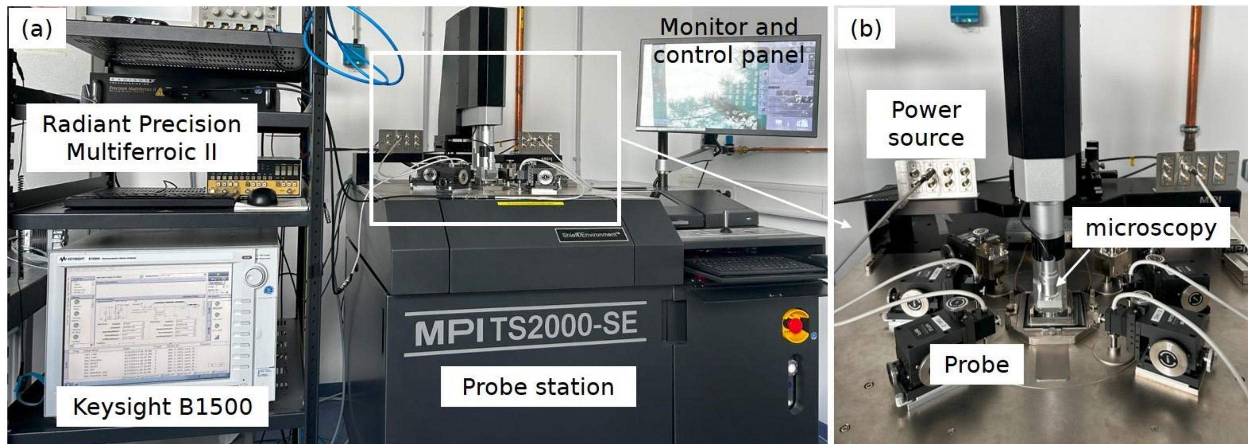

Figure 2.20: (a) Photo of the probe station setup, Radiant Precision Multiferroic II, and Keysight B1500. (b) Magnified image of the probe station setup.

2.3.7.1 Impedance measurement

To study the inductive and capacitive behaviors of the devices in ON and OFF states, impedance measurements including (Z, f) and (Z, V) were conducted. These measurements were performed at frequencies ranging from 1 kHz to 5 MHz, applying an AC signal of 20 mV. Circuit simulations were carried out using QucsStudio software to extract resistance (R), inductance (L) and capacitance (C) values. Further details will be provided in Chapter 3.

2.3.7.2 Ferroelectric characterization

The ferroelectric properties of the manganite thin films were investigated by measuring polarization-voltage (P-V) hysteresis loops. A conventional approach, based on the modified Sawyer-Tower circuit – virtual ground method (shown in Figure 2.21), was employed to assess the P-V loops in this study. This method involves applying a sequence of waves such as AC triangular voltage waves, enabling the direct measurement of integrated voltage, which is proportional to the integrated sample charges. Subsequently, polarization is calculated based on these charges. The response obtained from the measurements can exhibit characteristics including remanent polarization and several parasitic elements, such as linear components and non-remanent polarization. Hence, subtracting the parasitic elements from the overall hysteresis response is essential for accurately determining the remanent polarization from the measurements.

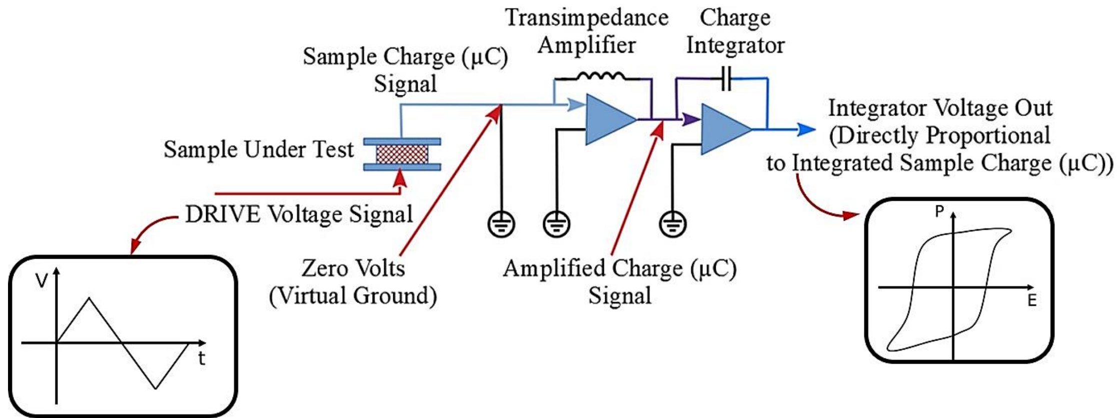

Figure 2.21: Virtual ground method for dynamic hysteresis measurement (DHM). The image is reproduced from ref.[259]

To study the remanent polarization, Positive Up Negative Down (PUND) method was applied. Figure 2.22 shows the simplified pulse sequence for the PUND measurement. In PUND measurement, polarization measurements are conducted with repeating sequence of five pulses, each having the same pulse width, delay time, and voltage magnitude. The sequence begins with a negative voltage pulse in order to preset the sample into a specific polarization state. Subsequently, two positive pulses follow; the first pulse switches the polarization and the second does not, resulting in switched (P^*) and non-switched (P^) polarization states, respectively. This is followed by two negative voltage pulses. Similarly, the first pulse switches the polarization while the second pulse maintains it. Hence, by subtracting the non-switching response from the switching response, the leakage and charge injection conduction are deducted and the remanent polarization can be calculated (P^*-P^).[260]

In our measurements, the Radiant ferroelectric tester utilizes a modified approach for the PUND measurement by obtaining two distinct hysteresis loops named Logic 1 (contains both remanent and non-remanent components) and Logic 0 (contains only non-remanent components). The remanent polarization is obtained by subtracting Logic 0 from Logic 1.[259]

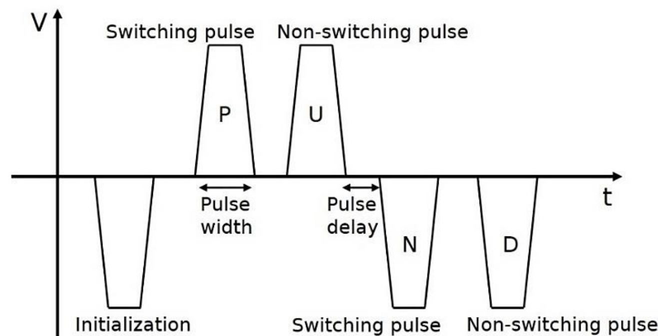

Figure 2.22: Positive Up Negative Down (PUND) method for remanent polarization characterization.

2.3.7.3 Current-voltage characteristic

Current-voltage (I-V) measurements with quasi-static DC sweeps were performed for the study of resistive switching. In these electrical measurements, the Pt bottom electrode was grounded, and a DC bias was applied to the top electrode. Figure 2.23 shows a typical I-V curve depicting resistive switching behavior, with the arrows indicating the DC sweep directions. Above a certain threshold voltage (V_{Set}), the device switches from a high resistance state (HRS) to a low resistance state (LRS), corresponding to the Set process. A compliance current (I_{CC}) was applied to prevent an irreversible hard breakdown of the device. For the Reset process, the current decreases at the Reset voltage (V_{Reset}), corresponding to the switching of the device from LRS to HRS. ON and OFF resistances were determined at 50 mV at the same polarity as the one of the Set processes. Additionally, endurance tests were done by performing multiple DC sweeps.

Further details regarding the measurement parameters such as applied bias, sweeping rate, and compliance current, will be presented for the different sample systems in the following chapters.

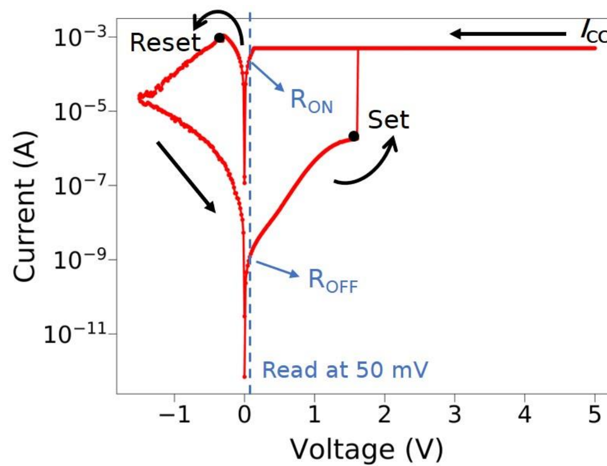

Figure 2.23: A typical current-voltage (I-V) curve on a capacitive structure. I_{CC} is the compliance current.

2.3.7.4 Kelvin (4-wire) resistance measurement

Kelvin (4-wire) resistance measurements were performed to calibrate the cable and contact parasitic resistance while measuring the ON resistances. These measurements require four terminals – a pair of current-carrying probes and a pair of voltage-carrying probes, as illustrated in Figure 2.24. The resistance of the device under test can be calculated based on the actual voltage dropping over it and the current flowing through it (see Equation 2.5).

$$R = \frac{V_2 - V_3}{I_1} \qquad \text{Equation 2.5}$$

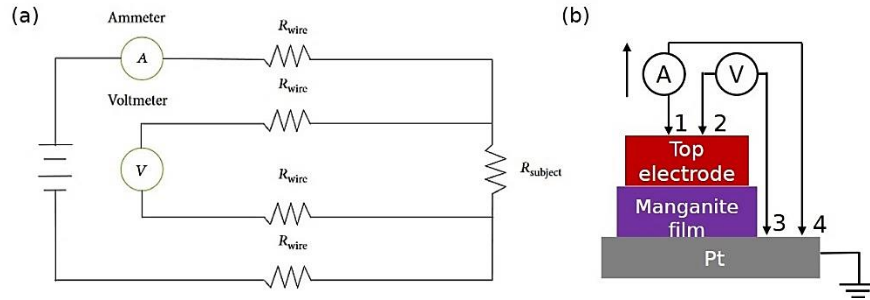

Figure 2.24: (a) A equivalent circuit of Kelvin (4-wire) resistance measurement. This figure is from ref.[261] (b) A schematic diagram of the device under test. The current is measured through probe 1 to probe 4, the voltage is measured between probes 2 and 3.

2.3.7.5 Retention measurement

Retention measurements of the devices in ON and OFF states were carried out at room temperature. The devices were first switched to LRS (ON) and HRS (OFF) states by applying a DC triangular bias, followed by determining the resistance values with a small read DC bias for 6×10^3 s (see Figure 2.25).

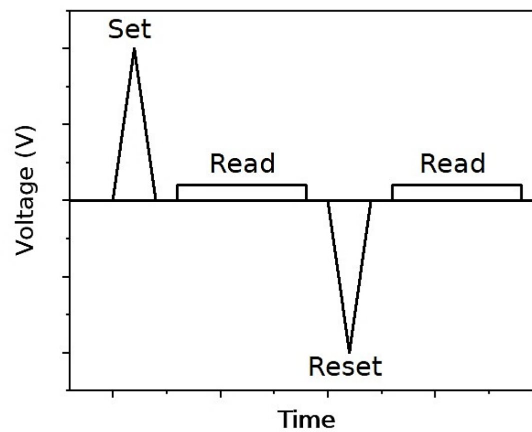

Figure 2.25: Retention measurement during the resistive switching tests.

2.3.8 Operando time-resolved X-ray diffraction during PUND measurement

Time-resolved X-ray diffraction (XRD) is performed to investigate real-time structural changes within a crystalline specimen which undergoes a certain reaction, phase transition, or physical changes under a stimulus.[262]

We employed operando time-resolved XRD at the synchrotron BESSY II (beamline XPP-KMC3) to study the piezoelectric response of manganite thin films in metal/film/metal stacks. The time resolution is at the nanosecond range.

The experimental setup is sketched in Figure 2.26.[263] The sample was placed and grounded on a goniometer. The top electrode of the stack was contacted electrically using a tungsten tip. The monochromatic X-ray beam with energy at 9 keV was collimated to about 150 × 300 µm^2, so that only the material below a single electrode could be tested. Theta-two theta scans were recorded by a 2D PILATUS pixelated detector during the electrical biasing – PUND measurements or triangular pulses. The electric-field-induced strain was extracted from the shift of the two-theta position of the Bragg reflection. The results will be discussed in Chapter 5.

These experiments were performed in collaboration with Dr. Thomas Cornelius from the Institute Matériaux Microélectronique Nanosciences de Provence (Marseille, France) and Dr. Matthias Rössle from HZB/Uni Potsdam.

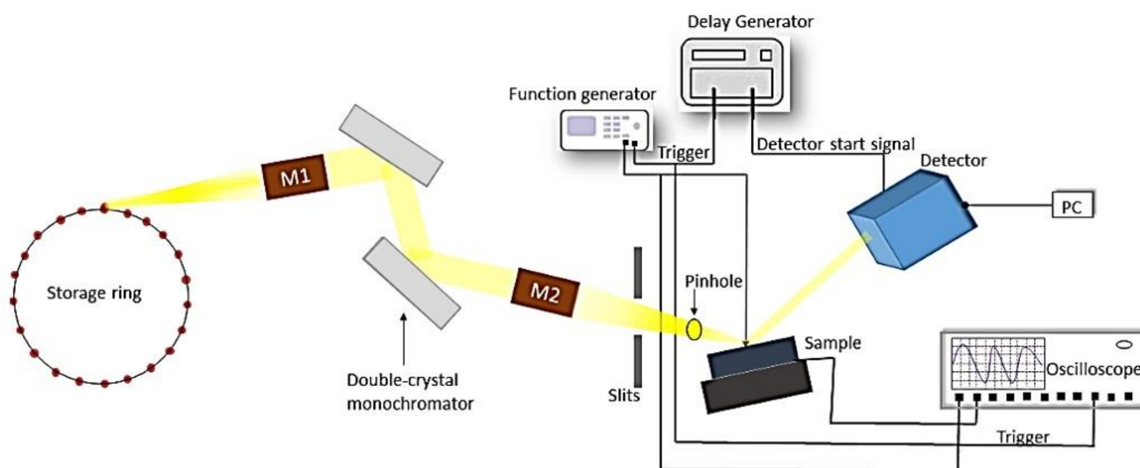

Figure 2.26: Principle of time-resolve XRD setup at the XPP-KMC3 beamline at BESSY II. This figure is from ref.[263]

Chapter 3: Investigation of the impedance (*R*, *L*, *C*) of metal/$RMnO_3$/metal stacks

3 Investigation of the impedance (*R*, *L*, *C*) of metal/$RMnO_3$/metal stacks 72

3.1 Device architecture and electrical measurement configurations 74

3.2 Package-based measurement 76

3.2.1 Parasitic calibration 76

3.2.2 Reference inductor 77

3.2.3 $YMnO_3$-based device characterization 78

3.3 Probe station-based measurement 79

3.3.1 Parasitic calibration 79

3.3.2 $RMnO_3$-based device characterization 83

3.3.2.1 Device characterization without calibrations 83

3.3.2.2 Device characterization with calibrations 83

3.4 Summary 86

Highly compact and energy-efficient power supplies are essential for high-performance microelectronic systems, particularly in growing sectors such as mobility, industrial applications and energy.[227, 228] In response to this need, the research project named "Erforschung rekonfigurierbarer, passiver Mikroelektronikbauelemente für Energieeffizienz und Flexibilität" (ERMI), was funded by BMBF as part of the ForMikro program. This project aims to utilize novel passive components (inductors *L* and capacitors *C*) to develop energy-efficient voltage transformers for local power supply.[18–20] Ultimately, the project seeks to develop novel multiphase voltage transformers in conjunction with adapted integrated circuits, which will significantly advance the state of the art in power supply technology.

Building on the work of Heidemarie Schmidt *et al.*, who explored topological vortex states coupled with resistance states in multiferroelectric manganite $RMnO_3$ thin films,[15–17] the ERMI project explored the use of manganites with a large vortex density as inductors and those with small vortex density as capacitors. The concept envisioned for the reconfigurability between capacitive (OFF state) and inductive (ON state) states in the devices is illustrated in Figure 3.1.

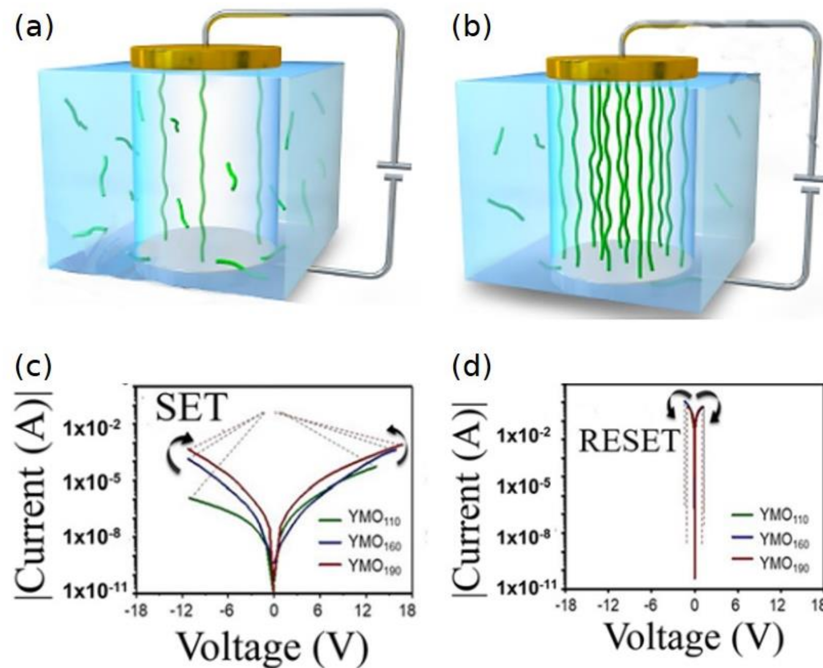

Figure 3.1: Sketches of reconfigurable devices based on ferroelectric manganite thin films ($RMnO_3$) (a) in OFF state with a small vortex density and large resistance, (b) in ON state with a large vortex density and small resistance. These figures were made by Heidemarie Schmidt from the ForMikro kickoff meeting. (c) and (d) Current-voltage (*I*-*V*) characteristics of the devices in OFF and ON states. These figures are from ref.[15]

In this chapter, we explore capacitive and inductive behaviors in ferroelectric manganite thin films using two-terminal devices. The chapter is organized as follows: In Section 3.1, we introduce the device

architecture and electrical configurations. In Sections 3.2 and 3.3 we present the analysis of impedance measurements two different setups, coupled with circuit simulations. This analysis aims to study the circuit elements (R, L, C) in both OFF and ON states, providing a comprehensive understanding of their electrical characteristics and a potential reconfigurability between L and C. Lastly, a summary is presented in Section 3.4.

3.1 Device architecture and electrical measurement configurations

Impedance measurements were carried out to study the inductive and capacitive behaviors of devices in ON and OFF states. In Figure 3.2 we present two types of impedance measurement setups used in this work. One setup involves a package-based configuration where a printed circuit board (PCB) or diode package is directly connected to the impedance analyzer (Figure 3.2a). The other setup is probe station-based (MPI TS2000-SE) and conducted on chips (Figure 3.2b), which includes cable extension – shielded two terminal (S-2T) configuration (Figure 3.2c), which contributes with series parasitics to the device response.

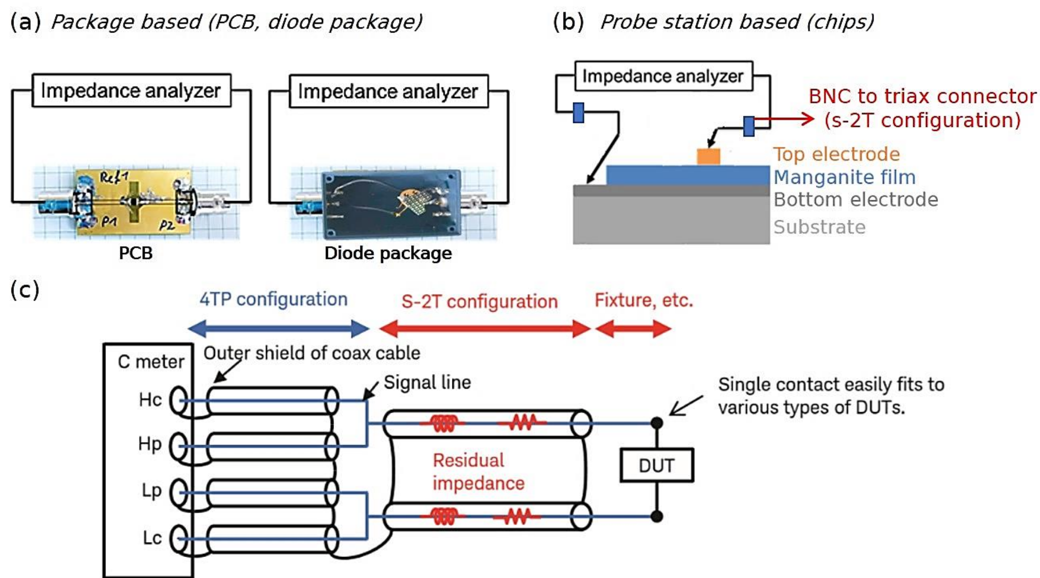

Figure 3.2: Impedance measurement setups. (a) Package-based measurement with PCB or diode package directly connected to the impedance analyzer. (b) Probe station-based measurement on chips, including shielded two terminal (S-2T) configuration. (c) Cable extension using the shielded two terminal configuration, leading to series parasitics contribution to the device under test (DUT) response.[264]

We propose an equivalent circuit (Figure 3.3) to analyze the impedance measurements of the devices. The circuit consists of two main parts. The section highlighted in green represents parasitic elements, including a series inductor and resistor, along with a parallel capacitor. The rest (in the black box) refers to the

components of the device. When the device is in the OFF state, two pairs of parallel capacitors and resistors connected in series are considered as the equivalent elements, which reflects the top electrode/film interface and bottom electrode/film interface in the stack. When the device is switched to the ON state, a series of inductor and resistor is added, since the vortex density increases in the devices and the vortices can be potentially regarded as inductors.

Calibrating out the parasitics from impedance measurements is crucial to ensure accuracy, since the presence of parasitics in cables can significantly impact and impede the device response, especially for the probe station-based measurements due to cable extension. In addition, the residual inductance in the cable varies due to random cable arrangement, making it challenging to maintain constant and stable inductive parasitics. Hence, we need to perform the OPEN calibration to calibrate capacitive parasitics, and the SHORT calibration to addresses inductive and resistive parasitics.

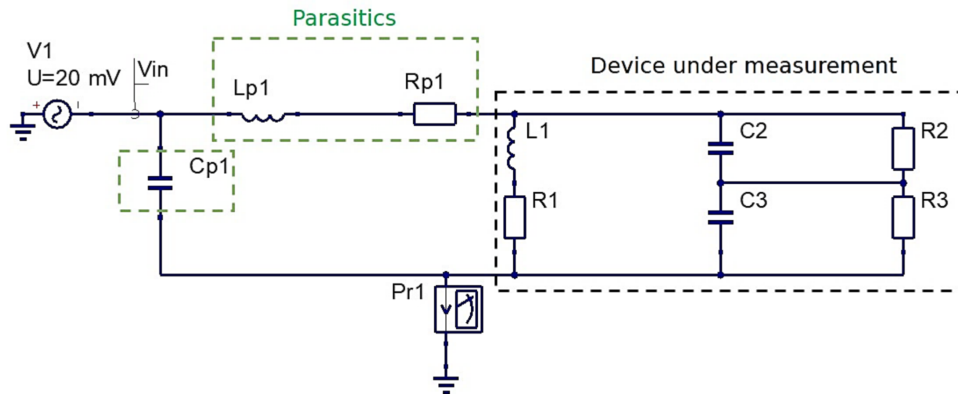

Figure 3.3: Equivalent circuit including the device under measurement and parasitics. This circuit was proposed by Heidemarie Schmidt.

To systematically study the reconfigurability between the capacitive (OFF state) and inductive (ON state) behaviors of the devices, electrical measurements were conducted as illustrated in Figure 3.4. Initially, OPEN and SHORT calibrations were performed to determine the parasitics. Subsequently, impedance measurements were carried out to study the devices in their pristine state, which is expected to show a capacitive behavior. Detailed investigations of the switching between OFF and ON states via *I-V* measurements will be discussed in Chapter 4. Impedance measurements were then performed both in the ON state to examine inductive or resistive behaviors, and upon resetting to the OFF state to examine the capacitive behavior.

To analyze the impedance measurements of the devices and explore the relevant device elements, circuit simulations were then performed based on the proposed circuit model (see Figure 3.3) using QucsStudio software.

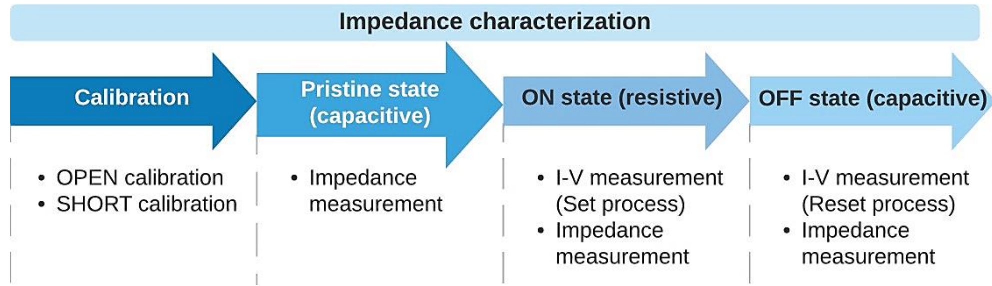

Figure 3.4: Electrical characteristic of devices including *I-V* measurements and impedance measurements, to study the reconfigurability between the capacitive and resistive/inductive states.

3.2 Package-based measurement

3.2.1 Parasitic calibration

Package-based impedance measurements involve smaller uncompensated series parasitics since diode legs and cables are shorter. Short corrections can be made through a 'wire' shorting both BNC terminals, and open corrections can be made by simply disconnecting the package from the BNC terminals. Figure 3.5a shows the equivalent circuit of an inductor and a resistor in series as parasitics through the short configuration (SHORT structure) in the package-based setup. The circuit, simulated based on experimental Bode plots (impedance magnitude and phase vs. frequency, in Figure 3.5b, c), yielded inductance and resistance values of 58.66 nH and 8.2 mΩ, respectively. Open correction reveals capacitive parasitics with negligible capacitance (10^{-14} F), as depicted in Figure 3.6.

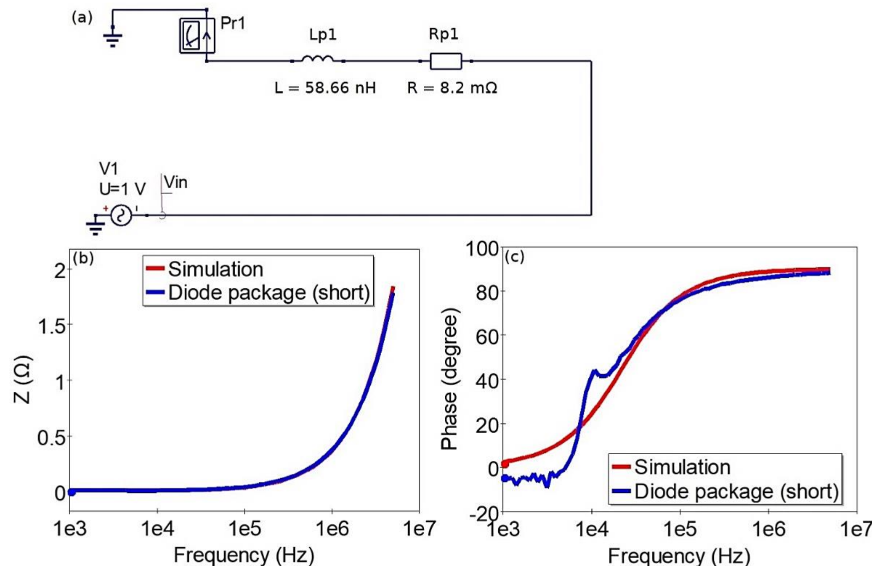

Figure 3.5: Parasitics (inductance and resistance) in a package-based measurement. (a) Equivalent circuit for the impedance measurement of SHORT structure, and their experimental and simulated Bode plots showing (b) Impedance magnitude Z and (c) phase as a function of frequency.

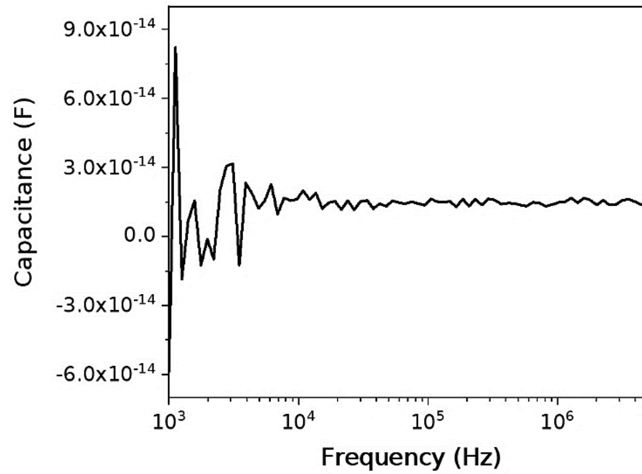

Figure 3.6: Capacitance of OPEN structure in a package-based measurement.

3.2.2 Reference inductor

Now with the identified parasitics, we characterized a reference sample – a commercial inductor on a PCB board – to establish a measurement standard within our ERMI project partners. Impedance measurements were conducted in a 'thru' configuration, reaching up to 5 MHz by us (HZB) and up to 1 GHz by our collaborator (IMS, Hannover), as depicted in Figure 3.7. The Bode plots from both measurements align up to 5 MHz, indicating consistent results. The measurement recorded by IMS reveals a self-resonant peak at a higher frequency range, indicating the presence of internal parasitics such as a winding capacitor (C2 in Figure 3.7) and coil resistance (R2 in Figure 3.7) in parallel. Below the self-resonant frequency, inductive behavior dominates, while above it, the reference sample exhibits more capacitive characteristics, with the impedance decreasing as frequency increases.

Hence, we propose an equivalent circuit model for this reference inductor as shown in Figure 3.7a. The model was adjusted to match the experimental Bode plots by optimizing the values of circuit elements, resulting in a good agreement between the simulation curves and the experimental results (see Figure 3.7b, c). The derived equivalent circuit determines an inductance value of 5.6 μH for the reference sample. Studying this reference sample helps us understand inductive response and validate our impedance characterization and analysis.

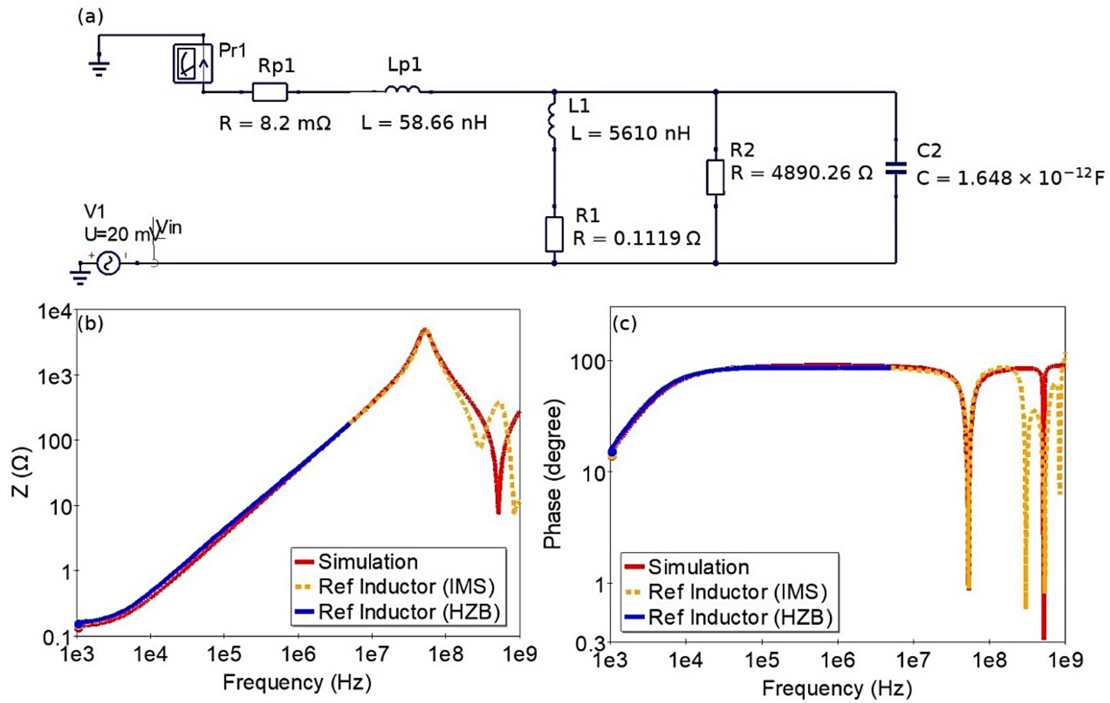

Figure 3.7: (a) Equivalent circuit for the impedance measurements of reference inductor in a PCB-based package, along with experimental Bode plots from HZB and IMS using different electrical configurations and the simulated Bode plots showing (b) impedance magnitude *Z* and (c) phase as a function of frequency.

3.2.3 $YMnO_3$-based device characterization

Impedance measurements were performed on the $YMnO_3$-based devices in the ON state using the package-based setup. The parasitics of the package-based measurements were determined in the Section 3.2.1. We applied the same inductance and resistance values to the equivalent circuit. For devices in the ON state, inductive behavior with an inductor (L1) and resistor (R1) in series is expected, as shown in Figure 3.8a. The values of L1 and R1 were tuned to fit the experimental impedance magnitude and phase as a function of frequency (see Figure 3.8b, c). The inductance value of the device is determined to be around 16 nH, which is smaller than the parasitic inductance and below our measurable error in this configuration. To better characterize these devices, probe station-based measurements can be explored, with on-chip calibration structures included to minimize parasitics.

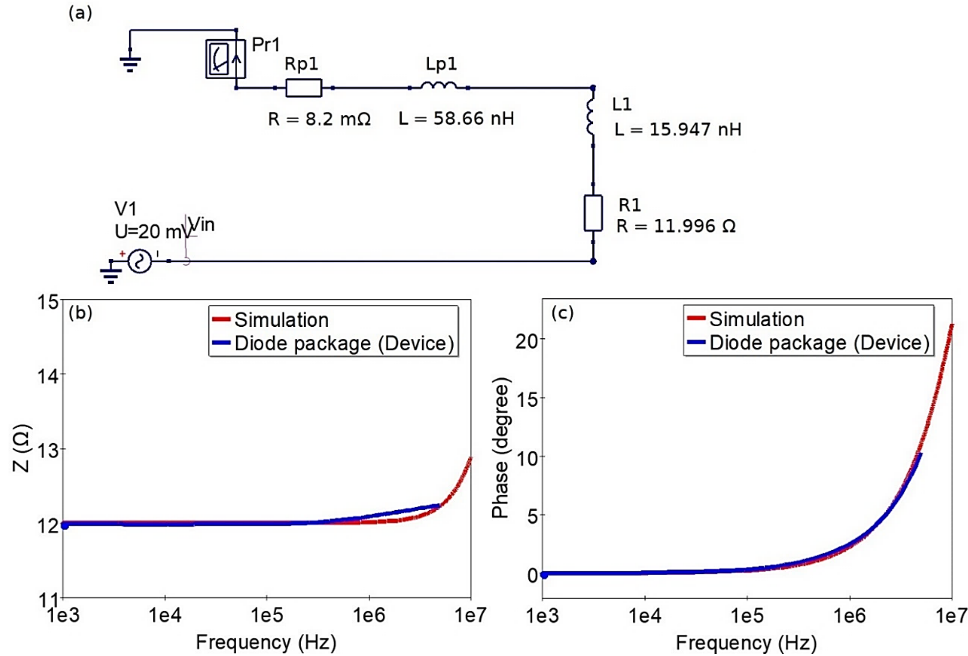

Figure 3.8: (a) Equivalent circuit for the impedance measurements of a $YMnO_3$-based device (ON state) in a diode package, and their experimental and simulated Bode plots showing (b) impedance magnitude *Z* and (c) phase as a function of frequency.

3.3 Probe station-based measurement

Probe station-based measurements often introduce significant parasitics, particularly inductance, owing to the extended cables involved. In this section, we present an illustration of impedance measurement analysis both without and with the calibration of these parasitics. This demonstration aims to point out the importance of proper calibrations, ensuring precise inductive measurements, when devices exhibit small inductance necessitating enhanced accuracy.

3.3.1 Parasitic calibration

A dedicated photolithography mask design containing metal/insulator/metal (MIM) devices and test structures for on-chip calibration were developed to fabricate and electrically characterize manganite thin films integrated in MIM stacks.

Figure 3.9 illustrates the process flow of Pt/$YMnO_3$/Al devices and on-chip OPEN and SHORT calibration structures. Photolithography with a dedicated mask and deposition of 200 nm-thick Pt and 30 nm-thick Ti by E-beam evaporation were carried out on SiO_2 (1 µm)/Si substrates, to obtain patterned bottom electrodes. A $YMnO_3$ thin film was deposited on the patterned Pt bottom electrode by RF sputtering at room temperature in an Ar atmosphere using a RF power of 200 W and an Ar pressure of 10 µbar. Subsequent post-deposition annealing in N_2 at 750 °C for 30 min in a furnace was performed. The optimization of the

polycrystalline $YMnO_3$ films is discussed in Chapter 4. Pt/$YMnO_3$/Al devices, OPEN and SHORT structures were fabricated with ~ 500 nm-thick Al top electrodes by lift-off using photolithography and E-beam evaporation of Al.

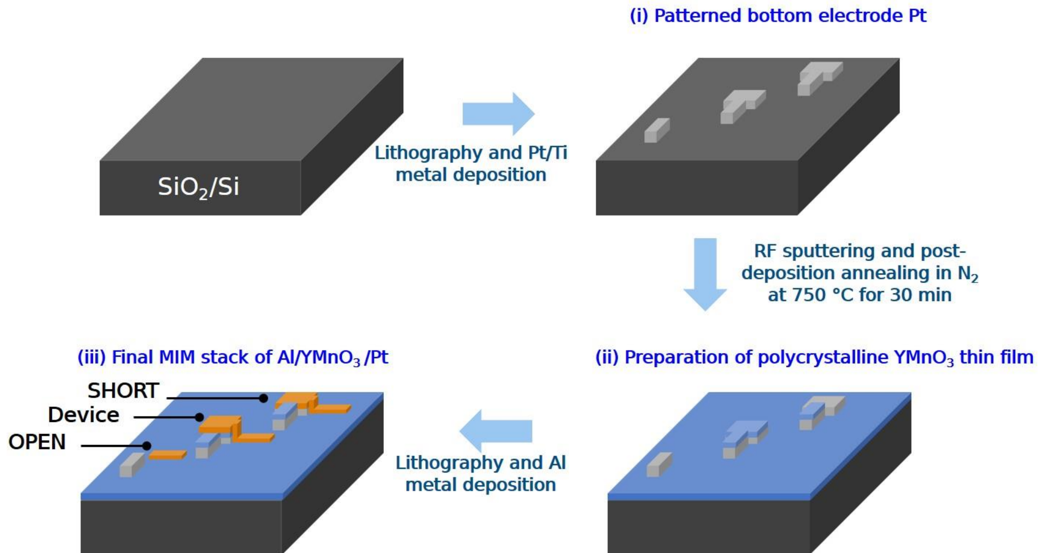

Figure 3.9: Process flow of Pt/$YMnO_3$/Al stack with both patterned top and bottom electrodes, with on-chip OPEN and SHORT calibration structures. (i) Preparation of patterned Pt bottom electrodes. (ii) Preparation of polycrystalline $YMnO_3$ films. (iii) Final MIM stack of Pt/$YMnO_3$/Al devices, OPEN and SHORT structures.

The impedance measurements of on-chip calibrations are illustrated in Figure 3.10. The on-chip OPEN structure allows to calibrate capacitive parasitics, and the on-chip SHORT structure addresses inductive and resistive parasitics. Detailed discussions of these calibrations, along with circuit simulations, will be provided later.

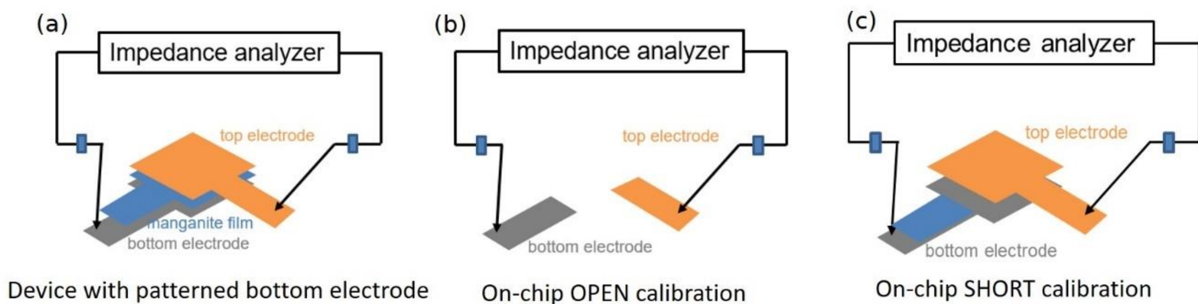

Figure 3.10: Sketches of impedance measurements of (a) a device, (b) the on-chip OPEN calibration, (c) the on-chip SHORT calibration.

The on-chip SHORT structure (Figure 3.10c) can be described by an ideal equivalent circuit, as depicted in Figure 3.11a. This circuit comprises a series configuration of an inductor (Lp1) and a resistor (Rp1). However, error in mask alignment during the top electrode preparation and edge effects may induce additional parasitic elements, specifically a capacitor (Cp2) and a resistor (Rp2) arranged in parallel to Lp1 and Rp1, as illustrated in Figure 3.11b. Based on this, we propose the equivalent circuit for the real SHORT structure, shown in Figure 3.11c.

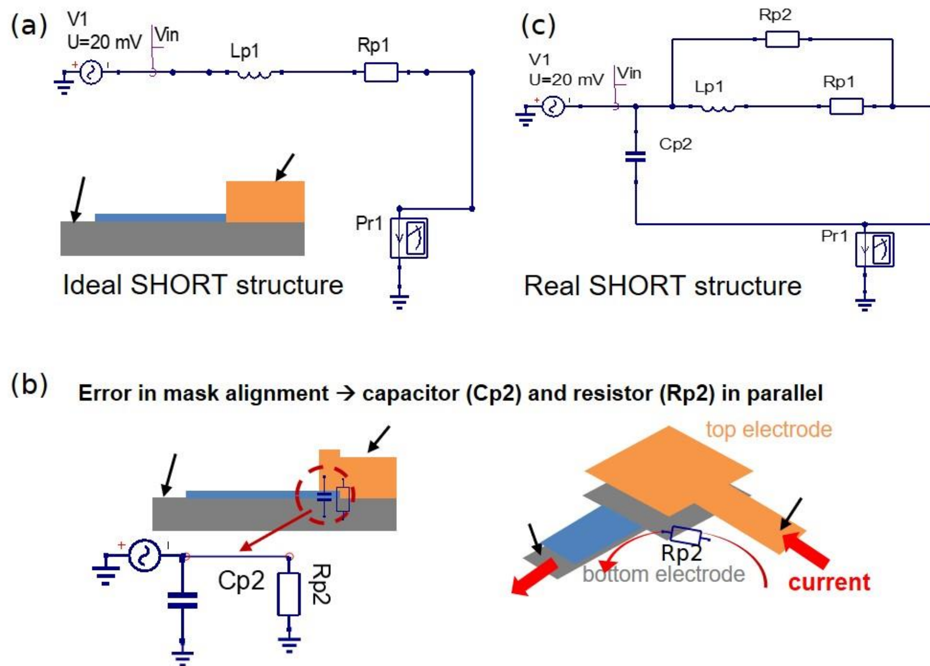

Figure 3.11: Equivalent circuits of (a) an ideal on-chip SHORT structure and (c) a real on-chip SHORT structure. (b) Sketch of the real device structure due to the error in mask alignment, causing additional capacitance and resistance in parallel.

Impedance measurements were conducted for the on-chip SHORT structure, and the corresponding equivalent circuit was employed to extract information about parasitic elements, as presented in Figure 3.12. The derived values for the inductor (Lp1) and DC resistor (Rp1) originate from the extended cable and the chip. Incorporating these values later in the circuit simulation of devices ensures an accurate determination of their electrical characteristics. However, errors in mask alignment may result in slightly different values for the additional capacitor (Cp2) and resistor (Rp2) in the SHORT structure and devices. Therefore, meticulous tuning of Cp2 and Rp2 is necessary during fitting for the devices to ensure accurate simulations.

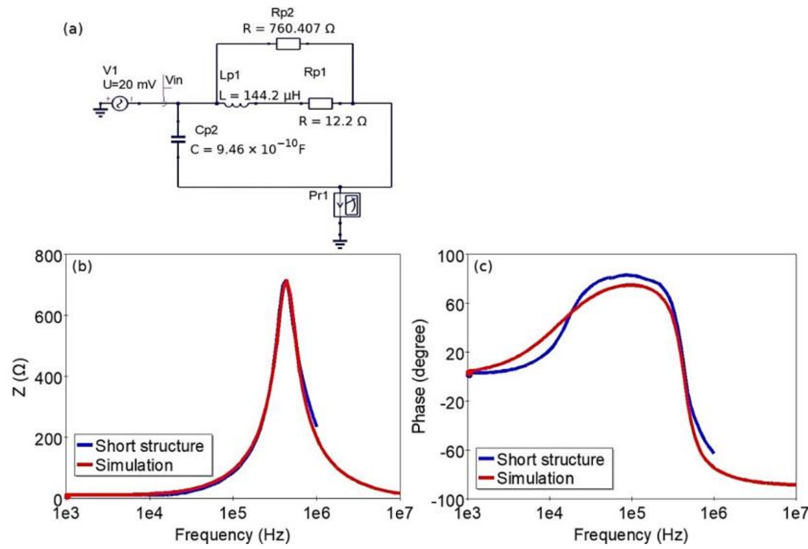

Figure 3.12: Parasitics in probe station-based measurements. (a) Equivalent circuit for the impedance measurements of on-chip SHORT structures, and their experimental and simulated Bode plots showing (b) impedance magnitude *Z* and (c) phase as a function of frequency.

The on-chip OPEN structures allow to determine the parasitic capacitor Cp1, which is approximately 3.4×10^{-13} F, as shown in Figure 3.13. The experimental impedance magnitude as a function of frequency is well reproduced by the simulation curve plotted in Figure 3.13b. However, the experimental impedance phase as a function of frequency (see Figure 3.13c) exhibits changes between -90 and 90 °, whereas it is expected to be constant at -90 ° for an ideal capacitor. The deviation from ideality may be due to the small capacitance value in the on-chip OPEN structures.

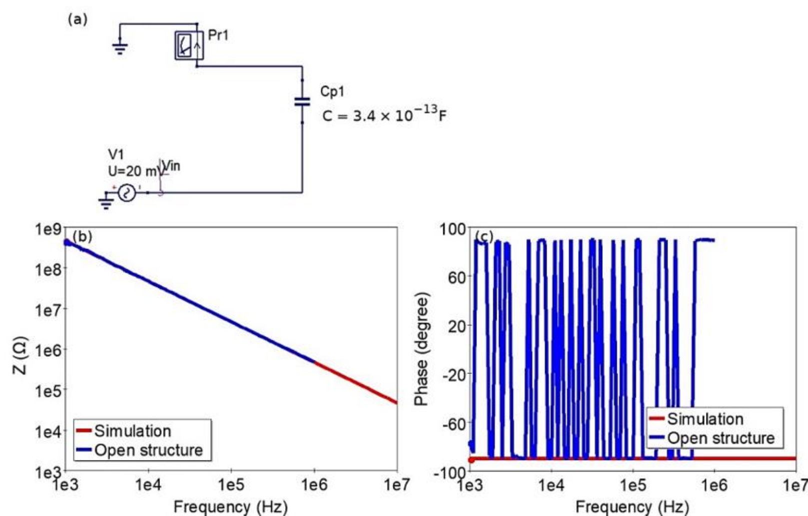

Figure 3.13: Parasitics (capacitance) in probe station-based measurements. (a) Equivalent circuit for the impedance measurements of the on-chip OPEN structures, and their experimental and simulated Bode plots showing (b) impedance magnitude *Z* and (c) phase as a function of frequency.

3.3.2 $RMnO_3$-based device characterization

3.3.2.1 Device characterization without calibrations

Firstly, impedance measurements were performed on 100 nm-thick $ErMnO_3$-based devices without calibration structures. Figure 3.14 shows the simulated equivalent circuit without parasitic elements, indicating an inductance value of around 1.5 μH. This value includes contributions from parasitics, as we will show below.

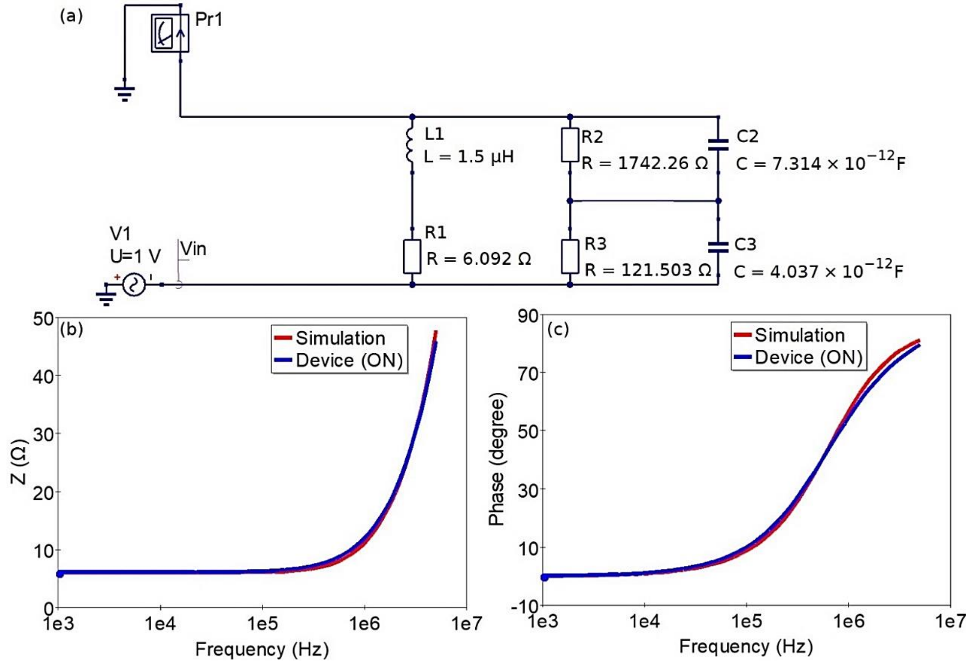

Figure 3.14: (a) Equivalent circuit without parasitic part for the impedance measurement of an $ErMnO_3$-based device (ON state) in probe station-based measurement, and their experimental and simulated Bode plots showing (b) impedance magnitude Z and (c) phase as a function of frequency.

3.3.2.2 Device characterization with calibrations

Device in ON state

Now we study the impedance measurements of Pt/$YMnO_3$/Al devices in the ON state, using the parasitic elements determined from the on-chip SHORT and OPEN structures. An inductive response characterized by an inductor (L1) and a resistor (R1) in series, along with other parasitic elements, is anticipated, as depicted in Figure 3.15a. The resistance value (R1) can be determined by evaluating the impedance magnitude in the low-frequency region, shown in Figure 3.15b. The value of L1 was adjusted to align with the experimental impedance characteristics in terms of magnitude and phase for varying frequencies. Bode plots in Figure 3.15b, c illustrate simulations incorporating the tuning of inductance values ranging from

1 nH to 1 μH. The model fitting reveals that better fitting could not be achieved with larger inductance values, and optimization is attained with the smallest inductance value. **This observation indicates the absence of noticeable inductive behavior in the device in the ON state.** Consequently, the device predominantly exhibits a resistive behavior. If there is any inductance value, it is too small for meaningful measurement.

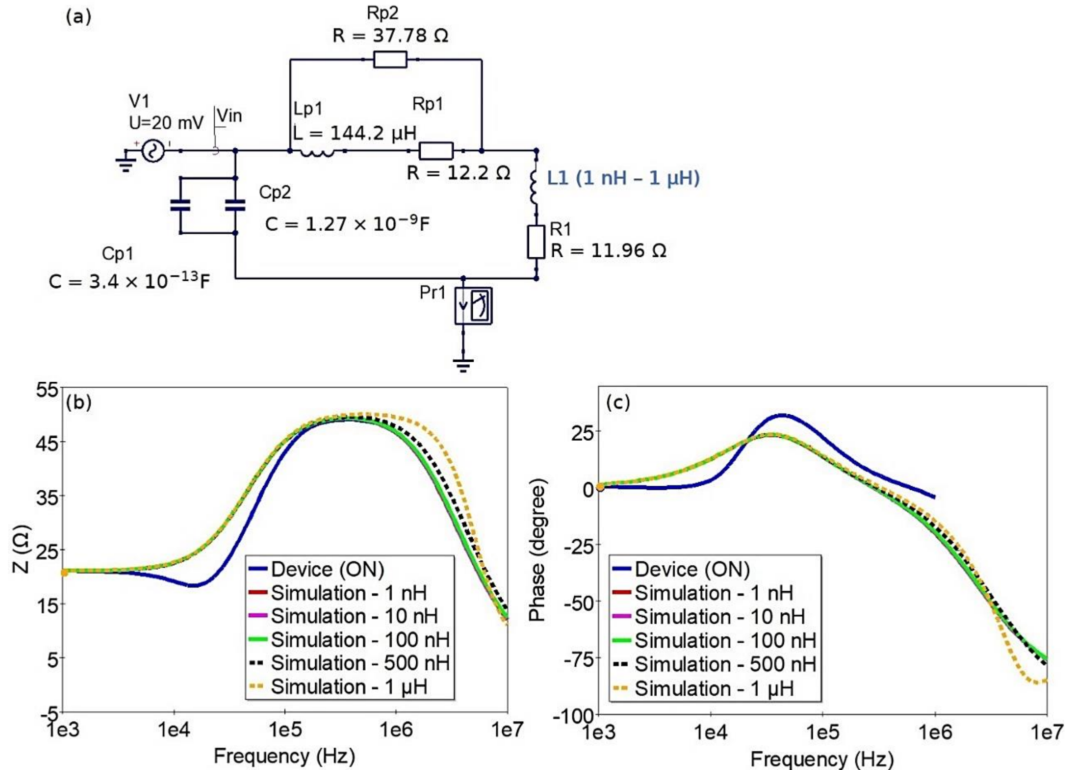

Figure 3.15: (a) Equivalent circuit for the impedance measurement of Pt/$YMnO_3$/Al device (ON state) with both patterned top and bottom electrodes (fabricated as shown in Figure 3.9), and their experimental and simulated Bode plots showing (b) impedance magnitude *Z* and (c) phase as a function of frequency. The simulation curves were modulated by changing the inductance value from 1 nH to 1 μH.

Device in OFF state

The impedance measurements were performed in both pristine and OFF states. As depicted in Figure 3.16, the capacitances of the devices were analyzed using on-chip OPEN and SHORT calibrations. Notably, the capacitance value of the device in pristine state (first cycle) is slightly larger than that observed in OFF state for all subsequent cycles. This difference is attributed to the presence of only partially ruptured filaments in OFF state, contributing to variations in the device's capacitance characteristics. Further insights into the formation and rupture of filaments during the resistive switching of these devices will be discussed in Chapter 4.

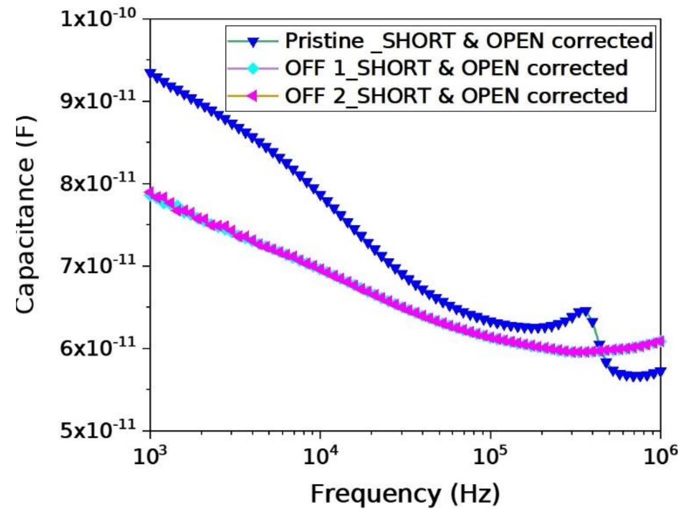

Figure 3.16: Capacitances of Pt/$YMnO_3$/Al devices in pristine and OFF states with on-chip OPEN and SHORT calibrations.

From this study, we demonstrate that the original concept of the vortices in $RMnO_3$ leading to a significant inductive behavior is not valid in polycrystalline films. A recent study in 2022 has shown that the ferroelectric domain size of $ErMnO_3$ polycrystals (ceramics) increases with decreasing grain size.[265] For a grain size of 1.5 µm, the ceramics exhibit a single domain configuration for the polarization. Since the grain size in our films is of 40 ± 15 nm, it is likely that the films are monodomains, without vortices.

We have then focused on only exploring the reconfigurability of devices between resistive and capacitive states (*R*-*C*). The partner at Jena developed inductive Cu coils on chips to take care of the inductive component of the final targeted circuit in the ERMI project.

3.4 Summary

- A standardized impedance measurement procedure was established, which includes the characterization of a commercial inductor component as a reference sample on a PCB board.
- Dedicated on-chip OPEN and SHORT calibrations were developed for impedance measurements on the probe station. These calibrations coupled with circuit simulations, enabled the determination of parasitics.
- Impedance measurements were conducted on Metal-Insulator-Metal (MIM) stacks with $YMnO_3$ and $ErMnO_3$. Both package- and probe station-based setups were used. Only low inductances in the nH range were determined which are at the detection limit (nH). Devices show a capacitive behavior in the OFF state and resistive behavior in the ON state, allowing the possibility for reconfigurable *R*-*C*.
- There is no possibility to have a *L*-*C* reconfigurability in the devices.

Our research has then focused on the reconfigurability of the $RMnO_3$-based devices between resistive and capacitive states (*R*-*C*). The results are presented in the next chapters.

Chapter 4: $YMnO_3$ thin film-based electrochemical metallization (ECM) devices

4 $YMnO_3$ thin film-based electrochemical metallization (ECM) devices 88
4.1 Polycrystalline $YMnO_3$ thin film optimization 90
4.1.1 Sputtering conditions 91
4.1.1.1 Effect of RF power 91
4.1.1.2 Effect of Ar pressure 93
4.1.2 Annealing conditions 94
4.2 Identification and quantification of the crystalline phases 101
4.3 Ferroelectric properties 104
4.4 Resistive switching in Pt/$YMnO_3$/Al devices 107
4.4.1 Device fabrication 108
4.4.2 Bipolar resistive switching of Pt/$YMnO_3$/Al devices 108
4.4.3 Thickness effect 112
4.4.4 Discussion on the filamentary mechanism 113
4.5 Reconfigurability between capacitive and resistive states 121
4.6 Summary 125

Research into the resistive switching behavior of polycrystalline hexagonal $YMnO_3$ thin films has demonstrated potential for applications in neuromorphic devices.[17, 21–25] Few studies have explored different electrodes, $YMnO_3$ compositions, and microstructures, leading to different observed mechanisms. Yan *et al.* described unipolar resistive switching in Pt/$YMn_{1-\delta}O_3$/Pt stacks, attributing the behavior to the formation and rupture of conductive filaments induced by Mn vacancies.[21] Bogusz *et al.* investigated unipolar resistive switching in h-$YMnO_3$ films with Au or Al top and Pt bottom electrodes, identifying oxygen vacancies as the cause of conductive filament formation along grain boundaries and charged domain walls.[17, 22] Wei *et al.* observed multilevel bipolar resistive switching in In/$YMnO_3$/Nb:$SrTiO_3$ devices, explaining it as resulting from modifications to the depletion region at the pn junction interface between h-$YMnO_3$ and Nb:$SrTiO_3$ upon polarization reversal.[23] Additionally, a recent study on cations doped h-$YMnO_3$ by Rayapati *et al.* demonstrated electroforming-free filamentary unipolar resistive switching in Al/h-$YMnO_3$/Pt stacks.[24] K. N. Rathod *et al.* showed interface-type bipolar resistive switching in Ag/h-$YMnO_3$/Si systems.[25] Thus far, research has been focused on polycrystalline hexagonal $YMnO_3$ thin films with different bottom and top electrodes.

However, due to difficulties in achieving single-phase polycrystalline h-$YMnO_3$ thin films[138, 146, 147, 150, 154] and the limitations of X-ray diffraction in conclusively identifying the absence of orthorhombic $YMnO_3$ (o-$YMnO_3$), it is conceivable that the reported resistive switching behaviors in the literature may be influenced by contributions from both crystalline phases. Moreover, all the devices mentioned above can be categorized as valence change memory devices, involving either a filamentary or an interfacial mechanism.[196] There are no reports of electrochemical metallization memory using $YMnO_3$ to date.

In this chapter, we develop a method to identify and locate the orthorhombic with hexagonal matrix, even when it is present at a few percent in h-$YMnO_3$ films. We then investigate Pt/$YMnO_3$/Al memristive devices with polycrystalline $YMnO_3$ films containing a mixture of o-$YMnO_3$ and h-$YMnO_3$ phases.

The chapter is organized as follows. We present the optimization of polycrystalline $YMnO_3$ thin films in Section 4.1. We study the microstructure of the films using multiple characterization methods to identify and quantify the different crystalline phases in Section 4.2. In Section 4.3, the ferroelectricity of $YMnO_3$ thin films is probed by piezoresponse force microscopy (PFM). Next, the resistive switching behavior in Pt/$YMnO_3$/Al is investigated in Section 4.4. Finally, reconfigurability between capacitive and resistive states of Pt/$YMnO_3$/Al stack is discussed in Section 4.5, followed by a short summary in Section 4.6.

The results presented in Sections 4.2 and 4.4 have been published in the journal *Small Structures*, ref.[266]

4.1 Polycrystalline $YMnO_3$ thin film optimization

The impact of different RF sputtering conditions and post-deposition annealing conditions on crystalline phases and film quality were investigated.

Si/SiO_2/Ti/Pt substrates were prepared by E-beam evaporation of 200 nm Pt and 30 nm Ti (as adhesion layer) on SiO_2 (1µm)/Si wafers. $YMnO_3$ films were deposited on the Si/SiO_2/Ti/Pt substrates by RF sputtering in Ar ambient at room temperature using $YMnO_3$ target. Subsequently, polycrystalline $YMnO_3$ films were obtained by post-deposition annealing.

First of all, the thickness uniformity of the as-deposited films was investigated (Figure 4.1). A film was deposited on a 5 × 5 cm^2 Si/SiO_2/Ti/Pt substrate at a RF power of 200 W and Ar pressure of 10 µbar. The thickness was mapped by spectroscopic ellipsometry. Measurements were taken within 4 × 4 cm^2 from the center of the substrate and the thickness was determined using the Tauc-Lorentz model. The thickness normalized to the value at the center of the film is also indicated in Figure 4.1. We observe a radially decreasing thickness across the film, with a maximum thickness at the center and a minimum thickness at the corners. This finding is consistent with the modeled thickness distribution of a sputtered film grown on a flat substrate with a centered circular target, reported by Susan Trolier-McKinstry and coauthors.[267] Hence, the effective deposition area to achieve a sample with less than 5% thickness difference across the entire film is 3 × 3 cm^2 placed at the center of the sample stage.

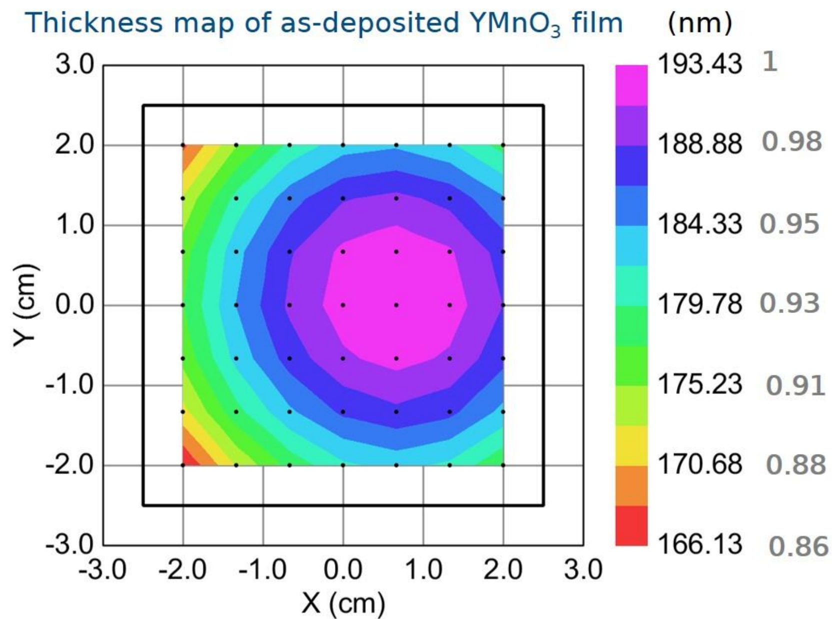

Figure 4.1: Thickness map over an area of 5 × 5 cm^2 of an as-deposited $YMnO_3$ film with sputtering conditions of RF power 200 W and Ar pressure 10 µbar. The thickness is determined by spectroscopic ellipsometry. The thickness and its value normalized to that at the center of the film (shown in grey) are presented.

4.1.1 Sputtering conditions

RF sputtering deposition is affected by a lot of parameters, such as RF power, Ar pressure, substrate temperature, deposition time, target tilt, etc. In this work, we mainly investigate the impact of RF power and Ar pressure on film growth, especially its crystalline phases and microstructure. All films had a similar thickness and were annealed under the same conditions.

4.1.1.1 Effect of RF power

As one of the main deposition factors, the RF power has a significant role in obtaining smooth and uniform thin films. At powers lower than 100 W, the ignited plasma was not stable; at powers higher than 300 W, the target might be damaged. Hence, different RF powers from 100 to 300 W were applied, as shown in Table 4.1, with the same Ar pressure of 10 µbar. The deposition time was adjusted to ensure the same film thickness. The film growth rate as a function of RF power is plotted in Figure 4.2. The growth rate increases linearly with RF power. The increase in RF power leads to an increase of ejected species from the $YMnO_3$ target, resulting in an increase of the growth rate.

Table 4.1: Impact of RF power on film thickness.

RF power (W)	Film thickness (nm)	Growth rate (nm/s)
100	243	0.08
200	287	0.27
300	268	0.45

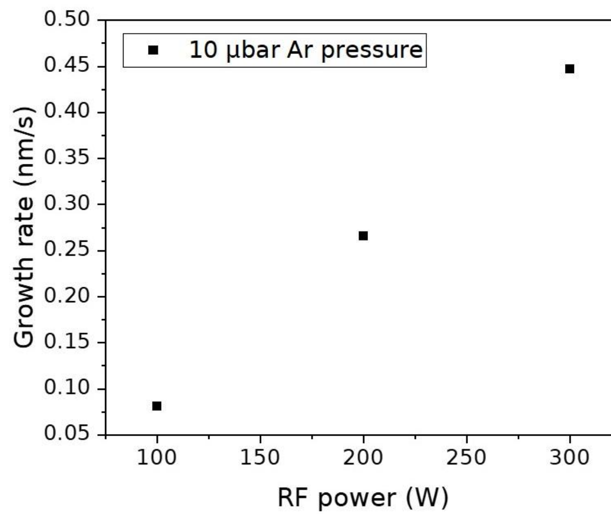

Figure 4.2: Growth rate of as-deposited $YMnO_3$ films as a function of RF power. Note that the thickness error determined from ellipsometry is at the sub-Angstrom scale, hence, the growth rate error is negligible in the plot.

All the films were annealed at 900 ºC under N_2 at 1 atm with flowing rate of 1 L/min in a furnace for 120 min. The GIXRD patterns of the annealed films deposited with different RF powers are shown in Figure 4.3. An as-deposited film (sputtered with RF power of 200 W) was measured as a reference. The film is amorphous and the peaks observed correspond to the Pt substrate [PDF 00-001-2680[268]] and to the amorphous signature (2θ ~ 32°). All annealed films are crystallized. The peaks can be assigned to the hexagonal $YMnO_3$ (h-$YMnO_3$) [PDF 04-011-9915[269]], orthorhombic $YMnO_3$ (o-$YMnO_3$) [PDF 04-007-4495[270]] and orthorhombic Mn_3O_4 (o-Mn_3O_4) [PDF 04-020-3526[271]] phases. Note that several peaks of h-$YMnO_3$ and o-$YMnO_3$ are very close or overlap, so some peaks can be assigned to both phases. The film sputtered with 200 W crystallizes mainly in the h-$YMnO_3$ with few possible peaks from o-$YMnO_3$. A minor peak from o-Mn_3O_4 appears in the films sputtered with 100 and 300 W. In addition, the intensity of the peak 00l is suppressed at 300 W, which suggests a change in texture. These results show that the RF power impacts the crystalline structure and preferred orientations, which can be attributed to the stress induced in the films by changing the RF power. Since we want to obtain polycrystalline $YMnO_3$ films with a pronounced *c*-axis orientation of h-$YMnO_3$, a RF power of 200 W was selected for further film optimization.

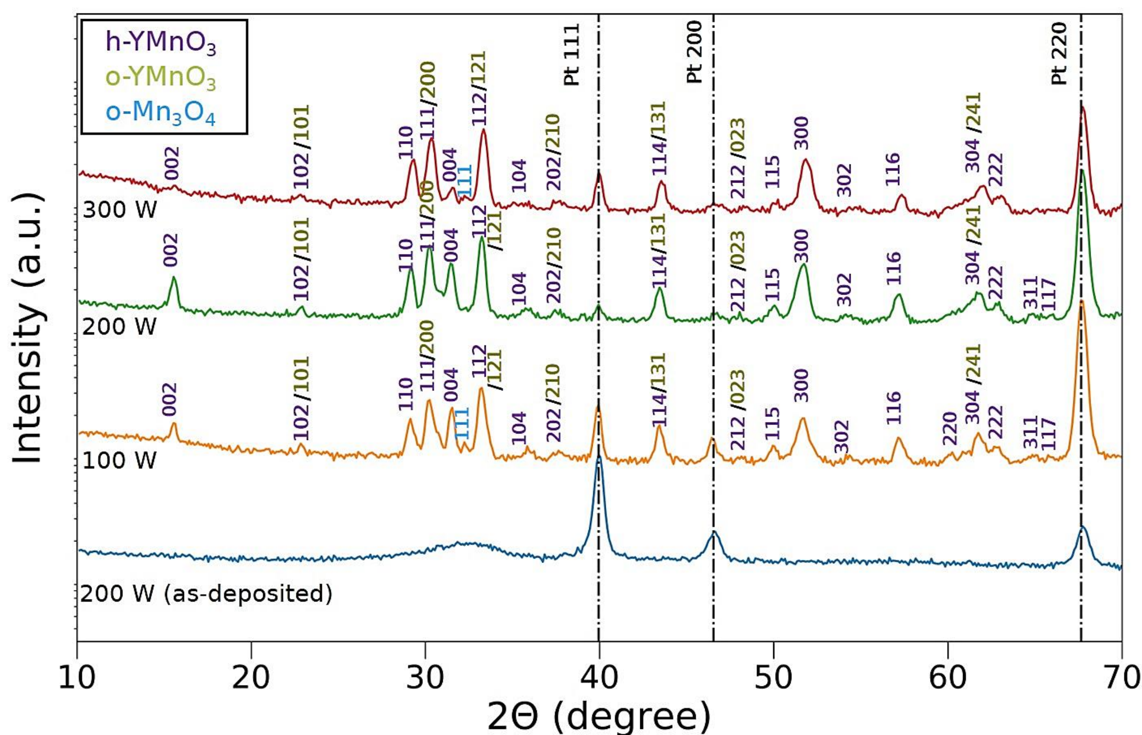

Figure 4.3: GIXRD patterns of $YMnO_3$ thin films deposited at different RF powers (films annealed in a furnace at 900 °C for 120 min in N_2). Film thicknesses are listed in Table 4.1.

4.1.1.2 Effect of Ar pressure

Figure 4.4 shows the thin film growth rate as a function of Ar pressure ranging from 2 to 20 µbar (RF power of 200 W). At pressures lower than 2 µbar, the plasma cannot be ignited. The growth rate increases slightly as Ar pressure increases up to 20 µbar. When Ar pressure increases, the number of ionized Ar^+ ions increases, resulting in a larger number of sputtered particles from the $YMnO_3$ target, therefore in an enhanced growth rate.

Table 4.2: Impact of Ar pressure on film thickness.

Ar pressure (µbar)	Film thickness (nm)	Growth rate (nm/s)
2	259	0.26
10	255	0.26
20	274	0.28

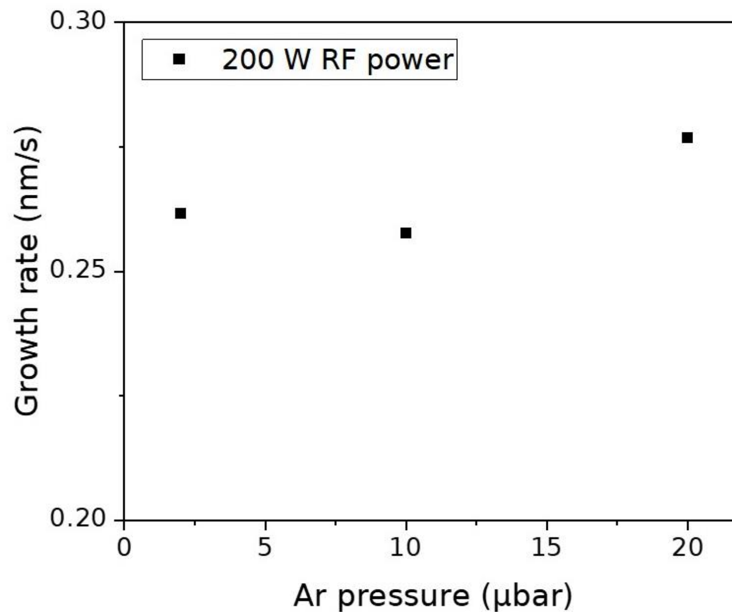

Figure 4.4: Growth rate of as-deposited $YMnO_3$ films as a function of Ar pressure. Note that the thickness error determined from ellipsometry is at the sub-Angstrom scale, hence, the growth rate error is negligible in the plot.

Figure 4.5 shows the GIXRD patterns of the films sputtered at different Ar pressures and annealed at 800 °C for 120 min in N_2 in a furnace. The peaks from the Pt substrate [PDF 00-001-2680[268]] are shown with dashed lines. The films sputtered at 2 and 10 µbar crystallize mainly in h-$YMnO_3$ [PDF 04-011-9915[269]] with few possible peaks from o-$YMnO_3$ [PDF 04-007-4495[270]]. At 20 µbar, additional peaks appear that

are attributed to o-$YMnO_3$. A weak peak from o-Mn_3O_4 is also observed. Hence, lower Ar pressure should be applied to avoid the secondary phase o-Mn_3O_4. The 004 diffraction peak from h-$YMnO_3$, shaded in blue, shifts towards lower 2θ values as the Ar pressure increases, which indicates that the out-of-plane lattice parameter increases. An Ar pressure of 10 µbar was selected for the further film optimization.

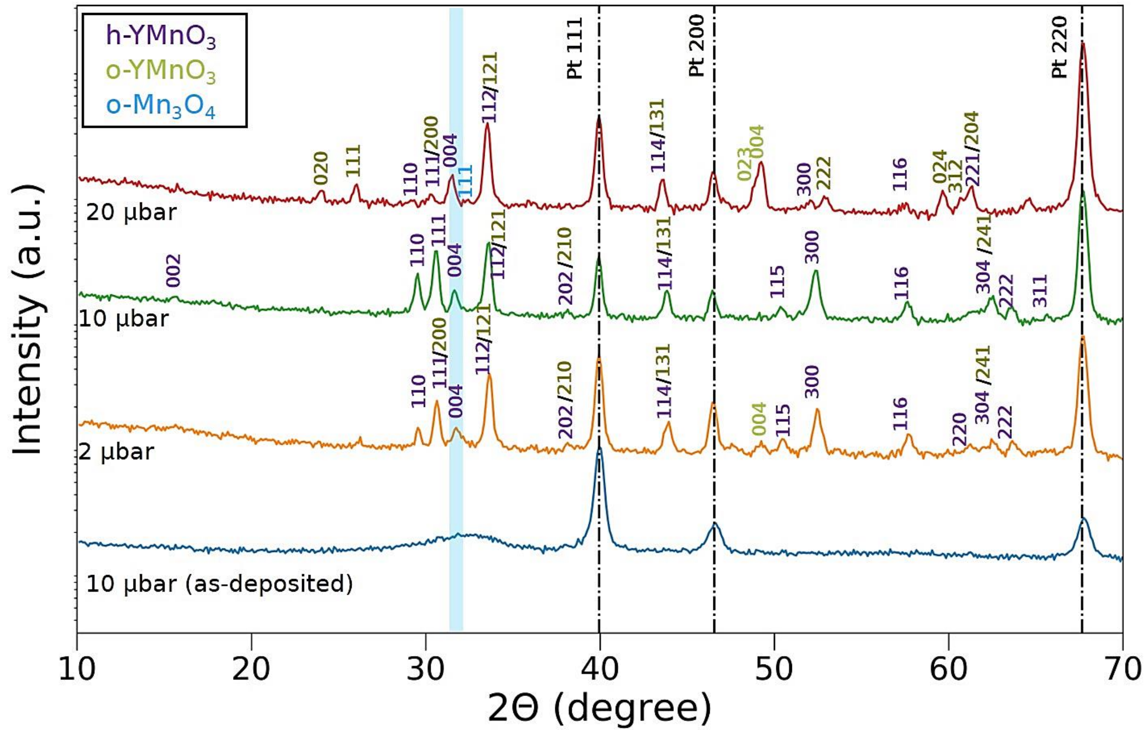

Figure 4.5: GIXRD patterns of $YMnO_3$ thin films deposited with different Ar pressures (films annealed in a furnace at 800 °C for 120 min in N_2). Film thicknesses are listed in Table 4.2.

4.1.2 Annealing conditions

A RF power of 200 W and an Ar pressure of 10 µbar were selected as the optimized sputtering conditions. Here we continue the study with the effect of annealing conditions on the crystalline phases formed in $YMnO_3$ films. In Table 4.3 we present the different annealing parameters.

Table 4.3: Impact of annealing conditions on the crystalline phases formed in $YMnO_3$ films. All films were sputtered with a RF power of 200 W and an Ar pressure of 10 μbar.

Film thickness (nm)	Annealing temperature (°C)	Annealing time (min)	Atmosphere
234	900	120	Furnace – N_2 (with residual O_2)
77	725	30	Furnace – N_2
76	800	30	Furnace – N_2
74	900	30	Furnace – N_2
261	1000	120	Furnace – N_2

The GIXRD pattern of the film annealed in a furnace with N_2 flow and O_2 residue is shown in Figure 4.6. The presence of residual O_2 leads to the dominant formation of o-YMn_2O_5 [PDF 00-034-0667[272]] with minor h-$YMnO_3$ and o-$YMnO_3$ phases. Hence, to avoid the secondary phase o-YMn_2O_5 in this work, inert atmosphere with only N_2 was applied to crystallize the films.

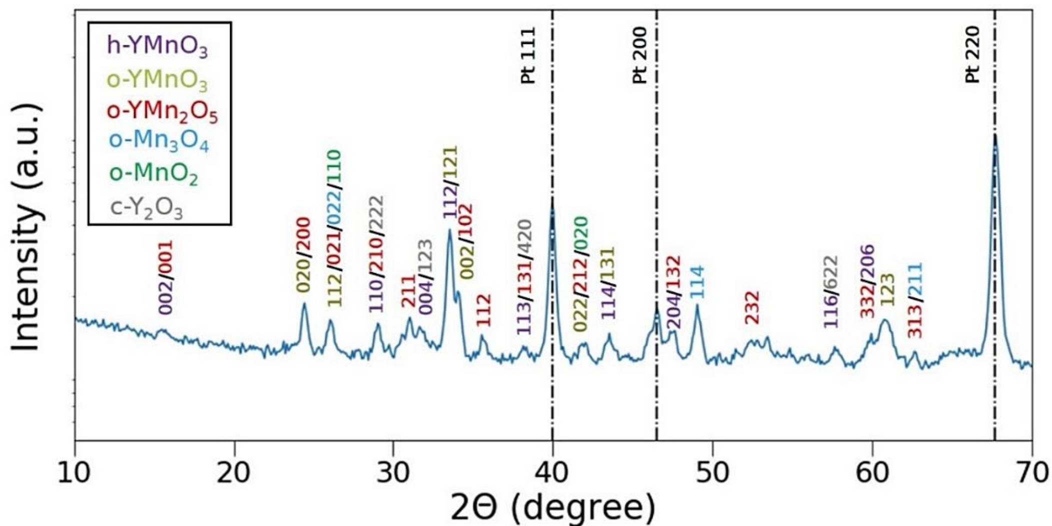

Figure 4.6: GIXRD pattern of $YMnO_3$ thin film (sputtered with a RF power of 200 W and an Ar pressure of 10 μbar) annealed at 900 ºC for 120 min in a furnace with N_2 and residual O_2. The film thickness is listed in Table 4.3.

The as-deposited amorphous films were annealed in a furnace in N_2 at different temperatures ranging from 725 to 1000 °C. The GIXRD patterns are shown in Figure 4.7. At 725 °C the films crystallize mainly in the hexagonal phase[269] but a few peaks from the orthorhombic phase[270] also appear. These peaks are no more observed for the samples annealed at 800 °C and 900 °C. **However, we will show later, using other techniques, that the orthorhombic phase is still present.** At 1000 °C, there are several peaks from the orthorhombic phase, indicating the transition from hexagonal phase to orthorhombic phase at high annealing temperature.

We observe that the effect of the annealing temperatures on the crystalline phases formed is more significant than that of the initial deposition parameters.

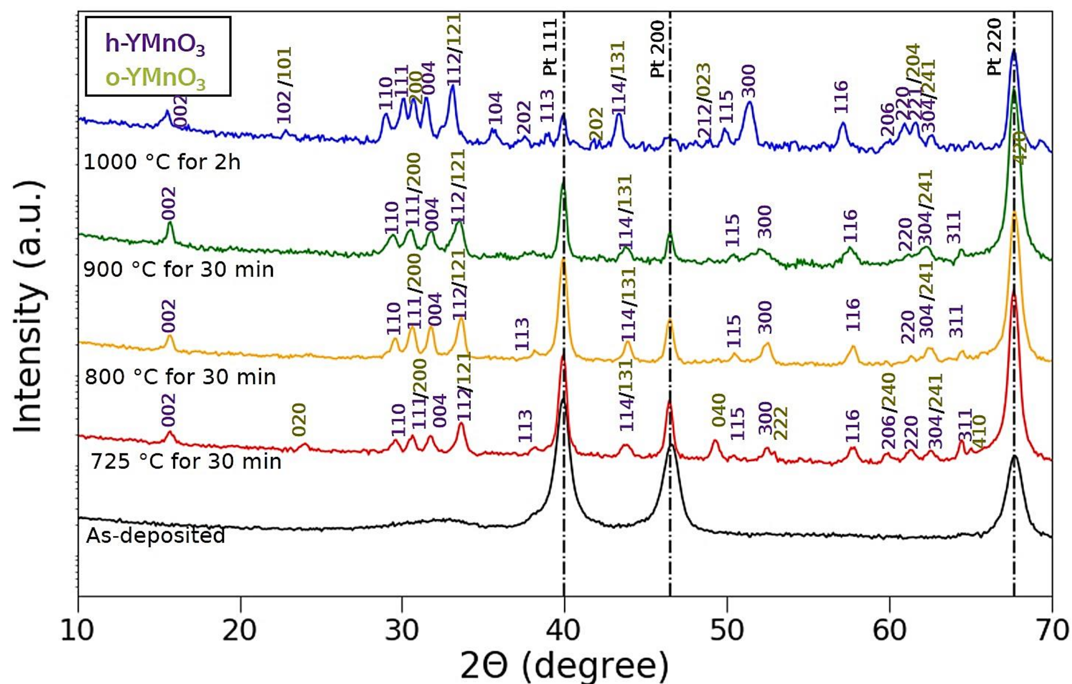

Figure 4.7: GIXRD patterns of $YMnO_3$ thin films annealed at different annealing temperatures in a furnace with N_2 flow. The annealing condition and film thickness of the films are shown in Table 4.3.

In some films we observe the coexistence of o- and h-$YMnO_3$ while the thermodynamically stable phase is the hexagonal one. Calculations of the free energy of $RMnO_3$ formation from R_2O_3 and Mn_2O_3 at 900 °C[45, 46] indicate only a slight difference between the thermodynamically stable hexagonal and the metastable orthorhombic phases for $YMnO_3$ (see Figure 1.3 in Chapter 1). Consequently, under specific conditions such as high pressure synthesis,[47–50] soft chemistry synthesis[53, 54] and epitaxial strain in thin films, the metastable orthorhombic phase of $YMnO_3$ can be stabilized.[56, 57] Romaguera-Barcelay *et al.* reported that in polycrystalline thin films prepared on Si/SiO_2/Ti/Pt substrates by chemical solution deposition and annealed at 875 °C, the o-$YMnO_3$ phase coexisted with the h-$YMnO_3$ one. They linked this to strain induced

by the substrate.[150] Similarly, the presence of the orthorhombic phase in our films may be attributed to the strain resulting from the significant mismatch in lattice expansion coefficients between $YMnO_3$ and the Pt metal substrate.

While ceramics typically demand a quite high temperature of 800 °C for the crystallization of the h-$YMnO_3$ phase under atmospheric pressure,[112, 146] the films in this study achieve crystallization at a lower temperature of 725 °C. This can be attributed to the enhanced reactivity and mobility of atoms in thin films, as well as the influence of substrates.

Table 4.4 presents the estimated lattice parameters of h-$YMnO_3$ in the different samples, compared to those of single crystals.[269] We observed that both *a* and *c* lattice parameters in the films annealed below 1000 °C are significantly smaller than the ones of single crystals prepared under atmospheric pressure. Studies on h-$YMnO_3$ powders have shown deviations in crystal structure for nanocrystallites smaller than 80 nm, with alterations in unit cell distortion and unit cell volume.[112] Our observed lattice parameters for h-$YMnO_3$ with grain sizes of 40 ± 15 nm (SEM data in Figure 4.9) are much lower than the expected values.[112] An explanation for the relatively small *a* and *c* values emerges when our data are compared with those from single crystals prepared under 5 GPa (Table 4.4, ref[269]). The close alignment between our values and those of high-pressure single crystals suggests that the strain imparted by the Pt substrate during the cooling process from high temperatures (725 – 900 °C) to room temperature mimics the effects of high pressure.

There is indeed a tensile stress induced by the thermal mismatch between the thin film and the platinum coated silicon substrate during the cooling in annealing process.[138, 273] Moreover, stress is easily promoted due to the highly anisotropic thermal expansion coefficients of the h-$YMnO_3$ unit cell.[138]

The film annealed at 1000 °C shows larger *a* and *c* values than those of films annealed below, closer to the ones of single crystals prepared under atmospheric pressure.[269] The film has a larger grain size and exhibits microcracks (Figure 4.8), which likely originate from strain relaxation as the tensile strain becomes too large to accommodate within the crystalline cell. Hence, in order to obtain crack-free thin films, the annealing temperature should be below 1000 °C.

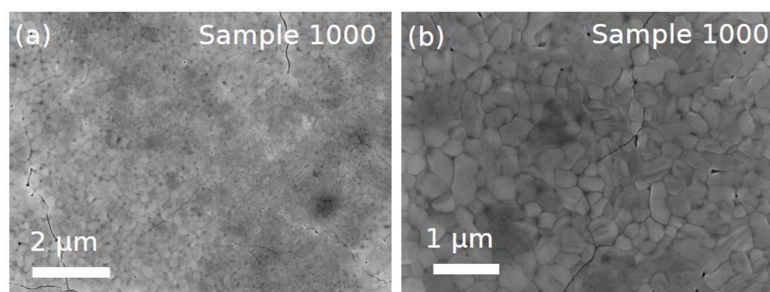

Figure 4.8: SEM images of $YMnO_3$ thin films annealed at 1000 °C (sample 1000) with in-lens detector and acceleration voltage of 10.0 kV. Microcracks are observed. The figures are from ref.[266]

Table 4.4: Lattice parameters and unit cell volume of the hexagonal phase in $YMnO_3$ films annealed at 725 to 1000 °C and of hexagonal $YMnO_3$ single crystal from ref.[269] The in-plane a and the out-of-plane c lattice parameters were calculated from the 110 and 004 peaks, respectively. The 111 peak at 2θ = 40.05° of Pt was taken as a reference.

Samples	**In plane lattice *a* (Å)**	**Out of plane lattice *c* (Å)**	**Volume of cell (Å^3)**
Single crystal (0 GPa)[269]	6.151	11.410	373.86
Single crystal (5 GPa)[269]	6.067	11.305	360.37
Annealed at 725 °C	6.00	11.23	350.12
Annealed at 800 °C	6.02	11.23	352.45
Annealed at 900 °C	6.04	11.20	353.85
Annealed at 1000 °C	6.13	11.36	369.68

The surface morphology of the films should be pinhole free and of good quality to enable the fabrication of high-quality devices. In Figure 4.9, we show SEM images of an as-deposited $YMnO_3$ thin film (A) and of the films annealed at 725, 800, and 900 °C (sample 725, sample 800, and sample 900). Film A exhibits a uniform greyscale contrast and a featureless morphology. Samples annealed at 725 and 800 °C reveal areas with distinct bright/dark contrast and a granular appearance with grain sizes of 40 ± 15 nm. The film annealed at 900 °C exhibits a different microstructure with pinholes, indicating that it is unsuitable for device fabrication.

Figure 4.10 shows the optical microscope images of the same films. The as-deposited film (sample A) and the film annealed at 900 °C (sample 900) show a uniform contrast. Films annealed at 725 and 800 °C (sample 725, sample 800) exhibit a bright/dark contrast, particularly sample 725 shows more dark regions than sample 800.

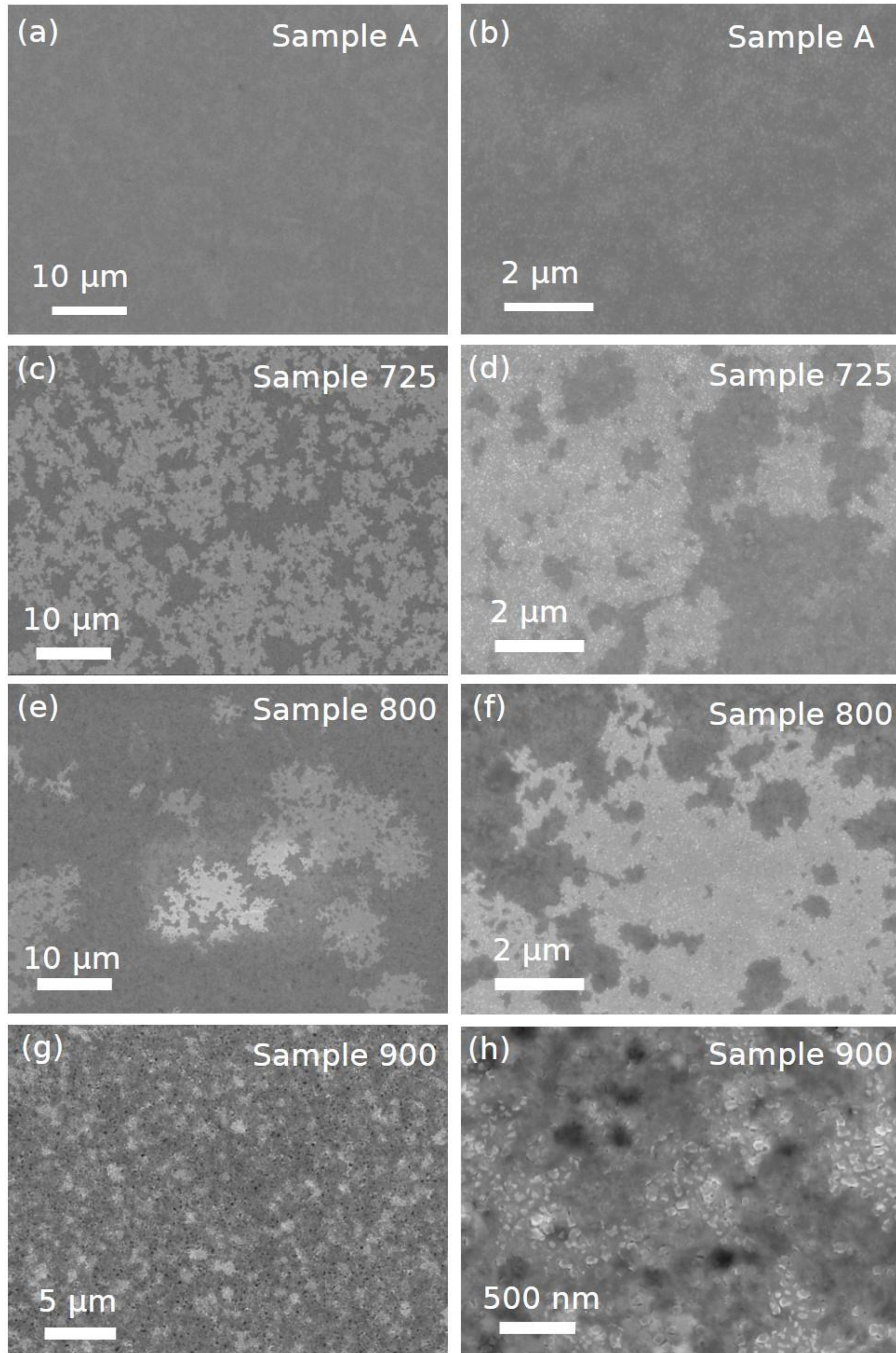

Figure 4.9: SEM images of (a, b) as-deposited $YMnO_3$ thin film (sample A), $YMnO_3$ thin films annealed at (c, d) 725 °C (sample 725), (e, f) 800 °C (sample 800), and (g, h) 900 °C (sample 900) with in-lens detector and acceleration voltage of 10.0 kV. The figures are from ref.[266]

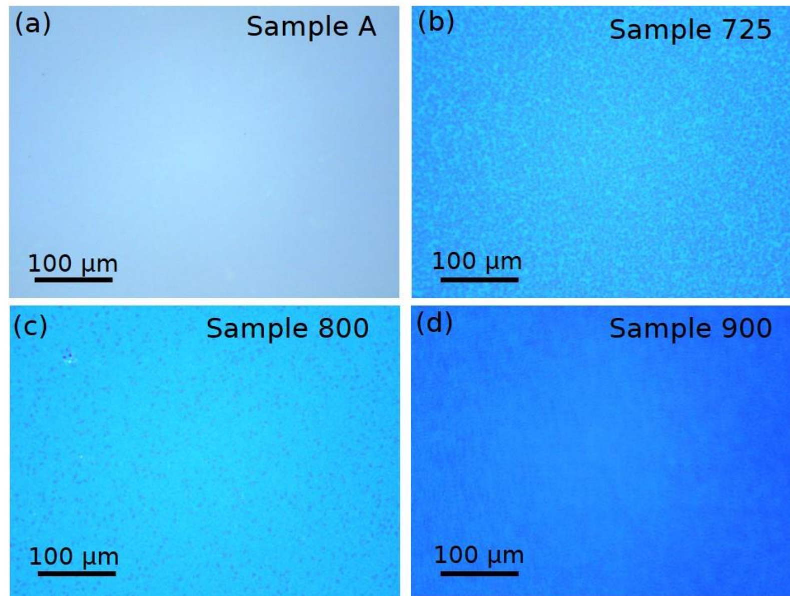

Figure 4.10: Optical microscope images of samples in Figure 4.9. The figures are from ref.[266]

Following annealing, all films exhibit significant roughness, as shown by AFM images in Figure 4.11. The amorphous film shows a root-mean-square (RMS) roughness of ~ 6.2 nm, slightly higher than that of the Pt substrate of ~ 4.9 nm. Upon annealing, the roughness of the polycrystalline $YMnO_3$ films undergoes a strong increase, ranging from a RMS value of 8.4 to 13.0 nm for films annealed at temperatures of 725 to 900 °C.

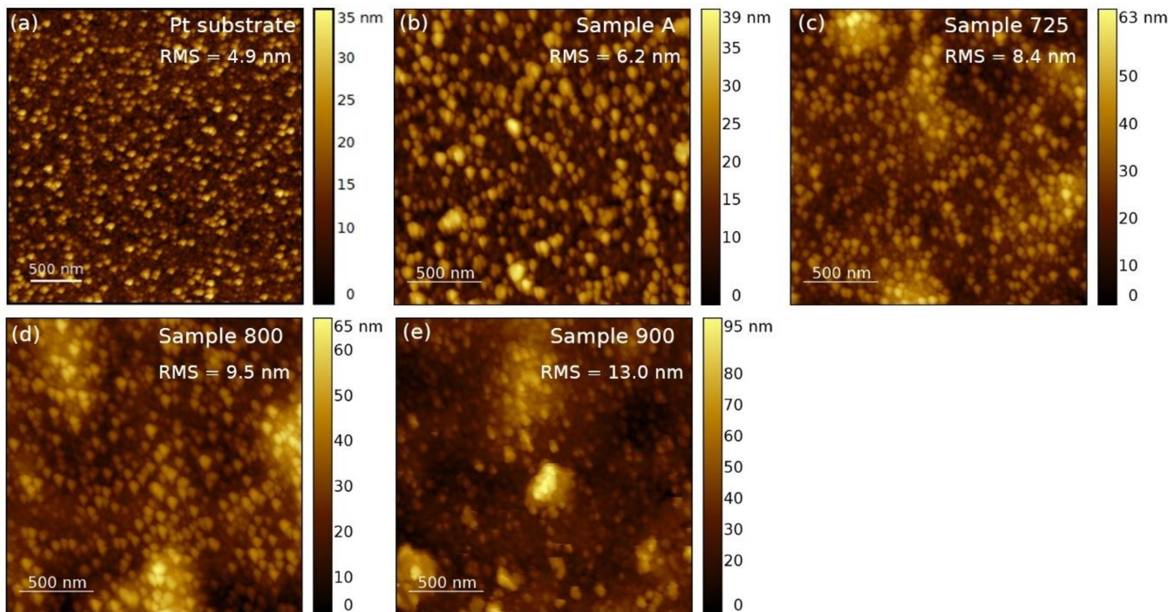

Figure 4.11: AFM images of Pt substrate, samples A, 725, 800 and 900 and their RMS values.

4.2 Identification and quantification of the crystalline phases

As we observed bright/dark contrast in both SEM images and optical microscope images of films annealed at 725 and 800 °C, it is important to find the origin of the contrast. SEM and optical microscope images were recorded at the same location of a film annealed at 800 °C (see Figure 4.12a, b), showing that high secondary electron yield regions in SEM image correspond to dark regions in optical microscope image. Compositional and topographic contrasts are the two dominant factors, which can be responsible for the contrast in SEM. Therefore, to disambiguate between the different possible origins we performed Raman spectroscopy on the area indicated by the black box in Figure 4.12a, b.

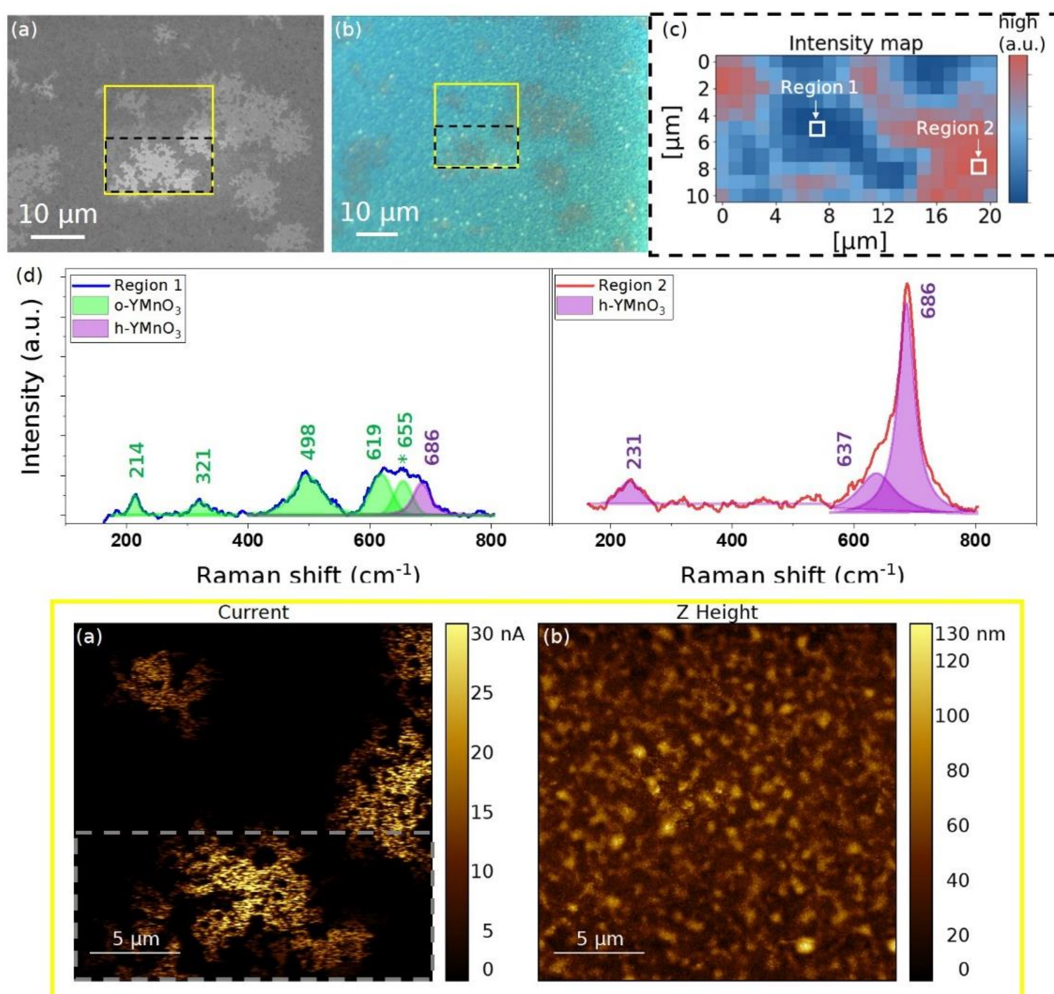

Figure 4.12: (a) SEM and (b) optical microscope images of sample 800 (film annealed at 800 °C). (c) Map of the intensity of the mode $A_1(TO_9)$ (686 cm^{-1}) characteristic of the h-$YMnO_3$ phase. The map was recorded in the area marked by the black box in (a, b). (d) Two Raman spectra representing "Region 1" (blue) and "Region 2" (red), marked with white boxes in (c). e) Current map measured with c-AFM in the area marked by the yellow box in (a, b). The grey rectangle indicates the location of the Raman map, shown in panel (c). (f) Topography map recorded simultaneously with the c-AFM map in (e). The figures are partially adapted from ref.[266]

Raman spectroscopy mapping was conducted with a scan size of 10 × 20 μm^2, a beam size of 1 µm and a spatial resolution of ~1 µm. The mapped area, marked by the black dashed box in Figure 4.12a, b, covers regions of both high and low secondary electron yield in the SEM images (or low and high brightness in the optical microscope images). In Figure 4.12c, the Raman intensity map is presented based on the intensity of the $A_1(TO_9)$ mode at 686 cm^{-1}, corresponding to the stretching of apical oxygen atoms (O1 and O2) along the *c*-axis. This mode is associated with the tilting and trimerization of the MnO_5 polyhedra in the hexagonal phase,[274] absent in the orthorhombic phase. We identify two distinct regions colored in blue ('Region 1') and red ('Region 2') based on the intensity of the peak at 686 cm^{-1}. Figure 4.12d shows typical Raman spectra from these regions. All the recorded peaks are listed in Table 4.5 together with the reported Raman active modes of h-$YMnO_3$ and o-$YMnO_3$ single crystals. The blue curve indicates the presence of o-$YMnO_3$ with a minor h-$YMnO_3$ contribution. The red curve indicates pure h-$YMnO_3$. The comparison of the Raman intensity map with Figure 4.12a, b reveals that high secondary electron yield in SEM and low brightness in optical microscopy are the signature of o-$YMnO_3$ phase ('Region 1' colored in blue in Figure 4.12c). Conversely, low secondary electron yield in SEM and high brightness in optical microscope correspond to h-$YMnO_3$ phase ('Region 2' colored in red in Figure 4.12c). Note that, as the bright features observed in the SEM image (Figure 4.12a) exhibit irregular, discontinuous and 'branched-like' shapes, each measured spot size of 1 × 1 μm^2 might include a small amount of h-$YMnO_3$, explaining why the Raman mode $A_1(TO_9)$ belonging to h-$YMnO_3$ is detected in 'Region 1'.

Table 4.5: Raman active modes recorded on sample 800 and reported in literatures.

Reported h-$YMnO_3$ (cm^{-1})			Reported o-$YMnO_3$ (cm^{-1})			Our work	
Mode	Calculated [274]	Measured [275]	Mode	Calculated [276]	Measured [276]	Region 1	Region 2
$E_2(5)$	243	215	$B_{2g}(5)$	162	220	214	231
$E_1(TO_5)$	274	238	$A_g(6)$	304	323	$A_g(6)$ 321	
$E_1(TO_{14})$	644	632	$A_g(3)$	466	497	$A_g(3)$ 498	$E_1(TO_{14})$ 637
$A_1(TO_9)$	691	681	$B_{2g}(1)$	617	616	B2g 619	$A_1(TO_9)$ 686
					653[a)]	655[a)]	
						$A_1(TO_9)$ 686	

a) This Raman shift is not related to a proper vibration mode from o-$YMnO_3$[276]; it might be originating from defects[277] or contributions from zone-boundary phonons[276].

Conductive atomic force microscopy (c-AFM) measurements further confirmed the presence of the orthorhombic phase in the hexagonal phase matrix. Note that these two crystalline phases have significant different conduction properties (see Section 1.2.3), as the orthorhombic phase has been reported to have a higher electrical conductivity compared to the hexagonal one.[278] A $20 \times 20\ \mu m^2$ c-AFM spatial map (Figure 4.12e) was performed in the yellow box area of Figure 4.12a, b. A direct correlation exists between the high conductive regions, the bright/dark regions in SEM/optical microscope images (Figure 4.12a, b), and the area identified as o-$YMnO_3$ in the Raman spectroscopy map (Figure 4.12c). The topography image (Figure 4.12f) indicates no significant difference in surface morphology between the high and low conductive regions, ruling out topographic contributions to the contrast observed in SEM and optical microscopies.

Through these correlative microscopy and spectroscopy analyses, the presence of o-$YMnO_3$ in polycrystalline h-$YMnO_3$ thin films is clearly identified. o-$YMnO_3$ cannot be discriminated by X-ray diffraction due to the low volume amount and nanosized grains leading to undetectable peaks or overlapping peaks with h-$YMnO_3$.

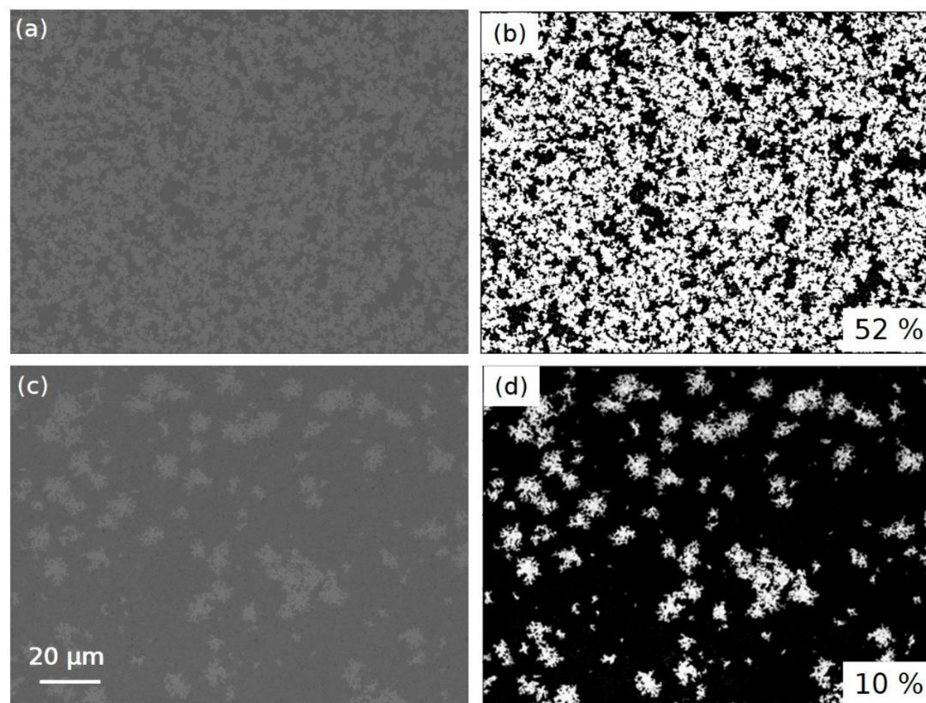

Figure 4.13: (a) and (c) SEM images of sample 725 and sample 800. (b) and (d) Segmentation results for the SEM images (a) and (b) respectively, of high/low electron yield regions for the estimation of the fraction of o-$YMnO_3$. The figures are from ref.[266]

Additionally, quantitative insights into the crystalline fraction (ratio of o-$YMnO_3$ to h-$YMnO_3$) are obtained through processing algorithms applied to dark/bright regions in SEM images. Films annealed at 725 and 800 °C contain ~52% and ~10% o-$YMnO_3$ phase, respectively (Figure 4.13). Note that these percentages, as derived from secondary electrons from the surface, do not necessarily represent the volume ratio. However, we assume that the orthorhombic phase regions extend down to the bottom interface (Pt substrate) since we can detect them by c-AFM.

4.3 Ferroelectric properties

Hexagonal $YMnO_3$ is an improper ferroelectric with a remanent polarization of around 5.5 $\mu C/cm^2$ in single crystal form.[40] The topological domain structures (six domains merging at a vortex line) have so far been observed in bulk single crystals,[70, 279, 280] ceramics[72, 265] and epitaxial high quality thin films.[80] As reported by H. Schmidt, interplay between the ferroelectric domains and vortices, and resistive switching behaviors in polycrystalline $YMnO_3$ thin films could bring multiple potential applications.[15] However, observing the ferroelectric domains and vortices in epitaxial $RMnO_3$ thin films at room temperature has remained very rare. We are aware of only one report.[80] If a similar trend holds same for polycrystalline films as seen in ceramics, an increase in domain size resulting in a single domain.[72, 265]

In polycrystalline hexagonal yttrium manganite thin films, Rayapati *et al.* reported that they observed charged ferroelectric domains by SEM using low acceleration voltage (1.0 kV) with in-lens detector.[281] They used in-lens detector instead of conventional secondary electron detector to avoid pronounced topographic information. Bright and dark contrast regions were observed, and the authors concluded that bright and dark regions correspond to upward and downward polarizations, respectively.

For comparison, SEM images with a low acceleration voltage of 1.0 kV were also captured by in-lens detector on our film annealed at 800 ºC, as presented in Figure 4.14. We also observe a bright and dark contrast pattern. However, we have shown that this contrast originates from the presence of o-$YMnO_3$ in h-$YMnO_3$ matrix. Hence, we think that the contrast observed in SEM in this case does not allow to support the existence of ferroelectric domains in polycrystalline thin films.

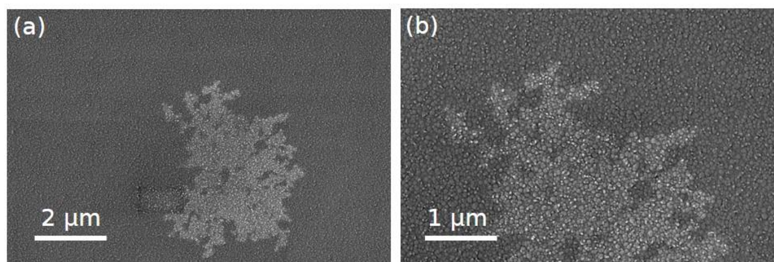

Figure 4.14: SEM images of film annealed at 800 °C with in-lens detector and acceleration voltage of 1.0 kV. The figures are from ref.[266]

In order to get insight into the ferroelectric properties and domain structures of our films, vertical piezoresponse force microscope (PFM) was carried out. Figure 4.15 shows the surface topography, PFM amplitude and phase images for a film annealed at 750 °C. No topological clover-leaf like domain structures, as seen in single crystals,[70, 80] are observed, but high and low amplitude regions (Figure 4.15b) and noisy phase (Figure 4.15c). As discussed in previous sections, o-$YMnO_3$ is more conductive than h-$YMnO_3$. Hence, the conductive phase could enhance the accumulation of surface charges, causing electrostatic interactions between the tip and surface charges and therefore a higher amplitude.

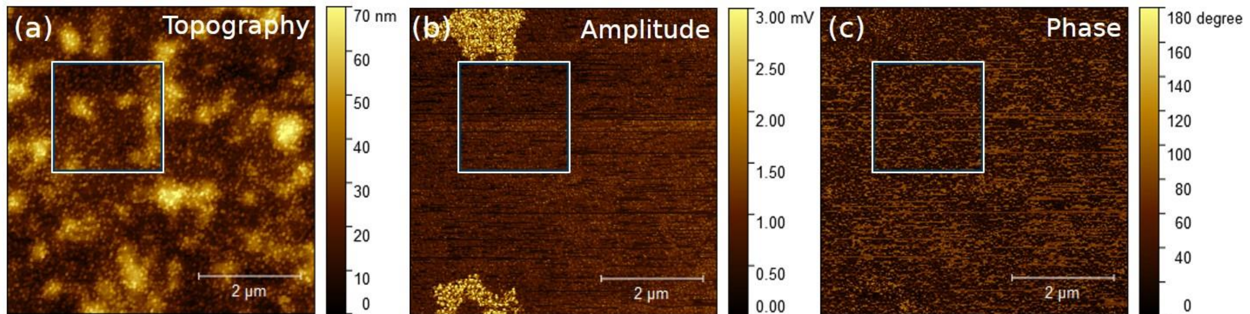

Figure 4.15: Vertical PFM images of pristine polycrystalline $YMnO_3$ thin film annealed at 750 ºC. (a) Topography, (b) Piezoresponse amplitude and (c) Piezoresponse phase images.

A region with h-$YMnO_3$ was further investigated by electrical poling measurements. A $2 \times 2\ \mu m^2$ area of the film inside the white box marked in Figure 4.15 was poled through the tip by applying a DC bias of + 5 V (half left) and -5 V (half right). Figure 4.16 shows the PFM topography, amplitude and phase images of the film after poling. The surface topography remains unchanged after poling, as seen in Figure 4.16a. Poling at -5 V leads to a partial change in phase contrast, compared to the pristine area outside the poled area (see Figure 4.16c), suggesting regions of upward polarization; +5 V poling does not change either amplitude or phase significantly, indicating that the pristine state is single domain with downward polarization. However, the phase signal in the area with upward polarization has mixed bright and dark contrasts, indicating that the upward polarization is not as stable and switches back to down direction.

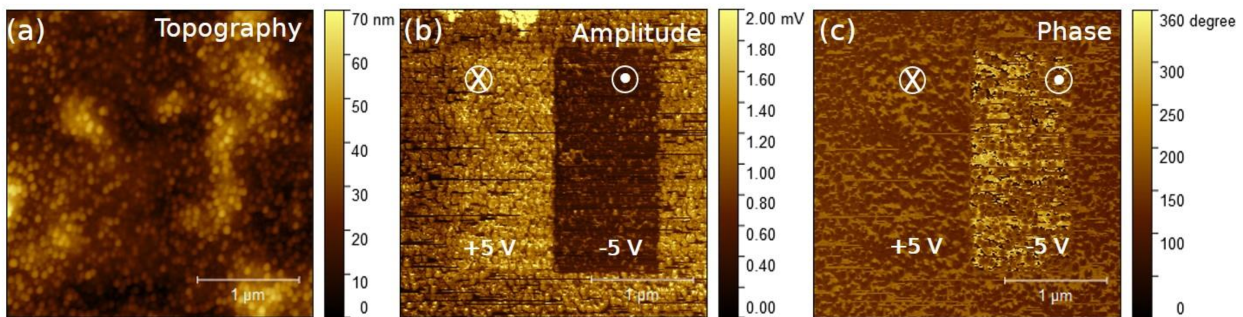

Figure 4.16: Vertical PFM images of polycrystalline $YMnO_3$ thin film annealed at 750 ºC after electrical poling of ± 5V. (a) Topography, (b) Piezoresponse amplitude and (c) Piezoresponse phase images.

Mechanical switching via flexoelectricity has been demonstrated as a method to study electrical polarization in ferroelectric thin films, where the stress gradient from an AFM tip can induce polarization switching within nano-scale volumes.[282–284] A mechanical switching experiment was performed on a 1×1 μm^2 region by applying different loading forces from 150 to 1500 nN through the tip on a pre-poled area, as illustrated in Figure 4.17a. Note that cantilever NSC14 was used for mechanical writing due to its larger stiffness (force constant of 5 N/m). A sketch of the strain gradient and of the corresponding flexoelectric field induced by the probe is shown in Figure 4.17b.

Figure 4.18a, b shows the PFM amplitude and phase images after the mechanical writing. When the loading force increases from 150 to 1500 nN, the PFM phase contrast in the right of the image (initially electrical poled upward) changes from bright to dark, suggesting the reversal of the polarization. Line scans were extracted from the phase image, as marked lines (1, 2) shown in Figure 4.18b. As the initial upward poled polarization was not stable, the phase change across both electrically poled regions with downward and upward polarizations under lower loading force (as indicated by profile 1) is less than 60°. When the loading force increases, the phase of the region poled upward decreases to be the same as that of the downward poled area, shown as line 2 in Figure 4.18c. This observation indicates that the tip-induced stress results in the inversion of the polarization from up to down as a result of flexoelectric switching. Since no voltage is applied during the mechanical writing, charge injection or accumulation at the surface can be minimized.

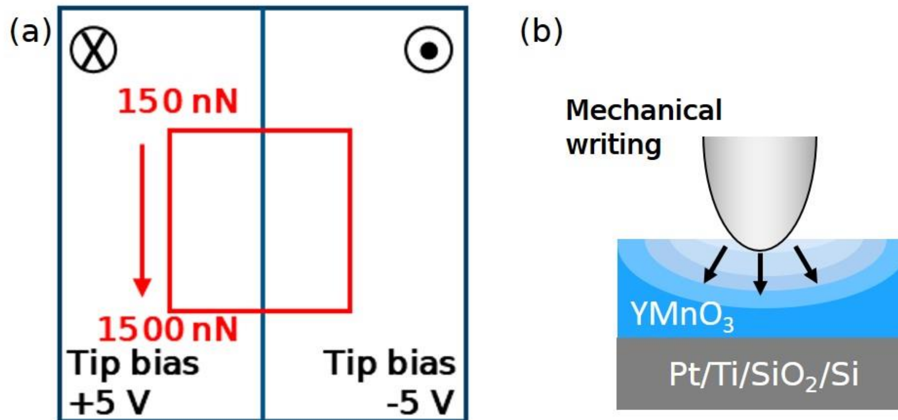

Figure 4.17: (a) Electrical poling with tip bias of ± 5V and mechanical writing with loading force from 150 to 1500 nN. (b) Sketch of the strain gradient and the flexoelectric field induced by the AFM tip by pressing the surface of $YMnO_3$ during the mechanical writing.

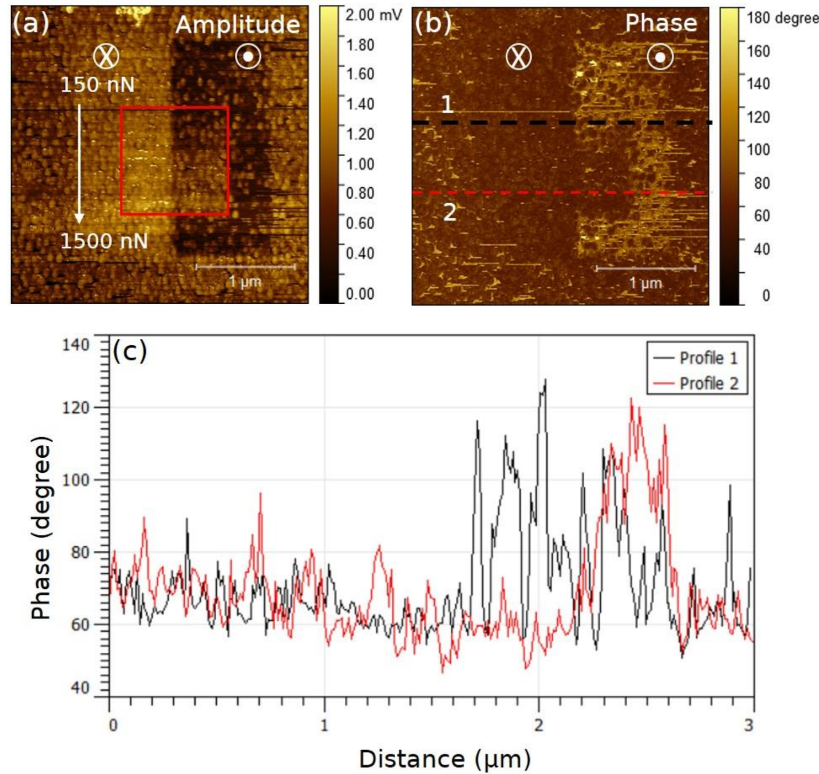

Figure 4.18: Vertical PFM images of a polycrystalline $YMnO_3$ thin film annealed at 750 ºC after mechanical writing with different loading forces from 150 to 1500 nN. (a) Piezoresponse amplitude and (b) Piezoresponse phase images. (c) Line scan of phase through the mechanical written area, corresponding to the lines marked in (b).

In summary, the typical domain pattern for h-$YMnO_3$ (six domains merging at a vortex line, see Figure 1.6 in Chapter 1) was not observed in the pristine state of polycrystalline h-$YMnO_3$ thin films. However, evidence of ferroelectricity was observed upon electrical and mechanical poling. According to a recent study by J. Schultheiß *et al.*,[265] the ferroelectric domain size of $ErMnO_3$ ceramics increases with decreasing grain size. A single domain is reported for a grain size of ~ 1.5 µm or lower. From this recent study on ceramics, we can expect that our films have a single domain configuration (with a grain size of 40 ± 15 nm). From the writing/switching PFM experiments, the polarization is oriented downward.

4.4 Resistive switching in Pt/$YMnO_3$/Al devices

In this section, we investigate Pt/$YMnO_3$/Al memristive devices with polycrystalline $YMnO_3$ films containing a mixture of o-$YMnO_3$ and h-$YMnO_3$ phases. The mixed phases are achieved by controlling the annealing conditions of the amorphous $YMnO_3$. The mechanisms involved in the switching behavior are investigated. The impact of the microstructure and crystalline phase ratio will be discussed.

4.4.1 Device fabrication

Figure 4.19 shows the process flow of Pt/$YMnO_3$/Al stacks. Polycrystalline $YMnO_3$ films with thickness of 75 nm and 215 nm were prepared on Pt-coated Si substrates (by E-beam evaporation) at room temperature by RF sputtering using a RF power of 200 W and an Ar pressure of 10 µbar. The films were annealed for 30 min in a quartz tube furnace under 1 atm of N_2 at different temperatures (725, 800 and 900 °C, named as samples 725, 800 and 900). Pt/$YMnO_3$/Al capacitive devices were fabricated with ~ 500 nm-thick Al top electrodes by lift-off process using photolithography and E-beam evaporation of Al. We examined different active device areas, ranging from 1.12×10^{-4} to 11.00×10^{-4} cm^2. In addition, to study devices with single crystalline phase regions by conductive AFM, small circular Al top electrodes with a thickness of ~ 60 nm and a diameter of 1.5 µm were patterned using lift-off process with direct laser writing lithography and thermal evaporation of Al.

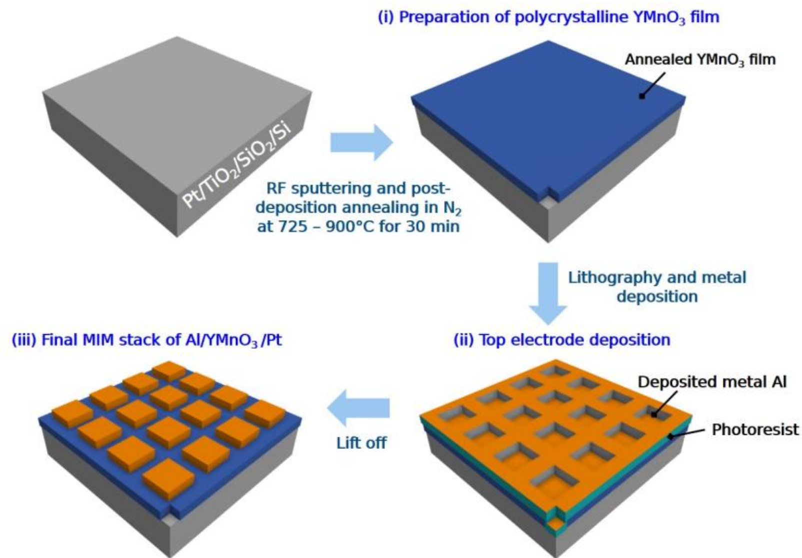

Figure 4.19: Process flow of Pt/$YMnO_3$/Al metal/insulator/metal (MIM) stack. (i) Preparation of polycrystalline $YMnO_3$ film. (ii) Top electrode deposition. (iii) Final MIM stack of Pt/$YMnO_3$/Al.

4.4.2 Bipolar resistive switching of Pt/$YMnO_3$/Al devices

Current-voltage (*I-V*) measurements were conducted on Pt/$YMnO_3$/Al devices. In the measurements, the Pt bottom electrode was grounded and the DC voltage bias was applied to the Al top electrode (Figure 4.20a). The leakage current densities at 50 mV of the pristine devices were measured for various device areas (see Figure 4.20b) and were found to be area independent. The devices with an amorphous film (sample A) have the smallest current density of ~10^{-8} A/cm^2. The device with the film annealed at 900 °C show a higher leakage current density ranging from ~ 10^{-4} up to 10^{-3} A/cm^2. The large current density is due to the presence

of pinholes (see Figure 4.9d, h). The devices fabricated with films annealed at 725 and 800 °C exhibit current densities on the order of ~10^{-6} A/cm^2.

To study the resistive switching characteristics of the devices, *I-V* curves were measured. A positive voltage sweep was performed starting from the high resistance state (HRS). The sweep was from 0 to 5 V with a sweep rate of 75 mV/s. When the voltage exceeds a threshold voltage (V_{Set}), the device transitions to a low resistance state (LRS), which is known as the Set process. To avoid an irreversible hard breakdown of the device, a compliance current of 500 μA was applied. To initiate the Reset process, a negative voltage sweep was conducted, ranging from 0 to -1.5 V with a sweep rate of 75 mV/s. This results in a reduction in in the current at the Reset voltage (V_{Reset}), leading the device to switch from LRS to HRS.

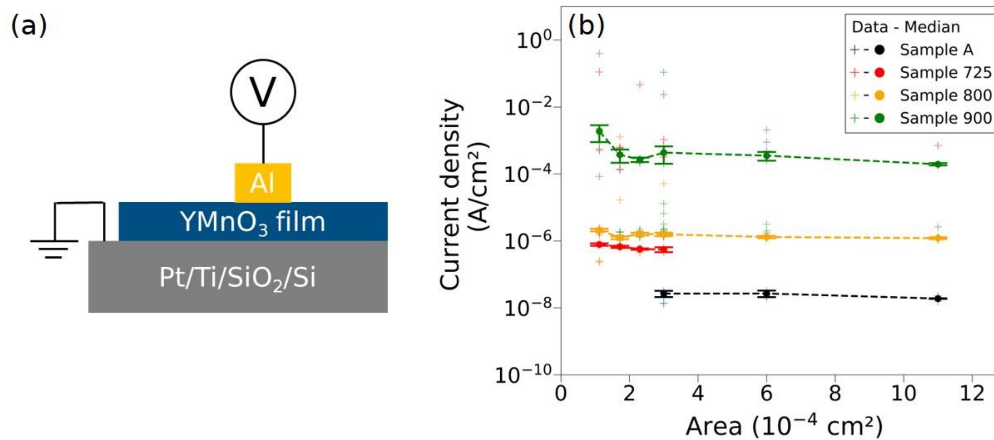

Figure 4.20: (a) Sketch of the Pt/$YMnO_3$/Al device under the bias. The Pt bottom electrode was grounded, and the DC voltage bias was applied to the top Al electrodes. (b) Variation of the leakage current density of the pristine devices with samples A, 725, 800 and 900 as a function of device dimensions. The read voltage is 50 mV. Note that the median values and their corresponding median absolute deviations are represented. The figures are partially adapted from ref.[266]

In the following, we focus on the Pt/$YMnO_3$/Al devices prepared with films annealed at 800 °C, which are composed of mainly h-$YMnO_3$ with ~10% o-$YMnO_3$.

Figure 4.21a presents typical *I-V* characteristic, showing a bipolar resistive switching behavior. The *I-V* curve shown in red represents the first sweep with a switched voltage similar to the Set voltages of the subsequent sweeps, indicating that the device does not need an electroforming process. Figure 4.21b displays the Set and Reset voltages, whereas Figure 4.21c shows the HRS and LRS resistance values (determined at 50 mV) for various device dimensions. The values of V_{Set} (+1.71 ± 0.36 V) and V_{Reset} (-0.36 ± 0.08 V) are relatively low, and the R_{OFF}/R_{ON} ratio is quite large, of the order of 10^3 to 10^4. The resistance in the LRS is independent of the device size, indicating that resistive switching is more likely to occur through the formation of a conductive filament rather than through the movement of carriers distributed

along an interface.[285] The wide variability of HRS values and the area independence suggest that the filament is only partially ruptured during the device switching from LRS to HRS. Retention measurements were performed at room temperature (read voltage of 10 mV) for more than 6×10^3 s, showing no drift in the ON and OFF states (Figure 4.21d).

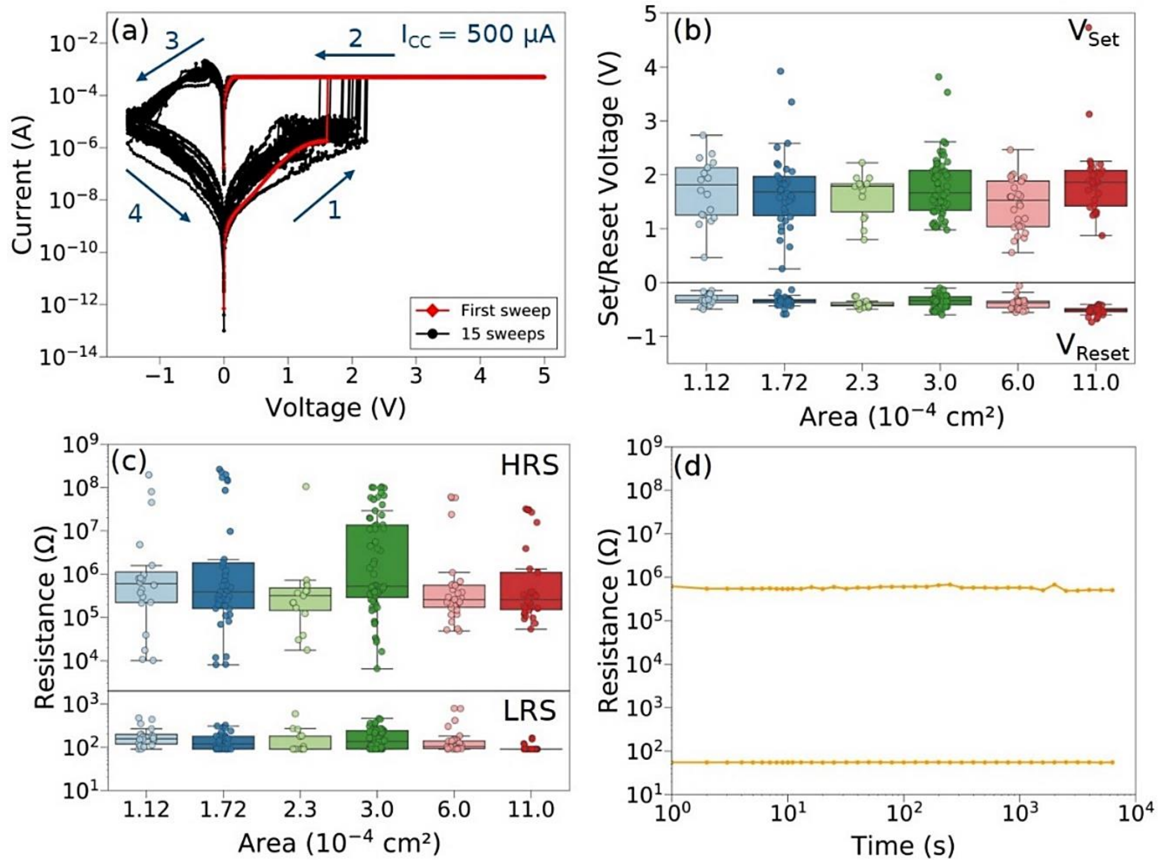

Figure 4.21: Characteristics of devices with a film annealed at 800 °C. (a) Typical *I*-*V* curves (15 cycles are shown). The *I*-*V* curve shown in red represents the first sweep. Variations of (b) Set, Reset voltages and (c) resistances in HRS and LRS (read voltage of 50 mV) for different device areas. Three devices were measured for each device area. (d) Retention of HRS and LRS for one typical device (read voltage of 10 mV at room temperature). For the box plot in (b) and (c), median values and their corresponding median absolute deviations are represented. The figures are partially adapted from ref.[266]

Electroforming-free bipolar resistive switching with V_{Set} of + 0.98 ± 0.19 V and V_{Reset} of -0.44 ± 0.22 V was observed in the devices with the film annealed at 900 °C (Figure 4.22). Nevertheless, their endurance is quite poor, as they remain in a conducting LRS after a few switching cycles without undergoing a Reset process. This issue likely results from the presence of pinholes in the thin film (see Figure 4.9g, h). These devices were not further investigated.

Devices with the amorphous films do not exhibit any resistive switching behavior but rather remain in an HRS or experience a single irreversible breakdown. This observation suggests that the resistive switching behavior in the polycrystalline films likely occurs in crystalline grain boundaries and/or phase boundaries between h-$YMnO_3$ and o-$YMnO_3$.

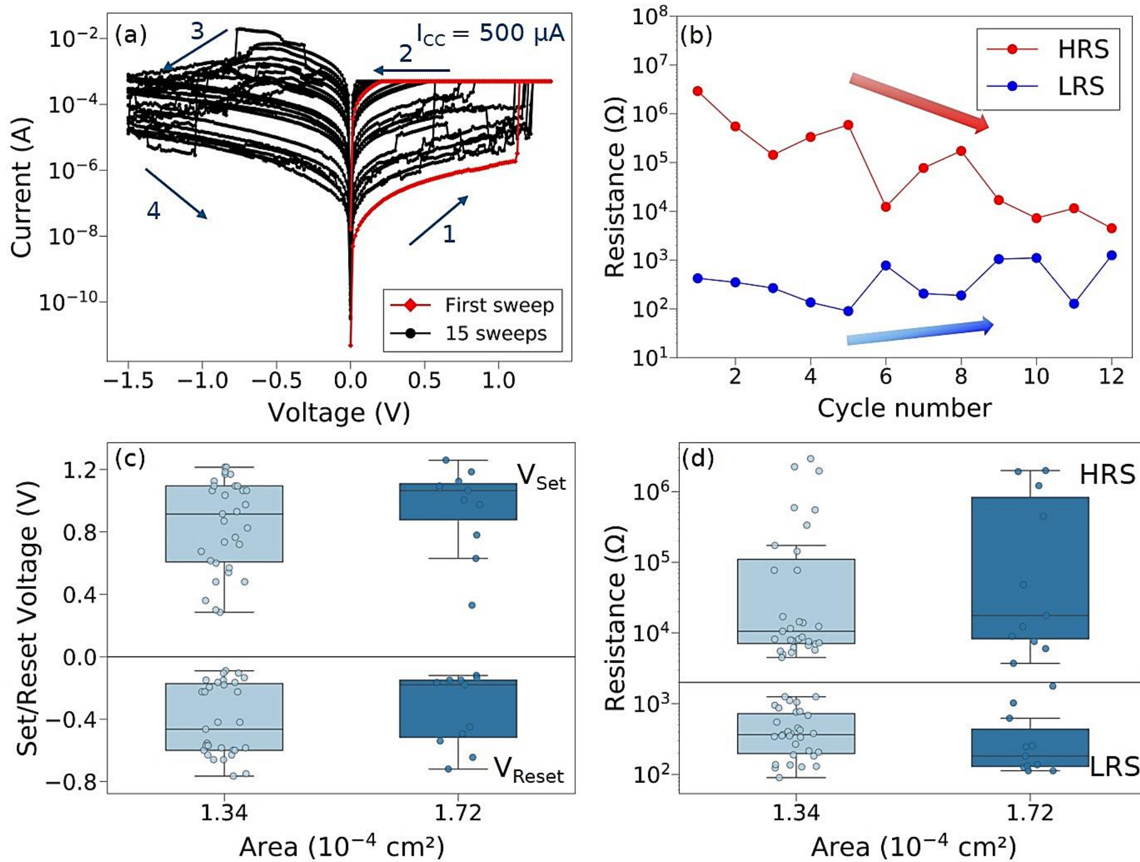

Figure 4.22: (a) Typical *I-V* curves (15 cycles are shown) of Pt/$YMnO_3$/Al devices with a film annealed at 900 °C. The first sweep is shown in red. (b) Distribution of resistances in HRS and LRS over switching cycles. Variation of (c) Set and Reset voltages and (d) resistances in HRS and LRS states. The read voltage is 50 mV. Median values and their corresponding median absolute deviations are represented. The figures are partially adapted from ref.[266]

In Figure 4.23, we compare the resistive switching behaviors of the devices containing different amounts of secondary o-$YMnO_3$ phase (sample 725 with ~52% and sample 800 with ~10%), both showing comparable leakage current densities in their pristine states (see Figure 4.20b). Switching performances such as the Set and Reset voltages, OFF and ON resistances (read at 50 mV), and retention exhibit similarity across both types of devices. Thus, there appears to be no significant influence of the crystalline phase ratio on the macroscopic resistive switching of the devices.

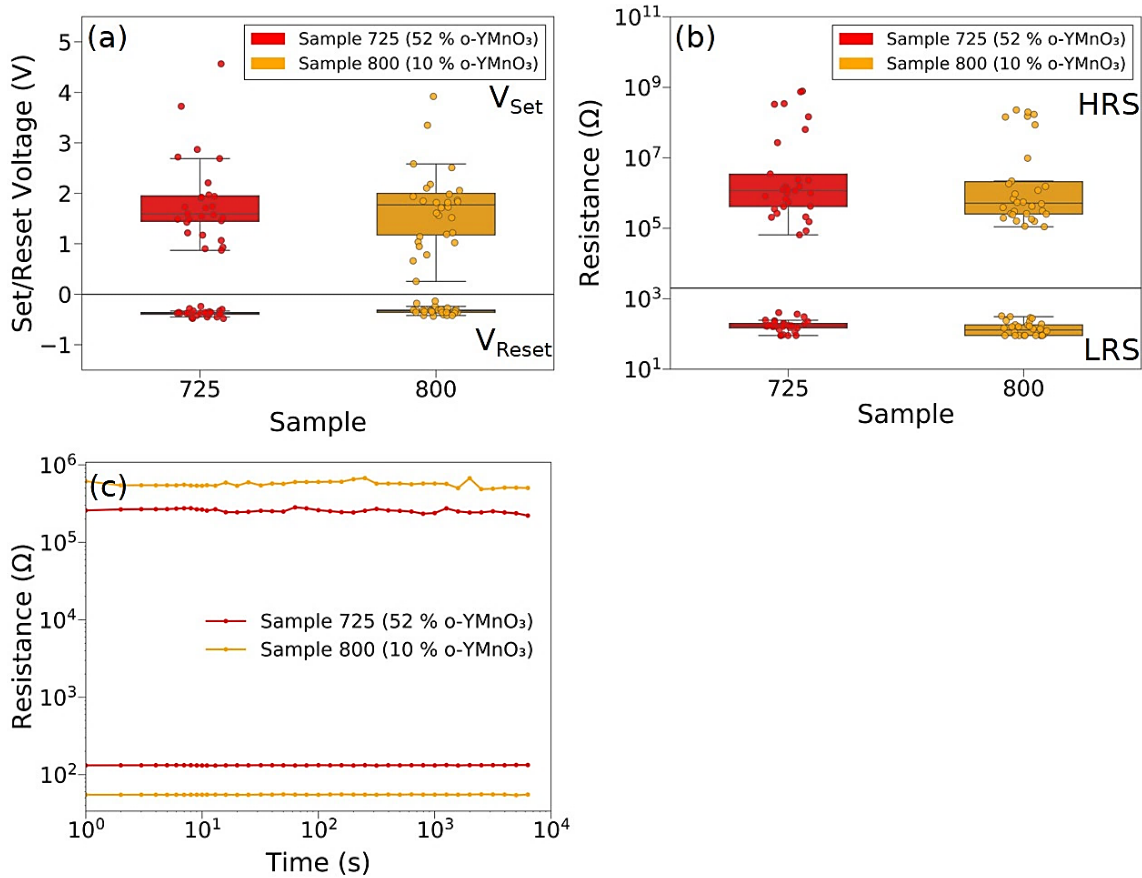

Figure 4.23: Variations of (a) Set and Reset voltages and (b) resistances in HRS and LRS states of devices with films annealed at 725 and 800 °C (read at 50 mV). (c) Retention measurements of HRS and LRS for sample 725 and sample 800 (read at 10 mV). Median values and their corresponding median absolute deviations are represented. The figures are partially adapted from ref.[266]

4.4.3 Thickness effect

Figure 4.24a illustrates the *I*-*V* characteristics of a Pt/$YMnO_3$/Al device based on a $YMnO_3$ film with a thickness of 215 nm. Note that the device necessitates a forming step requiring a high voltage exceeding 30 V. In Figure 4.24b, Set and Reset voltages are shown. It is evident that for thicker $YMnO_3$ films, the device exhibits a higher Set voltage, which is consistent with a reduction in electric field with increasing film thickness for a given voltage. The increase in V_{Set} is proportional to the increase in thickness (from 75 to 215 nm). The significant variation observed in V_{Set} aligns with the stochastic nature of filament growth along multiple grain boundaries with thicker films. A thickness of 75 nm is preferred, to minimize V_{Set}, V_{Reset} and their variabilities. This choice represents a compromise between the necessity for a thicker film to potentially foster ferroelectric domains (for future co-development integrating resistive switching and ferroelectricity) and the consideration of operational Set voltage and stochasticity.

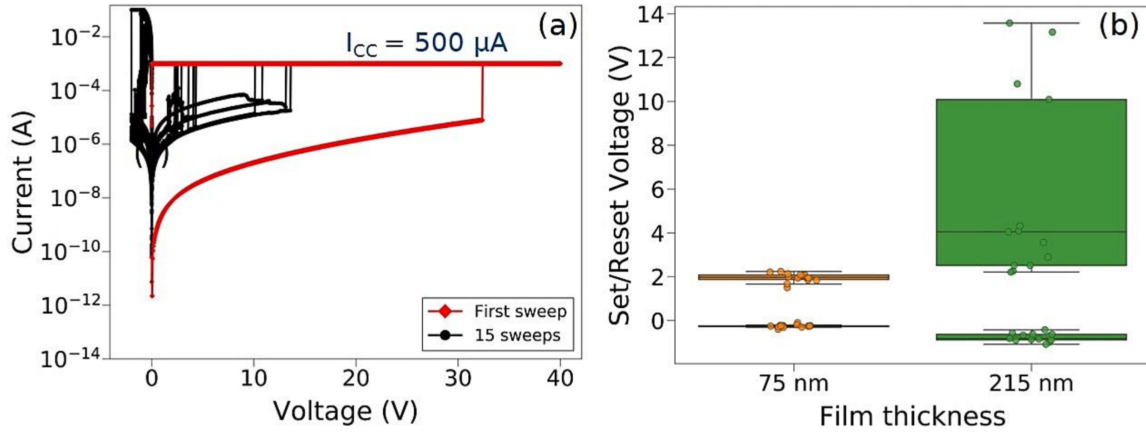

Figure 4.24: Typical *I-V* curves (15 cycles are shown) of Pt/$YMnO_3$/Al devices with a 215 nm-thick $YMnO_3$ film. The *I-V* curve shown in red represents the first cycle (forming step). (b) Variations of Set and Reset voltages of Al/$YMnO_3$/Pt devices with 75 nm- and 215 nm-thick $YMnO_3$ films. Median values and their corresponding median absolute deviations are represented. The figures are partially adapted from ref.[266]

Compared to the reported polycrystalline $YMnO_3$-based resistive switching devices (see Table 1.2 of Chapter 1), our devices exhibit the lowest operation voltages. We can conclude that the abruptness of both Set and Reset operations, along with a high OFF/ON ratio of the resistances, and no dependence of the ON resistance with device dimensions, collectively suggest a filamentary mechanism.

In the following section, we discuss electrochemical metallization (ECM) as the underlying mechanism governing the resistive switching in our devices.

4.4.4 Discussion on the filamentary mechanism

An ECM memristive device operates based on the redox processes of the active electrode and the movement of ions in the solid electrolyte. This process (Set operation) results in the formation of a metallic filament on the passive electrode, giving rise to a LRS when it bridges both electrodes.[179, 192] These redox reactions are reversible, allowing the filament to be ruptured during the Reset process, returning the device to a HRS.

In Figure 4.25a, we observe the first positive voltage sweeps (0 → 5 V → 0) for devices that failed to switch under 5 V. Regardless of the device area, all *I-V* curves exhibit a current peak at around 1.7 V. Indeed, Al undergoes oxidation to Al^{3+} ions at around 1.676 V.[286] Subsequent cycles do not display such a current peak, as shown in cyclic voltammograms in Figure 4.25b. It is attributed to the irreversible oxidation of Al, leading to the formation of an Al_2O_3 layer,[287] which explains the absence of switching behaviors in these devices. Figure 4.25c depicts cyclic voltammograms conducted at various sweep rates during the first cycle

on several pristine devices. The observed increase in total current and the shift of the redox potential towards more positive values with increasing sweep rates are consistent with a redox behavior.

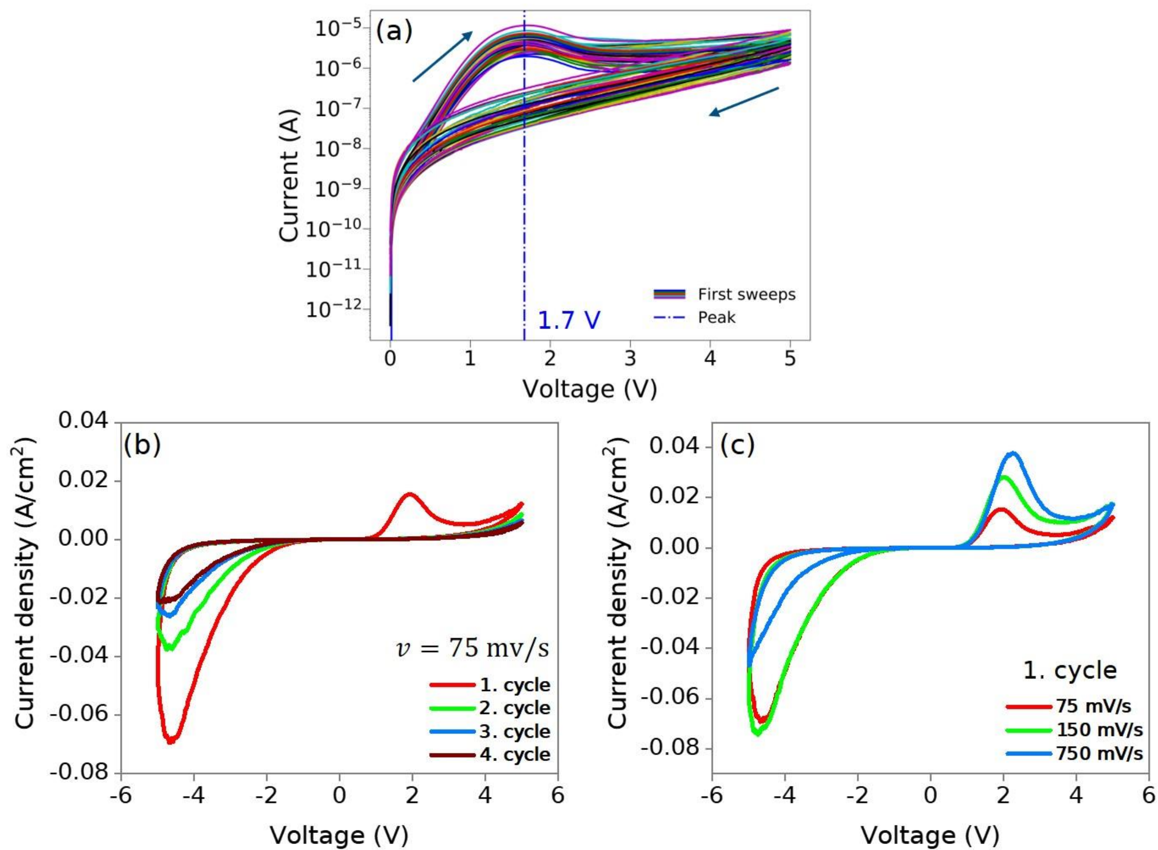

Figure 4.25: (a) First positive voltage sweeps (0 → 5 V → 0) conducted on multiple devices unable to be formed under 5 V, with various device dimensions in sample 800. (b) Cyclic voltammograms of Pt/$YMnO_3$/Al devices for 4 cycles using a sweep rate of 75 mV/s. (c) Cyclic voltammograms of Pt/$YMnO_3$/Al devices at different sweep rates. The $YMnO_3$ films used for all devices have a thickness of 75 nm. The figures are partially adapted from ref.[266]

Pt/$YMnO_3$/Pt devices were investigated using the same *I-V* measurement parameters (applying voltage from 0 to 5 or 10 V, with a sweep rate of 75 mV/s for the Forming/Set processes), to study the role of Al electrodes. A distinct behavior is evident compared to Pt/$YMnO_3$/Al devices. Within the range of ± 5 V, no resistive switching is observed (Figure 4.26a). However, resistive switching is observed in all devices upon applying a high Forming voltage of ~ 9 V (Figure 4.26b). Given Pt's inert nature, no redox processes are anticipated. The $YMnO_3$/Pt Schottky barrier is significantly lower than that of $YMnO_3$/Al, resulting in considerably higher leakage currents.

A filamentary resistive switching mechanism is probable (evidenced by the abruptness of the Set process), with stochastic Set voltages ranging from ~ 0.5 to 8.4 V. Note that a high voltage is not only required for the forming step but is also needed for some Set processes. The large variability of V_{Set} suggests that the

switching mechanism may mainly involve the formation or movement of defects already present in the $YMnO_3$ active layer. The switching mechanism significantly differs for the devices with the Pt top electrode. Therefore, for devices with Al top electrodes we exclude a switching mechanism primarily driven by the formation or movement of defects in the polycrystalline film, and instead conclude that on an ECM-type mechanism is the origin.

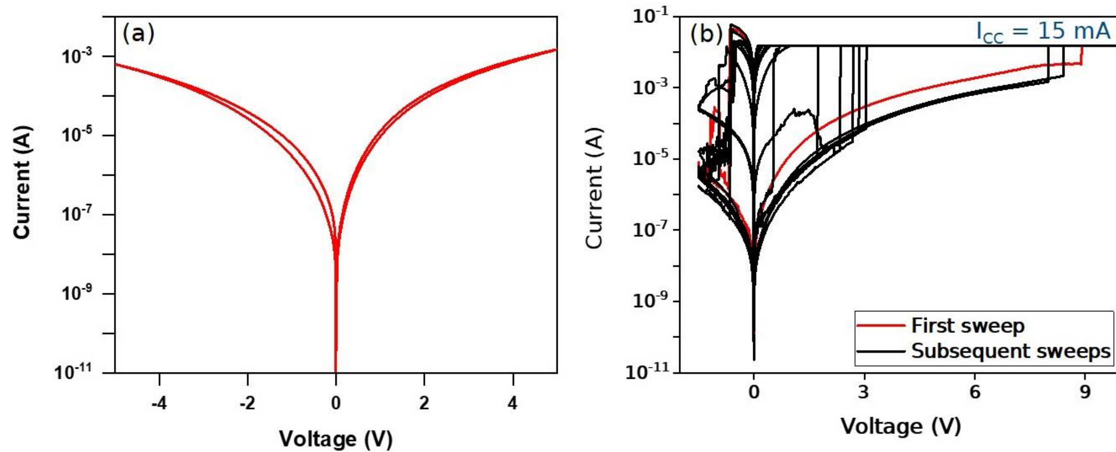

Figure 4.26: *I-V* characteristics of Pt/$YMnO_3$/Pt devices with (a) voltage sweep (0 → 5 V → 0 → -5 V → 0) and (b) voltage sweep (0 → 10 V → 0 → -1.5 V → 0). The sweep rate is 75 mV/s, and the compliance current is set at 15 mA. In (b), the Forming voltage is recorded at 8.9 V. Set voltages vary within the range of 0.5 to 8.4 V. Note that cycles #4 and #8 require a high Set voltage of 8.4 and 8.0 V, respectively. The figures are partially adapted from ref.[266]

A schematic of the proposed ECM type mechanism in the Pt/$YMnO_3$/Al stack and its typical *I-V* characteristics for resistive switching behavior are shown in Figure 4.27. As a positive bias is applied during the Set process, the active electrode Al undergoes oxidation (at $V_{Set} \sim 1.7$ V) and the injected Al^{3+} metal cations move towards the inert Pt electrode under the electric field. Upon reaching the surface of the Pt electrode, they are reduced and form an Al filament, which grows as the subsequent Al^{3+} cations are reduced (see A to B and C in Figure 4.27). When the filament bridges the two electrodes (or close enough to allow tunneling), the current increases (D in Figure 4.27). Conversely, the Al filaments can be ruptured by dissolution of Al in the film when a negative bias is applied, along with Joule heating effects during the Reset process (see D to E and A in Figure 4.27).

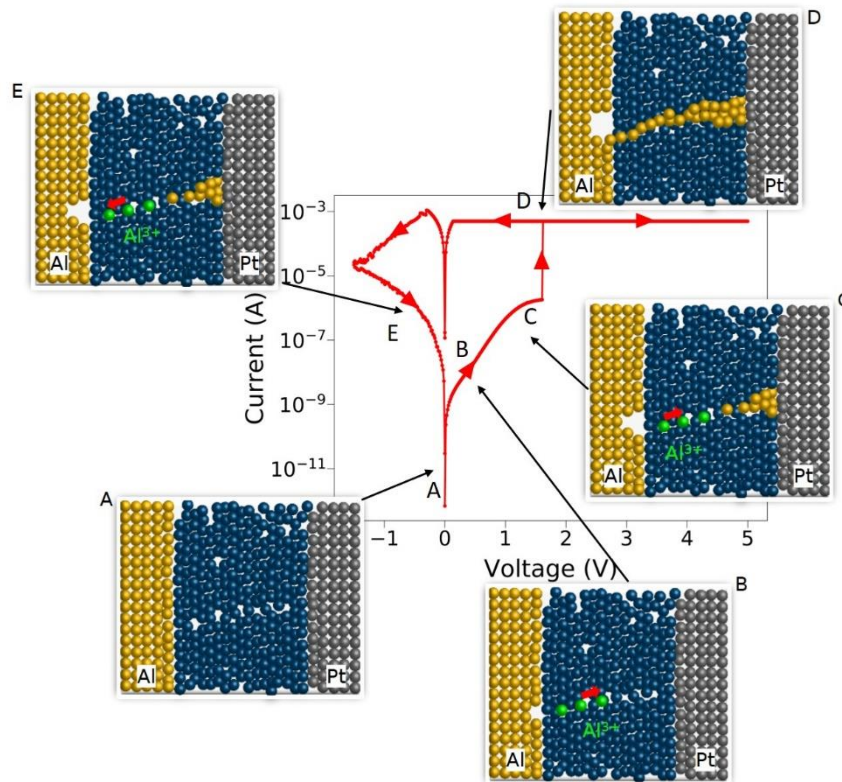

Figure 4.27: Schematic of the resistive switching behavior of the Pt/$YMnO_3$/Al stack and its representative *I-V* curve. The device switches from a high resistive state (A) to a low resistive state (D) due to the electroformation of a nanoscale conducting Al filament (B, C). The device switches back to the high resistive state by applying an opposite voltage to rupture the Al filament (E). Partially adapted from ref.[179]

Cu and Ag metals are commonly chosen as the active electrode material in ECM devices.[187, 288–293] When Al is used with an amorphous electrolyte such as SiO_2, its strong affinity for oxygen leads to the formation of a passive and stable Al_2O_3 barrier. This barrier reduces current flow and subsequent oxidation, as demonstrated by Luebbens *et al.*[287] The irreversible Al oxidation prevents oxidized Al from reverting to its metallic state, thereby hindering Set/Reset operations.[287] Consequently, ECM resistive switching cells combining Al and SiO_2 or any amorphous oxide are not commonly reported. In our switched devices, the migration of Al^{3+} ions likely occurs along oxygen-deficient defect lines such as grain boundaries, facilitating the reversible formation of Al/Al^{3+} rather than Al_2O_3. While most devices with $YMnO_3$ annealed at 725 and 800 °C transition to a LRS at a Set voltage of 1.7 ± 0.36 V, some exceptions exist (as shown in Figure 4.25a), possibly due to the oxidation of Al to Al_2O_3 upon Al^{3+} cation formation, particularly if a percolation path through the grain boundaries is absent.

In our switching devices, the migration of the Al^{3+} ions towards the bottom inert electrode is driven by the electric field at the Set voltage, along with the Al^{3+} reduction, Al nucleation, and growth of the Al filament.

Several studies have highlighted that these processes do not necessarily require a large electric field. For instance, ultralow voltages of 250 – 400 mV have been reported for Cu electrodes and dense 10 nm SiO_2 films.[187, 192] Additionally, specific microstructures and defect configurations within the electrolyte can significantly impact ECM switching behavior. For example, ECM cells based on ITO/280 nm SiO_2/Ag exhibit a low switching voltage of only 0.2 V due to metallic Ag filaments growing in the nano-channels of a porous SiO_2 film.[191] In our devices, grain boundaries serve as migration channels for the Al^{3+} ions. Furthermore, the relatively high roughness of the $YMnO_3$ polycrystalline films may contribute to the relatively low operating voltage by promoting shorter migration paths as the electric field is the largest.

The characteristics of our devices, including high resistance values in HRS, a high OFF/ON ratio, abrupt Set/Reset transitions, the absence of switching under reverse bias, and the observation of a Set voltage corresponding to the potential of Al oxidation, as well as the comparison to devices with Pt top electrodes, strongly support the attribution of the switching mechanism to the ECM type.[287]

We further investigated the resistive switching behavior of the pure hexagonal and orthorhombic phases, to study the role of the $YMnO_3$ phases and their phase boundaries in the formation of Al filaments. The measurements were conducted using microscopic Al electrodes (~1.5 µm diameter) locally patterned on each of the two phases on the film annealed at 725 °C. Local conductance mapping and local *I-V* measurements were carried out on the bare film and on the Al electrodes using c-AFM (Figure 4.28a). The cantilever tip was grounded and the DC bias was applied to the bottom electrode, with the compliance current set at 100 nA during the experiment. Given that both h-$YMnO_3$ and o-$YMnO_3$ are p-type semiconductors,[116, 278] the metal-semiconductor-metal structures are back-to-back Schottky diodes, either in symmetric structures (Pt/$YMnO_3$/Pt coated tip) or in asymmetric ones (Pt/$YMnO_3$/Al), as schematically presented in Figure 4.28b.

Figure 4.28c, d display topography and c-AFM current maps, respectively, where Al top electrodes are denoted by white circles. Based on the Raman spectroscopy analysis discussed earlier, the highly and lowly conductive regions in the film correspond to the orthorhombic and hexagonal phases, respectively. Interestingly, no conduction is observed at the locations of the Al electrodes positioned in the orthorhombic phase regions, a finding confirmed by *I-V* measurements shown in Figure 4.28e. We performed *I-V* characteristics of four different stacks, including both symmetric back-to-back Schottky diode structures (Pt/$YMnO_3$/Pt coated tip) and asymmetric ones (Pt/$YMnO_3$/Al). The distinct electrical properties of these four configurations can be explained by energy band diagrams with different crystalline phases and electrodes, as illustrated in Figure 4.29.

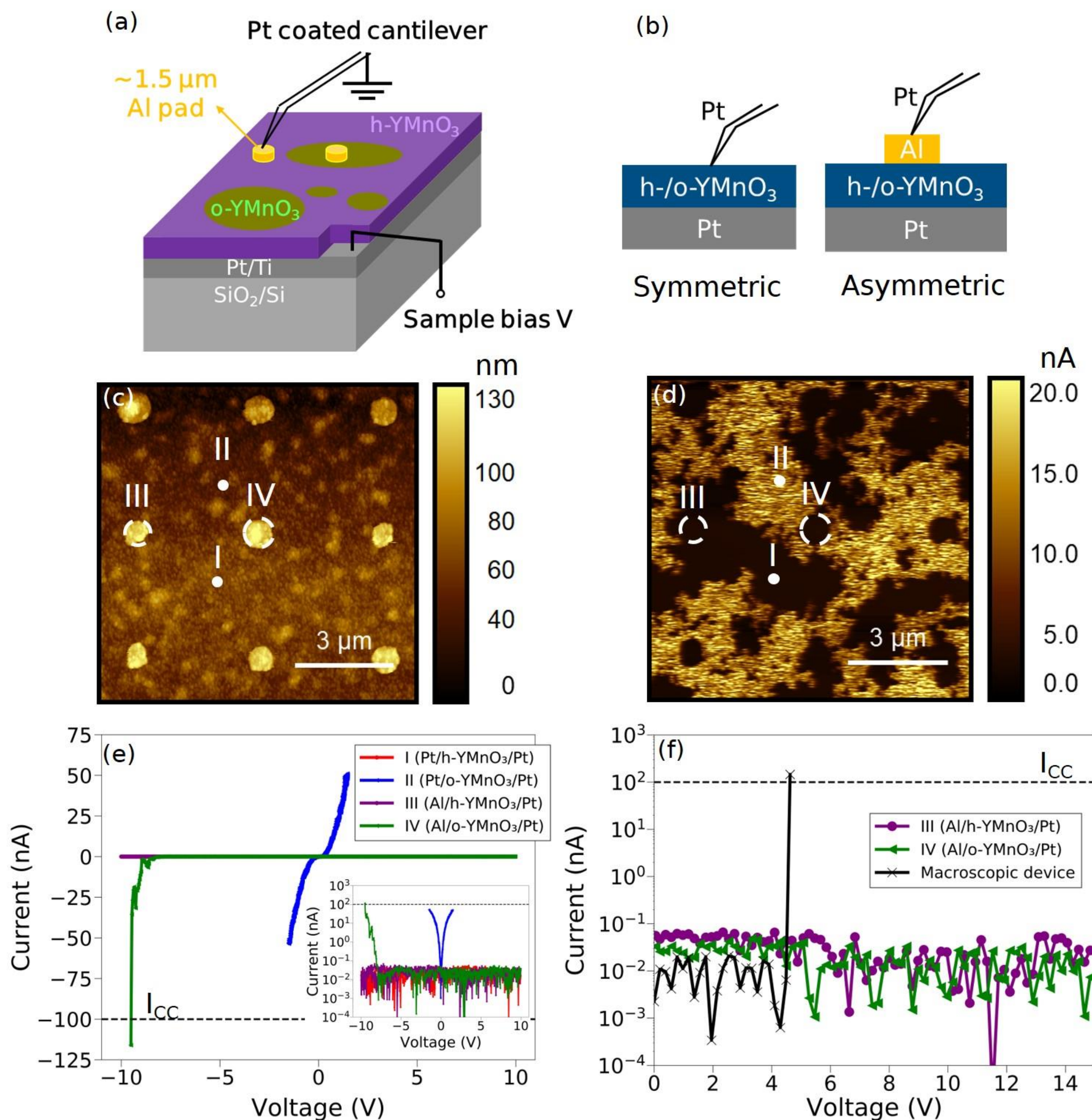

Figure 4.28: (a) Sketch of the devices with Al top electrodes (diameter of 1.5 µm and thickness of 60 nm) deposited locally in regions of pure h-$YMnO_3$ and pure o-$YMnO_3$ for c-AFM measurements. The cantilever was grounded, and the DC bias was applied to the sample bottom electrode. (b) Sketches of the two types of stacks under study: Pt tip/h-(o-) $YMnO_3$/Pt and Al/h-(o-) $YMnO_3$/Pt. (c) Topography and (d) current maps measured with a DC bias of 1 V. White circles represent locations of the Al top electrodes. (e) *I-V* curves measured at four different locations (I and II: the tip was directly positioned on the film, III and IV: the tip was positioned on Al top electrodes). The tip DC bias (relative to sample bias) was: 0 → 10 V → 0 → -10 V → 0 and the compliance current was 100 nA. The *I-V* curves in semi-logarithmic scale are shown in the inset. (f) *I-V* characteristic of micro device III and IV (marked in panel d), with tip bias (relative to sample bias) 0 → 15 V. In addition, *I-V* measurement with tip bias (from 0 → 5 V) on a macroscopic device (100 × 100 µm^2) was performed for comparison. The compliance current was 100 nA. The figures are from ref.[266]

Figure 4.29a illustrates ideal *I-V* characteristics of Pt/h-$YMnO_3$/Pt and Pt/o-$YMnO_3$/Pt devices. The stack based on o-$YMnO_3$ exhibits higher conductivity compared to the one with h-$YMnO_3$. The symmetric *I-V* curves reflect the symmetry of the electrodes, depicting two back-to-back Schottky barriers at the Pt/$YMnO_3$ interfaces. The current in the Pt/$YMnO_3$/Pt stacks is governed by the Schottky barriers under reverse bias. For a deeper understanding of the conduction mechanism, Figure 4.29b presents a schematic energy band diagram with Pt electrodes, taking into account the electron affinity of $YMnO_3$ of 4.46 eV,[294] an energy band gap of 1.5 eV[87] and Pt's work function of $\emptyset_{\mathrm{Pt}} = 5.12$ eV.[91] Since electron affinity data for h-$YMnO_3$ and o-$YMnO_3$ are limited, similar values are assumed based on existing reports.[87, 294–296] The stack with o-$YMnO_3$ exhibits higher conductivity, likely due to a higher concentration of Mn^{4+} ions in o-$YMnO_3$ compared to h-$YMnO_3$, resulting in an increased p-type conductivity.[278] Consequently, when an electric field is applied, holes (h^+) may move from metal to oxide due to a narrower depletion region and to a lower Pt/o-$YMnO_3$ Schottky barrier in highly doped p-type o-$YMnO_3$ (Figure 4.29c). Conversely, in the case of h-$YMnO_3$, holes (h^+) are unable to cross over the Pt/h-$YMnO_3$ Schottky barrier, leading to low current prior to the hard breakdown of the stack, as illustrated in Figure 4.29d. This explains why o-$YMnO_3$ exhibits conductivity in the c-AFM current map under applied bias, while h-$YMnO_3$ does not.

Now, let us discuss the stacks with top Al electrodes. Figure 4.29e illustrates the ideal *I-V* characteristics of Pt/h-$YMnO_3$/Al and Pt/o-$YMnO_3$/Al (stacks III and IV). The asymmetric *I-V* curve of the Pt/o-$YMnO_3$/Al stack can be explained by the asymmetric band diagram, as shown in Figure 4.29f. The stack contains different Schottky barrier heights at the two interfaces, arising from the distinct metal work functions ($\emptyset_{\mathrm{Pt}} = 5.12$ eV, $\emptyset_{\mathrm{Al}} = 4.28$ eV).[91, 297] When a negative bias is applied to Al, the hole movement induced current is dominated by the Pt/o-$YMnO_3$ Schottky barrier, which is lower than the Al/o-$YMnO_3$ one (Figure 4.29g). Conversely, with a positive bias applied to Al, the current is dominated by the Al/o-$YMnO_3$ Schottky barrier, which is significantly higher than the Pt/o-$YMnO_3$ one and impedes easy across by holes (h^+), resulting in low current (Figure 4.29h). The current across the Al/h-$YMnO_3$/Pt stack remains low in both polarities, since both Schottky barrier heights at the metal/h-$YMnO_3$ interfaces are too high to be crossed (not shown in Figure 4.29). This explains why no conduction is observed when measuring locally with the Al electrodes (positioned as shown in Figure 4.28d).

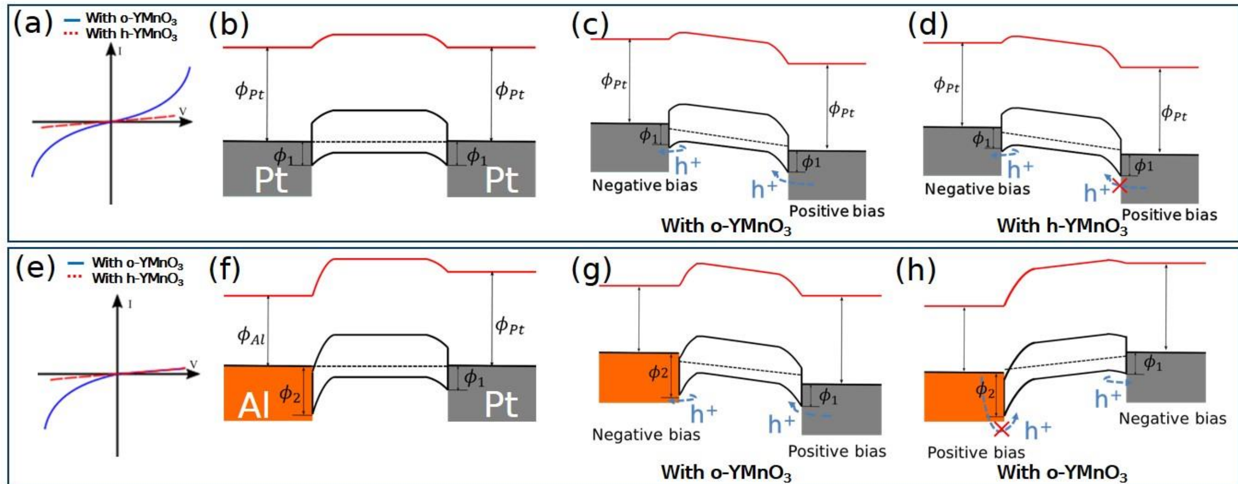

Figure 4.29: (a) Schematic ideal *I-V* characteristics of OFF states of Pt/o-$YMnO_3$/Pt (blue solid line) and Pt/h-$YMnO_3$/Pt (red dashed line). (b) Corresponding equilibrium energy band diagram of symmetric Pt/$YMnO_3$/Pt, (c) energy band diagram with bias of Pt/o-$YMnO_3$/Pt and (d) energy band diagram with bias of Pt/h-$YMnO_3$/Pt. (e) Schematic ideal *I-V* characteristics of OFF states of Al/o-$YMnO_3$/Pt (blue solid line) and Al/h-$YMnO_3$/Pt (red dashed line). (f) Corresponding equilibrium energy band diagram of asymmetric Pt/$YMnO_3$/Al, (g) energy band diagram with Pt positive bias of Al/o-$YMnO_3$/Pt and (h) energy band diagram with Pt negative bias of Al/o-$YMnO_3$/Pt. The figures are from ref.[266]

We investigated the resistive switching behavior of the micrometric-size Pt/$YMnO_3$/Al devices on single h-$YMnO_3$ or o-$YMnO_3$ by applying a DC tip bias from 0 to 15 V with a compliance current of 100 nA (see Figure 4.28f). For comparison, we examined a $100 \times 100\ \mu m^2$ device as discussed in the previous section, which comprises mixed hexagonal and orthorhombic $YMnO_3$ phases. In the case of the large device, an abrupt increase in current is observed at a Set voltage of 4.6 V, indicating the occurrence of resistive switching. However, no change in current is noted for the microscopic devices (at locations III and IV of Figure 4.28c, d), suggesting the absence of resistive switching behavior for voltages up to 15 V. With the grain size of 40 ± 15 nm, the microscopic devices contain at least approximately 30-40 grains of the same phase. These observations suggest that **Al diffusion and filament formation likely occur along the boundaries between the orthorhombic and hexagonal phases** (see Figure 4.30c), which are absent in the microscopic devices prepared in a pure single phase, rather than along the grain boundaries between adjacent grains of a same phase.

Further investigation is required to unveil nanoscale details regarding nature of the grain/phase boundaries. This local c-AFM study shows the significance of boundaries between two phases of $YMnO_3$ in the functionality of the devices.

The fact that there is no resistive switching behavior in $YMnO_3$-based devices with a single crystalline phase indicates the key role of boundaries between the two crystalline phases in providing oxygen-deficient paths for diffusion of Al^{3+} ions within the $YMnO_3$ film. These nanochannels for Al^{3+} migration enable the utilization of Al as an active electrode. The ability to localize/control cation migration at the nanoscale level presents an interesting avenue for ECM cells, as it mitigates much of the stochasticity associated with metal cation migration from the active metal in the electrolyte.[298]

Further research will be focused on the study of the mechanisms and their dynamics at the nanoscale within these phase boundaries, with methods such as operando TEM offering promising avenues for exploration.[184]

As a future perspective, it should be possible to fabricate nanoscale ECM cells that contain such a phase boundary (highlighted by the red dotted line in Figure 4.30b, illustrated in Figure 4.30c) along with a few nanograins on either side of the boundary (as marked by the blue box in Figure 4.30b).

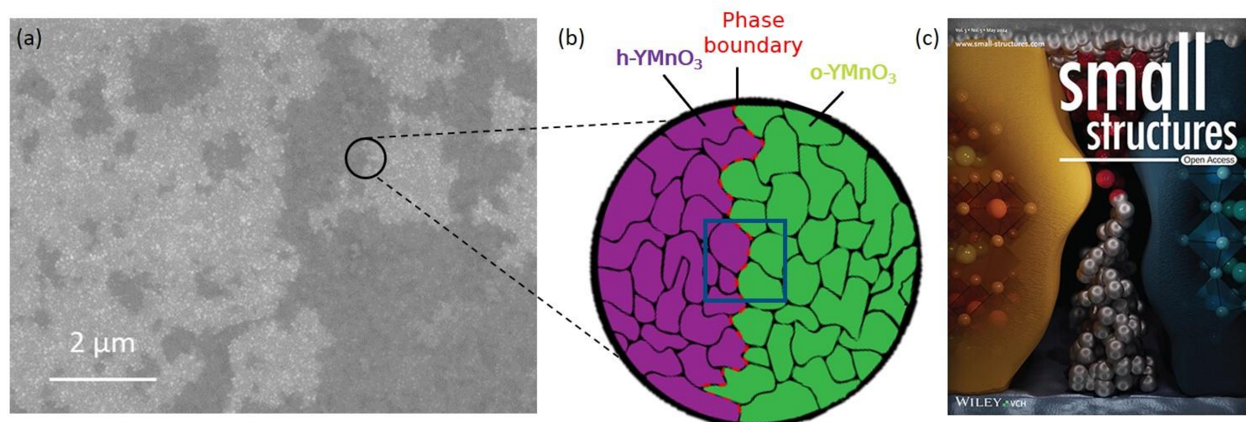

Figure 4.30: (a) SEM image of a polycrystalline $YMnO_3$ film annealed at 725 °C. (b) Sketch of the grains for the two phases (hexagonal and orthorhombic) to illustrate the situation in the black circle marked in (a) at the boundary between the hexagonal and orthorhombic phases of $YMnO_3$. The dotted line represents the boundary between the two phases. Nanoscale ECM cells could be fabricated on the area marked with the blue box. The figures are partially adapted from ref.[266] (c) The migration of the Al^{3+} and Al filament formation occur in the oxygen-free boundary between the hexagonal and orthorhombic phases (in yellow and blue, respectively). This figure is the cover page of the May 2024 issue of the journal *Small Structures* (volume 5, issue 5), where our work has been published (ref.[266]).

4.5 Reconfigurability between capacitive and resistive states

The objective of the ForMikro-ERMI project (discussed in Chapter 3) was redirected towards reconfigurability from a capacitive state (C) to a resistive state (R) in the devices described previously.

Ferdinand Pieper, under the supervision of Prof. Dr. Bernhard Wicht at the Institute of Microelectronic Systems, University of Hannover, designed a practical use case (depicted in Figure 4.31). He performed the circuit design and subsequent simulation.

The devices are integrated into a frequency compensation circuit for stability and performance optimization in DC-to-DC voltage converters in a closed-loop system (Figure 4.31).[299] Frequency compensator shapes the gain and phase characteristics of the system's feedback loop to ensure the stability and desired response time. Integrating a reconfigurable *R*-*C* network into the feedback loop (Z_0 in Figure 4.31) of a compensator enhance its adaptability. Error amplifiers are commonly implemented to the compensator, adjusting feedback signal gain and phase. The reconfigurable *R*-*C* network introduces an additional degree of freedom by allowing dynamic adjustment of the compensator's frequency response. The equivalent circuits of the devices in OFF and ON states include a capacitor in parallel with a resistor (C_E and G_E, respectively), and a resistor (R_E). Together with external capacitors (C_1, C_2), the circuit can be simulated to tune the frequency response.

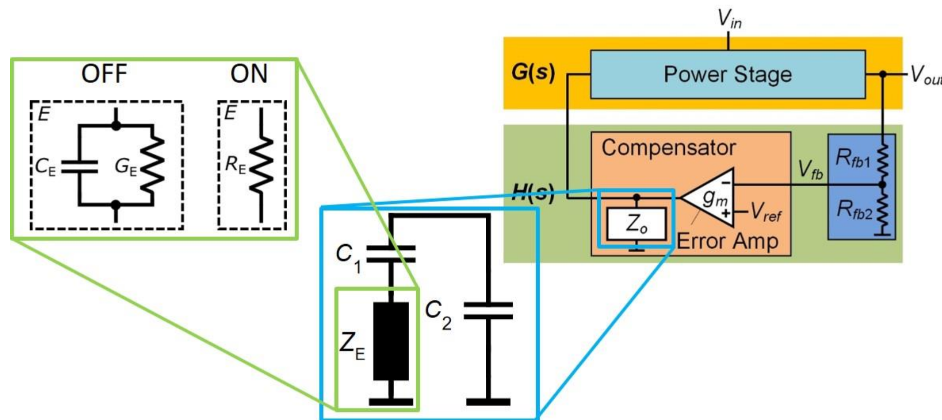

Figure 4.31: A real use case for the reconfigurable functionality (ERMI project). The devices are integrated into a frequency compensation circuit, in which the reconfigurability between a capacitive state (OFF state with C_E, G_E) and a resistive state (ON state, R_E) could change the circuit frequency response. This use case was designed by Ferdinand Pieper from the group of Prof. Dr. Bernhard Wicht at the Institute of Microelectronic Systems, University of Hannover.

The reconfigurability between *R* and *C* of the Pt/$YMnO_3$/Al devices with both patterned top and bottom electrodes was investigated. Impedance measurements were performed with OPEN calibration, as shown in Figure 3.10, to study the capacitive behavior in the OFF state. Resistance and capacitance values in pristine and OFF states, as well as resistance values in ON states were determined from *I*-*V* measurements and impedance measurements (see Figure 3.4). Figure 4.32 shows the *R*-*C* performance of devices with areas of 15×15 µm^2 and 100×100 µm^2 (same thickness of ~ 75 nm). The small devices show a strong variability in the OFF state. The capacitance *C* as a function of device area *A* shows a linear relationship

with a slope of 1.88 fF/μm² (Figure 4.33). From this value, the dielectric permittivity (ε_r) of the $YMnO_3$ films is calculated to be ~16, slightly lower than the values (~ 20) from the literature for thin films.[300, 301]

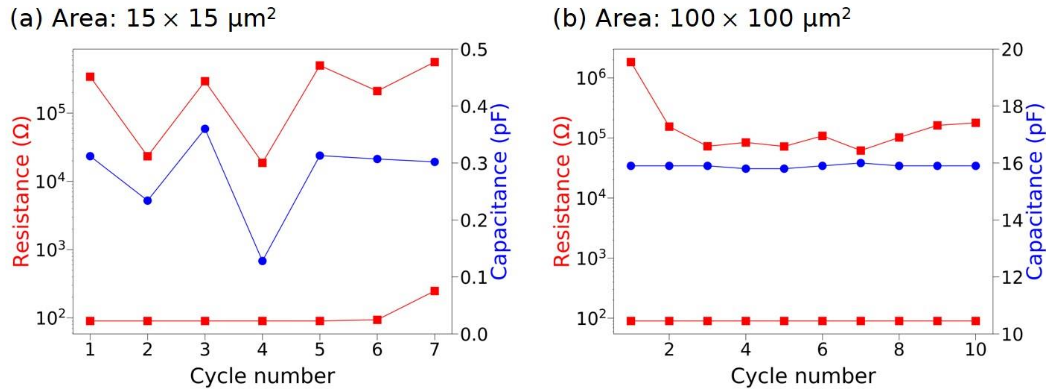

Figure 4.32: Resistance and capacitance values in OFF state and resistance in ON state of devices with device areas of (a) 15 × 15 μm² and (b) 100 × 100 μm². The presented capacitances were recorded at a frequency of 10 kHz.

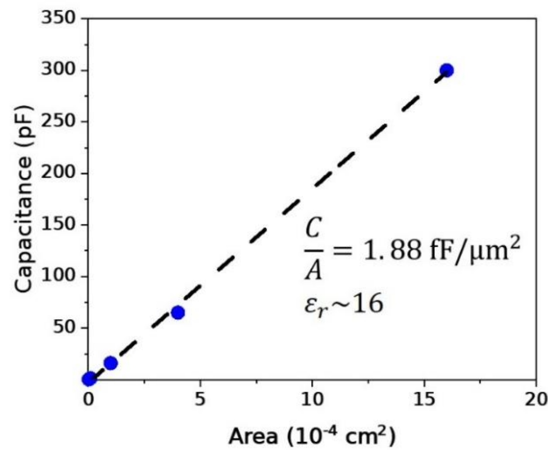

Figure 4.33: Capacitances as a function of device area in OFF states (recorded at a frequency of 10 kHz).

The step response of frequency compensation in a DC-to-DC converter illustrates how quickly and accurately the converter's output voltage stabilizes at the new desired level. To properly implement frequency compensation within the circuit, a frequency compensator circuit was simulated with the modelling parameters (G_E, C_E, R_E, C_1, C_2) as shown in Figure 4.31. These parameters were carefully chosen based on the actual electrical characteristics of our devices, aiming to adjust the circuit's loop gain to mitigate phase lag effectively. Simulated step responses of the circuit with the devices in both OFF and ON states are presented in Figure 4.34. The OFF state exhibits an overshoot and ringing, indicative of unstable circuit behavior. Conversely, the ON state demonstrates zero overshoot, indicating successful compensation of the simulated circuit.

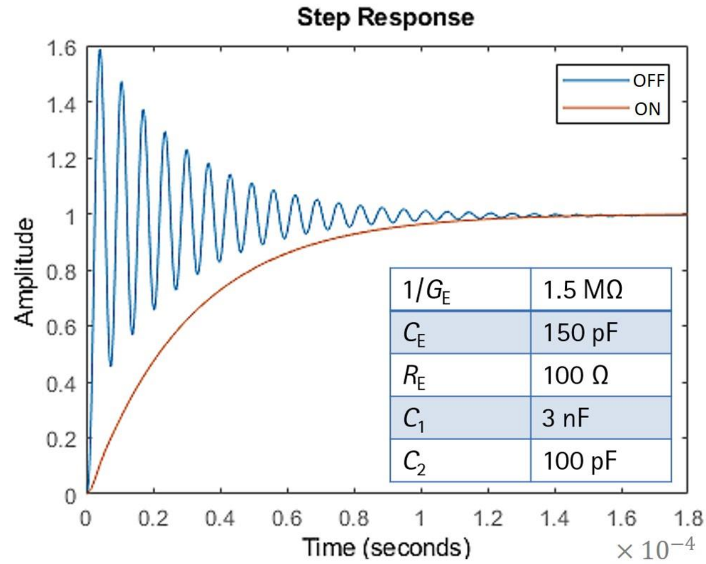

Figure 4.34: Simulated step response of frequency compensation circuit when the device is in OFF and ON states. The modelling parameters involved in the circuit shown in Figure 4.31 are listed. The simulation was conducted by Ferdinand Pieper from the group of Prof. Dr. Bernhard Wicht at the Institute of Microelectronic Systems, University of Hannover.

The reconfigurable nature of the circuit, with its ON and OFF states, enables dynamic adjustment, particularly valuable in adaptive control systems. Switching between these two compensation states allows the circuit to dynamically adapt its behavior in response to changing operating conditions. During normal operation, maintaining the circuit in the state with successful compensation ensures stable and optimal performance, crucial for consistent operation. However, when the system encounters unexpected conditions such as sudden load changes or external interference, the circuit can swiftly transition to the OFF state with unsuccessful compensation. While this state may not provide optimal performance, it serves as a fallback mechanism to mitigate issues and maintain essential functionality, ensuring the reliability and robustness of the DC-to-DC converter.

In conclusion, the investigation of the reconfigurability between capacitive and resistive states in Pt/$YMnO_3$/Al devices has been conducted for potential application in frequency compensation circuits. Results from impedance and *I*-*V* measurements indicate that the devices (100 × 100 μm^2) maintain stable capacitance levels upon successive switching cycles. As expected the capacitance scales linearly with device area. This study provides valuable insights into the feasibility of utilizing these devices for frequency compensation circuits.

4.6 Summary

- Polycrystalline $YMnO_3$ thin films with mixed hexagonal and orthorhombic phases were synthesized by room temperature RF sputtering and post-deposition annealing in N_2 atmosphere at temperatures ranging from 725 to 900 °C. X-ray diffraction is not sufficient to discriminate two phases due to the low volume amount and nanosized grains leading to undetectable peaks or overlapping peaks within hexagonal and orthorhombic phases.
- We developed a way to evidence unambiguously the presence of the orthorhombic phase, even in few percent amount, to locate it and to quantitively estimate the fraction of the two crystalline phases by correlative spectroscopies and microscopies (Raman spectroscopy, SEM, c-AFM and optical microscopy).
- Electrochemical metallization memristive devices with Al active electrodes were developed using polycrystalline $YMnO_3$ thin films with ~ 10% and ~ 52% orthorhombic phase. These devices show an electroforming-free bipolar resistive switching with a high R_{OFF}/R_{ON} ratio of 10^4, low Set (~ 1.7 V) and Reset (~ -0.36 V) voltages, and good retention performance.
- The origin of the resistive switching is attributed to the formation and rupture of an Al filament *via* electrochemical metallization along oxygen-deficient crystalline phase boundaries. These oxygen-deficient paths provide nanochannels for Al^{3+} migration and remove the randomness of the Al filament formation in the matrix, therefore, allow the use of Al as an active electrode, which otherwise would be readily oxidized into Al_2O_3.
- The presence of both hexagonal and orthorhombic phases could significantly influence the physical properties of the films. Hence, this study provides insights on more investigations into the potential coexistence of polymorphs in other polycrystalline $RMnO_3$ films.
- Pt/$YMnO_3$/Al devices can be integrated into frequency compensation circuits as demonstrated by a real use case. The reconfigurability between capacitive (OFF state) and resistive (ON state) states allows for changes in the frequency response of the circuit.

Chapter 5: $ErMnO_3$ thin film-based valence change memory (VCM) devices

5 $ErMnO_3$ thin film-based valence change memory (VCM) devices 128
5.1 Polycrystalline $ErMnO_3$ thin film optimization 129
5.1.1 Deposition on polycrystalline Pt coated Si substrates 129
5.1.2 Deposition on textured (111) Pt coated Si substrates 138
5.2 Identification and quantification of the crystalline phases 140
5.3 Ferroelectric properties 144
5.3.1 Polarization-voltage measurement 144
5.3.2 Piezoelectric response 148
5.4 Valence change memory (VCM)-type Pt/$ErMnO_3$/Ti/Au devices 150
5.4.1 Device fabrication 150
5.4.2 Electrical characterization of Pt/$ErMnO_3$/Ti/Au devices with minor o-$ErMnO_3$ content 151
5.4.2.1 Filamentary-type resistive switching 151
5.4.2.2 Impact of compliance current and sweeping voltage window 155
5.5 Impact of the crystalline phases 156
5.6 Role of top electrodes 162
5.7 Summary 164

Within the realm of multiferroelectric compounds, hexagonal $ErMnO_3$ stands out as one of the most intensively researched systems. However, most of the studies to date were mainly focused on single crystals, which limits scalability for integrating devices towards potential applications. In this chapter, we investigate bipolar resistive switching behaviors in $ErMnO_3$ thin film-based memristive devices. In a long term, combining resistive switching with multiferroelectricity could offer additional functionalities for devices.[76]

The hexagonal phase of $ErMnO_3$ is thermodynamically stable, with only a small difference in free energy compared to the metastable orthorhombic phase.[46] Previous works have shown that the orthorhombic phase can be formed at high pressure, suggesting the presence of mixed crystalline phases in thin films due to the substrate-induced strain.[51, 266] It is expected that the orthorhombic phase exhibits a higher electrical conductivity than the hexagonal phase.[266, 278] Hence, we propose to explore the impact of the crystalline phases and their relative content on the resistive switching. The role of each will be investigated which may provide a path to modulate the resistive switching behavior. **There has been so far no report on resistive switching in $ErMnO_3$ devices.**

The chapter is organized as follows. We present the optimization of polycrystalline $ErMnO_3$ thin films in Sections 5.1. We study the microstructure of the films using multiple characterization methods to identify and quantify the different crystalline phases in Section 5.2. In Section 5.3, we explore the ferroelectric properties of the films through polarization-voltage (*P*-*V*) measurements and time-resolved XRD. Then, the resistive switching behavior is investigated in Pt/$ErMnO_3$/Ti/Au stacks with minor o-$ErMnO_3$ in Section 5.4. We study the impact of the crystalline phases and role of the top electrodes on resistive switching performance in Sections 5.5 and 5.6, respectively. We summarize our results in Section 5.7.

5.1 Polycrystalline $ErMnO_3$ thin film optimization

Polycrystalline $ErMnO_3$ thin films were prepared on different types of Pt coated Si substrates. The impact of post-deposition annealing conditions on the crystalline phases and film microstructures was investigated.

5.1.1 Deposition on polycrystalline Pt coated Si substrates

Figure 5.1 illustrates the process flow to grow $ErMnO_3$ either as a film or in pre-patterned areas. The $ErMnO_3$ films were deposited on a Si/SiO_2/Ti/Pt substrate by RF sputtering at room temperature in Ar ambient, using a RF power of 200 W and an Ar pressure of 10 µbar (Figure 5.1a). Film thickness was measured by spectroscopic ellipsometry.

Patterned $ErMnO_3$ structures were also prepared, the reason for this will be discussed later. Figure 5.1b illustrates the process flow for growing pre-patterned polycrystalline $ErMnO_3$ areas. Pre-defined areas were patterned using photolithography (dimension of 100×100 µm^2). $ErMnO_3$ was deposited by RF sputtering

under the same conditions as previously mentioned. A lift-off process was used to remove the resist and leave the patterned $ErMnO_3$ areas. Two different lift-off processes were tested. Residual resist along the edges of the structures was observed after ultrasonic cleaning of $ErMnO_3$ on the patterned photoresist in DMSO at 50 °C for 25 min. Clean structures with no resist residue were obtained after ultrasonic cleaning in acetone at 50 °C for 1 h 40 min followed with rinsing by DMSO for 10 s. The structure thickness was measured by AFM.

Post-deposition annealing was then performed to crystalize the $ErMnO_3$. Different post-deposition annealing conditions were studied. The annealing parameters are listed in Table 5.1.

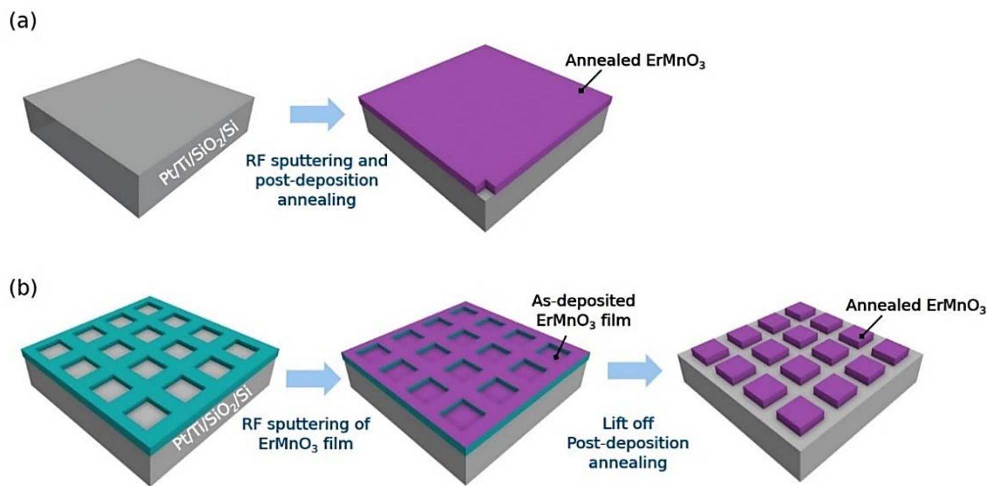

Figure 5.1: Process flow of growing planar and pre-patterned polycrystalline $ErMnO_3$ on $Si/SiO_2/Ti/Pt$ substrates. (a) Preparation of planar film with RF sputtering and post-deposition annealing. (b) Photoresist is patterned by photolithography on $Si/SiO_2/Ti/Pt$ substrate, followed with RF sputtering to obtain $ErMnO_3$ on the patterned photoresist, subsequently annealed $ErMnO_3$ structures are obtained by lift-off and post-deposition annealing.

Table 5.1: Post-deposition annealing parameters. All the films or structures were deposited by RF sputtering with a RF power of 200 W and an Ar pressure of 10 μbar.

Design	Film thickness (nm)	Annealing temperature (°C)	Annealing time (min)	Atmosphere
Planar	75	750	5	RTP – N_2
	71	700	30	Furnace – N_2
	71	750	30	Furnace – N_2
	71	800	30	Furnace – N_2
	71	750	30	Furnace – O_2
Patterned	60	750	30	Furnace – N_2

The GIXRD pattern of an $ErMnO_3$ thin film annealed by rapid thermal processing (RTP) at 750 °C for 5 min in N_2 is shown in Figure 5.2. The XRD peaks marked with dotted lines correspond to the Pt bottom electrode (PDF 00-001-2680[268]). Most of the XRD peaks can be attributed to cubic Er_2O_3 (c-Er_2O_3, PDF 03-065-3175[302]), and some of them can be assigned to hexagonal $ErMnO_3$ (h-$ErMnO_3$, PDF 04-016-1782[50]), orthorhombic $ErMnO_3$ (o-$ErMnO_3$, PDF 04-014-5221[303]), orthorhombic $ErMn_2O_5$ (o-$ErMn_2O_5$, PDF 00-050-0296[104]) and orthorhombic MnO_2 (o-MnO_2, PDF 01-087-9108 [304]). This film crystalizes mainly in the c-Er_2O_3 phase, which pints to a deficiency in Mn element.

The surface morphology of the film after RTP (Figure 5.3a and b) shows a dense and uniform microstructure consisting of sub-100 nm grains and of larger grains of few 100 nm in size. The EDX compositional analysis of both types of grains (marked as 1 and 2 in Figure 5.3c) is given in Table 5.2. A similar percentage of elements is observed at both locations and both exhibit Mn deficiency. These findings are consistent with the XRD results, showing that the film is mainly composed of c-Er_2O_3. Mn loss during the RTP might be associated with the rapid heating and cooling rates.

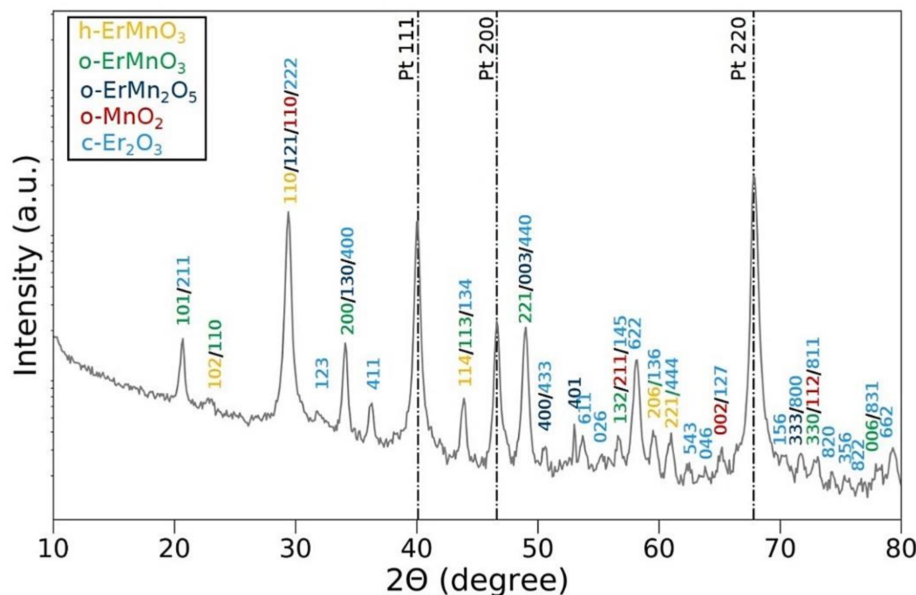

Figure 5.2: GIXRD pattern of an $ErMnO_3$ thin film annealed in N_2 by RTP (as shown in Table 5.1).

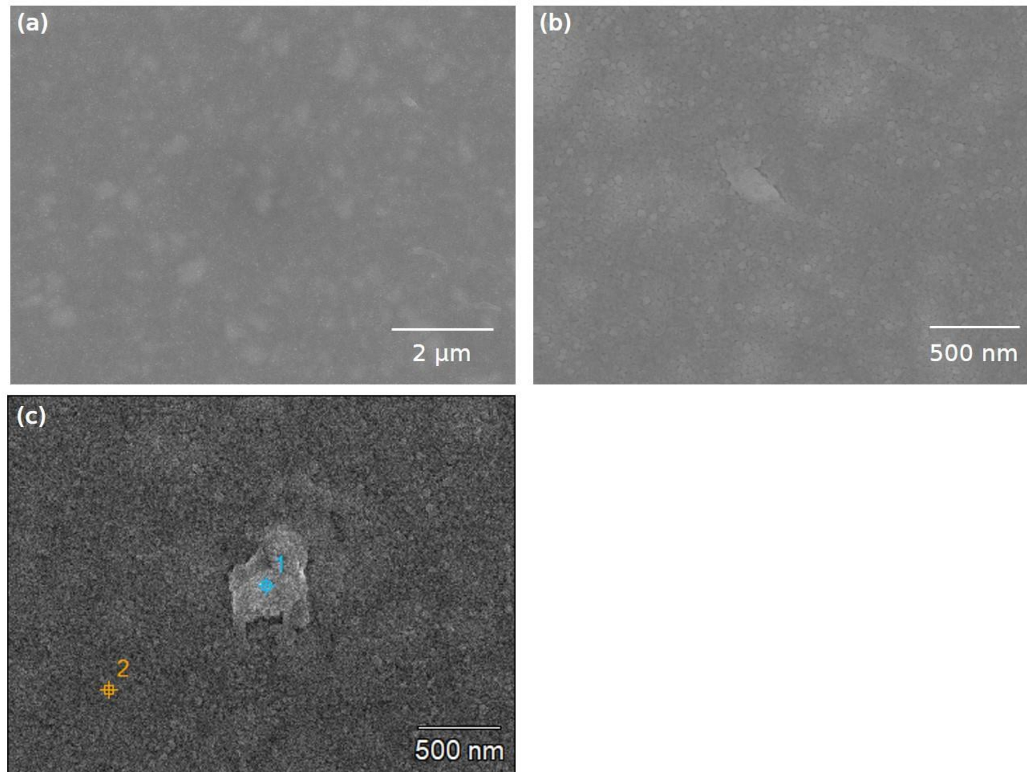

Figure 5.3: (a) and (b) SEM images of a $ErMnO_3$ thin film annealed in RTP at 750 °C for 5 min in N_2 with the acceleration voltage of 10.0 kV and in-lens detector. (c) SEM-EDX image of this $ErMnO_3$ thin film with the acceleration voltage of 20.0 kV. The atom percentage of elements of the two different locations marked 1 and 2 in (c) are listed in Table 5.2.

Table 5.2: Atom percentage of elements investigated by SEM-EDX (acceleration voltage of 20.0 kV) on the two different locations (marked 1 and 2 in Figure 5.3c) of a $ErMnO_3$ thin film annealed in RTP at 750 °C for 5 min in N_2.

(%)	O-K	Si-K	Ti-K	Mn-K	Er-M	Pt-L
1	45.78 ± 1.20	6.61 ± 0.31	1.73 ± 0.11	4.75 ± 0.33	13.88 ± 0.41	27.24 ± 0.81
2	42.31 ± 3.79	11.20 ± 0.82	2.45 ± 0.55	4.18 ± 0.78	12.13 ± 1.76	27.74 ± 2.60

For all further investigations, we performed post-deposition annealing in a conventional quartz tube furnace to avoid Mn loss. Figure 5.4 shows the GIXRD pattern of a film annealed in O_2 at 750 °C for 30 min. It indicates the presence of secondary phases such as o-$ErMn_2O_5$, o-MnO_2 and c-Er_2O_3. The oxygen atmosphere favors the formation of secondary phases such as $ErMn_2O_5$, MnO_2 and Er_2O_3.

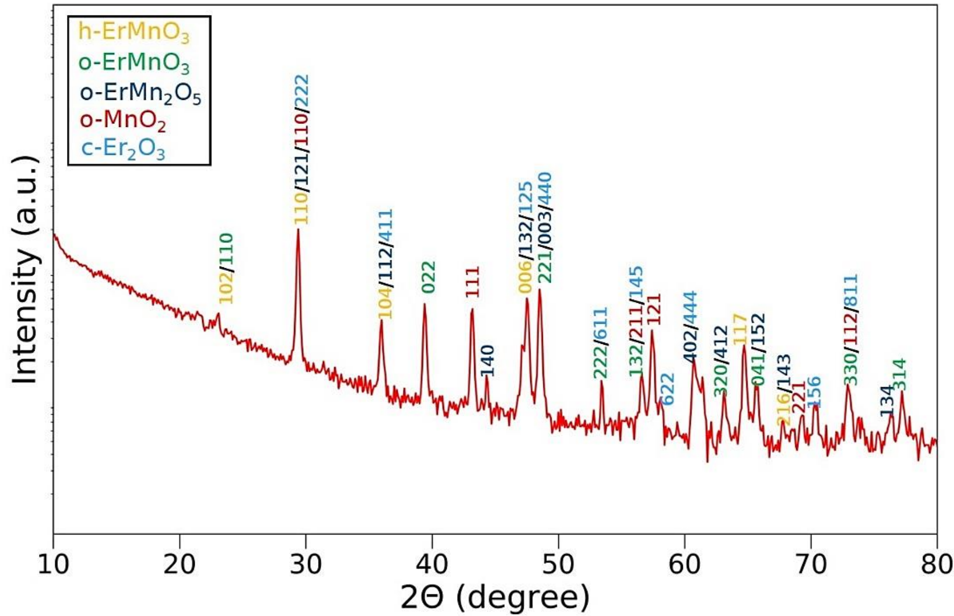

Figure 5.4: GIXRD pattern of an $ErMnO_3$ films annealed in O_2 in a furnace (as shown in Table 5.1).

To obtain the targeted stochiometric $ErMnO_3$ crystalline phase(s), an inert N_2 atmosphere was used for annealing. Films were annealed at different temperatures ranging from 700 °C to 800 °C for 30 min in N_2 (Figure 5.5). At 700 °C, the films were not well crystallized. At 750 °C, the films show a majority of h-$ErMnO_3$ and a minority of metastable o-$ErMnO_3$. The trend is similar at 800 °C with a slight increase in o-$ErMnO_3$.

Considering the thermal budget of Pt coated substrates and the observation that the film annealed at 750 °C reveals a higher proportion of the h-$ErMnO_3$ phase, we selected 750 °C in an N_2 atmosphere for our study.

The lattice parameters of the film are listed in Table 5.3. The values of the film closely match those of single crystal prepared under atmospheric pressure.

Obtaining pure h-$ErMnO_3$ films is challenging due to the potential appearance of the secondary phase o-$ErMnO_3$. It results from the small difference in free energy of $RMnO_3$ formation from R_2O_3 and Mn_2O_3[45, 46] for $ErMnO_3$ between the thermodynamically stable hexagonal and the metastable orthorhombic phases. This phenomenon is illustrated in Figure 1.3 in Chapter 1.

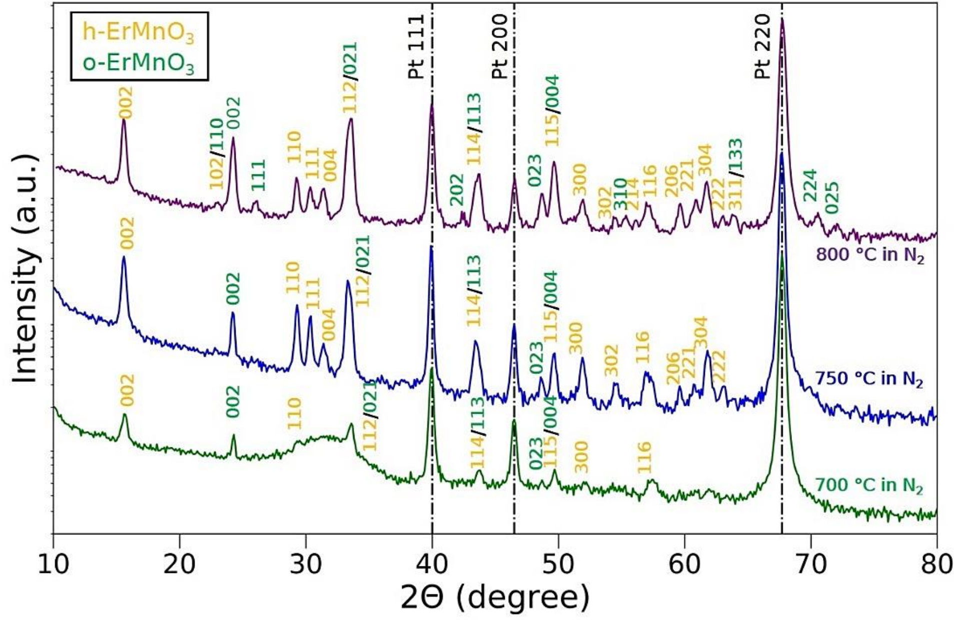

Figure 5.5: GIXRD patterns of $ErMnO_3$ thin films annealed in N_2 in a furnace for 30 min at different annealing temperatures (as shown in Table 5.1).

Table 5.3: Lattice parameters and unit cell volume of hexagonal phase in the $ErMnO_3$ film and structures annealed at 750 °C for 30 min in N_2 in a furnace, and of $ErMnO_3$ single crystal from ref.[50] The 111 peak at $2\theta = 40.0°$ of Pt was taken as a reference. The in-plane a and out-of-plane c lattice parameters were calculated from the highest intensity peaks – 004 and 112, respectively.

Samples	**In plane lattice *a* (Å)**	**Out of plane lattice *c* (Å)**	**Volume of cell (Å^3)**
Single crystal (0 GPa)[50]	6.12	11.41	370.28
Film	6.10	11.38	366.47
Structures	6.03	11.34	357.88

Figure 5.6 presents the surface morphology of the films annealed at 700, 750 and 800 °C. All films show regions of bright and dark contrasts and crystallites with grain sizes of ~ 50 nm. As the annealing temperature increases, more bright regions appear. The origin of these dark/bright contrasts will be explored in the coming sections.

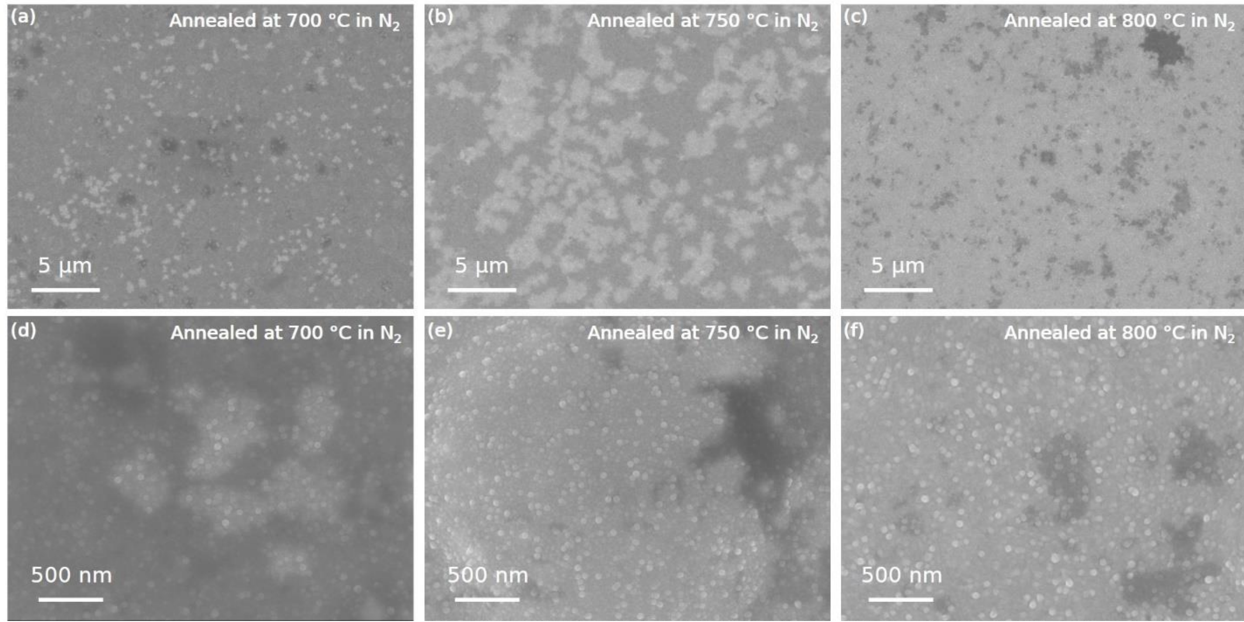

Figure 5.6: SEM images of films annealed at different temperatures for 30 min in N_2 in a furnace with the acceleration voltage of 10.0 kV and in-lens detector.

Figure 5.7a, b, c shows topographic information of an as-deposited film, as studied by AFM and SEM. After annealing at 750 ºC for 30 min in N_2, the film becomes rougher (Figure 5.7d) and shows buckling in both AFM and cross-section SEM images (Figure 5.7e, g, f). The buckling effect often appears as the film is under compressive stress after the annealing process, as illustrated in a sketch in Figure 5.7h.

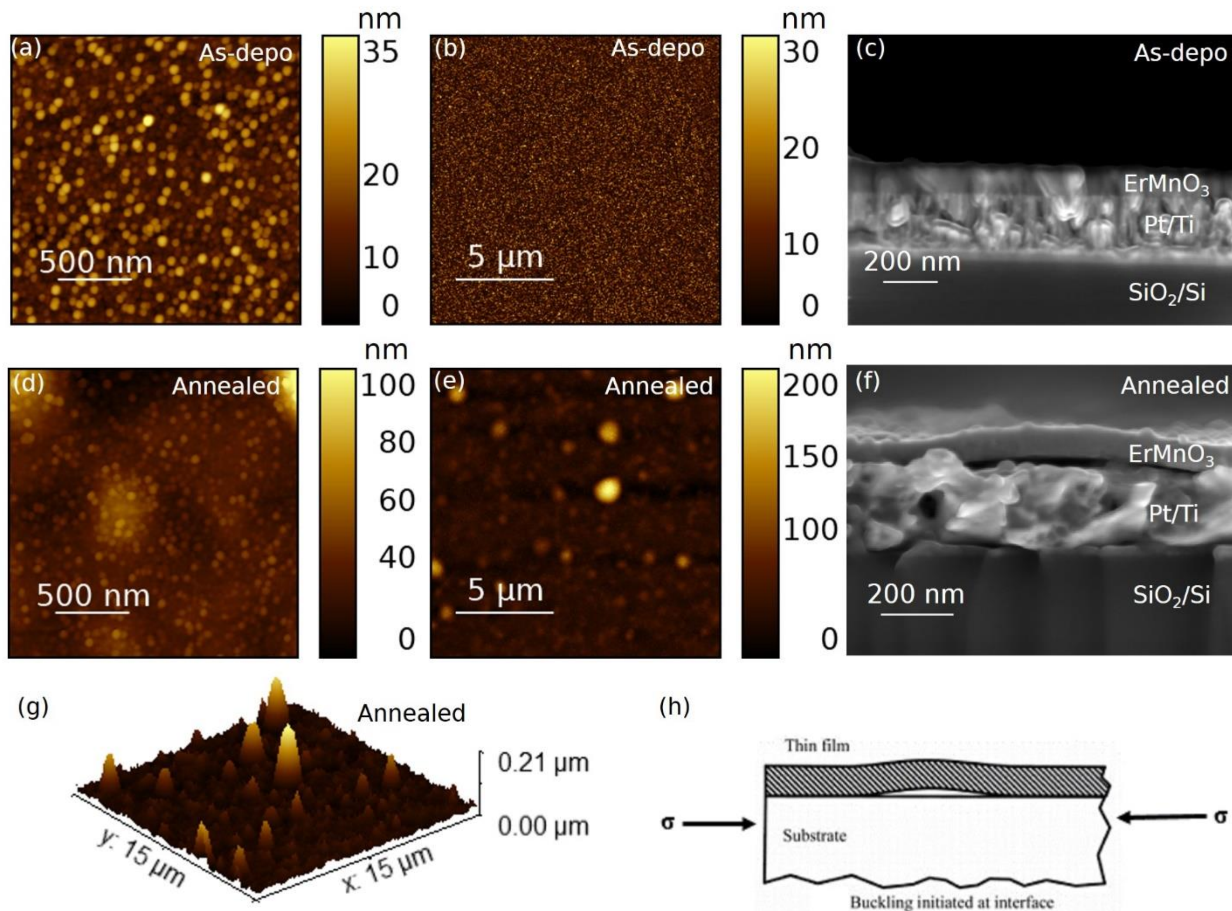

Figure 5.7: (a, b) AFM and (c) SEM images of an as-deposited $ErMnO_3$ film. (d, e) AFM, (g) AFM 3D and (f) SEM images of a film annealed at 750 °C in N_2 in a furnace. (f) Sketch of typical thin film failure mode (buckling) due to compressive straining.[305] SEM images were taken with in-lens detector and acceleration voltage of 5.0 kV.

The GIXRD pattern of the $ErMnO_3$ square structures annealed at 750 °C for 30 min in N_2 is shown in Figure 5.8, and compared to the one of a continuous film. Pt is used as a common reference. The annealed $ErMnO_3$ structures consist of a majority of hexagonal and a minority of orthorhombic $ErMnO_3$ crystalline phases. Compared to the continuous film, the intensity of the XRD peaks is lower, which we attribute to the smaller overall volume of the structures. The peaks for the $ErMnO_3$ structures are shifted towards larger angles (smaller interplanar spacings), indicating smaller lattice parameters (listed in Table 5.3).

For the $ErMnO_3$ structures, there is no buckling observed, as shown in Figure 5.9. The structures (area of $100 \times 100\ \mu m^2$) can undergo strain relaxation at the edges during the annealing, preventing global buckling, while the continuous film experience uniform compressive strain throughout its surface.

To conclude, patterned $ErMnO_3$ structures on polycrystalline Pt coated Si substrate after annealing at 750 °C under N_2 for 30 min in a furnace, show buckling-free $ErMnO_3$. These structures will be further characterized in the following sections.

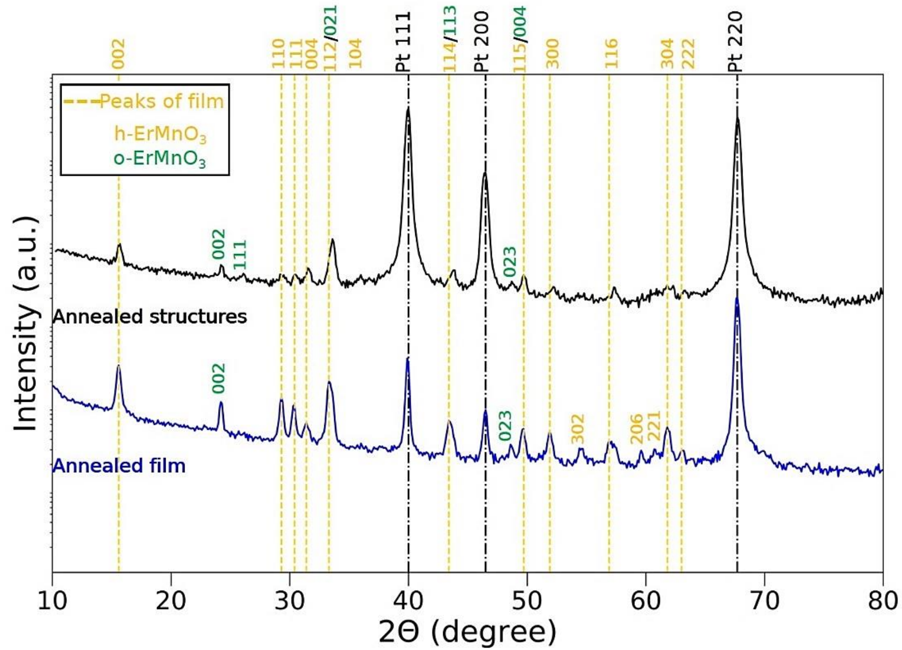

Figure 5.8: GIXRD patterns of an $ErMnO_3$ film and $ErMnO_3$ structures (both annealed at 750 °C for 30 min in N_2 in a furnace).

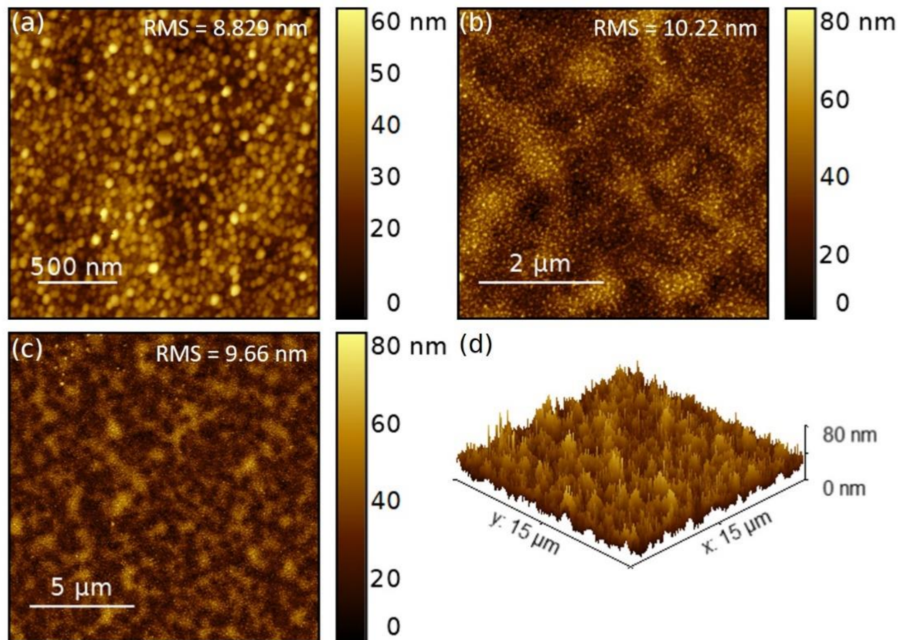

Figure 5.9: (a-c) AFM images with different scan area sizes and (d) AFM 3D image of $ErMnO_3$ structures annealed at 750 °C for 30 min in N_2 in a furnace.

5.1.2 Deposition on textured (111) Pt coated Si substrates

The Pt substrates used in the previous section are polycrystalline. In this section, we investigate the use of textured (111) Pt for $ErMnO_3$ growth. Local epitaxy on each Pt grain may occur.

The lattice mismatch between the hexagonal $ErMnO_3$ and Pt is explained in Figure 5.10. The (111) plane of the Pt layer has a hexagonal structure, as sketched in Figure 5.10a. There are two possible arrangements of $ErMnO_3$ on Pt. The lattice arrangement shown in Figure 5.10b may be unstable due to a lattice mismatch of up to 11.6% (Equation 5.1). A more stable configuration, illustrated in Figure 5.10c, involves a 30° rotation between $ErMnO_3$ and Pt, reducing the lattice mismatch to a tensile strain of -3.3% (Equation 5.2).

$$lattice\ mismatch = [a_{EMO}(crystal) - 2a_{h-Pt}]/2a_{h-Pt} \qquad \text{Equation 5.1}$$

$$lattice\ mismatch = [\sqrt{3}a_{EMO}(crystal) - 4a_{h-Pt}]/4a_{h-Pt} \qquad \text{Equation 5.2}$$

where a is the in-plane lattice parameter.

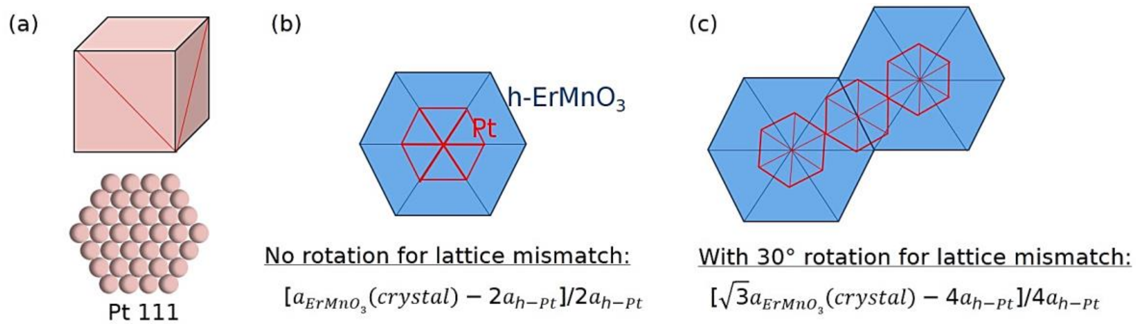

Figure 5.10: (a) Sketch of cubic Pt with (111) plane and its Pt layer in the hexagonal structure. Schematic diagram of the in-plane epitaxial relationships between hexagonal $ErMnO_3$ film and (111) Pt layer while (b) without and (c) with 30° rotation. The lattice mismatch was calculated respectively.

Commercial $Si/SiO_2/TiO_2$/(111) Pt substrates from MTI Corporation were used (the inset of Figure 5.11). The XRD pattern recorded on Pt substrate is shown in Figure 5.11. The FWHM of the rocking curve of the 111 peak is of 1.659°, which confirms the 111 texture.

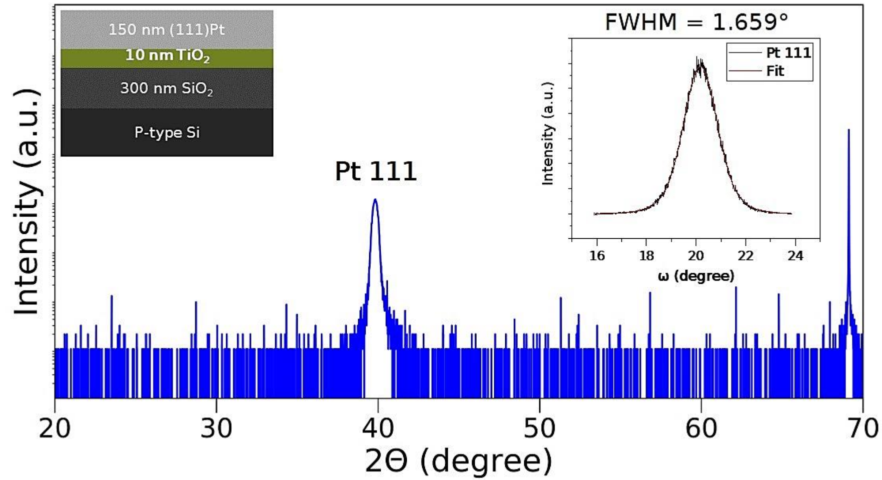

Figure 5.11: 2theta-ω scan of a commercial substrate (111) $Pt/TiO_2/SiO_2$/p-type Si, as sketched in the inset. The X-ray rocking curve of Pt 111 has a FWHM of 1.659º.

$ErMnO_3$ films were deposited by RF sputtering at room temperature with a RF power of 200 W and an Ar pressure of 10 µbar. The thickness of the as-deposited $ErMnO_3$ thin films (~ 70 nm) was determined by spectroscopic ellipsometry. After post-deposition annealing at 750 °C for 30 min in N_2, the films consist of different fractions of hexagonal and orthorhombic $ErMnO_3$ phases, despite using the same sputtering conditions (Figure 5.12). The reproducibility is lower on commercial textured Pt substrates compared to E-beam evaporated polycrystalline Pt substrates, although the reason for this is not clear.

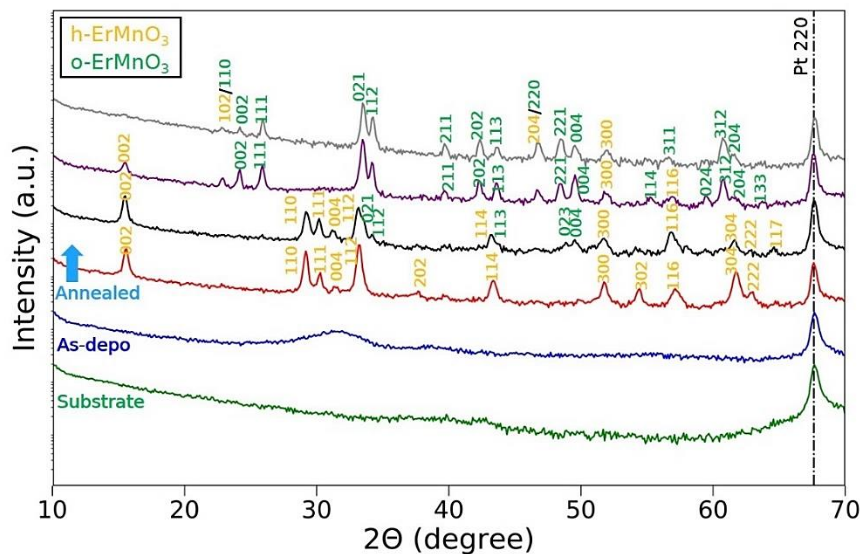

Figure 5.12: GIXRD patterns of the commercial (111) $Pt/TiO_2/SiO_2/Si$ substrate, as-deposited and annealed $ErMnO_3$ films (all annealed at 750 °C for 30 min in N_2 in a furnace).

As observed in AFM images (see Figure 5.13a, b), the crystalline grains of the as-deposited films grow along the Pt crystallites. The roughness of both as-deposited and annealed films is similar to that of the Pt substrate (RMS ~ 2 nm, see Figure 5.13a-c), and much lower than that of films (RMS ~ 9 nm) grown on E-beam evaporated polycrystalline Pt substrates. No buckling is observed in the annealed films (Figure 5.13d).

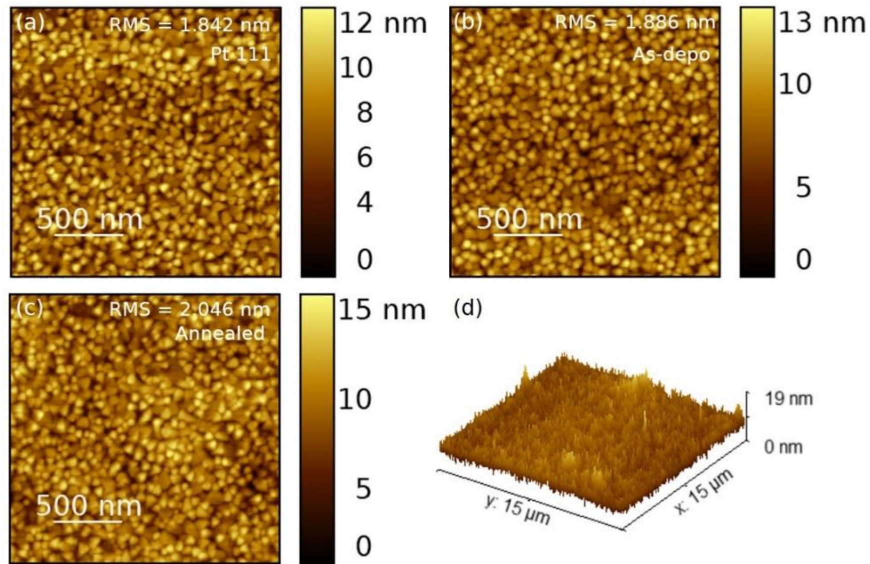

Figure 5.13: AFM images of (a) commercial Pt substrate. (b) as-deposited $ErMnO_3$ film. (c) annealed $ErMnO_3$ film (750 ºC for 30 min in N_2 in a furnace). (d) AFM 3D image of the annealed $ErMnO_3$ film.

5.2 Identification and quantification of the crystalline phases

The o-$ErMnO_3$ phase (metastable phase) easily appears in polycrystalline hexagonal $ErMnO_3$ thin films. GIXRD often does not allow to accurately quantify the fraction of both crystalline phases, because many peaks cannot be unambiguously assigned to either phase. In this section, we develop a method to quantitively determine the amount of each crystalline phase.

All $ErMnO_3$ structures were grown on polycrystalline Pt coated Si substrate. Optical microscope and SEM images are shown in Figure 5.14a, b. Both types of images exhibit regions of bright/dark contrasts, with similar features. Composition and topography are the two dominant factors which are responsible for the contrasts. Dennis Meier *et al.* reported an SEM investigation of $ErMnO_3$ single crystals and associated bright and dark areas to upward and downward ferroelectric domain polarizations, respectively.[306, 307] Therefore, to disambiguate between the different possibilities of the origin of the contrast, we performed Raman spectroscopy on the area indicated by the yellow box in Figure 5.14a, b to gain local information.

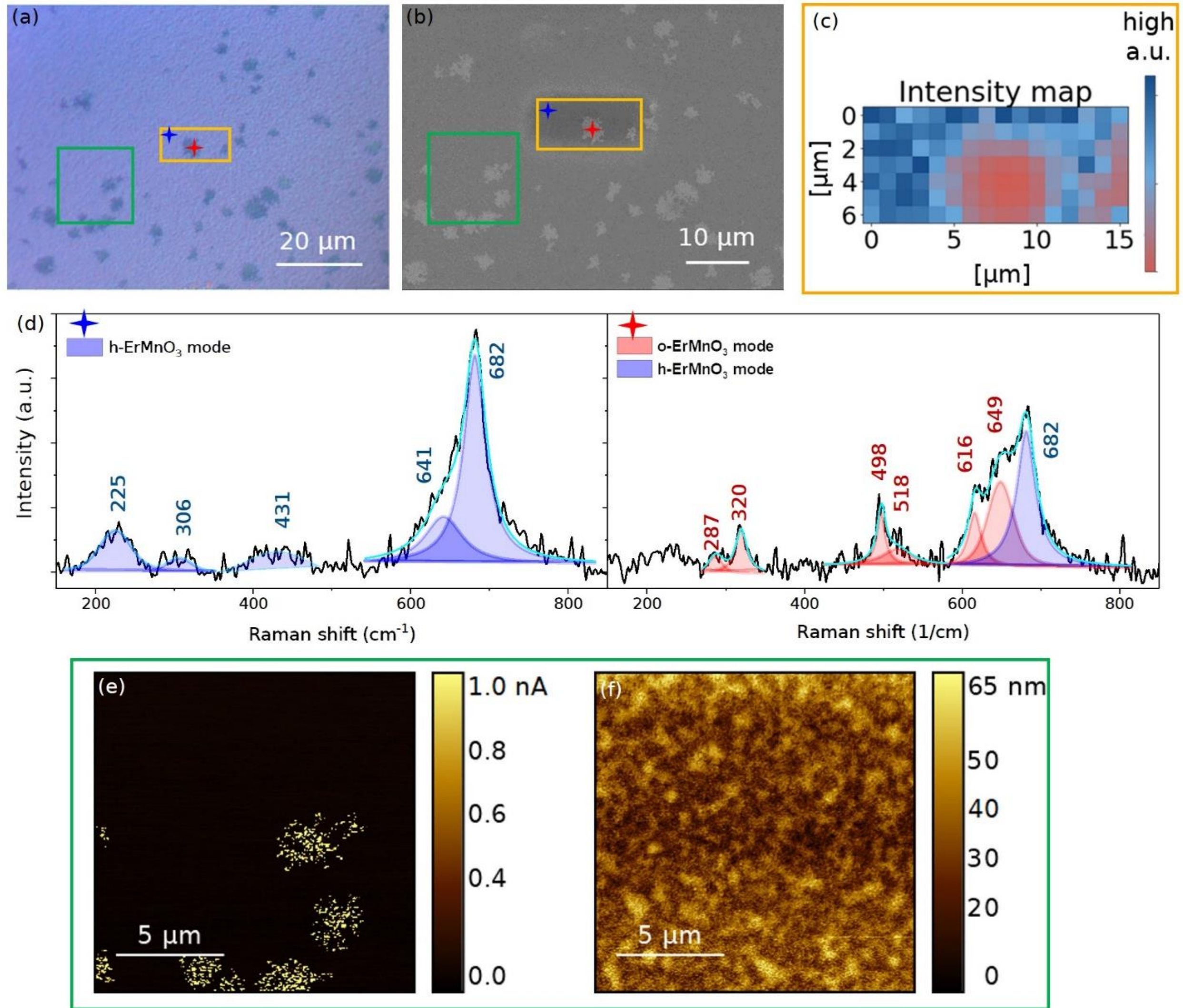

Figure 5.14: (a) Optical microscopy and (b) SEM image of the annealed $ErMnO_3$ structure (at 750 ºC for 30 min in N_2 in a furnace) on polycrystalline Pt coated Si substrate (by E-beam evaporation). (c) Raman intensity map based on the mode $A_1(TO_9)$ at 682 cm^{-1} from h-$ErMnO_3$ phase, which is mapped within the yellow box marked in (a) and (b). (d) Two Raman spectra with their fitted Raman modes representing positions with markers – red and blue stars indicated in (a) and (b). (e) Current and (f) topographic maps collected from the green rectangles shown in panel (a) and (b) with conductive-AFM (c-AFM) on annealed $ErMnO_3$ structure.

Raman spectroscopy mapping was performed with the intensity of the $A_1(TO_9)$ mode at 682 cm^{-1} (scan size of 6 ×15 μm^2, beam size of 1 µm and spatial resolution of ~ 1 µm). This mode corresponds to the apical oxygen atoms (O1 and O2) stretching along the c-axis in hexagonal $ErMnO_3$ phase and is associated with the tilting and trimerization of MnO_5 polyhedra.[145, 308] This mode is absent in the orthorhombic phase. The Raman intensity map shown in Figure 5.14c presents two distinct regions colored in blue and red, based on the intensity of the peak at 682 cm^{-1}. Figure 5.14d displays two typical Raman spectra marked with red and blue stars, performed in these two regions. The spectra are indexed with the Raman modes, and spectral

positions are compared to those of a single crystal (Table 5.4). The spectrum obtained from the spot marked with blue star indicates the presence of pure hexagonal phase, while the spectrum from the region marked with red star indicates the presence of orthorhombic phase with a minor contribution from the hexagonal phase.

Table 5.4: Raman active modes of references (single crystals) and experimental data.

Reported h-$ErMnO_3$[145]	Reported o-$ErMnO_3$[309]	Spectrum in blue [This work]	Spectrum in red [This work]
E_2(5) 218	B_{1g} 280	E_2(5) 225	B_{1g} 287
E_2(8) 295	A_g 316	E_2(8) 306	A_g 320
E_2(11) 417	A_g 490	E_2(11) 431	A_g 498
E_1(TO_{14}) 639	A_g 520	E_1(TO_{14}) 642	A_g 518
A_1(TO_9) 683	B_{1g} 610	A_1(TO_9) 682	B_{1g} 616
	653[a)]		649[a)]
			A_1(TO_9) 682

a) Raman shift is not related to a proper vibration mode from o-$ErMnO_3$[309] it might be from defects[277] or contributions from zone-boundary phonon[276].

Comparing the Raman intensity map with the optical and SEM images indicates that low brightness in optical microscopy and high secondary electron yield in SEM are signatures of the o-$ErMnO_3$ crystalline phase. Vice versa, high brightness in optical microscopy and low secondary electron yield in SEM are signatures of the h-$ErMnO_3$ crystalline phase. The bright regions observed in SEM exhibit irregular and discontinuous shapes. Hence, each measured spot (1×1 µm^2, Raman spectroscopy spatial resolution) might include small amounts of the surrounding hexagonal phase, which explains the detected Raman mode A_1(TO_9) from h-$ErMnO_3$ in the Raman spectrum at the position of the red star.

The presence of the orthorhombic phase in the hexagonal phase matrix is further confirmed by c-AFM measurements. The c-AFM spatial mapping was performed on the area indicated by the green box in Figure 5.14a, b. During the measurement, the platinum coated tip was grounded, and a sample bias of 1.5 V DC voltage was applied. The current image of the mapped area is presented in Figure 5.14e. The highly conducting regions correlate directly to the dark and bright regions in the optical and SEM images,

respectively (Figure 5.14a, b), identified as o-$ErMnO_3$ by Raman spectroscopy (Figure 5.14c). Previous studies have shown that o-$ErMnO_3$ contains a higher amount of Mn^{4+} ions than h-$ErMnO_3$,[278] resulting in increased conductivity.[103] The high conductivity of o-$ErMnO_3$ is fully consistent with our c-AFM results. The topographic image shown in Figure 5.14f reveals no significant surface morphology difference between the highly and lowly conductive regions. We can therefore exclude topographic contribution on the observed bright/dark contrast in the optical and SEM images.

From these correlated microscopy and spectroscopy analyses, we clearly identify the presence of the orthorhombic phase in the polycrystalline hexagonal $EMnO_3$, which cannot be determined by X-ray diffraction due to either low volume amount and nanosize grains leading to non-detectable peaks and/or the fact that several peaks of the hexagonal and orthorhombic phases overlap or are very close. The optical microscopy images clearly reveal the presence of distinct bright and dark contrast regions corresponding to the hexagonal and orthorhombic phases, respectively (Figure 5.14a). Hence, optical microscopy offers a rapid and straightforward method to assess the coexistence of both phases and enable a quantitative analysis. We assume that the orthorhombic phase regions extend down to the bottom interface (Pt substrate) since we can detect them by c-AFM.

Optical microscopy images were captured on individual $ErMnO_3$ structures (100×100 μm^2). Representative images with different fractions of dark/bright regions are presented in Figure 5.15a-c, which were then processed with signal processing algorithms to separate the bright and dark areas representing orthorhombic and hexagonal phases, respectively. With this method, we estimated the fraction of the two crystalline phases in the selected areas. The results of the segmentation treatment of the optical images are displayed in Figure 5.15d-f, with various o-$ErMnO_3$ fraction ranging from 1.6 to 49.5%.

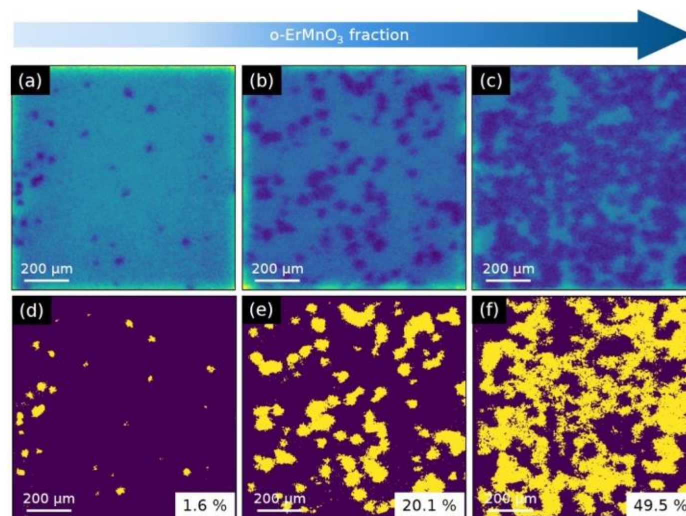

Figure 5.15: (a-c) Optical microscope images with different fraction of bright/dark regions. (d-f) The results of the segmentation treatment of images regarding bright/dark regions for estimation of fraction of dark region area (o-$ErMnO_3$).

5.3 Ferroelectric properties

The remanent polarization (P_r) of $ErMnO_3$ single crystals is around 5.5 μC/cm^2 (measured at 1 kHz and 120 K).[310] Epitaxial $ErMnO_3$ thin films deposited on epitaxial (111) Pt coated Al_2O_3 substrates were reported to have a P_r value of 1.3 μC/cm^2 at 1 kHz and 150 K.[145] No room temperature P_r value has been measured in epitaxial films to date due to high levels of leakage currents.

The polarization of a polycrystalline $ErMnO_3$ thin film is expected to be lower than that of a single crystal, since polarization occurs only along the *c*-axis of the hexagonal phase. Here, films with a majority of hexagonal phase were selected to study their ferroelectric properties.

5.3.1 Polarization-voltage measurement

In this section, we studied the polarization of polycrystalline $ErMnO_3$ films by ferroelectric hysteresis measurements conducted at room temperature and 77 K (the low-temperature measurements were performed by Maximilian Winkler in the group of Experimental Physics V from the University of Augsburg).

The ferroelectric hysteresis measurements at 77 K required wire bonding for contacting the device electrodes. The devices were designed as schematically shown in Figure 5.16, where the micro-sized devices could be contacted via gold wire bonding with silver paste. An insulating SiO_2 layer (~ 200 nm-thick) was deposited by PECVD and patterned by laser lithography and on the planar polycrystalline $ErMnO_3$ thin film. Subsequently, top Pt electrodes (~ 125 nm-thick) were patterned by lift-off (laser lithography and DC sputtering). Pt/$ErMnO_3$/Pt capacitive devices with dimensions ranging from 30 × 30 to 70 × 70 μm^2 were fabricated (Figure 5.16).

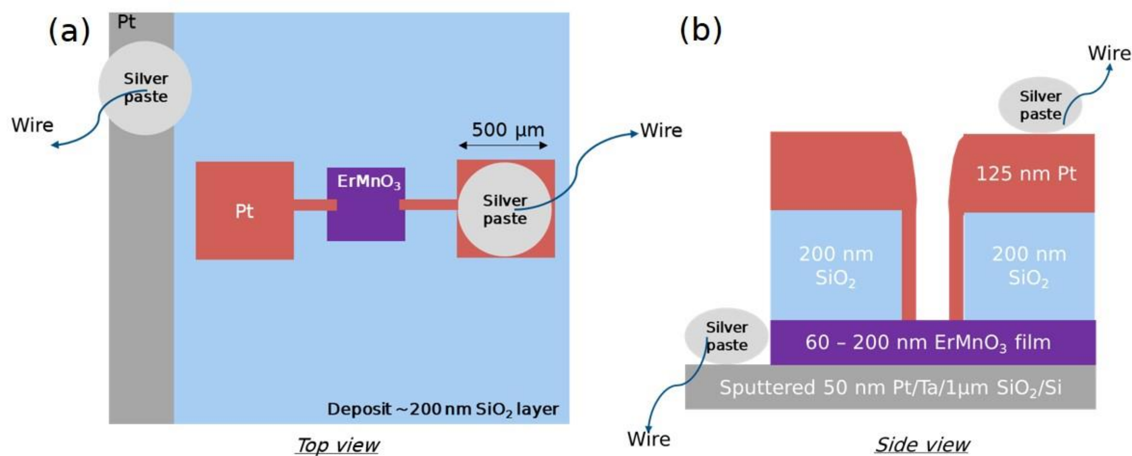

Figure 5.16: Schematics of designed device structure for PE hysteresis loop measurements in (a) top view and (b) side view.

To avoid the buckling effect observed in planar films deposited on polycrystalline Pt coated Si substrate (E-beam evaporated Pt), the films were instead deposited on Pt/Ta/SiO_2/Si substrates prepared by DC sputtering of 50 nm Pt and 20 nm Ta (as adhesion layer) on SiO_2 (1µm)/Si wafers. No buckling is observed in these films (Figure 5.18).

The sputtered Pt is found to be polycrystalline Pt (Figure 5.17) with relatively low surface roughness (RMS value of 0.26 nm, as shown in Figure 5.18). $ErMnO_3$ films (~ 60 and ~ 200 nm-thick) were deposited on these substrates by RF sputtering at room temperature with a RF power of 200 W and an Ar pressure of 10 µbar, followed by post-deposition annealing at 750 °C for 30 min in N_2. The presence of mostly hexagonal $ErMnO_3$ phase is evidenced by XRD (Figure 5.17). The 60 nm-thick $ErMnO_3$ film shows a much lower crystallinity. The lattice parameters of 200 nm-thick film (listed in Table 5.5) indicate that the cell volume is slightly larger than that of a single crystal prepared under atmospheric pressure. It suggests the absence of compressive strain in the films, which may explain the absence of buckling.

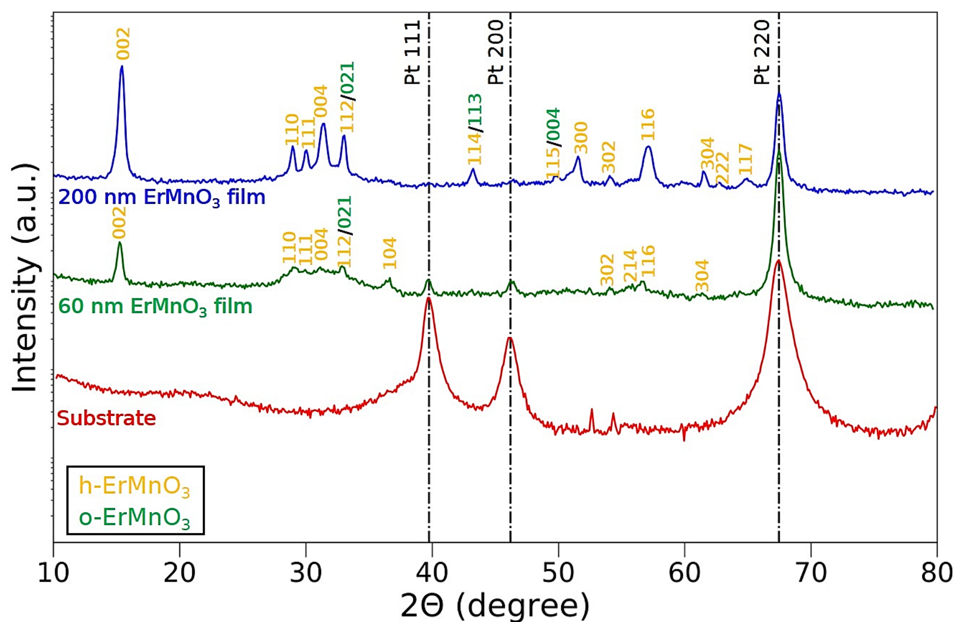

Figure 5.17: GIXRD patterns of the sputtered Pt/Ta/SiO_2/Si substrate, ~60 and ~200 nm-thick $ErMnO_3$ films annealed at 750 °C for 30 min in N_2 in a furnace.

Grain growth of the Pt/Ta thin films is observed after the annealing (Figure 5.18c, f), resulting in increased roughness and the possibility of inclusion of metallic Ta particles within Pt grains (as reported in ref.[311]). The polycrystalline $ErMnO_3$ film deposited on this substrate exhibits similar round particles (see bright dots in Figure 5.18d, g). The non-particle area in the film shows a relatively low RMS value of only 0.35 nm, as observed in Figure 5.18e.

Table 5.5: Lattice parameters and unit cell volume of hexagonal phase in 200 nm-thick $ErMnO_3$ film annealed at 750 °C for 30 min in N_2 in a furnace, and of $ErMnO_3$ crystal from ref.[50] The 111 peak at $2\theta = 39.75°$ of Pt was taken as a reference. The in-plane (*a*) and out-of-plane (*b*) lattice parameters were calculated from 004 and 112 peaks.

Samples	In plane lattice *a* (Å)	Out of plane lattice *c* (Å)	Volume of cell (Å^3)
Single crystal (0 GPa)[50]	6.12	11.41	370.28
~200 nm	6.15	11.36	373.22

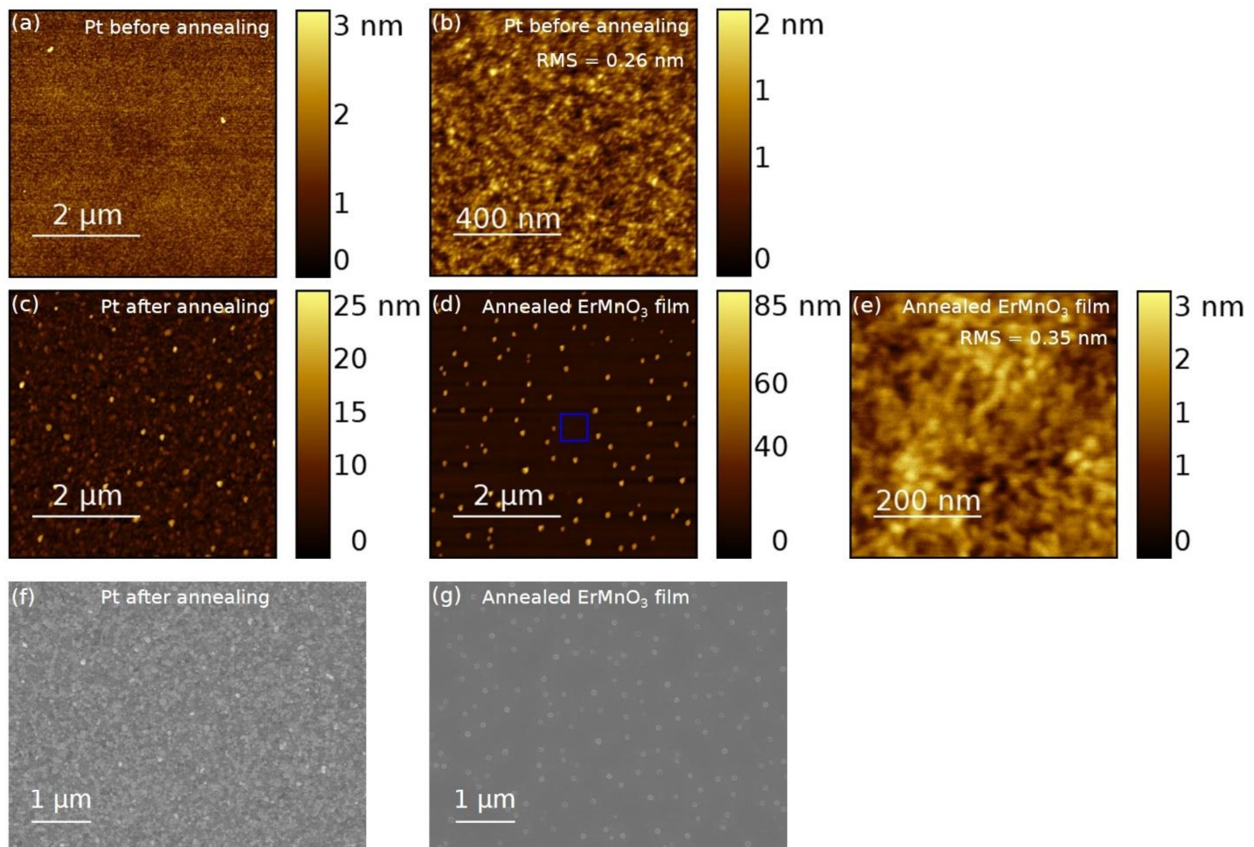

Figure 5.18: AFM images of $Pt/Ta/SiO_2/Si$ substrate (a, b) before and (c) after annealing at 750 °C for 30 min in N_2. AFM images of (d) 60 nm-thick $ErMnO_3$ film annealed at 750 °C for 30 min in N_2. (e) AFM image of the area marked as blue box in (d). SEM images of (f) $Pt/Ta/SiO_2/Si$ substrate and (g) 60 nm-thick $ErMnO_3$ film after annealing at 750 °C for 30 min in N_2.

Polarization-electric field (*P*-*E*) hysteresis loops were recorded at room temperature using a triangular signal at 1 kHz (Figure 5.19a). This *P*-*E* loop shape indicates a leaky dielectric. Figure 5.19b presents a *P*-*E* hysteresis loop recorded by PUND measurement. Ferroelectricity could not be proven.

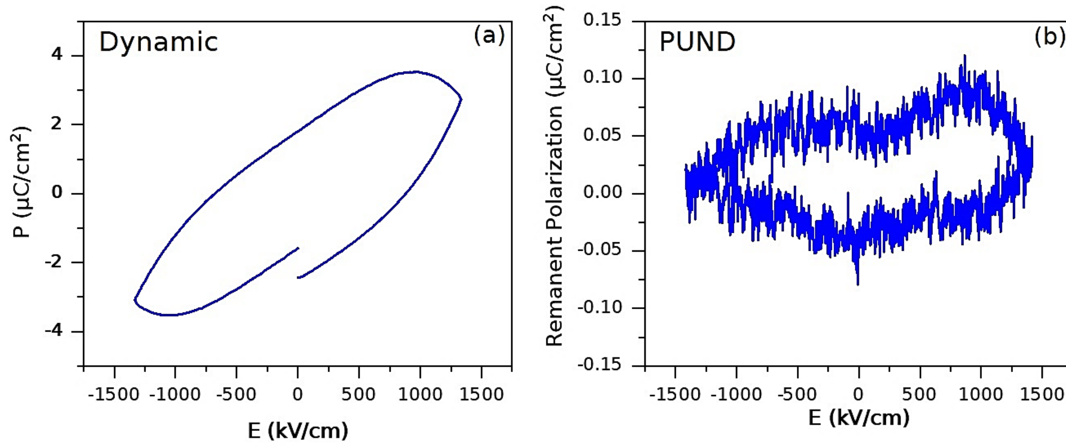

Figure 5.19: Polarization-electric field (*P*-*E*) hysteresis loop (1 kHz) of 60 nm-thick polycrystalline $ErMnO_3$ thin film at room temperature by (a) Dynamic hysteresis and (b) PUND measurements. The device area is 30 × 30 μm^2.

To decrease the large leakage currents of $ErMnO_3$ and perform reliable measurements, PUND measurements were performed at 77 K (25 Hz), as displayed in Figure 5.20a. A thicker $ErMnO_3$ film with potentially stronger polarization was measured. The P-E hysteresis loop is shown in Figure 5.20b. A linear dependence of *P* with *E* is observed, typical for a dielectric. No ferroelectric behavior is observed, and the reason for this remains unclear. $ErMnO_3$ is known to be an improper ferroelectric, and previous studies have shown that size reduction does not significantly impact polarization, as indicated by second harmonic generation measurement during the growth of epitaxial films.[312] Therefore, the nanometer-scale grains are not expected to significantly impact the resulting polarization.

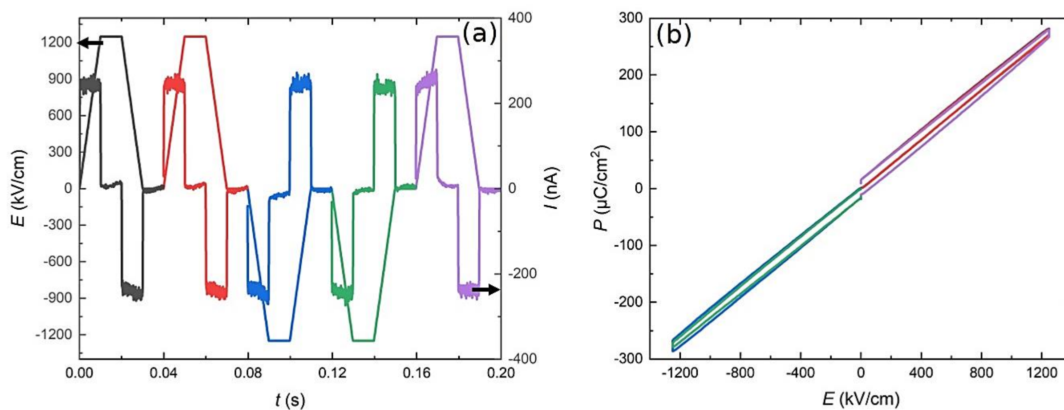

Figure 5.20: (a) PUND measurement of ~200 nm-thick polycrystalline $ErMnO_3$ thin film with frequency of 25 Hz at 77 K. (b) *P*-*E* hysteresis loop is obtained from (a) and the curves with different colors refer to each pulse accordingly.

5.3.2 Piezoelectric response

Time-resolved X-ray diffraction was performed at BESSY II, beamline XPP-KMC3, in collaboration with Dr. Thomas Cornelius from the Institute Matériaux Microélectronique Nanosciences de Provence (Marseille, France) and Dr. Matthias Rössle from HZB/Uni Potsdam. 200 nm-thick polycrystalline $ErMnO_3$ structures were studied. This measurement was performed to investigate the real-time structural changes (lattice parameters) under an electric field during PUND measurements.

Square-shaped W top electrodes with dimensions of a few hundred micrometers were patterned and deposited by photolithography and DC sputtering on top of the $ErMnO_3$ structures, which were deposited on E-beam evaporated Pt coated Si (see device structure in Figure 5.21a). During the experiments, the top electrodes were connected with a tungsten tip, and PUND electric field pulse sequences with a frequency of 2 kHz were applied. The incident X-ray beam was illuminated exclusively onto the contacted electrode. The X-ray diffraction patterns were monitored using a 2D PILATUS pixelated detector.

Figure 5.21a shows the applied PUND pulse sequence as a function of time with the specific times at which X-ray diffraction patterns were recorded shown in colors (see a representative example in Figure 5.21b). During the application of the electric field, the shifts of the Bragg reflections 004 and 112 were used to determine the piezoelectric strain in $ErMnO_3$. The diffraction peaks were fitted using a Pseudo-Voigt function (peak center and peak width were obtained). The peak 112 was deconvoluted with 2 peaks. The strain was calculated from the change in lattice parameters, defined by Equations 5.3 and 5.4.

$$\varepsilon(E) = \frac{a(E)-a(E=0)}{a(E=0)} \qquad \text{Equation 5.3}$$

$$\varepsilon(t) = \frac{a(t)-a(t=0)}{a(t=0)} \qquad \text{Equation 5.4}$$

where ε is the strain, a is the interplanar spacing, E is the applied electric field and t is the delayed time.

The Bragg peak width provides insight into the material disorder, such as strain distribution and domain orientation, which can indicate ferroelectric domain switching during the application of an electric field.[313]

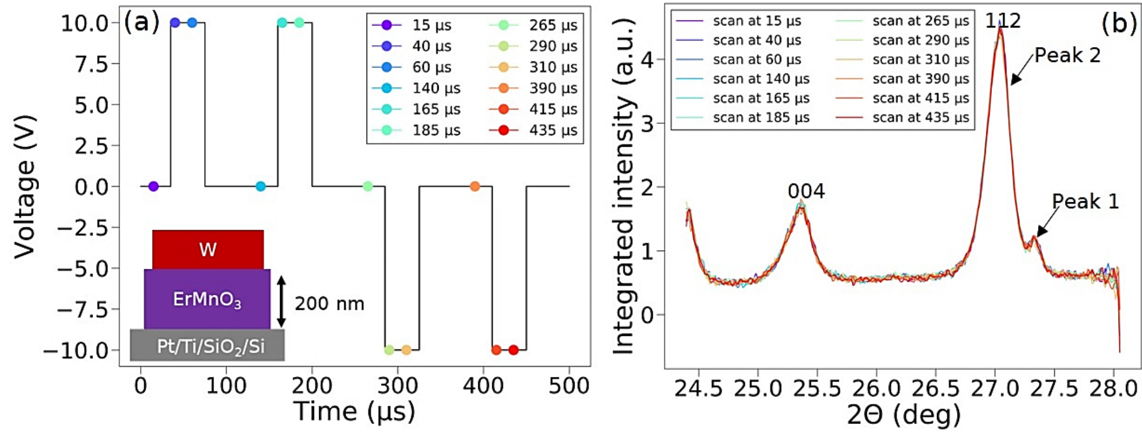

Figure 5.21: (a) Transient of the applied PUND pulse sequence. The dots illustrate the times at which diffraction patterns were recorded to follow the induced strain in the $ErMnO_3$ structures. Schematic of device W/$ErMnO_3$/Pt is shown in an inset. (b) The diffraction patterns recorded at delay times shown in (a) at the applied voltage of 10 V. 004 and 112 Bragg reflections from hexagonal $ErMnO_3$ were studied. Peak 112 can be deconvoluted to be two peaks.

The induced strains measured as a function of voltage using the Bragg peaks 004 and 112 are presented in Figure 5.22a-c. The strain values increase when the applied voltage exceeds 8 V. The strain determined from the 004 peak is about 4 times larger than that from the 112 peaks, suggesting a stronger piezoelectric response along the polarization direction (*c*-axis orientation). However, the strain value is only a few 10^{-4} at the highest applied electric field (500 kV/cm), which is within the resolution limit of the experimental setup. The weak piezoelectric coefficient of $ErMnO_3$, reported to be at the order of 1 pm/V,[314] would result in a strain of 5×10^{-5} for 10 V. Figure 5.22d-f present the peak width (σ) of the 004 and 112 peaks as a function of applied voltage. No significant difference is observed between the peak widths with or without electric field. We could not determine a piezoelectric coefficient from these experiments.

In future experiments, a higher electric field will be applied to ensure that the measured strain does not fall within the resolution limit, thus inducing a higher strain in $ErMnO_3$.

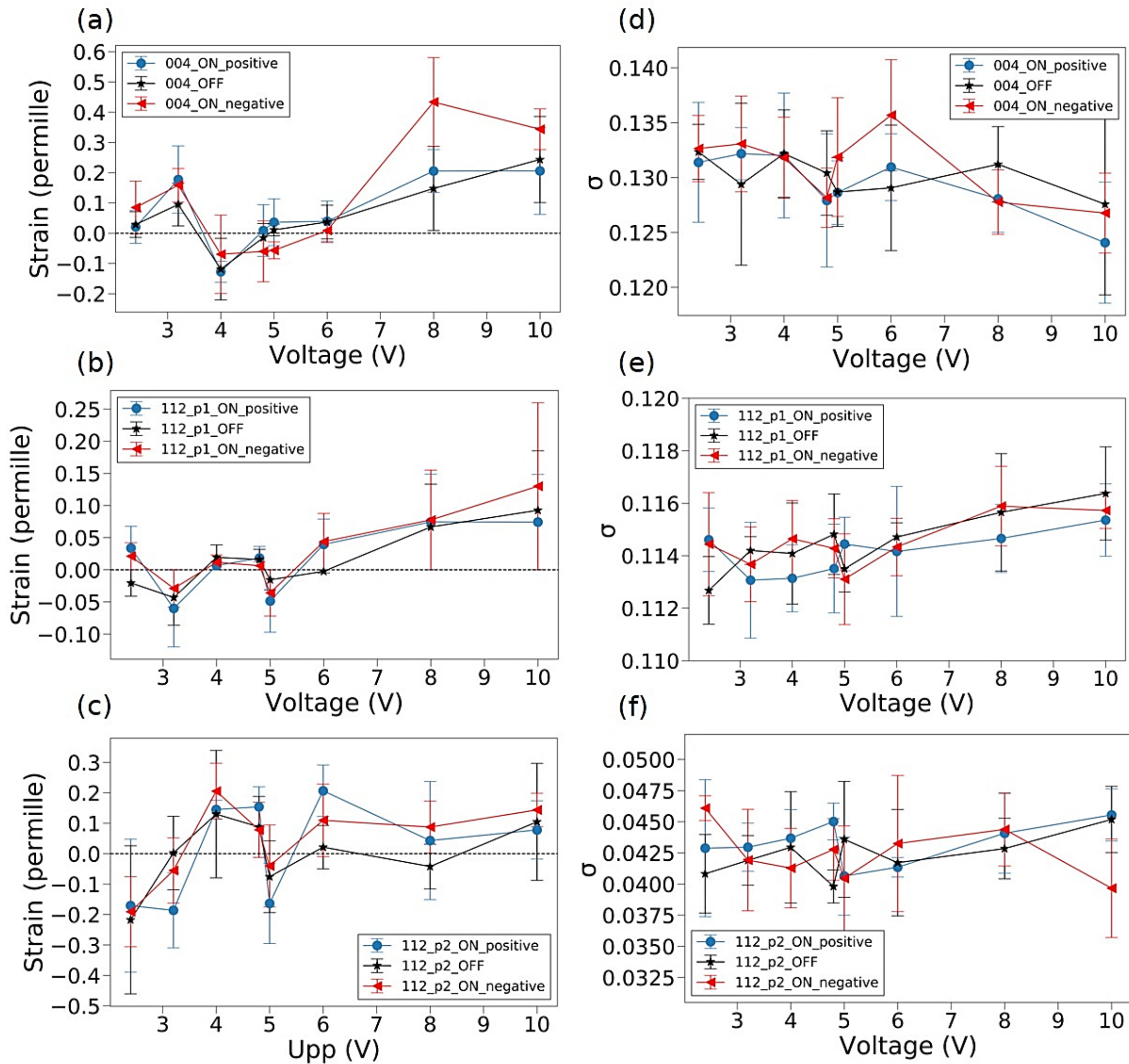

Figure 5.22: (a)-(c) Strain, (d)-(f) σ from fitted diffraction Bragg peaks as a function of the applied voltage for 004 and 112 (deconvoluted to two peaks p1, p2) Bragg peaks.

5.4 Valence change memory (VCM)-type $Pt/ErMnO_3/Ti/Au$ devices

5.4.1 Device fabrication

Figure 5.23a illustrates the $Pt/ErMnO_3/Ti/Au$ device fabrication based on pre-patterned $ErMnO_3$ structures on E-beam evaporated $Si/SiO_2/Ti/Pt$ substrates. To pattern the top metal contacts, a photoresist layer was spin-coated on the annealed $ErMnO_3$ structures and exposed by photolithography. A 20 nm-thick Ti layer and a 50 nm-thick Au capping layer were then deposited using thermal evaporation. Finally, the top electrodes were obtained by lift-off. The device dimensions are of 95×95 μm^2. More details about the growth and characterization of the $ErMnO_3$ structures were shown in Section 5.1 and 5.2.

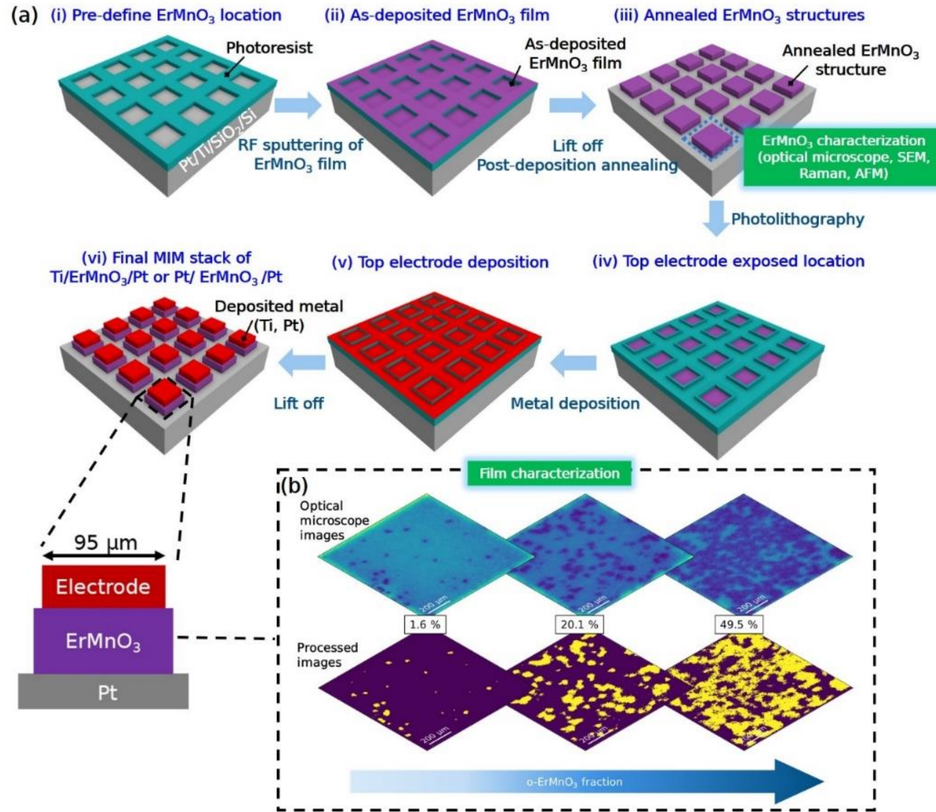

Figure 5.23: Schematics of the device fabrication process and film characterization. (a) Fabrication process flow. (b) Optical microscope images with different fraction of bright/dark regions. Segmentation results of microstructure images regarding bright/dark regions for estimation of fraction of dark region area (o-$ErMnO_3$).

5.4.2 Electrical characterization of Pt/$ErMnO_3$/Ti/Au devices with minor o-$ErMnO_3$ content

5.4.2.1 Filamentary-type resistive switching

The electrical measurements were performed on the metal/$ErMnO_3$/Pt stacks at room temperature by current-voltage (*I-V*) measurements. During the measurement, the Pt bottom electrode was grounded, and a DC bias was applied to the top electrodes. A negative voltage sweep (from 0 to -15 V) with a sweep rate of 75 mV/s was applied to the top electrode, with a series resistor in the circuit, to switch the device from pristine high resistance state (HRS, OFF state) to low resistance state (LRS, ON state). The series resistor was used to prevent the current overshoot and irreversible hard breakdown of the device. This process is called the Set process (for the first cycle, it is the electroforming step). Subsequently, the resistance in LRS was determined by Kelvin (4-wire) resistance measurements which allowed to calibrate the cable and contact parasitic resistance (Section 2.3.7.4). A positive voltage sweep (e.g. from 0 to 1.3 V) with a sweep rate of 15 mV/s was then applied to the top electrode to switch the device from LRS back to HRS. A slower

sweep rate was applied to enhance the dissolution of filaments inside the $ErMnO_3$ matrix during the Reset process. More details will be discussed later in this section.

I-V measurements were performed on Pt/$ErMnO_3$/Ti/Au devices with a majority of h-$ErMnO_3$ (less than 5% o-$ErMnO_3$, Figure 5.24a). Figure 5.24b shows *I-V* curves for 100 cycles. A bipolar resistive switching behavior is observed with Set occurring at negative voltages and Reset occurring at positive voltages. For the initial cycle, a voltage exceeding -10 V is necessary to switch the device from its pristine state to the LRS. Subsequent cycles reveal slightly lower Set voltages, suggesting an electroforming-based resistive switching mechanism. The log-log scale of the *I-V* curves in LRS (for $V > 0$), as presented in Figure 5.24d, demonstrates a current versus voltage slope approximately equal to 1, indicative of ohmic conduction. This behavior is attributed to a metallic filament formed during the Forming and Set processes, which has an ohmic conduction characteristic.[315, 316]

The distribution of Set and Reset voltages over the 100 cycles (Figure 5.25a) shows a relatively large variability in V_{Set} (-2.33 ± 0.49 V) and a low dispersion in V_{Reset} (0.35 ± 0.07 V). Figure 5.25b presents the distribution of R_{OFF} and R_{ON} over 100 sweeps. A high R_{OFF}/R_{ON} up to 10^5 and an ultra-low ON resistance (10.34 ± 1.68 Ω) are achieved.

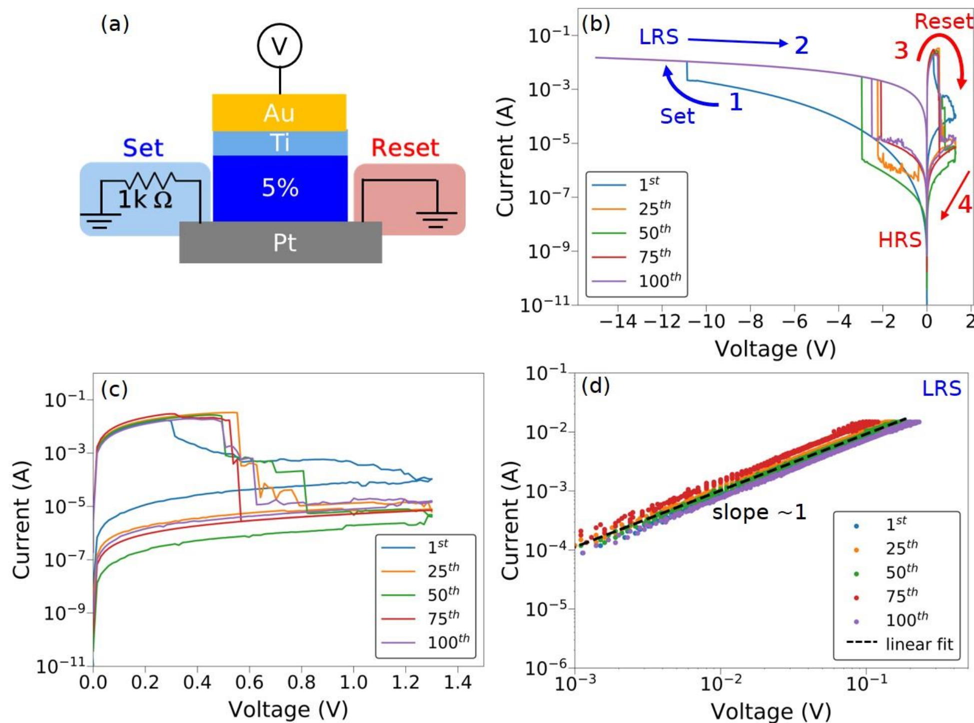

Figure 5.24: *I-V* characteristics of Pt/$ErMnO_3$/Ti/Au stack based on 5% o-$ErMnO_3$. (a) Device architecture and its operational configuration with a 1 kΩ resistor connected as compliance current during Set process. (b) Typical *I-V* curves of the device. (c) *I-V* curves of the Reset process. (d) Log-log scale *I-V* curves in LRS. The contribution of the 1 kΩ resistor has been subtracted. The linear fit (black dotted line) with a slope of 1 indicates ohmic conduction in LRS.

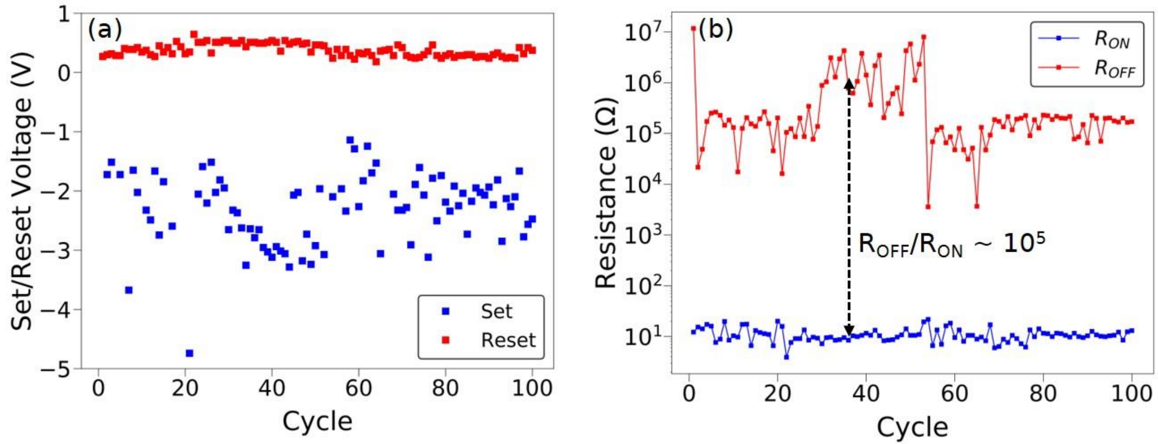

Figure 5.25: (a) Variations of Set, Reset voltages and (b) resistances between OFF and ON states for 100 switching cycles, read at -50 mV. All voltages and resistances have been subtracted the impact of the 1 kΩ resistor.

The ON resistances of the devices are independent of the electrode area, as shown in Figure 5.26, suggesting a localized filamentary rather than interfacial conduction mechanism.[285] Since the forming and Set processes occur with a negative electric field, the formation of the filaments is mostly based on a valence change mechanism involving oxygen vacancies. When a negative electric field is applied, the oxygen vacancies migrate and align to form conductive channels in the $ErMnO_3$ layer, resulting in switching from HRS to LRS. As a positive electric field is applied, filament rupture takes place due to electrochemical re-oxidation and Joule heating, causing the device to switch back from LRS to HRS. The presence of the conductive filament can be in hexagonal phase, orthorhombic phase or the phase boundaries between the two phases.

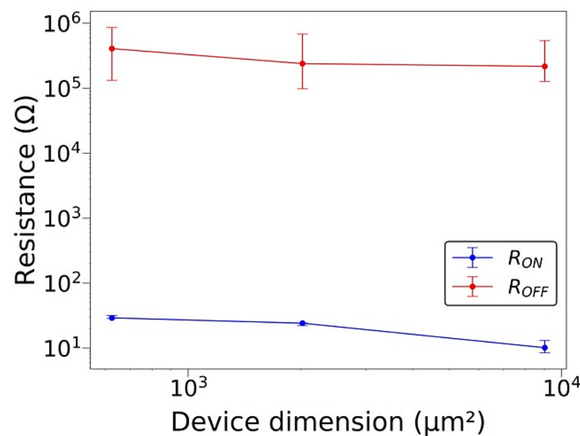

Figure 5.26: Area dependence of the resistances in HRS and LRS, respectively.

Figure 5.27 presents the retention measurement of a device, showing no drift in resistances in HRS and LRS over more than 6×10^3 s.

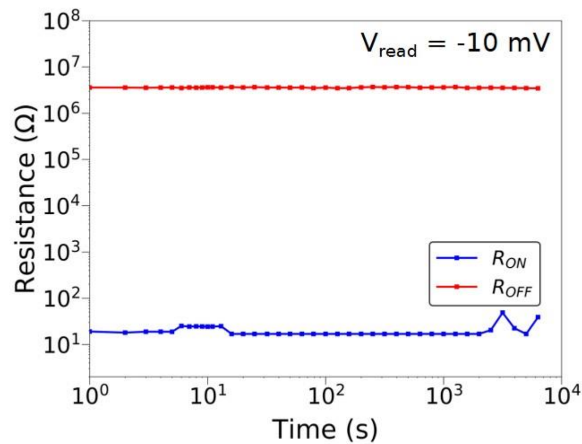

Figure 5.27: Retention measurement for the two resistance states, read at -10 mV at room temperature.

As the ON resistance of devices is ultra-low (~ 10 Ω), the accumulated Joule heating during the Reset process is high enough to dissolve the filament and Reset the device. The morphology of the device top electrodes changes after switching, as shown in the optical microscope images of Figure 5.28a, b. The damage of the top electrode can be attributed to Au dewetting at high temperatures[317] induced by Joule heating during the Reset process. This is supported by the 3D AFM image of the switched device top electrode illustrated in Figure 5.28c. The roughness of the top electrode increases and irregular shaped holes appear. These individual holes could be due to Au dewetting, as reported in ref.[317], which can impact the endurance of the devices.

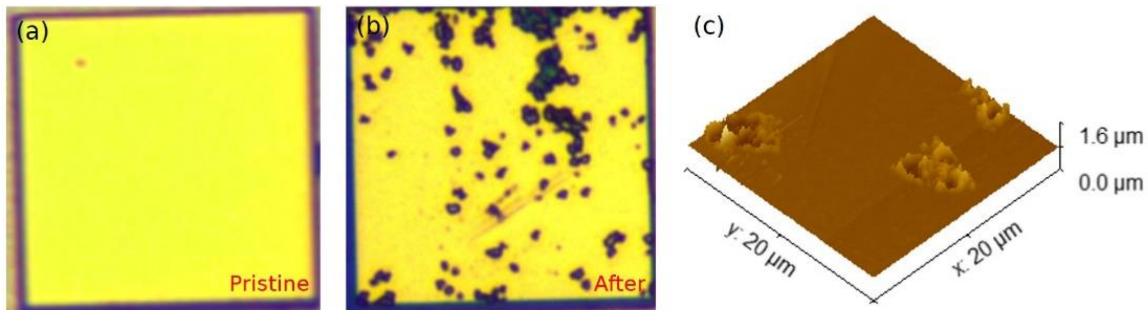

Figure 5.28: (a) Optical microscope image of top electrode (Ti/Au) of pristine device. (b) Optical microscope image and (c) 3D AFM image of top electrode (Ti/Au) after device switching.

5.4.2.2 Impact of compliance current and sweeping voltage window

To establish a real use case for the reconfigurability aspect of the ERMI project (as introduced in Section 1.5), devices can be integrated into a frequency compensation circuit, in which the reconfigurability could change the frequency response. Specifically, the circuit demands a relatively low R_{ON} at the level of 1 Ω. Our objective is to reduce the ON resistance of the devices while ensuring endurance and consistent performance upon cycling.

Resistive switching relies on the formation and rupture of conductive filaments. Increasing the filament expansion through higher compliance currents and voltages during the forming or Set process can lead to a lower R_{ON}.[203, 204] During the forming and Set processes, either a 1 kΩ or 500 Ω resistor was connected in series. This resulted in a compliance current of 15 mA or 30 mA, respectively, when the voltage reached -15 V (maximum compliance current). The corresponding resistive switching performances of the devices are shown in Figure 5.29 and summarized in Table 5.6. With increasing compliance current, R_{OFF} increases, R_{ON} decreases and the endurance becomes poor.

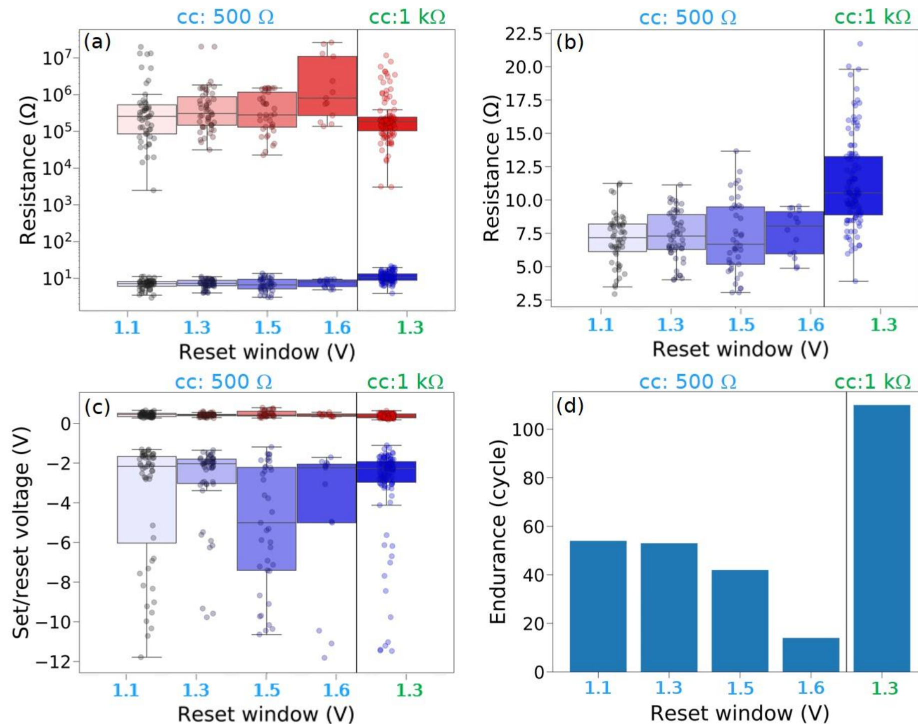

Figure 5.29: Impact of compliance current and Reset voltage window on the resistive switching performance of devices with a majority of h-$ErMnO_3$ (with less than 5% o-$ErMnO_3$). (a) Distribution of resistances in ON and OFF states. (b) Distribution of resistances in ON state. (c) Distribution of Set and Reset voltages. (d) Endurance of devices.

Increasing the Reset voltage window and using a slower sweep speed can enhance the filament dissolution during the Reset process.[203] We studied the impact of different voltage windows (1.1 V, 1.3 V, 1.5 V and

1.6 V) on switching performance. Expanding the voltage window during the Reset process leads to an increase in the R_{OFF} and a decrease in device endurance, while R_{ON} and V_{Reset} remain relatively unaffected. The narrowest distribution of V_{Set} occurs with a Reset voltage window of 1.3 V.

Hence, to achieve a relative low R_{ON}, good endurance, and consistent cycle-to-cycle performance, a compliance current with 1 kΩ and a Reset window of 1.3 V were selected for further investigation.

Table 5.6: Electrical configurations and the resulted resistive switching performance in devices with a majority of h-$ErMnO_3$ (with less than 5% o-$ErMnO_3$). IQR refers to interquartile range.

Reset window (V)	**Compliance current**	**R_{ON} (Ω)**	**R_{OFF} (Ω)**	**V_{Set} (V)**	**V_{Reset} (V)**	**Endurance (cycle)**
1.1	500 Ω	7.18 (IQR: 2.07)	0.26 M (IQR: 0.48 M)	-2.19 (IQR: 4.94)	0.45 (IQR: 0.16)	54
1.3	500 Ω	7.29 (IQR: 2.62)	0.29 M (IQR: 0.70 M)	-2.04 (IQR: 1.22)	0.43 (IQR: 0.07)	53
1.5	500 Ω	6.68 (IQR: 4.31)	0.28 M (IQR: 0.88 M)	-4.51 (IQR: 5.44)	0.44 (IQR: 0.24)	42
1.6	500 Ω	8.04 (IQR: 3.17)	0.99 M (IQR: 8.53 M)	-2.21 (IQR: 2.87)	0.4 (IQR: 0.12)	14
1.3 V	1 kΩ	10.53 (IQR: 4.38)	0.18 M (IQR: 0.14 M)	-2.3 (IQR: 1.02)	0.37 (IQR: 0.2)	110

5.5 Impact of the crystalline phases

As discussed in the previous section (Section 5.2), we have developed a straightforward method to quantify the relative amount of hexagonal and orthorhombic phases, which can contribute to a better understanding of the role of the crystalline phases in resistive switching performance in Pt/$ErMnO_3$/Ti/Au devices. We investigated 5 devices with 20 switching cycles each for 3 groups of devices with different o-$ErMnO_3$ fractions: less than 5%, 20% and 50%.

The setup for the measurement is depicted in the insert of Figure 5.30a. Note that instead of using a 1 kΩ resistor, a compliance current of 15 mA was employed during the forming and Set processes in the devices with 50% o-$ErMnO_3$, due to their large leakage currents.

As the o-$ErMnO_3$ fraction increases, the devices exhibit larger leakage currents, a decrease in Forming voltage, and similar Reset voltages (see Figure 5.30b, c). The large leakage currents are attributed to the fact that o-$ErMnO_3$ contains more Mn^{4+} ions than h-$ErMnO_3$.[114, 278]

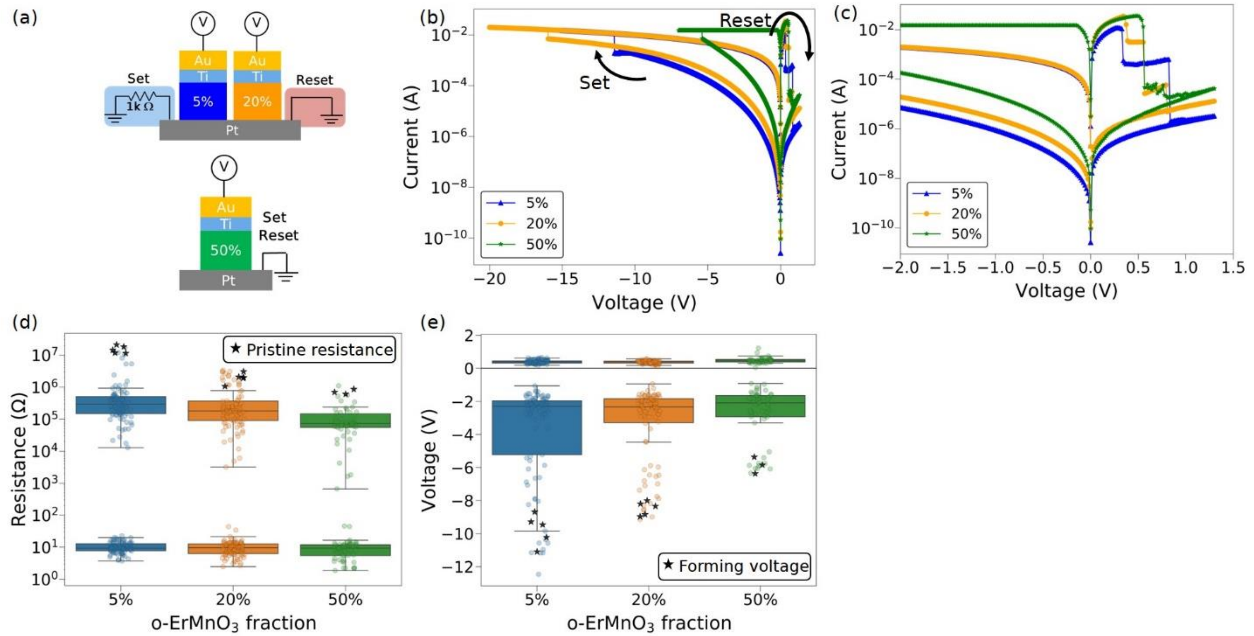

Figure 5.30: Scheme and *I*-*V* characteristics of Pt/$ErMnO_3$/Ti/Au stack based on different fractions of o-$ErMnO_3$ (5%, 20% and 50%). (a) Device architecture and its operational configuration during Set and Reset processes. A 1 kΩ resistor is connected as compliance current during Set process for devices with 5% and 20% o-$ErMnO_3$. (b) Forming *I*-*V* curves of the device with different fractions of o-$ErMnO_3$. (c) Zoom-in of curves shown in (b). (d) The distribution of pristine resistance, HRS, LRS and (e) Forming voltage, Set/Reset voltage at different o-$ErMnO_3$ fractions, respectively. The voltages and resistances have been subtracted the contribution of the 1 kΩ resistor.

To elucidate the different performances with varying fractions of o-phase, we conducted an analysis of the current conduction mechanisms in both pristine and LRS states. We examined log-log scale *I*-*V* curves within the Set region of the devices, and the results are presented in Figure 5.31a.

In the LRS, a current versus voltage slope of ~1 indicates an ohmic conduction behavior ($I \propto V$) in all devices with different o-$ErMnO_3$ fractions. LRS is governed by ohmic conduction due to the metallic filaments formed during the Set process. Conversely, in the pristine state, we investigated two mechanisms commonly observed in this complex oxide, as reported in prior research.[318–320] One of these mechanisms is Schottky emission, wherein thermally activated electrons can overcome the energy barrier and be injected

into the conduction band of the semiconductor.[90] This model allows us to express the current's dependence on applied voltage as:

$$\ln\left(\frac{I}{T^2}\right) = \frac{q\sqrt{q/4\pi\varepsilon_i d}}{kT}\sqrt{V} - \frac{q\phi_B}{kT} \qquad \text{Equation 5.5}$$

where I is the current, V is the external applied voltage, ϕ_B is the Schottky barrier height, ε_i is the permittivity of the switching layer, k is the Boltzmann's constant, T is the absolute temperature, and d is the Schottky distance.

Another mechanism is the Poole-Frenkel. It considers a bulk conduction process where thermally activated electrons are emitted from traps into the conduction band of the semiconductor[90]. This phenomenon can be mathematically described as:

$$\ln\left(\frac{I}{V}\right) = \frac{q\sqrt{q/\pi\varepsilon_i di}}{kT}\sqrt{V} - \frac{q\phi_T}{kT} + \ln\left(q\mu N_c\right) \qquad \text{Equation 5.6}$$

where ϕ_T is the trap energy barrier height, di is the dielectric distance, μ, and N_c are mobility and density of carriers, respectively.

At a low voltage regime ($V < 0.7$ V), a clear linear correlation between ln(I) and $V^{1/2}$ is observed in all devices with varying o-$ErMnO_3$ fractions, which indicates a Schottky conduction mechanism ($R^2 = 0.99$), as illustrated in Figure 5.31b. The values for the intercept and slope can be found in Table 5.7. The calculated ϕ_B values of three different devices, based on the intercepts ($-\frac{q\phi_B}{kT} + 2\ln(T)$), are also provided in Table 5.7, for a room temperature of $T = 298.15\ K$. The decreasing absolute values of the intercept with increasing o-$ErMnO_3$ fraction suggest a reduction in the Schottky barrier height ϕ_B as the o-$ErMnO_3$ fraction increases.

To validate the model, we compare the calculated barrier height $\phi_B = 0.85\ eV$ for the almost pure hexagonal structure (5% o-$ErMnO_3$) with the theoretical value of $\phi_B = 1.08\ eV$ for pure h-$ErMnO_3$, considering a band gap energy $E_g = 1.6$ eV,[88] an electron affinity $\chi = 4.6$ eV,[88] and a Pt work function $\phi_m = 5.12$ eV[91] (Equation 5.7).

$$\emptyset_B = E_g + \chi - \phi_m \qquad \text{Equation 5.7}$$

where E_g represents the band gap energy, χ is the electron affinity of semiconductor, and ϕ_m is the metal work function.

Nevertheless, the band gap energy of orthorhombic $RMnO_3$ decreases slightly compared to that of the hexagonal phase.[69] Therefore, the calculated value for the highest hexagonal fraction is expected to be slightly smaller than the theoretical value for pure h-$ErMnO_3$, which is in good agreement with our results. The experimentally calculated $\emptyset_B$ values decrease as the orthorhombic phase fraction increases, which aligns with the earlier argument. The Schottky slope values, derived from $\frac{q\sqrt{q/4\pi\varepsilon_i d}}{kT}$ remain independent of the o-$ErMnO_3$ fraction. This suggests that the Schottky emission distance d remains constant regardless of the relative o-$ErMnO_3$ content.

At a higher voltage regime (V > 0.7 V), the I-V characteristics of the pristine state in all devices with different o-$ErMnO_3$ fractions closely adhere to the Poole-Frenkel emission model (Equation 5.6, $R^2 = 0.99$), as evidenced in Figure 5.31c. The corresponding extracted intercepts and slopes are presented in Table 5.7.

As established in previous studies,[21, 69, 306] h-$ErMnO_3$ and o-$ErMnO_3$ have been reported as p-type materials. They are characterized by hopping conduction between non-stoichiometric Mn^{3+} and Mn^{4+} ions within the trap states located in grain boundaries or structural defects in $ErMnO_3$. The absolute values of the intercept decrease as the o-$ErMnO_3$ fraction increases (Figure 5.31c). The numerical intercept values are derived from the expression $-\frac{q\phi_T}{kT} + \ln{(q\mu N_c)}$, where the trap energy barriers ϕ_T in h-$ErMnO_3$ and o-$ErMnO_3$ are expected to be similar, given that the mobile carrier source comes from Mn^{4+} associated holes in the valence band in both scenarios.[113, 322] However, due to a higher concentration of Mn^{4+} in o-$ErMnO_3$ compared to h-$ErMnO_3$,[114, 278] there is a higher carrier density N_c, resulting in smaller absolute intercept values as the o-$ErMnO_3$ fraction increases. Additionally, the Poole-Frenkel (PF) slope values, determined from $\frac{q\sqrt{q/\pi\varepsilon_i di}}{kT}$, remain similar with the increase of o-$ErMnO_3$ fraction. This observation implies that the dielectric film thickness remains uniform across all devices, indicating that the o-$ErMnO_3$ phase extends from the bottom electrode to the film surface.

Table 5.7: Conduction mechanism parameters obtained in the pristine state.

Conduction	5% o-$ErMnO_3$	20% o-$ErMnO_3$	50% o-$ErMnO_3$
Schottky intercept	-21.58	-20.22	-19.08
Schottky slope	10.5	9.8	10.1
Schottky barrier	0.85 eV	0.81 eV	0.78 eV
PF intercept	-16.68	-15.59	-14.13
PF slope	3.3	2.8	2.8

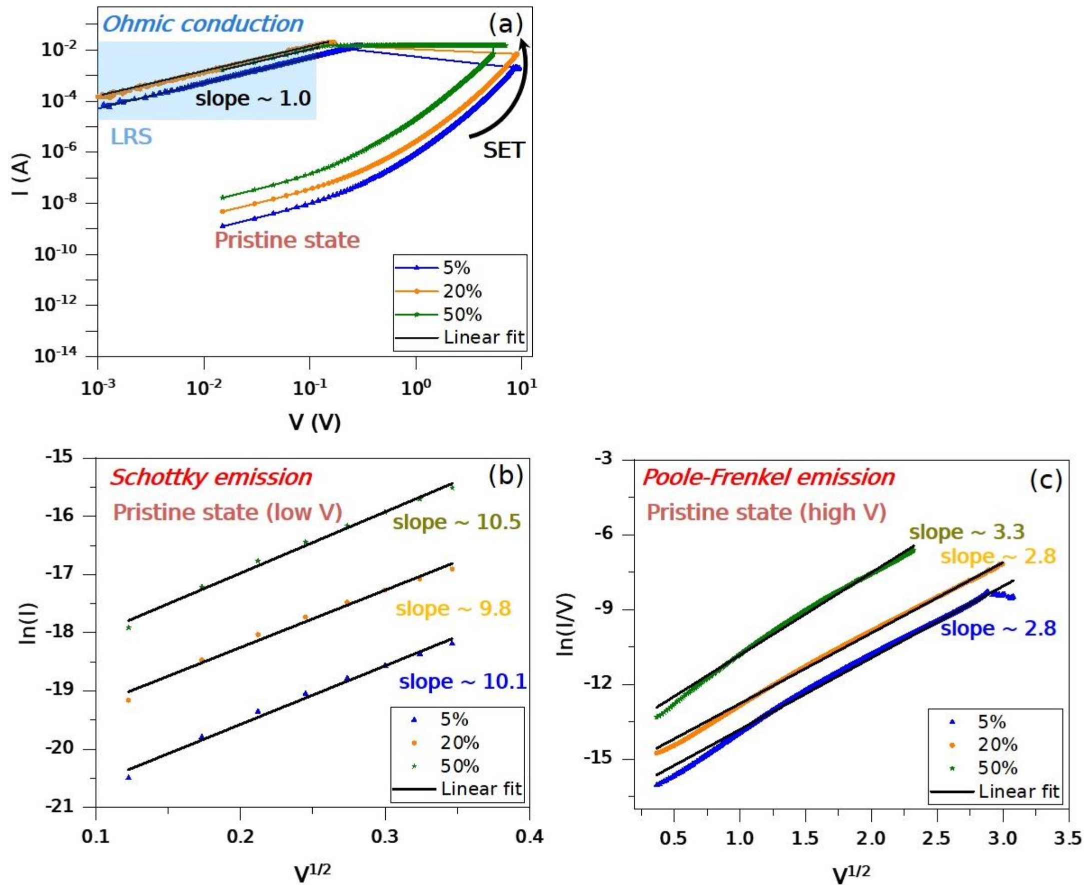

Figure 5.31: (a) Log-log scale *I*-*V* curves for the Pt/$ErMnO_3$/Ti/Au stack based on different fractions of o-$ErMnO_3$ (5%, 20% and 50%) during the forming process, the impact of the 1 kΩ resistor has been subtracted. Linear fit (black lines) reveal LRS for all devices with varying o-$ErMnO_3$ fraction, indicating ohmic conduction. (b) Devices in the pristine states show ln(I)-$V^{1/2}$ plots with linear fit at low electric field regime ($V < 0.7$ V), consistent with the Schottky emission model. (c) Pristine states of devices display ln(I/V)-$V^{1/2}$ plots with linear fit at high electric field regime ($V >$ 0.7 V), suggesting Poole-Frenkel emission model.

To summarize the electrical modeling findings, the LRS demonstrates ohmic conduction behavior, the pristine state exhibits Schottky emission at low electric field and Poole-Frenkel emission at high electric field. An increase in the o-$ErMnO_3$ fraction corresponds to a higher conductivity in both low and high voltage regimes of the pristine state.

The distribution of resistances in pristine, HRS and LRS in devices with varying orthorhombic phase fractions is shown in Figure 5.30d and Table 5.8. The LRS resistances remain relative constant, around 10 Ω. The resistances in pristine and HRS decrease as o-$ErMnO_3$ fraction increases, resulting in a narrower memory window (smaller R_{OFF}/R_{ON}). The resistances in the HRS states of all devices do not fully return to

their initial pristine state values, suggesting that the filament rupture during the Reset process remains incomplete.

Figure 5.30e and Table 5.8 show the variations in Forming, Set, and Reset voltages for all investigated devices. A clear trend emerges where the forming voltage experiences a strong reduction as the fraction of o-$ErMnO_3$ increases. Devices containing 5% o-$ErMnO_3$ exhibit an average forming voltage of ~ -9.5 V, which consistently diminishes to ~ -8.4 V with a 20% o-$ErMnO_3$ fraction, and further decreases to ~ -5.8 V with a 50% o-$ErMnO_3$ fraction.

Table 5.8: Resistive switching performance of Pt/$ErMnO_3$/Ti/Au stack based on different fractions of o-$ErMnO_3$ (5%, 20% and 50%). The voltages and resistances have been subtracted the contribution of the 1 kΩ resistor. IQR refers to interquartile range.

o-$ErMnO_3$ (%)	R_{ON} **(Ω)**	R_{OFF} **(Ω)**	V_{Form} **(V)**	V_{Set} **(V)**	V_{Reset} **(V)**
5	9.31 (IQR: 5.13)	0.29 M (IQR: 0.36 M)	-9.46 (IQR: 0.95)	-2.31 (IQR: 3.30)	0.39 (IQR: 0.13)
20	9.71 (IQR: 6.37)	0.18 M (IQR: 0.28 M)	-8.35 (IQR: 0.63)	-2.40 (IQR: 1.70)	0.39 (IQR: 0.12)
50	9.36 (IQR: 6.46)	0.07 M (IQR: 0.09 M)	-5.82 (IQR: 0.29)	-2.07 (IQR: 1.29)	0.45 (IQR: 0.13)

The resistive switching behavior is influenced by thermal-driven oxygen migration during electroforming and Set operations.[201] It suggests that a higher amount of oxygen vacancies in devices with a higher o-$ErMnO_3$ content facilitate the filament formation. The inclusion of a higher o-$ErMnO_3$ content also induce a higher content of phase boundaries between the hexagonal and orthorhombic phase. Hence, the formation of the conductive filament is more likely to happen in orthorhombic phase or at the boundary between the two phases. The study shown in Chapter 4 highly suggests that the phase boundaries between the two phases are oxygen-deficient. However, this hypothesis would need further validation through additional experiments, such as Atom Probe Tomography (APT) in future.

The V_{Set} variability decreases as o-$ErMnO_3$ fraction increases, as the interquartile range (IQR) is 3.30 for 5%, 1.70 for 20% and 1.29 for 50%. Due to the stochastic nature of the filament formation, in some cases, the Set operating voltages increase and reach V_{Form} values. Therefore, lower V_{Form} values correspond to a

reduced variability in V_{Set} with increasing o-$ErMnO_3$ fraction. Furthermore, the o-$ErMnO_3$ fraction does not significantly affect V_{Reset}. The V_{Reset} variability is relatively low compared to the V_{Set} one. This behavior can be explained by electrochemical re-oxidation and Joule heating during the Reset operation, which facilitate the switching from LRS to HRS. The Joule heating induced by similar LRS resistance values in the devices with varying o-$ErMnO_3$ fractions, promotes the filament rupture at comparable Reset operating voltages.

In conclusion, our study reveals that an increased fraction of the orthorhombic phase reduces the operating voltage (V_{Form} of ~ -5.8 V, V_{Set} of ~ -2.07 for 50% o-$ErMnO_3$) with a moderate reduction of R_{OFF}/R_{ON} ratio, and reduces significantly the V_{Set} variability. The addition of o-$ErMnO_3$ in h-$ErMnO_3$ affect therefore as a good path to improve the device performance.

5.6 Role of top electrodes

Prior studies have reported that defects, such as oxygen vacancies, can be induced in the oxide switching layer due to the oxygen gettering activity of the Ti electrode.[198, 323, 324] These defects at the interface region facilitate the forming process. To investigate this aspect, Pt/$ErMnO_3$/Pt stacks were characterized and compared to Pt/$ErMnO_3$/Ti/Au ones (Figure 5.32).

For both cases, devices containing 5% o-$ErMnO_3$ were selected. In general, the resistances in pristine state of Ti top electrode devices were found to be larger than those with Pt top electrodes (Figure 5.32a). This can be attributed to the higher Ti/$ErMnO_3$ Schottky barrier height compared to the Pt/$ErMnO_3$ one (Figure 5.33). HRS and LRS display no significant resistance changes, as seen in Figure 5.32a.

Figure 5.32b presents the distribution of Set/Reset voltage for both stacks. There is a minimal impact of the top electrode type on the Forming voltages, indicating that the switching does not occur at the interface but rather within the $ErMnO_3$ layer. However, a larger variation in both Set and Reset voltages was observed for Pt top electrode. To explain this observation, we propose the following hypothesis: Under an electric field, conductive filaments based on oxygen vacancies form. Consequently, both Pt/$ErMnO_3$/Pt and Pt/$ErMnO_3$/Ti/Au stacks can switch from HRS to LRS. However, during the Reset process, Pt cannot work as a reservoir or source for oxygen ions, resulting in difficult and uncompleted recovery of oxygen vacancies. Thus, greater Joule heating energy is required to switch the device back to HRS, leading to a higher V_{Reset} for Pt/$ErMnO_3$/Pt stacks. Additionally, the Pt/$ErMnO_3$/Pt stack with symmetric electrode configuration does not have a preferential switching polarity, which increases the variability in operating voltages and limits the switching yield.[323] The Pt/$ErMnO_3$/Pt stack devices have a very poor endurance (less than 20 cycles).

These results demonstrate that the top electrodes play a crucial role in the resistive switching performance in $ErMnO_3$-based stacks.

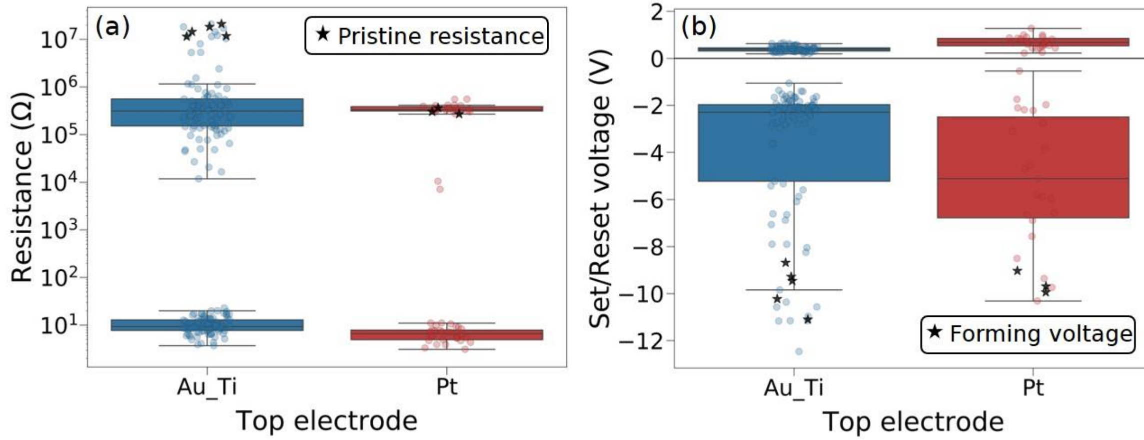

Figure 5.32: Resistive switching performance of Pt/$ErMnO_3$/Ti/Au stack and Pt/$ErMnO_3$/Pt stack with 5% o-$ErMnO_3$. (a) The distribution of resistances in pristine, HRS, LRS and (b) Forming, Set/Reset voltages, for various top electrodes including Ti and Pt. The voltages and resistances have been subtracted the impact of the 1 kΩ resistor.

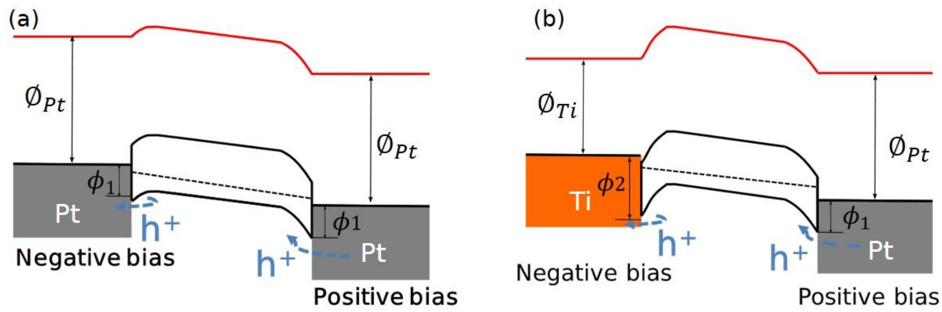

Figure 5.33: Energy band diagram of (a) Pt/o-$ErMnO_3$/Pt stack and (b) Ti/o-$ErMnO_3$/Pt stack, respectively.

5.7 Summary

- Polycrystalline $ErMnO_3$ thin films with different fraction of hexagonal and orthorhombic phases were synthesized. The presence of the orthorhombic phase was evidenced using a set of correlative microscopies (optical, SEM, c-AFM) and Raman spectroscopy. We developed an easy and straightforward way to quantitively estimate the fraction of the two crystalline phases using optical microscopy or SEM.

- Bipolar resistive switching behavior was demonstrated for the first time in $ErMnO_3$-based devices. Pt/$ErMnO_3$/Ti/Au devices with a low amount of o-$ErMnO_3$ (< 5%) exhibit a remarkable R_{OFF}/R_{ON} ratio of ~10^5, an ultra-low resistance of only 10 Ω in the low resistance state (R_{ON}), and a good retention for ~10^4 s.

- The underlying mechanism of resistive switching in Pt/$ErMnO_3$/Ti/Au devices has been attributed to the dynamic formation and rupture of conductive filament(s) based on oxygen vacancies. The presence of the filament is more likely to be in the orthorhombic phase or at the boundary between the orthorhombic and hexagonal phases.

- An increased fraction of the orthorhombic phase significantly reduces the operating voltage in Pt/$ErMnO_3$/Ti/Au devices. V_{Form} decreases from ~ -9.5 V for 5% o-$ErMnO_3$ to ~ -5.8 V for 50% o-$ErMnO_3$, V_{Set} decreases from ~ -2.31 V (IQR: 3.30 V) for 5% o-$ErMnO_3$ to ~ -2.07 V (IQR: 1.29 V) for 50% o-$ErMnO_3$.
- This finding provides important insights for engineering the $ErMnO_3$ switching layer for enhanced performance.

- The selection of top electrodes is crucial to obtain better resistive switching performance. The Pt/$ErMnO_3$/Pt stack devices have a very poor endurance (less than 20 cycles).

Chapter 6: $ErMnO_3$ thin film-based threshold switching devices

6 $ErMnO_3$ thin film-based threshold switching devices........166

6.1 Device fabrication and sample information........168

6.2 Threshold switching in Pt/$ErMnO_3$/Pt devices........176

6.2.1 Effect of the second thermal annealing on resistive switching........176

6.2.2 Volatile threshold switching characterization........176

6.2.3 Physical model of the threshold switching in Pt/$ErMnO_3$/Pt devices........179

6.2.4 On the roles of the orthorhombic and hexagonal phases........185

6.3 Applications (implementation of the NDR devices into circuits)........188

6.3.1 Reconfigurability between resistive and inductive states........188

6.3.2 NDR devices as artificial neurons........190

6.4 Summary........192

The exploration of volatile threshold switching behavior holds significant promise for various applications, particularly in neuromorphic computing. It can be used as a scalable selector device in resistive random access memory (RRAM) crossbar circuits.[325, 326] Additionally, threshold switching devices with self-sustained oscillations are promising candidates for building leaky integrate-and-fire (LIF) spiking neurons,[12, 327, 328] for applications in threshold logic, [208] and tunable chaotic oscillators.[329, 330] Threshold switching has been reported in several material systems, such as metal oxides (e.g. NbO_x,[208–214] VO_2,[215] TiO_2,[216] TaO_x,[217] $PrMnO_3$,[218] MoO_3[331]), chalcogenide glasses (e.g. GeTe[326]) and fast-diffusion metals (e.g. Ag[207, 332]). Previous studies have shown that most metal-oxide-based threshold switches with S-type negative differential resistance (NDR) can be explained by self-heating triggered mechanisms,[210, 212, 216–221] with mainly two localized conduction paths, either filamentary (e.g. NbO_x) or from a metal phase that has formed upon an insulator to metal phase transition (IMT) (e.g. VO_2). The self-heating triggered devices reported in the literature typically need to be electroformed to obtain a small-diameter conductive filament.[225] However, it is challenging to know and control the size, composition and location of the filament formed in the switching layer, and therefore to comprehend the material parameters that can be tuned to optimize the device performance. As a result, the devices exhibit variability in threshold voltages, endurance limitations and reliability issues. As the Joule effect plays a fundamental role in the occurrence of NDR,[333] an interesting design would be one in which the conduction, and the heat conducting paths could be locally controlled.

In this spirit, we propose to use $ErMnO_3$ thin films with both hexagonal and orthorhombic phases, to investigate threshold switching devices. The stable phase of $ErMnO_3$ at room temperature and atmospheric pressure is the hexagonal phase.[64] As we have discussed it in Chapter 5, the orthorhombic phase can be stabilized by stress imparted by the substrates. At room temperature, the orthorhombic phase is not ferroelectric and shows p-type conductivity.[278] In accordance with literature,[266] we have shown in Chapter 5 that in conductive atomic force microscopy experiment, h-$ErMnO_3$ does not show conduction while o-$ErMnO_3$ does.

Using the combination of the two crystalline phases, we show the first demonstration of electroforming-free threshold switching behavior in Pt/$ErMnO_3$/Pt memory devices. The chapter is organized as follows: We present in Section 6.1 the device fabrication and sample information. In Section 6.2, we explore the volatile threshold switching behavior in Pt/$ErMnO_3$/Pt devices and propose a physical model of threshold switching to address the underlying physical mechanism. Additionally, we investigate the roles of orthorhombic and hexagonal phases on triggering the threshold switching. We show the premilitary results of the spiking neuron applications in Section 6.3. Lastly, we summarize our results in Section 6.4.

6.1 Device fabrication and sample information

The $ErMnO_3$ films were deposited by RF sputtering at room temperature in Ar with a RF power of 200 W and an Ar pressure of 10 µbar (Figure 6.1a). We used $Si/SiO_2/TiO_2/(111)$ Pt substrates from MTI Corporation. The thickness of the as-deposited films was determined by spectroscopic ellipsometry (~ 58 nm). A first post-deposition annealing step at 750 °C for 30 min in a furnace with a N_2 atmosphere was done to crystalize the films (Figure 6.1b). This was followed by a second thermal annealing of the polycrystalline films in a furnace at 400 °C in air for 1 hour (Figure 6.1c).

$Pt/ErMnO_3/Pt$ stacks were fabricated by patterning top electrodes using photolithography, metal deposition and lift-off. 50 nm-thick Pt top electrodes were deposited by sputtering, as shown in Figure 6.1d, e. The capacitive structure areas (defined by the top electrode) were 20 × 20 µm^2 or 30 × 30 µm^2. Two types of devices were prepared with polycrystalline $ErMnO_3$ films annealed twice (first at 750 °C in N_2 and then at 400 °C in air, as described above, Figure 6.1d) or with $ErMnO_3$ films annealed only once, at 750 °C in N_2 (Figure 6.1e). The sample information is listed in Table 6.1.

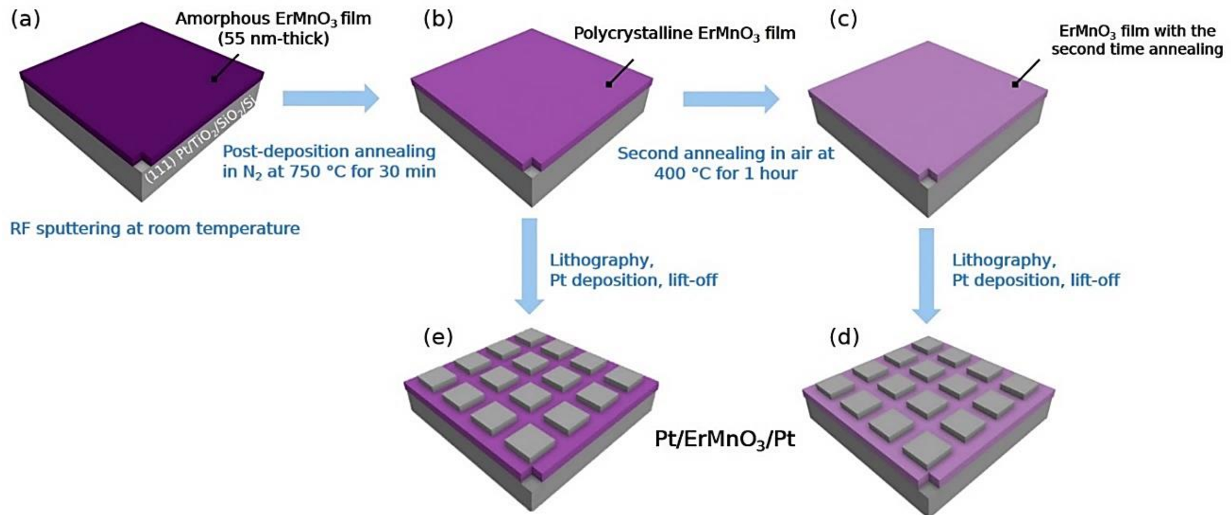

Figure 6.1: Schematics of the device fabrication process flow.

As discussed in Chapter 5, the annealing at 750 ºC of as-grown amorphous $ErMnO_3$ films leads to the crystallization of a mixture of h- and o-$ErMnO_3$ phases. $Pt/ErMnO_3/Pt$ stacks with different h-/o-$ErMnO_3$ ratios were investigated. All films were characterized before the second annealing in air. The orthorhombic phase was quantified by analyzing the SEM images (Figure 6.2), with the quantification method developed in Chapters 4 and 5.

Table 6.1: Sample information of the devices.

Sample	**Film**	**o-$ErMnO_3$ fraction (%)**	**Annealing**	**Switching type**
For devices under study	Mixed phases	~ 20	750 ºC (N_2)	Resistive switching
			750 ºC (N_2) + 400 ºC (air)	Threshold switching
Reference 1	Mainly h-phase	~ 1	750 ºC (N_2) + 400 ºC (air)	Resistive switching
Reference 2	Mainly o-phase	~ 75	750 ºC (N_2)	Threshold switching
Reference 3	Mainly o-phase	~ 99	750 ºC (N_2), 750 ºC (N_2) + 400 ºC (air)	(For XPS)

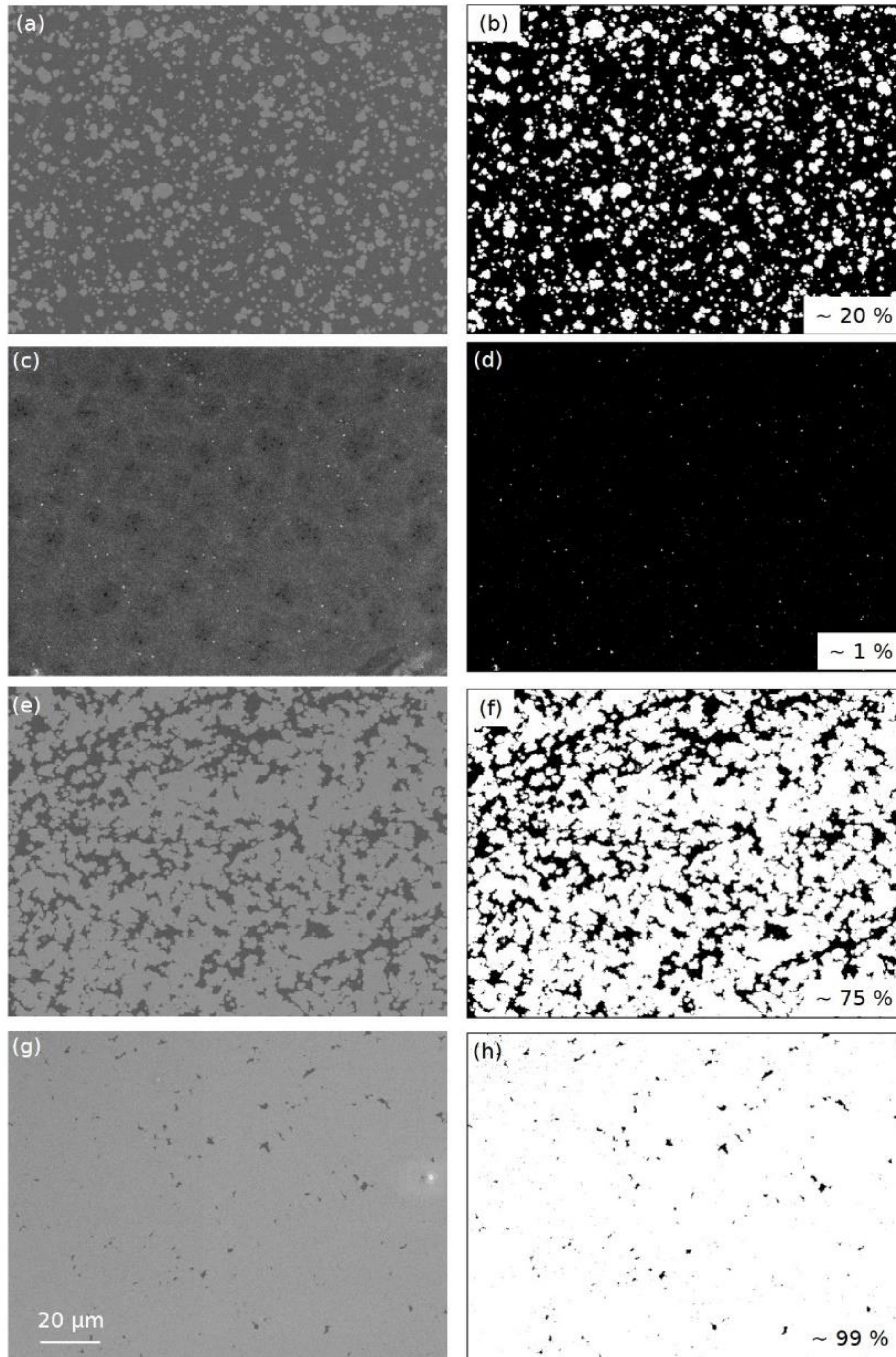

Figure 6.2: (a, c, e, g) SEM images of films with mixed phases (test), mainly h- o-$ErMnO_3$ (reference 1) and o-$ErMnO_3$ (reference 2 and 3). (b, d, f, h) Segmentation results of SEM images regarding high/low electron yield regions for estimation of fraction of o-$ErMnO_3$.

Figure 6.3 shows GIXRD patterns and Raman spectra of films annealed at 750 ºC (N_2, 30 min) with mainly h-$ErMnO_3$ (reference 1) or o-$ErMnO_3$ (reference 3). The Raman spectra are fitted with Raman modes. The spectral positions are compared to those of single crystals in Table 6.2.

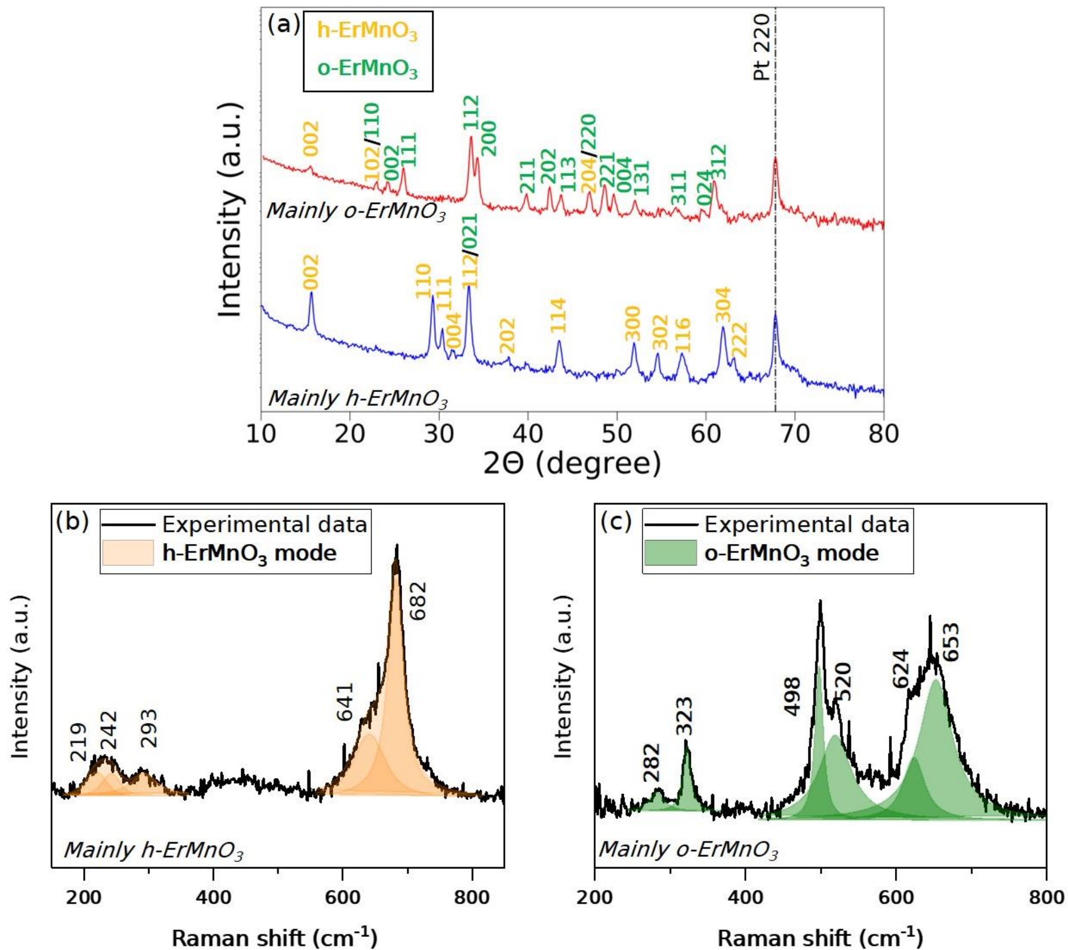

Figure 6.3: (a) GIXRD patterns and (b, c) Raman spectroscopy spectra of mainly h- and o-$ErMnO_3$ polycrystalline films (without the second annealing in air).

Figure 6.4 shows GIXRD patterns of the film with mixed phases (~20% o-$ErMnO_3$) before and after the second annealing. There are no significant differences observed.

We further characterized the film (~20% o-$ErMnO_3$) after the first anneal at 750 °C. Optical microscopy reveals regions of bright and dark contrasts (see Figure 6.5a). These regions were further investigated by Raman spectroscopy. Mapping was performed within the area marked with the black box in Figure 6.5a, which includes both bright and dark contrast regions. The Raman intensity map was recorded on the $A_1(TO_9)$ mode, which is unique for the hexagonal phase (see Figure 6.5b). Two distinct regions colored in blue and red are observed. Figure 6.5c shows two representative Raman spectra from these regions (marked as A and B in Figure 6.5a, b), and the indexed Raman modes are shown in Table 6.3. As discussed in Chapter 5,

the dark regions in optical microscopy correspond to o-$ErMnO_3$ and bright regions to h-$ErMnO_3$. c-AFM mapping was performed in the area shown by the yellow box in Figure 6.5a. An enhanced conductivity for o-$ErMnO_3$ is observed while h-$ErMnO_3$ is non-conducting (Figure 6.5d). The corresponding topographic image, shown in Figure 6.5e, indicates that there is no significant surface morphology difference between the two crystalline phases.

Table 6.2: Raman active modes in single crystals and in polycrystalline films. The experimental data is shown in Figure 6.3.

Single crystal h-$ErMnO_3$[145]	**Single crystal o-$ErMnO_3$[309]**	**Mainly h-$ErMnO_3$ [This work]**	**Mainly o-$ErMnO_3$ [This work]**
E_2(5) 218	B_{1g} 280	E_2(5) 219	B_{1g} 282
A_1(3) 252	A_g 316	A_1(3) 242	A_g 323
E_2(8) 295	A_g 490	E_2(8) 293	A_g 498
E_1(TO_{14}) 639	A_g 520	E_1(TO_{14}) 641	A_g 520
A_1(TO_9) 683	B_{1g} 610	A_1(TO_9) 682	B_{1g} 624
	653[a)]		653[a)]

a) Raman shift is not related to a proper vibration mode from o-$ErMnO_3$[309] it might be from defects[277] or contributions from zone-boundary phonon[276].

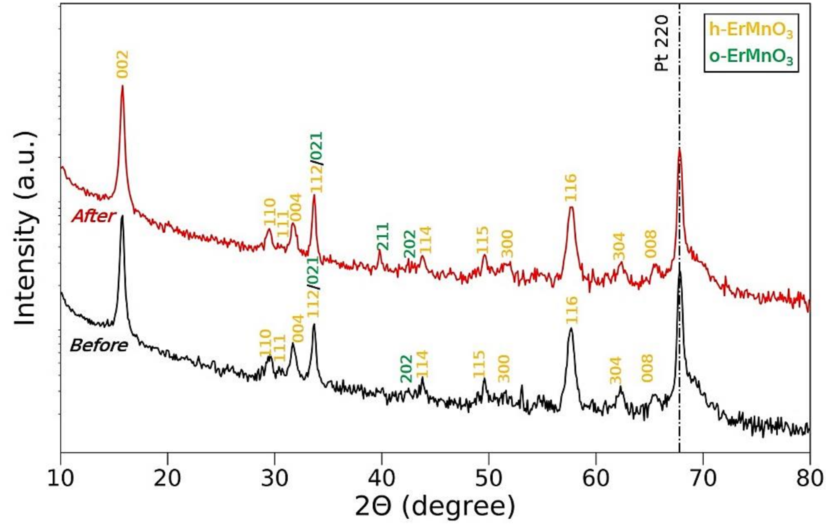

Figure 6.4: GIXRD patterns of films with mixed $ErMnO_3$ before and after the second annealing.

Table 6.3: Raman active modes in single crystals and polycrystalline films. The experimental data is shown in Figure 6.5.

Single crystal h-ErMnO$_3$[145]	**Single crystal o-ErMnO$_3$** [309]	**Spectrum A [This work]**	**Spectrum B [This work]**
E_2(5) 218	A_g 316	E_2(5) 235	A_g 325
E_2(8) 295	A_g 490	E_2(8) 307	A_g 498
A_1(TO_9) 468	A_g 520	E1 457	A_g 516
E_1(TO_{14}) 639	B_{1g} 610	A_g 521	B_{1g} 614
A_1(TO_9) 683	653[a)]	E_1(TO_{14}) 641	651[a)]
		A_1(TO_9) 689	

a) Raman shift is not related to a proper vibration mode from o-$ErMnO_3$[309] it might be from defects[277] or contributions from zone-boundary phonon[276].

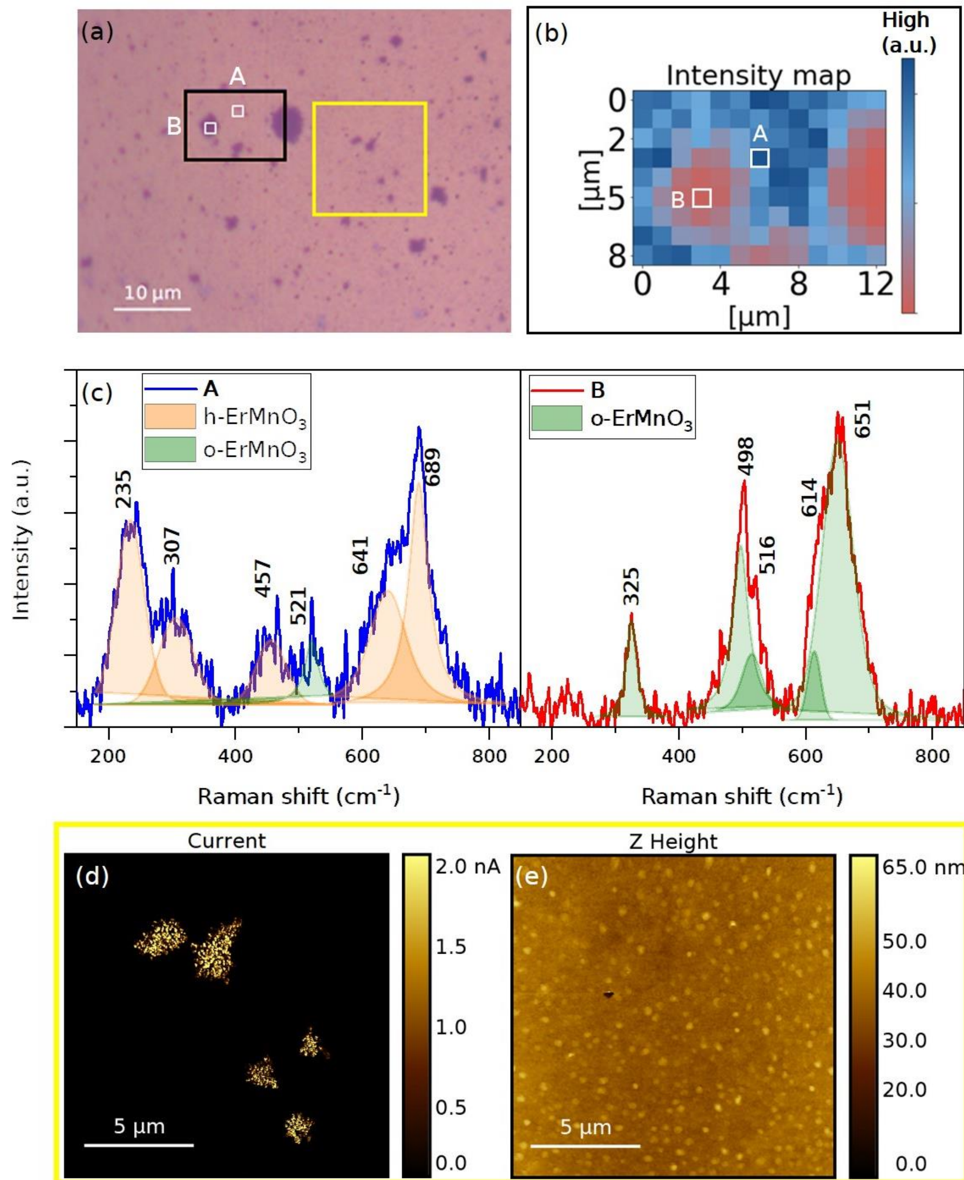

Figure 6.5: (a) Optical microscopy image of polycrystalline $ErMnO_3$ film (20% o-$ErMnO_3$, without second time annealing). (b) Raman intensity map based on the mode $A_1(TO_9)$ at 689 cm^{-1} from h-$ErMnO_3$ spectrum, which is mapped on the $ErMnO_3$ film within the black box marked in the optical image in (a). Raman spectroscopy mapping with a scan size of 9 ×13 μm^2, beam size of 1 µm and spatial resolution of ~1 µm was performed. (c) Two Raman spectra with their fitted Raman modes representing positions A and B indicated on the Raman intensity map. (d) and (e) c-AFM current and topographic images mapped on $ErMnO_3$ film within the yellow box marked in the optical microscopy image in (a). The tip was grounded and a sample bias of 0.5 V was applied.

After the second annealing (400 °C in air), no significant differences in terms of h-$ErMnO_3$/o-$ErMnO_3$ crystalline phase proportion or surface morphology are observed. This is indicated by the X-ray diffraction (Figure 6.4), SEM, Raman spectroscopy, and AFM studies conducted at the same locations on the film

before and after the second annealing (Figure 6.6). However, an enhanced electrical conductivity in o-$ErMnO_3$ is observed by c-AFM after the second annealing, which will be discussed later in the chapter.

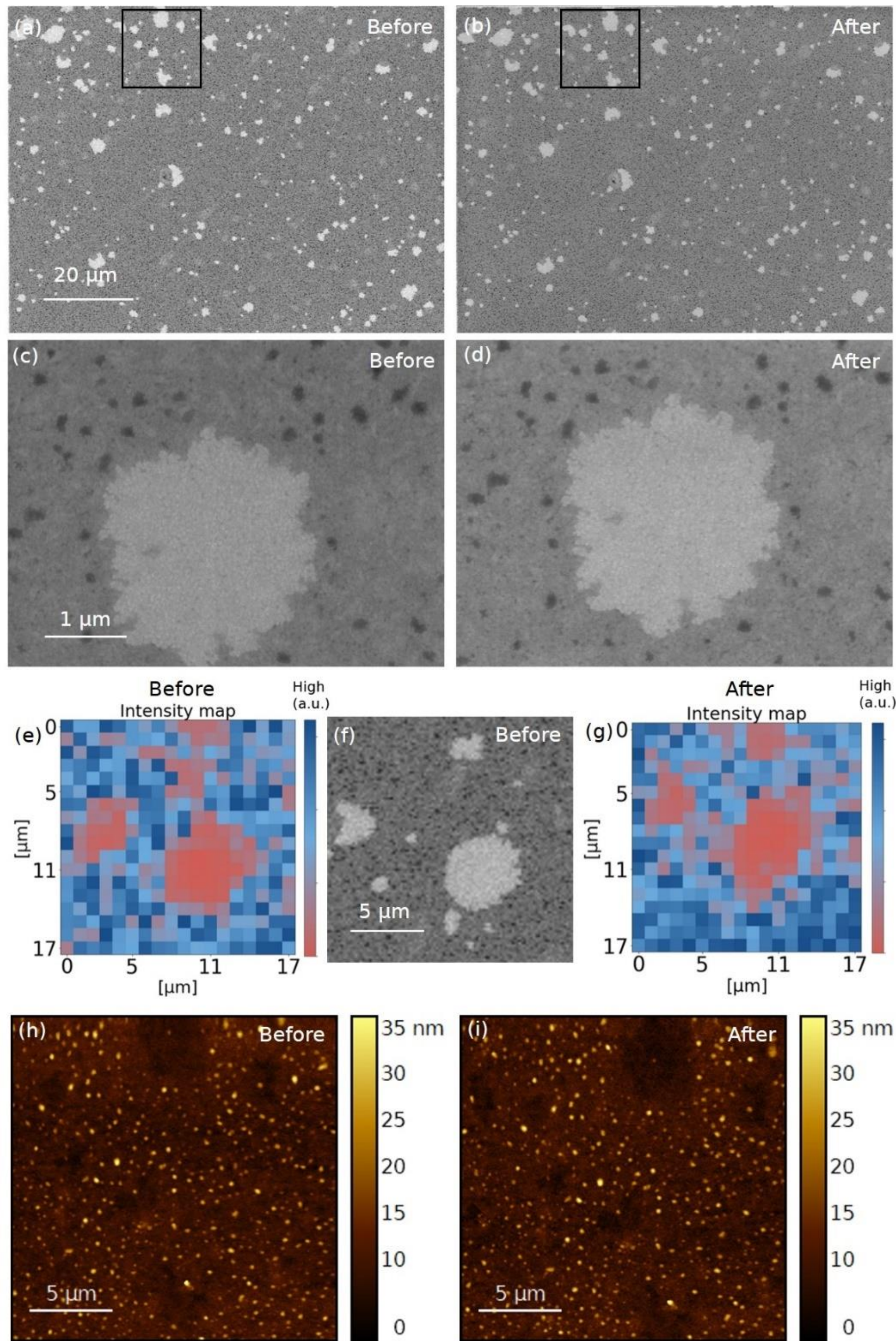

Figure 6.6: SEM images of the film (~20% o-$ErMnO_3$) for (a, c, f) before and (b, d) after the second annealing. (e) and (g) Raman spectroscopy intensity maps based on the mode $A_1(TO_9)$ at 689 cm^{-1} from h-$ErMnO_3$ spectrum, mapped on the film in (f), before and after the second annealing, respectively. Raman spectroscopy mapping with a scan size of 18 ×18 μm^2, a beam size of 1 µm and a spatial resolution of ~1 µm was performed. (h) and (i) AFM topographic images mapped on the film in (a) and (b) before and after the second annealing, respectively.

6.2 Threshold switching in Pt/$ErMnO_3$/Pt devices

6.2.1 Effect of the second thermal annealing on resistive switching

Current-voltage (*I-V*) measurements were performed on the Pt/$ErMnO_3$/Pt stacks at room temperature. The $ErMnO_3$ films have ~20% o-$ErMnO_3$ (Table 6.1). The Pt bottom electrode was grounded and a DC bias was applied to the Pt top electrode. Typical *I-V* characteristics are presented in Figure 6.7 for both types of devices (without and with the second annealing in air). Two very different resistive switching behaviors are observed. The device shown in Figure 6.7a (annealed once, at 750 ºC) exhibits a non-volatile bipolar resistive switching. It switches from pristine high resistance state (HRS) to a low resistance state (LRS) under a negative bias and back to HRS while sweeping the voltage to positive bias. All devices measured prior to the second annealing exhibit a similar response, indicative of a filamentary-based switching mechanism (abrupt Set and Reset). In contrast, all devices that have undergone a subsequent 1-hour annealing at 400 ºC under air exhibit a volatile threshold resistive switching behavior, as shown in Figure 6.7b. The device switches abruptly from pristine HRS to LRS under both positive and negative biases (0→ ± 5 V) and switches back abruptly to HRS once the voltage is swept back below a certain value. To the best of our knowledge, this is the first demonstration of volatile threshold switching behavior in $ErMnO_3$-based two-terminal devices.

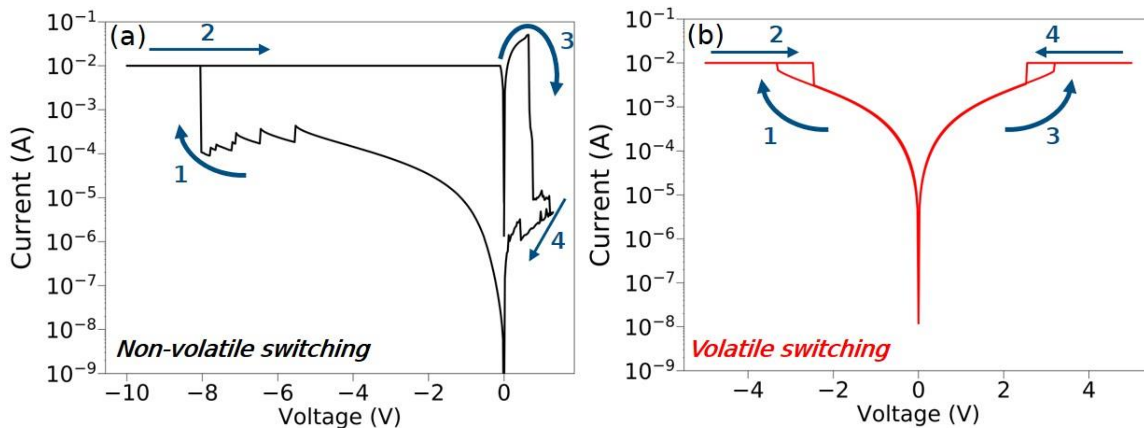

Figure 6.7: (a) and (b) *I-V* characteristics of devices based on $ErMnO_3$ without or with the second annealing in air, showing non-volatile switching behaviors and symmetric volatile switching, respectively.

In the following, we explore the devices with this unique threshold switching behaviors.

6.2.2 Volatile threshold switching characterization

Figure 6.8a shows representative *I-V* characteristic after 1000 voltage sweeps. A compliance current of 10 mA was used to avoid irreversible device breakdown. As the voltage sweeps from 0 to -5 V, the current exhibits an exponential increase at low electric field. At a threshold voltage V_{TH}, the current rises abruptly,

corresponding to a switch from HRS to LRS and hits the current compliance. When the voltage sweeps from -5 V back to 0, the device switches back to its initial HRS once the voltage drops below a certain voltage, referred to as the holding voltage V_{HO}. This behavior indicates a volatile threshold switching. Given that the Pt/$ErMnO_3$/Pt stack is symmetric, a similar switching behavior is observed in positive polarity (0 → 5 V → 0). The behavior observed in the first cycle is similar to that of subsequent cycles, indicating an electroforming-free threshold switching in both polarities.

The evolution of the threshold voltages V_{TH} and holding voltages V_{HO} over 1000 cycles is presented in Figure 6.8b. Positive values increase while negative values decrease until reaching constant values. The memory window of ~ 0.7 V (difference between V_{TH} and V_{HO}) is about constant.

In addition, the devices achieve an endurance larger than 10^4 cycles as shown in Figure 6.9.

In the following, devices are further examined under negative voltage polarity (similar results were obtained in both negative and positive polarities). The impact of the compliance current value on the threshold switching performance is investigated. *I-V* characteristics are shown in Figure 6.8c. With an increase of the compliance current, there is no change in V_{TH}, but there is an increase of V_{HO}, as illustrated in Figure 6.8d. Increasing the compliance current allows to expand the hysteresis window.

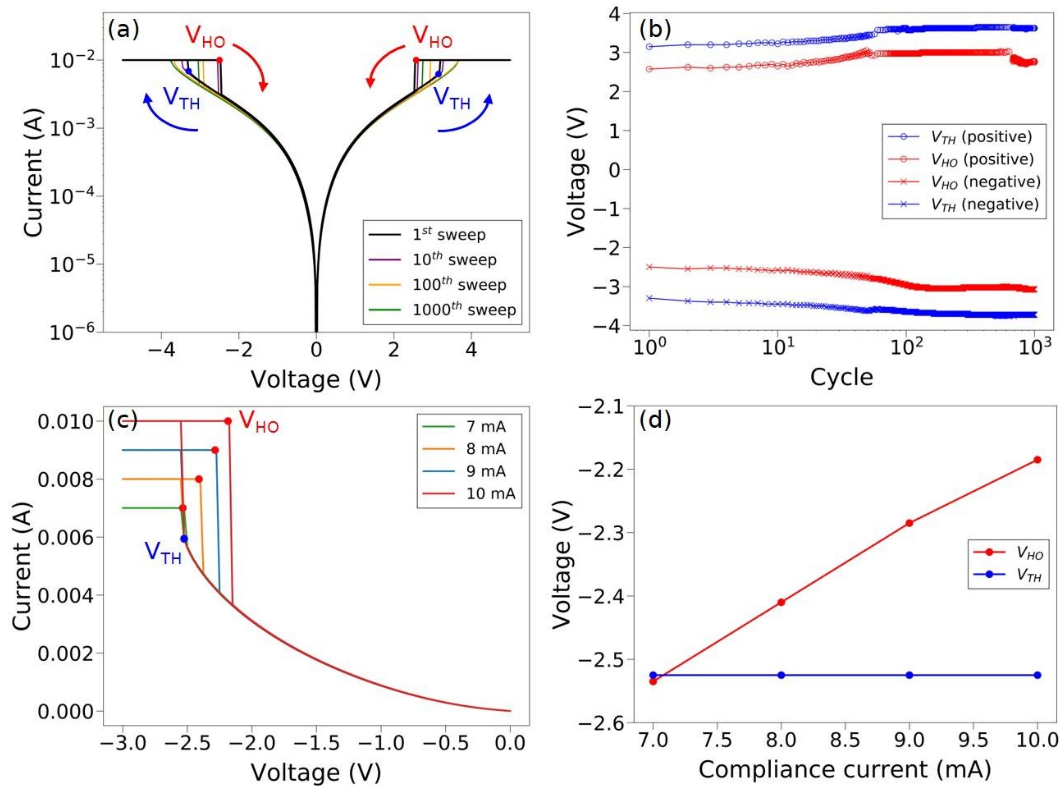

Figure 6.8: (a) *I-V* characteristic of Pt/EMO/Pt device, marked with threshold voltage (V_{TH}) and holding voltage (V_{HO}). (b) The distribution of threshold and holding voltages for 1000 cycles. (c) *I-V* characteristics with different compliance current 7, 8, 9, 10 mA. (d) Threshold and hold voltages with different compliance currents.

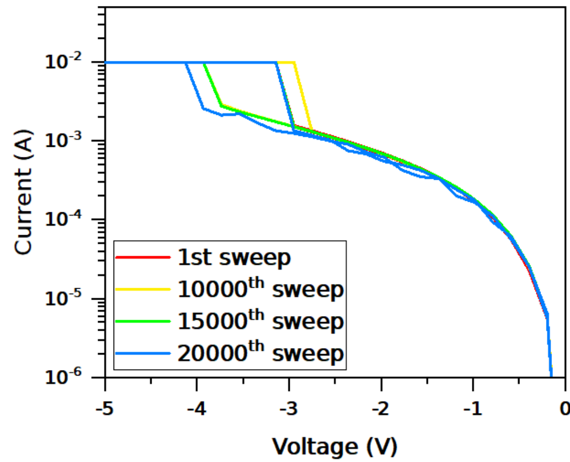

Figure 6.9: *I-V* characteristics of Pt/$ErMnO_3$/Pt device based on the second time annealing in air for more than 10^4 sweeps.

The abrupt increase of current at V_{TH} comes from the direct application of voltage on the devices. To investigate the sharp switching region, it is crucial to employ a controlled current to stabilize the device.[219] As illustrated in the inset in Figure 6.10a, a series resistor of 100 Ω was inserted into the circuit to prevent a steep increase in current through the device. Initially, at low applied voltage, the resistance of the device under study is much larger than that of the series resistor, causing most of the voltage to be dropped across the device. As the applied voltage increases, the device undergoes a transition from HRS to LRS at the threshold voltage. At this point, the device's resistance is relatively low compared to the series resistor, resulting in an increase in current but a decrease in voltage across the device due to the voltage drop across the series resistor. This effect results in a region called S-type negative differential resistance (NDR), where the current increases while the voltage decreases. This region is shaded in green in Figure 6.10a. The stabilized NDR region starts with the threshold voltage and ends with the holding voltage. The *I-V* characteristics with and without the series resistor are very well overlapped. Thus, the NDR region determines the hysteresis window. Figure 6.10b displays the current controlled *I-V* characteristics of the same device with different compliance currents ranging from 10 to 100 mA. The NDR region extends with increasing compliance current, leading to a larger hysteresis window. This aligns well with the result presented in Figure 6.8c, d.

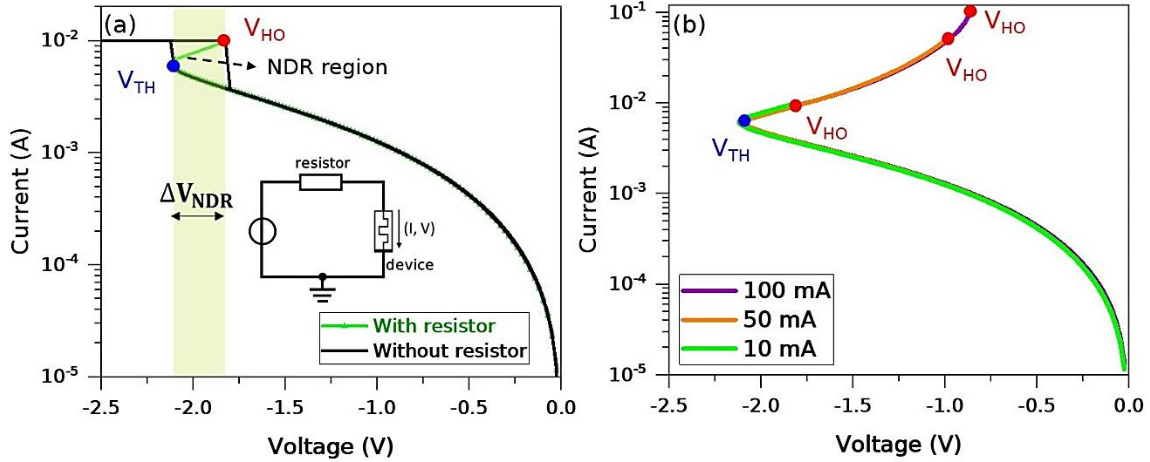

Figure 6.10: (a) Quasi-static *I-V* characteristics of the Pt/$ErMnO_3$/Pt device with and without a stabilizing resistor of value 100 Ω. The inset shows the measurement circuit with a series resistor (100 Ω). (b) Measured *I-V* characteristics with different compliance current 10, 50 and 100 mA, with a stabilizing resistor in series.

6.2.3 Physical model of the threshold switching in Pt/$ErMnO_3$/Pt devices

As a threshold switching behavior has not been previously reported in $ErMnO_3$ films, we now investigate the underlying physical mechanism. To test different conduction mechanism schemes, temperature-dependent *I-V* measurements were performed. The measurements were carried out together with Moritz Engl, using a semiconductor parameter analyzer (Keithley 400-SCS) and a cryogenic probe station (CPX-VF) in NaMLab, Dresden.

Figure 6.11a shows current controlled *I-V* characteristics of a Pt/$ErMnO_3$/Pt device at different stage temperatures from 240 to 320 K with a compliance current of 8 mA.

As the stage temperature increases, the leakage current increases and the threshold voltage decreases.

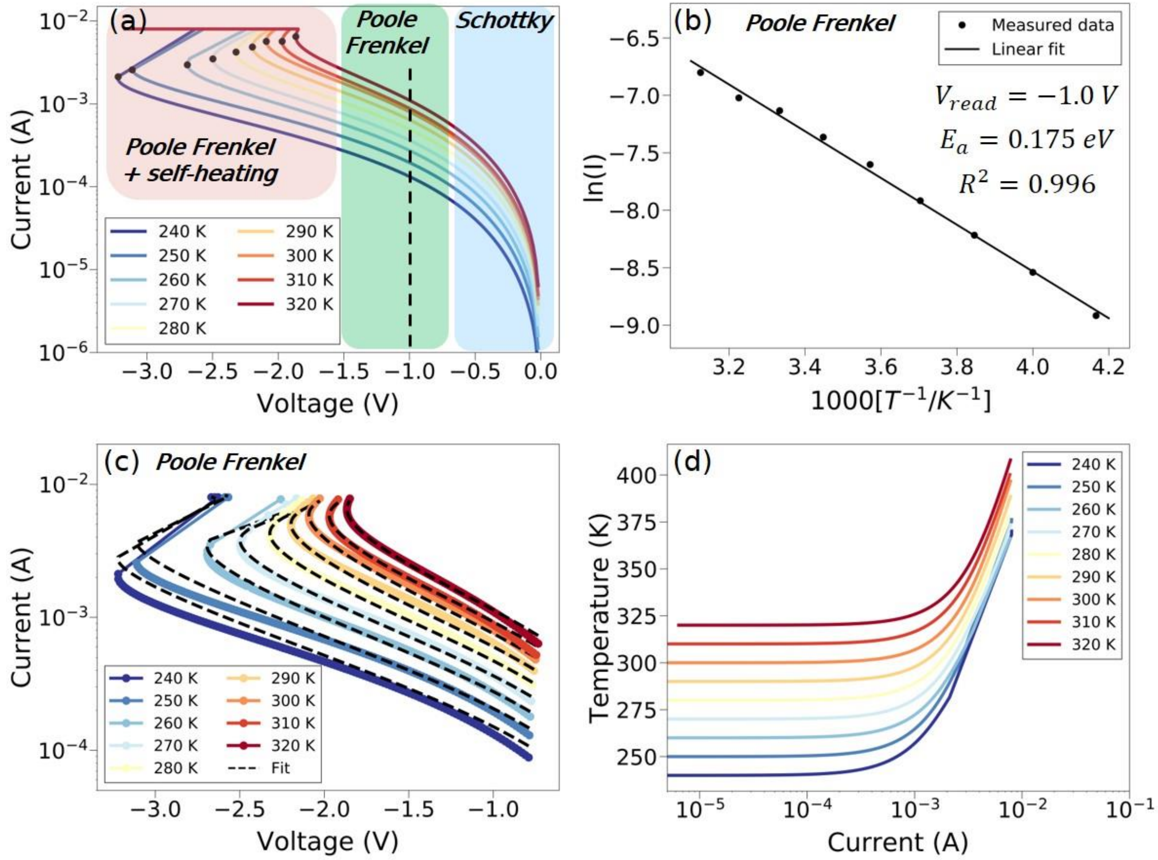

Figure 6.11: (a) Current-controlled *I-V* curves of a Pt/$ErMnO_3$/Pt device with different stage temperatures 240 K – 320 K, showing different regions of conduction mechanisms. Schottky emission at low electric field, Poole-Frenkel conduction pronounces at high electric field. After a threshold voltage, Joule self-heating enhanced Poole-Frenkel leads the device to NRD region. A current compliance current 8 mA was applied to avoid device hard break down. (b) Arrhenius plot of the currents extracted at a read voltage of -1.0 V, a voltage at which the conduction is dominated by Poole-Frenkel. The trap energy barrier *Ea*, extracted from the Arrhenius plot, is around 0.175 eV. (c) Measured and modelled current-controlled *I-V* curves of the Pt/$ErMnO_3$/Pt device with different stage temperatures. (d) Calculated device internal temperature over the device currents at different stage temperatures. The device dimension is $20 \times 20\ \mu m^2$.

Self-heating triggered mechanisms are at the origin of the majority of metal-oxide-based threshold switching with S-type NDR.[210, 212, 216–221] Such devices are primarily governed by a thermally activated conduction mechanism in the pre-threshold region. To investigate the dominating conduction mechanisms, different models were tested: Schottky emission, Poole-Frenkel, space-charge-limited conduction and Fowler-Nordheim tunneling. Before reaching the threshold voltage V_{TH}, conduction is dominated by Schottky emission at low electric field ($0 < V < 0.7$ V) and trap-assisted Poole-Frenkel conduction at higher electric field ($0.7\ V < V$). Once the applied bias exceeds V_{TH}, Poole-Frenkel conduction with self-heating predominates, leading to the NDR behavior (see Figure 6.11a). In this regime ($0.7\ V < V$), we tested the

widely accepted physical model on thermal feedback-based 3D Poole-Frenkel conduction, previously applied to systems such as NbO_x,[212, 213, 221] and TaO_x.[217] In this model, the conductivity is written as follow:

$$\sigma(F,\ T) = \sigma_p e^{-\frac{E_a}{k_B T}} \left\{ \left(\frac{k_B T}{\beta\sqrt{F}}\right)^2 \left[1 + \left(\frac{\beta\sqrt{F}}{2k_B T} - 1\right) e^{\frac{\beta\sqrt{F}}{2k_B T}}\right] + \frac{1}{2} \right\} \quad \text{Equation 6.1}$$

where $\beta = (\frac{q^3}{\pi\varepsilon_0\varepsilon_r})^{\frac{1}{2}}$, ε_r is the high frequency dielectric constant, E_a is the activation energy, $\sigma_p = \frac{L}{R_p A}$ is a prefactor constant, L is the film thickness, A is the active region area, R_p is the resistance, F is the electric field, and T is the internal temperature of the active region.

The internal temperature is supposed to be spatially uniform within the active region of the device and the heat transfer occurs at the quasi-static limit,[212] which can be described by the following equation:

$$C_{th}\frac{dT_N}{dt} = (T - T_{stage})\tau_{th} + IV_{dev},\ \frac{dT_N}{dt} \sim 0 \quad \text{Equation 6.2}$$

$$T = T_{stage} + IV_{dev}/\tau_{th} \quad \text{Equation 6.3}$$

where C_{th} is the thermal capacitance, T_{stage} is the stage temperature, V_{dev} is the voltage drop over the device, and τ_{th} is the thermal conductance. Here we assume that τ_{th} is temperature independent in the investigated temperature range.

Let us consider the region dominated by Poole-Frenkel conduction, where the internal temperature is T_{stage} (highlighted in green in Figure 6.11a). The current measured at $V_{dev} = -1.0\ V$ is plotted in a logarithmic scale as a function of $1/T$ in Figure 6.11b. From the Arrhenius law (ln $(I) \sim -\frac{E_a}{k_B T}$), an activation energy of $E_a = 0.175\ eV$ can be extrapolated for $V_{dev} = -1.0\ V$.

Combining Equations 6.1 and 6.3, the analytical model can be solved self-consistently to fit the quasi-static *I-V* characteristics of the $ErMnO_3$ threshold switching devices at different stage temperatures. With the previously extrapolated activation energy E_a, the material-dependent parameters – thermal conductance (τ_{th}), dielectric permittivity (ε_r) and resistance (R_p) were fitted in the pre-threshold and NDR regions, which are shaded in green and red in Figure 6.11a. The fits are shown in Figure 6.11c. Table 6.4 summarizes the single set of parameter values used for the fits. The relative permittivity ε_r of $ErMnO_3$ is found to be 14.1. This is in excellent agreement with the expected value (ε_r of ~ 12 in $ErMnO_3$ single crystal).[310] The thermal conductance τ_{th} is determined to be 1.6×10^{-4} WK^{-1}, which involves the active region dimensions and the thermal property of the $ErMnO_3$ thin film.[210] Using the reported thermal conductivity value of 1.4 $Wm^{-1}K^{-1}$,[334] a filament diameter of ~3 μm could be estimated by assuming a cylindrical shape, which corresponds well with the dimensions observed for the o-$ErMnO_3$ phase (as the active region) in SEM or optical images.

The very good agreement between the measured and modeled I-V characteristics at the different stage temperatures, along with the physical values determined for ε_r and Γ_{th} indicate that the proposed physical model is well suited to our $ErMnO_3$-based devices.

Figure 6.11d shows the calculated internal temperatures of the active region in the devices, using Equation 6.3 and based on the estimated thermal conductance τ_{th} (see Table 6.4). The internal temperature is constant for current up to 0.7 mA and then increases strongly. The maximum internal temperature during device operation is estimated to be ~ 400 K (Figure 6.11d), which suggests that the internal temperature required to trigger the threshold switching is even lower. Note that, in the domain where the Poole-Frenkel alone is responsible for conduction (green shaded region in Figure 6.11a), the currents at a read voltage of -1.0 V are below 10^{-3} A (dash line in Figure 6.11a), therefore the internal temperature is equal to the stage temperature (Figure 6.11d), which validates our calculation of the activation energy E_a for the Poole-Frenkel mechanism.

Another widely-discussed mechanism for S-shape NDR is thermally driven IMT.[208, 215] As shown in previous studies, non-stoichiometric orthorhombic perovskite $ErMnO_3$ is a p-type semiconductor involving hopping of holes between Mn^{4+} and Mn^{3+} ions, resulting in a much larger conductivity than h-$ErMnO_3$.[266, 278, 321] We can preclude a phase transition from h-$ErMnO_3$ to o-$ErMnO_3$ since the estimated internal temperature (~ 400 K) during the threshold device operation is low, and a high pressure would be required.[51] Any phase transition, if it occurs, would rather be from the metastable o-$ErMnO_3$ to the stable h-$ErMnO_3$ phase.

Table 6.4: Model parameter definitions, symbols and values for the fitting shown in Figure 6.11c.

Physical quantity	**Symbol**	**Value**	**Unit**
Thermal conductance	Γ_{th}	1.6×10^{-4}	W K^{-1}
Relative permittivity	ε_r	14.1	--
Fitting constant	R_p	1.5	Ω

The phenomenon of self-heating-triggered threshold switching is associated with a notable increase in leakage currents.[221] This is because the rate of volumetric heat generation must be sufficiently high to induce the threshold switching, while keeping the electric field below the breakdown limit. This is consistent with the behaviors observed in our devices. After the second annealing in air, the device becomes

much leakier (as shown in Figure 6.7b), resulting in a large current level available to trigger the threshold switching behavior.

Since the second annealing is necessary to obtain the threshold switching, let us discuss its effect on the film. We did not observe significant differences before and after the second annealing (in air) in the XRD, Raman spectra, SEM and AFM topographic images. X-ray Photoelectron Spectroscopy (XPS) was performed to get insights on the Mn ion valences (Figure 6.12). As a reference sample, almost single-phase o-$ErMnO_3$ film (reference 3 in Table 6.1) was studied before and after a second annealing (XRD and Raman spectra of the film are given in Section 6.1). The Mn $2p_{3/2}$ core level spectra and their deconvolution are shown in Figure 6.12a, b. The o-$ErMnO_3$ film (before/after) only contains Mn^{3+} and Mn^{4+} contributions. The atomic concentrations of these two valence states were estimated and are presented in Figure 6.12c. An increase in Mn^{4+} concentration by 3% is observed after the second annealing.

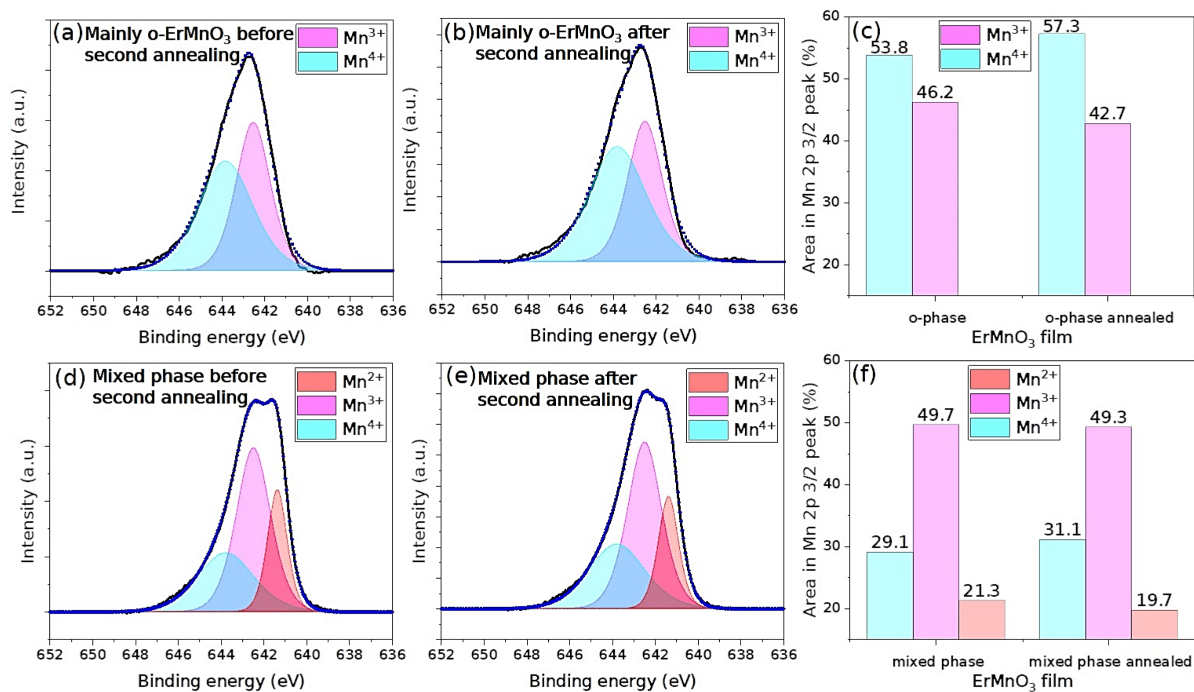

Figure 6.12: X-ray photoelectron spectroscopy (XPS) analysis. Mn $2p_{3/2}$ XPS spectrum and their deconvoluted curves for Mn^{2+}, Mn^{3+} and Mn^{4+} after background subtraction. (a) and (c) XPS spectrum of almost single-phase o-$ErMnO_3$ film before and after the second annealing in air, their comparison of the concentrations (area in peak, %) of Mn^{3+} and Mn^{4+} in (e). (b) and (d) $ErMnO_3$ film with mixed phases (~ 20% o-$ErMnO_3$) before and after second annealing in air, their comparison of the concentrations (area in peak, %) of Mn^{2+}, Mn^{3+} and Mn^{4+} in (f).

Now, let us consider the mixed o- and h-$ErMnO_3$ films as used in the above devices. To fit the Mn $2p_{3/2}$ XPS spectra, an additional component attributed to Mn^{2+} is required, which is situated at a lower binding energy than Mn^{3+} and Mn^{4+}, as shown in Figure 6.12d, e. The Mn^{2+} contribution originates from the

hexagonal $ErMnO_3$ phase or from the grain boundaries between the two phases, as it was absent in the reference o-$ErMnO_3$ film. Sandra H. Skjærvø *et. al.* reported that hexagonal manganite structure can accommodate Mn^{2+}, which would primarily arise due to the variations in oxygen stoichiometry (oxygen vacancies) while being processed at high temperature and low pO_2.[335, 336] Figure 6.12f presents the concentrations of the different oxidation states. A higher amount of Mn^{4+} and a lower concentration of Mn^{2+} are observed after the second annealing. In a study on $YMnO_3$ films annealed in oxygen atmosphere at around 400 °C, an oxygen uptake has been reported.[337] The added oxygen is suggested to fill the oxygen vacancies and further oxidize Mn^{2+} to Mn^{3+} or Mn^{3+} to Mn^{4+}. This leads to a hole dominated conduction mechanism and a higher conductivity in oxygen or air processed $RMnO_3$ (both phases).[103, 114, 337] In our films the increase in Mn^{4+} is likely to occur in the o-$ErMnO_3$ as we shown below.

To gain additional insight into the local conductive properties, c-AFM mapping was performed with a sample bias of 2 V on the same location of the film before and after the second annealing, shown in Figure 6.13a, b. No difference in surface morphology is observed (Figure 6.6h, i). However, there is a significant increase in current in o-$ErMnO_3$ after the second annealing, as also shown in Figure 6.13c-g. *I-V* characteristics of o- and h-$ErMnO_3$ phases before and after the second annealing were measured as presented in Figure 6.13g (see corresponding locations in Figure 6.13e, f). There is no discernible difference in the conductivities of the hexagonal phase whether the films have undergone or not a second annealing in air. In contrast, a strong enhancement of about one order of magnitude in current is observed in o-$ErMnO_3$ after the second annealing. This enhancement is attributed to the increased Mn^{4+} content, which reflects an increased conductivity in the o-$ErMnO_3$ regions. The locally increased current explains the overall increased leakage currents observed macroscopically on the devices (Figure 6.7b).

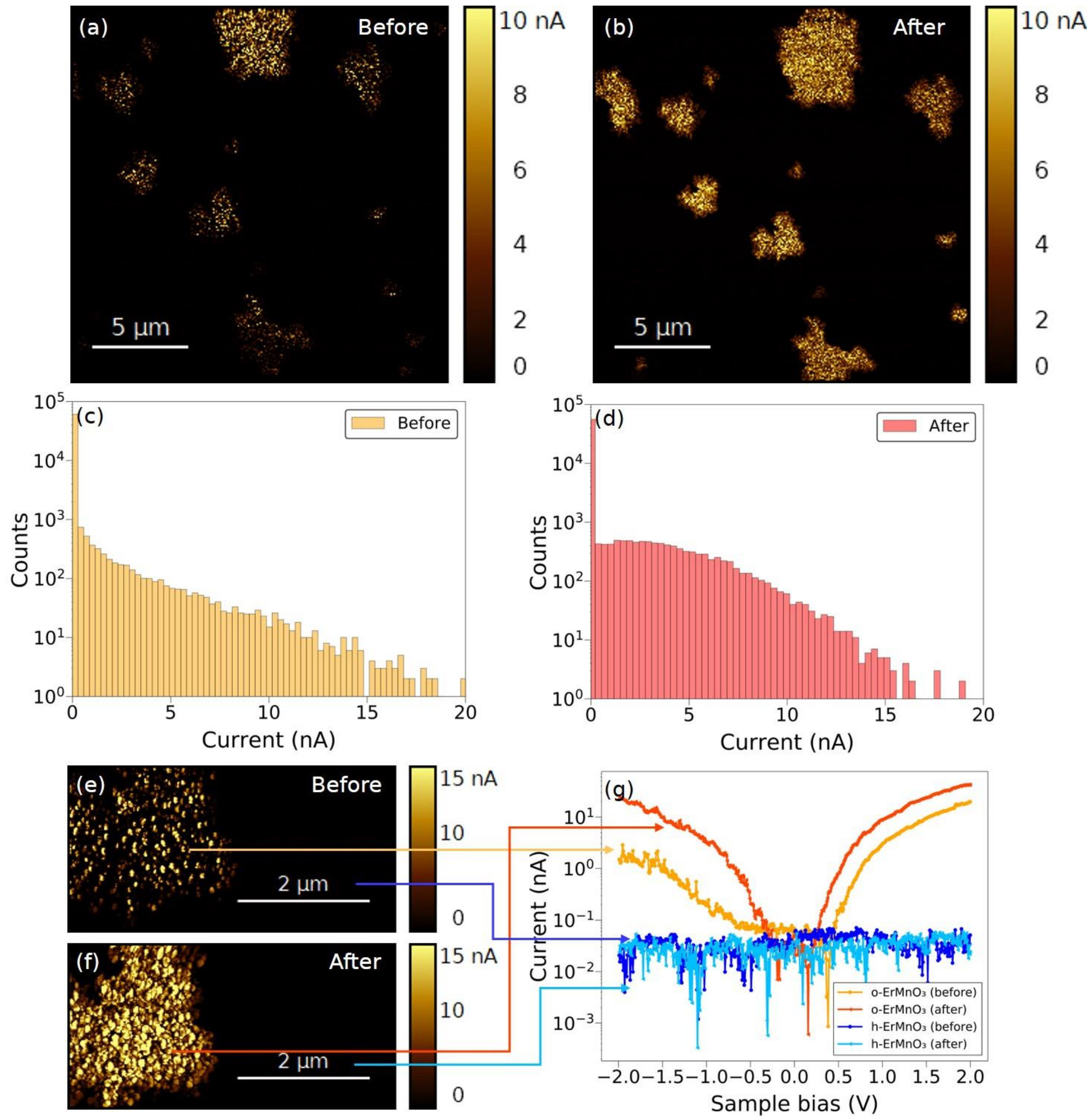

Figure 6.13: (a, e) c-AFM current map and (c) current distribution of $ErMnO_3$ film before the second annealing, within the black box marked in the SEM image in Figure 6.6a. (b, f) c-AFM current map and (d) current distribution of $ErMnO_3$ film after the second annealing, within the black box marked in the SEM image in Figure 6.6b. The tip was grounded and a sample bias of 2 V was applied. (g) *I-V* characteristics by c-AFM on o-$ErMnO_3$ and h-$ErMnO_3$ before and after the second annealing.

6.2.4 On the roles of the orthorhombic and hexagonal phases

To further explore the contribution of the crystalline phases on triggering the threshold switching behavior, *I-V* measurements were performed on the Pt/h-$ErMnO_3$/Pt stack after the second annealing (reference 1 in Table 6.1), and are shown in Figure 6.14. The leakage currents are lower compared to those with 20% o-$ErMnO_3$. A non-volatile resistive switching instead of threshold switching is observed with h-$ErMnO_3$.

Thus, this finding suggests that the inclusion of orthorhombic phase in the devices is crucial to provide the required localized conductive paths inside the switching layer, in order to trigger the threshold switching.

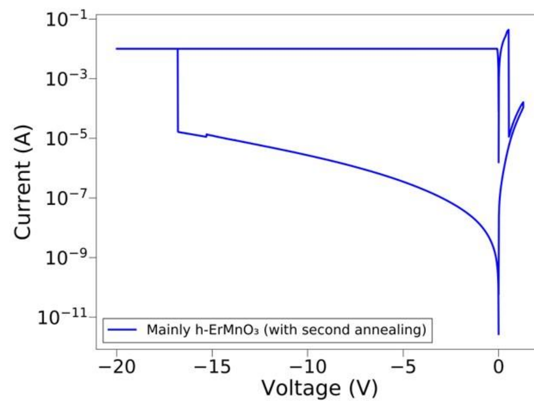

Figure 6.14: *I-V* characteristics of Pt/h-$ErMnO_3$/Pt devices. The film underwent the second annealing in air at 400 ºC (reference 1 in Table 6.1).

A schematic presentation of the physical model based on Poole-Frenkel conduction and self-heating to explain the origin of threshold switching, is given in Figure 6.15. Mn^{4+} can be described as Mn^{3+} with holes, where the defects – holes – are initially trapped, resulting in low leakage currents (see A in Figure 6.15). As an electric field is applied, the trap barrier is lowered and holes get detrapped, leading to increased leakage currents, as shown in B in Figure 6.15. As o-$ErMnO_3$ is more conductive than h-$ErMnO_3$, most current flows through o-$ErMnO_3$, leading to a temperature increase by local Joule heating (B to C in Figure 6.15). As the temperature increases, more thermal excited holes are detrapped, as illustrated by C in Figure 6.15. As the applied bias decreases, less leakage current flows through o-$ErMnO_3$ (C to D in Figure 6.15), further resulting in a temperature decrease due to heat dissipation (D to E in Figure 6.15). The device then returns to its initial state with low leakage currents at a low temperature.

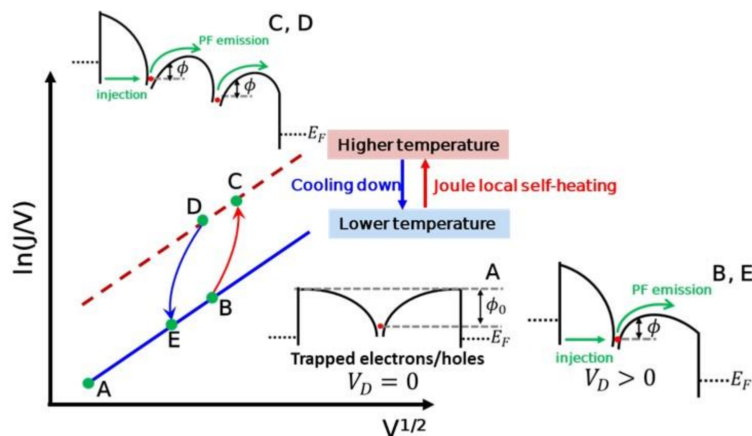

Figure 6.15: Schematic presentation of the physical model for the origin of threshold switching in Pt/$ErMnO_3$/Pt devices.

Figure 6.16 show sketches of the $ErMnO_3$ films with mixed crystalline phases – minor conductive o-$ErMnO_3$ (marked in yellow) embedded in less conductive h-$ErMnO_3$ (marked in blue) before (Figure 6.16a) and after (Figure 6.16b, c) the second annealing. After the second annealing, the minor o-$ErMnO_3$ has a higher conductivity and is sufficiently localized in the h-$ErMnO_3$ matrix to accumulate Joule self-heating to trigger the threshold switching, as presented in Figure 6.16c.

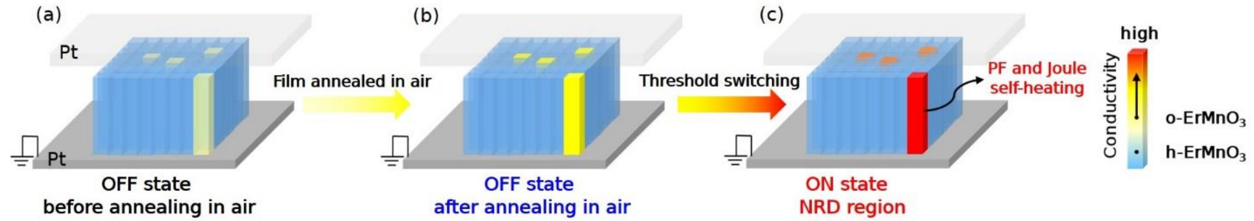

Figure 6.16: (a) Schematic diagrams of Pt/$ErMnO_3$/Pt devices showing threshold switching mechanisms. Before annealing in air, o-$ErMnO_3$ is more conductive than h-$ErMnO_3$. (b) After annealing in air, o-$ErMnO_3$ becomes more conductive, forming local conductive paths and h-$ErMnO_3$ remains as similar as before. (c) As above the threshold switched voltage, the formed local conductive paths lead devices to negative differential region, due to enhanced Poole-Frenkel conduction by local Joule self-heating.

In NbO_x studies,[209, 211, 219, 338] the threshold switching behavior is based on a conductive filament, for which the electroforming process is stochastic. In this work, the threshold switching is attributed to a conduction mechanism based on hole hopping from Mn^{4+} to Mn^{3+} sites together with Joule effect in the conductive o-$ErMnO_3$ phase paths, which can be characterized and quantified in a more controllable way as compared to the stochastic formation of filaments. The hexagonal phase serves to prevent the overall device from having a too large electrical and thermal conductivity. However, it does not play a direct role in the electrical conduction. As shown in Figure 6.14, a mainly h-$ErMnO_3$ device show no threshold switching behavior but a classical filamentary non-volatile resistive switching. On the other hand, in a device mainly composed of o-$ErMnO_3$ (~ 75% o-$ErMnO_3$, see Table 6.1), the hysteresis window is obtained but is very narrow, compared to the device with 20% $ErMnO_3$ discussed in the previous sections (see Figure 6.17). It is not even necessary to perform a second annealing in air to observe the threshold switching. The very narrow memory window is due to the high thermal conductivity and conduction of the o-$ErMnO_3$ device. Hence, adding h-$ErMnO_3$ is a key knob for engineering the NDR properties.

In addition to mixing h- and o-$ErMnO_3$ phases in different amounts, another key knob is the electrical and thermal conductivities of the o-$ErMnO_3$ conduction paths. These properties could be fine-tuned through thermal treatments. Moreover, the geometry of the conduction paths is significant, and could be modified by varying the film thickness. These aspects are promising research paths to achieve tunability of the NDR memory window.

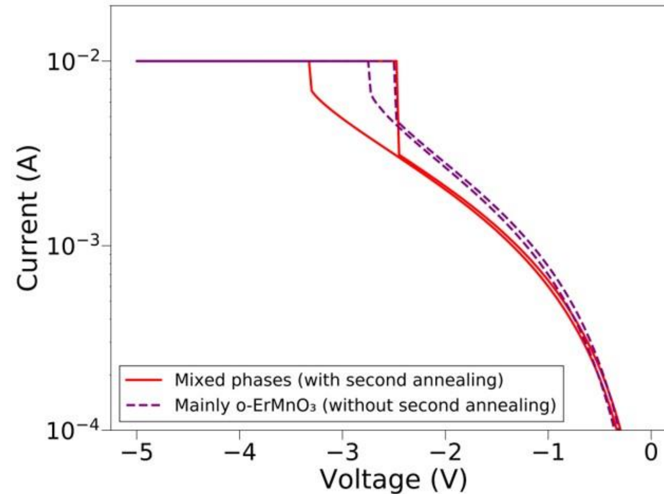

Figure 6.17: *I-V* characteristics of Pt/$ErMnO_3$/Pt devices with mainly o-$ErMnO_3$ film without the second annealing in air and with mixed phases with the second annealing in air.

6.3 Applications (implementation of the NDR devices into circuits)

NDR devices are known to exhibit an oscillatory behavior. They are modelled with a circuit that contain an inductive value. The S-shaped DC *I-V* characteristics in conjunction with thermal activation drives the dynamics of these devices as shown by several studies.[223, 339, 340] One of the applications for threshold switching devices is the design of compact artificial neurons.[11, 12, 328]

We have studied these aspects in collaboration with the group of Prof. Dr. Ronald Tetzlaff at TU Dresden, with Dr. Richard Schroedter and Dr. Ahmet Demirkol. I went to TU Dresden to participate to the measurements.

6.3.1 Reconfigurability between resistive and inductive states

A. Demirkol *et al.* proposed that the impedance function of the locally active (i.e., S-shaped) threshold switching devices can be represented by an RL circuit configuration.[341] Figure 6.18a illustrates the DC *I-V* curve of such a device under a current sweep, highlighting the NDR region in red. The device can be modeled as an equivalent circuit consisting of three components: a resistor (R_2) and an inductor (L) arranged in parallel, connected to another resistor (R_{1i}) in series (represented by the yellow dashed square in Figure 6.18b). The device exhibits an inductive behavior in the NDR region, hence, allowing a reconfigurability between the resistive and inductive states.

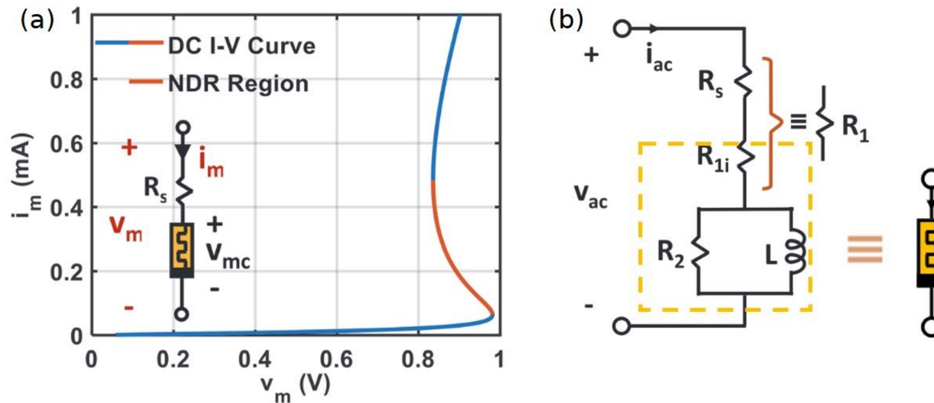

Figure 6.18: (a) DC *I-V* curve of a locally active memristor, with NDR region highlighted in red. (b) AC equivalent circuit of the entire memristor. The device is equivalent to a pair of a resistor (R_2) and an inductor (L) in parallel with another resistor (R_{1i}) in series. These figures are from ref.[341]

DC *I-V* measurements of several of our devices were carried out. The devices were connected to a series resistor of 330 Ω. A typical curve measured, and its corresponding fitting are shown in Figure 6.19.

The *L* value is not a constant but is different for each bias used inside the NDR region. The *L* values are found to be in the range of 100 – 150 µH, when a bias point is set to be in the middle of the NDR region. These values are quite large (much larger than the targeted values of 1 µH in the ERMI project).

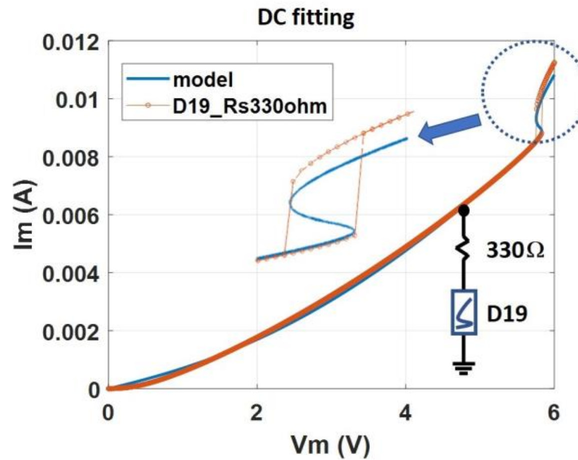

Figure 6.19: DC *I-V* curve of a Pt/$ErMnO_3$/Pt device with a series resistor of 330 Ω, and its corresponding DC fitting.

6.3.2 NDR devices as artificial neurons

Here, our devices were inserted in a neuristor circuit to establish the oscillatory dynamics. Its design and the electrical measurements were performed by the group of Prof. Dr. Ronald Tetzlaff at TU Dresden (I participated to the measurements).

For the neuristor circuit, a capacitor is connected in parallel to our threshold switching devices.[341] The proposed neuristor circuit is illustrated in Figure 6.20, where V_{DC} is DC voltage source, R_s = 100 Ω is the series resistor, R_p = 22 Ω is the parallel resistor and C_p = 10.7 pF is the parallel capacitor. The neuristor circuit parameters were carefully chosen, such that the $ErMnO_3$ device can be biased in the NDR region.

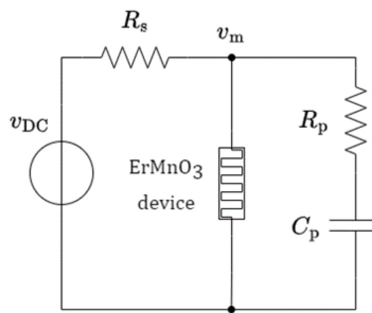

Figure 6.20: Neuristor circuit.

When the voltage drop *V*m across the device exceeds the threshold voltage and is sufficient to switch the device in the ON state, sustained oscillations are observed, as shown in Figure 6.21a, for different V_{DC} values. We find that sweeping the DC input voltage leads to changes in spike waveform. The frequency as a function of V_{DC} is plotted in Figure 6.21b, showing a frequency range from130 to 330 kHz for a voltage range from -3.82 to -4.70 V.

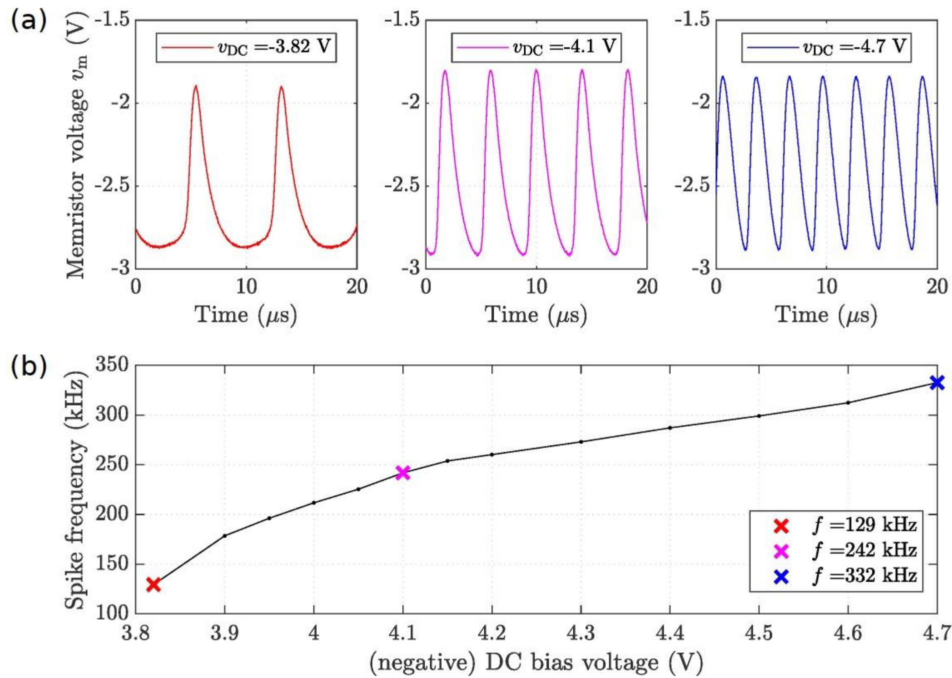

Figure 6.21: (a) Measured spiking behavior at different DC input voltages. (b) Spike frequency as a function of DC input voltages.

These preliminary results demonstrate that our NDR devices can be implemented in a neuristor circuit to obtain stable and repeatable oscillations. They are therefore good candidates for mimicking spiking neurons.

A next step would be to investigate the switching speed of our devices, which will be conducted by the group of Prof. Dr. Ronald Tetzlaff at TU Dresden.

6.4 Summary

- The first demonstration of electroforming-free threshold switching behavior in polycrystalline $ErMnO_3$ devices is reported. The Pt/$ErMnO_3$/Pt devices exhibit repeatable unipolar threshold switching (S-shape current-controlled negative differential resistance) with a memory window of 0.7 V, and high endurance (up to 10^4 sweeps).
- The threshold switching behavior is obtained in films containing a mixture of h-$ErMnO_3$ and o-$ErMnO_3$ phases and after an appropriate thermal treatment. The additional annealing at 400 °C in air enhanced the conductivity of the o-$ErMnO_3$ phase, which is associated to an increase in Mn^{4+} ion contents.
- The origin of the threshold switching is attributed to Joule heating-enhanced 3D Poole-Frenkel conduction mechanism. The IV curves in the range of $V > 0.7$ V are well fitted with a single set of parameters.
- Engineering of the film micro/nanostructure is key. The o-$ErMnO_3$ phase drives the conduction and Joule heating that triggers the threshold switching. The introduction of the insulating hexagonal phase, is necessary to avoid too large leakage currents, which otherwise leads to a very narrow NDR region.
- The fine control of the orthorhombic phase conductivity via the synthesis conditions provides potentially a unique means to tune the NDR region's characteristics.
- The devices in NDR region behave as an inductor, allowing the reconfigurability between the resistive and inductive states. The inductance values are estimated to be in the range from 100 to 150 μH.
- The oscillation characteristics of these devices, when implemented in a neuristor circuit are successfully demonstrated. Change of the DC input voltage leads to changes in the oscillation waveform and frequency.

Summary and outlook

Summary

Mixed hexagonal and orthorhombic polycrystalline $YMnO_3$ and $ErMnO_3$ thin films were prepared by room temperature RF sputtering and post-deposition annealing in a nitrogen atmosphere. Using correlative spectroscopic and microscopic techniques such as Raman spectroscopy, scanning electron microscopy, conductive atomic force microscopy, and optical microscopy, a method was developed to clearly identify and locate the orthorhombic phase within the hexagonal matrix. Subsequently, a quantitative estimation of the fraction of the two crystalline phases (orthorhombic and hexagonal) in the films was achieved. This method allows identification and quantification of both crystalline phases, which X-ray diffraction could not allow.

Impedance measurements were conducted on metal-insulator-metal stacks with $YMnO_3$ and $ErMnO_3$. Both package- and probe station-based setups with dedicated parasitic calibrations were applied. Low inductances (L) in the nH range were determined, which are at the detection limit. The devices exhibited a resistive switching behavior, with a capacitive behavior (C) in the OFF state and resistive behavior (R) in the ON state, allowing the possibility for reconfigurable *R-C* devices. *L-C* reconfigurability in the devices was not observed.

We then presented a comprehensive investigation of polycrystalline $RMnO_3$ (R = Y, Er) thin films-based resistive switching devices. We explored how the two polymorphs (hexagonal and orthorhombic phases) can be used to leverage their properties to design new memristive devices. The key findings of our studies are summarized as follows.

Electrochemical metallization memristive (ECM) devices with Al active electrodes were fabricated with polycrystalline $YMnO_3$ containing different fractions of the hexagonal and orthorhombic phases. These devices demonstrated electroforming-free bipolar resistive switching with a high R_{OFF}/R_{ON} ratio of 10^4, low Set (~ 1.7 V) and Reset (~ -0.36 V) voltages, and good retention performance. The origin of resistive switching was ascribed to the formation and rupture of an Al filament *via* electrochemical metallization along oxygen-deficient crystalline phase boundaries. These devices were integrated into frequency compensation circuits by our collaborators at the Institute of Microelectronic Systems, University of Hannover, to demonstrate a real use case.

We investigated valence change memory (VCM) type devices with Pt/$ErMnO_3$/Ti/Au stacks. Bipolar resistive switching behavior was observed with a R_{OFF}/R_{ON} ratio of ~ 10^5, an ultra-low resistance of only 10 Ω in the low resistance state (R_{ON}), and good retention performance. The underlying mechanism of resistive switching in these devices was attributed to the formation and rupture of conductive filament(s) based on oxygen vacancies, which likely occurred in the orthorhombic phase or at the boundary between

hexagonal and orthorhombic phases. An increased fraction of the orthorhombic phase strongly reduced the operating voltage in the devices. This finding provides important insights for engineering the $ErMnO_3$ switching layer for enhanced performance.

Finally, we reported the first demonstration of electroforming-free threshold switching behavior in Pt/$ErMnO_3$/Pt devices. The devices exhibited repeatable unipolar threshold switching with S-shape current-controlled negative differential resistance (NDR), a memory window of 0.7 V, and a high endurance (up to 10^4 sweeps). The threshold switching behavior was obtained in films containing a mixture of h-$ErMnO_3$ and o-$ErMnO_3$ phases and after an appropriate second thermal treatment. The additional annealing at 400 °C in air enhanced the conductivity of the o-$ErMnO_3$ phase, which was associated to an increase in Mn^{4+} ion content. The origin of the threshold switching was attributed to Joule heating-enhanced 3D Poole-Frenkel conduction mechanism. Engineering of the film micro/nanostructure was key, since Joule heating within localized conductive o-$ErMnO_3$ triggered the threshold switching, while the introduction of the insulating hexagonal phase was necessary to avoid too large leakage currents. Fine control of the orthorhombic phase content and of its conductivity via the synthesis conditions provided a unique means to tune the NDR region's characteristics. This new type of NDR devices based on two polymorphs provided unique capabilities in terms of tunability of the S-shape characteristics as compared to the known devices based on an insulator to metal transition like in VO_2 or on a filamentary process like in NbO_x. Devices operating in the NDR region exhibited inductive behavior, enabling reconfigurability between resistive and inductive states. The inductance values were estimated to be in the range from 100 to 150 μH. These devices inserted in a neuristor circuit, exhibited an oscillatory behavior, showing the potential for mimicking spiking neurons.

$ErMnO_3$ materials presented opportunities to achieve both non-volatile resistive switching and volatile threshold switching. There are two possible applications incorporating both types of devices. On the one hand, this capability enables the potential implementation of crossbar structures with RRAM cells and selectors using the same material without encountering compatibility issues. On the other hand, it opens avenues for neuromorphic applications to integrate synapses (RRAM) and spiking neurons (threshold switching) within the same material framework in future research.

Outlook

In the study of resistive switching behaviour in Pt/$YMnO_3$/Al devices, we proposed that the origin of switching is the formation and rupture of an Al filament *via* electrochemical metallization along oxygen-free boundaries between the orthorhombic and hexagonal phases. Future research should focus on exploring the mechanisms and their dynamics at the nanoscale within these phase boundary channels with methods

such as operando transmission electron microscopy.[184] Another milestone would be to scale these devices down to < 100 nm so that devices contain only one boundary along with a few nanograins of each polymorph on either side of the boundary.

In Pt/$ErMnO_3$/Ti/Au devices, we proposed that the formation of an oxygen vacancy-based filament occurs in the orthorhombic phase or at a boundary between the hexagonal and orthorhombic phases. This hypothesis requires further validation through additional experiments, such as operando hard X-ray photoelectron spectroscopy or Atom Probe Tomography, to study the evolution of oxygen vacancies in both ON and OFF states.

The most promising devices are the threshold switching devices. These devices demonstrate good endurance and repeatable switching with S-shape NDR behavior, making them well-suited for artificial neuron applications and more generally for all applications where the NDR property is used (oscillatory circuits). The most attractive aspect of these devices is that a fine-tuning of the characteristics of the NDR region should be possible by adjusting the orthorhombic phase conductivity. This could be realized by changing the parameters of the additional annealing (temperature, time).

Further investigations for oscillatory circuits, in particular for neuron applications, will be conducted in collaboration with the group of Prof. Dr. Ronald Tetzlaff at TU Dresden.

Additionally, given the ferroelectric properties displayed by $YMnO_3$ and $ErMnO_3$ crystals, further efforts in obtaining ferroelectric properties at room temperature in the films should be conducted, in order to combine resistive switching and ferroelectricity. It would offer a path to achieve multilevel analog resistive switching states for neuromorphic applications.[13, 14]

References

1. J. Zhu, T. Zhang, Y. Yang, R. Huang, "A comprehensive review on emerging artificial neuromorphic devices." *Appl. Phys. Rev.* 7, 011312, **2020**, doi:10.1063/1.5118217/997618.

2. K. Udaya Mohanan, "Resistive switching devices for neuromorphic computing: from foundations to chip level innovations." *Nanomaterials*. 14, 527, **2024**, doi:10.3390/NANO14060527.

3. J. Backus, "Can programming be liberated from the von Neumann style?" *Commun. ACM*. 21, 613–641, **1978**, doi:10.1145/359576.359579.

4. O. Mutlu, S. Ghose, J. Gómez-Luna, R. Ausavarungnirun, "Processing data where it makes sense: Enabling in-memory computation." *Microprocess. Microsyst.* 67, 28–41, **2019**, doi:10.1016/J.MICPRO.2019.01.009.

5. S. Yu, P. Y. Chen, Y. Cao, L. Xia, Y. Wang, H. Wu, "Scaling-up resistive synaptic arrays for neuro-inspired architecture: Challenges and prospect." *2015 IEEE International Electron Devices Meeting (IEDM)*, Washington, DC, USA, **2015**, 17.3.1-17.3.4, doi: 10.1109/IEDM.2015.7409718.

6. X. Zhang, S. Liu, X. Zhao, F. Wu, Q. Wu, W. Wang, R. Cao, Y. Fang, H. Lv, S. Long, Q. Liu, M. Liu, "Emulating short-term and long-term plasticity of bio-synapse based on Cu/a-Si/Pt memristor." *IEEE Electron Device Lett.* 38, 1208–1211, **2017**, doi:10.1109/LED.2017.2722463.

7. I. Raifuku, Y. P. Chao, H. H. Chen, C. F. Lin, P. E. Lin, L. C. Shih, K. T. Chen, J. Y. Chen, J. S. Chen, P. Chen, "Halide perovskite for low-power consumption neuromorphic devices." *EcoMat*. 3, e12142, **2021**, doi:10.1002/EOM2.12142.

8. M. Prezioso, F. Merrikh Bayat, B. Hoskins, K. Likharev, D. Strukov, "Self-adaptive spike-time-dependent plasticity of metal-oxide memristors." *Sci. Rep.* 6, 1–6, **2016**, doi:10.1038/srep21331.

9. M. Ismail, U. Chand, C. Mahata, J. Nebhen, S. Kim, "Demonstration of synaptic and resistive switching characteristics in W/TiO_2/HfO_2/TaN memristor crossbar array for bioinspired neuromorphic computing." *J. Mater. Sci. Technol.* 96, 94–102, **2022**, doi:10.1016/J.JMST.2021.04.025.

10. M. D. Pickett, G. Medeiros-Ribeiro, R. S. Williams, "A scalable neuristor built with Mott memristors." *Nat. Mater.* 12, 114–117, **2012**, doi:10.1038/nmat3510.

11. L. Gao, P. Y. Chen, S. Yu, "NbO_x based oscillation neuron for neuromorphic computing." *Appl. Phys. Lett.* 111, 103503, **2017**, doi:10.1063/1.4991917.

12. Y. Ding, Y. Zhang, X. Zhang, P. Chen, Z. Zhang, Y. Yang, L. Cheng, C. Mu, M. Wang, D. Xiang, G. Wu, K. Zhou, Z. Yuan, Q. Liu, "Engineering spiking neurons using threshold switching devices

for high-efficient neuromorphic computing." *Front. Neurosci.* 15, 786694, **2022**, doi:10.3389/FNINS.2021.786694/BIBTEX.

13. K. Ni, J. Smith, H. Ye, B. Grisafe, G. B. Rayner, A. Kummel, S. Datta, "A novel ferroelectric superlattice based multi-level cell non-volatile memory", *2019 IEEE International Electron Devices Meeting (IEDM)*, San Francisco, CA, USA, **2019**, 28.8.1-28.8.4, doi:10.1109/IEDM19573.2019.8993670.

14. J. Sun, Y. Li, Y. Ou, Q. Huang, X. Liao, Z. Chen, X. Chai, X. Zhuang, W. Zhang, C. Wang, J. Jiang, A. Jiang, J. Sun, Y. Li, Y. Ou, X. Zhuang, W. Zhang, C. Wang, J. Jiang, *et al.*, "In-memory computing of multilevel ferroelectric domain wall diodes at $LiNbO_3$ interfaces." *Adv. Funct. Mater.* 32, 2207418, **2022**, doi:10.1002/ADFM.202207418.

15. H. Schmidt, "Prospects for application of ferroelectric manganites with controlled vortex density." *Appl. Phys. Lett.* 118, 140502, **2021**, doi:10.1063/5.0032988.

16. S. M. Griffin, M. Lilienblum, K. T. Delaney, Y. Kumagai, M. Fiebig, N. A. Spaldin, "Scaling behavior and beyond equilibrium in the hexagonal manganites." *Phys. Rev. X.* 2, 1–10, **2012**, doi:10.1103/PhysRevX.2.041022.

17. V. R. Rayapati, N. Du, D. Bürger, R. Patra, I. Skorupa, P. Matthes, H. Stöcker, S. E. Schulz, H. Schmidt, "Electroforming-free resistive switching in polycrystalline $YMnO_3$ thin films." *J. Appl. Phys.* 124, **2018**, doi:10.1063/1.5040041.

18. P. Renz, M. Kaufmann, M. Lueders, B. Wicht, "A fully integrated 85%-peak-efficiency hybrid multi ratio resonant DC-DC converter with 3.0-to-4.5V input and 500μA-to-120mA load range." *International Solid-State Circuits Conference - (ISSCC)*, San Francisco, CA, USA, **2019**, doi:10.1109/ISSCC.2019.8662491.

19. J. Wittmann, T. Funk, T. Rosahl, B. Wicht, "A 48-V wide-Vin 9-25-MHz resonant DC-DC converter." *IEEE Journal of Solid-State Circuits*, 1936-1944, **2018**, doi:10.1109/JSSC.2018.2827953.

20. D. Lutz, P. Renz, B. Wicht, "An integrated 3-mW 120/230-V AC mains micropower supply." *IEEE Journal of Emerging and Selected Topics in Power Electronics*, 581-591, **2018**, doi:10.1109/JESTPE.2018.2798504.

21. Z. B. Yan, S. Z. Li, K. F. Wang, J. M. Liu, "Unipolar resistive switching effect in $YMn_{1-\delta}O_3$ thin films." *Appl. Phys. Lett.* 96, 012103, **2010**, doi:10.1063/1.3280380.

22. A. Bogusz, A. D. Müller, D. Blaschke, I. Skorupa, D. Bürger, A. Scholz, O. G. Schmidt, H. Schmidt, "Resistive switching in polycrystalline $YMnO_3$ thin films." *AIP Adv.* 4, 107135, **2014**,

doi:10.1063/1.4899188.

23. L. Wei, C. H. Jia, W. F. Zhang, "Distinguish and control the multi-level resistive switching for ferroelectric layer and interface in a $YMnO_3$/Nb:$SrTiO_3$ device." *RSC Adv.* 6, 1445–1451, **2016**, doi:10.1039/c5ra19986g.

24. V. R. Rayapati, D. Bürger, N. Du, R. Patra, I. Skorupa, D. Blaschke, H. Stöcker, P. Matthes, S. E. Schulz, H. Schmidt, "Electroforming-free resistive switching in yttrium manganite thin films by cationic substitution." *J. Appl. Phys.* 126, **2019**, doi:10.1063/1.5094748.

25. K. N. Rathod, K. Gadani, H. Boricha, K. Sagapariya, A. Vaisnani, D. Dhruv, A. D. Joshi, J. P. Singh, K. H. Chae, K. Asokan, P. S. Solanki, N. A. Shah, "Extraction of switching parameters for Sr-doped $YMnO_3$ thin film." *Phys. Status Solidi Appl. Mater. Sci.* 216, 1–5, **2019**, doi:10.1002/pssa.201900780.

26. H. Schmid, "Multi-ferroic magnetoelectrics." *Ferroelectrics*. 162, 317–338, **1994**, doi:10.1080/00150199408245120.

27. K. Aizu, "Possible species of ferromagnetic, ferroelectric, and ferroelastic crystals." *Phys. Rev. B*. 2, 754, **1970**, doi:10.1103/PhysRevB.2.754.

28. D. B. Litvin, "Ferroic classifications extended to ferrotoroidic crystals." *Acta Crystallogr. Sect. A Found. Crystallogr.* 64, 316–320, **2008**, doi:10.1107/S0108767307068262.

29. I. Dzyaloshinskii, "On the magneto-electrical effects in antiferromagnets." *Sov. Phys. JETP*. 10, 628–9, **1960**.

30. R. Ramesh, "Materials for a sustainable microelectronics future: electric field control of magnetism with multiferroics." *J. Indian Inst. Sci.* 102, 489–511, **2022**, doi:10.1007/s41745-021-00277-7.

31. N. A. Spaldin, R. Ramesh, "Advances in magnetoelectric multiferroics." *Nat. Mater.* 18, 203–212, **2019**, doi:10.1038/s41563-018-0275-2.

32. S. Kopyl, R. Surmenev, M. Surmeneva, Y. Fetisov, A. Kholkin, "Magnetoelectric effect: principles and applications in biology and medicine– a review." *Mater. Today Bio*. 12, 100149, **2021**, doi:10.1016/J.MTBIO.2021.100149.

33. D. Khomskii, "Classifying multiferroics: Mechanisms and effects." *Physics (College. Park. Md).* 2, 20, **2009**, doi:10.1103/Physics.2.20.

34. N. A. Spaldin, M. Fiebig, "The renaissance of magnetoelectric multiferroics." *Science (80-.).* 309, 391–392, **2005**, doi:10.1126/SCIENCE.1113357.

35. A. K. Bain, P. Chand, "Ferroelectrics: principles and applications", *John Wiley & Sons*, **2017**, doi:

10.1002/9783527805310.

36. J. Valasek, "Piezo-electric and allied phenomena in Rochelle salt." *Phys. Rev.* 17, 475, **1921**, doi:10.1103/PhysRev.17.475.

37. M. Wu, "100 years of ferroelectricity." *Nat. Rev. Phys.* 3, 726–726, **2021**, doi:10.1038/s42254-021-00383-6.

38. "A century of ferroelectricity." *Nat. Mater. 2020 192*. 19, 129–129, **2020**, doi:10.1038/s41563-020-0611-1.

39. H. Ishiwara, "Multifunctional oxide heterostructures", *Oxford Academic*, **2013**, doi: 10.1093/acprof:oso/9780199584123.001.0001.

40. E. F. Bertaut, F. Forrat, P. H. Fang, "A new class of ferroelectric: Rare Earth and Yttrium Manganites." *Compt. Rend. 256*, 1958, **1963**.

41. V. M. Goldschmidt, "Die Gesetze der Krystallochemie." *Naturwissenschaften*. 14, 477–485, **1926**, doi:10.1007/BF01507527/METRICS.

42. M. S. Vijaya Kumar, N. Higaki, K. Kuribayashi, T. Hibiya, S. Yoda, "Formation of orthorhombic and multiferroic hexagonal phases from an undercooled $RMnO_3$ (R = Rare-Earth element) melt using a containerless technique." *J. Am. Ceram. Soc.* 94, 281–288, **2011**, doi:10.1111/J.1551-2916.2010.04042.X.

43. T. Atsumi, T. Ohgushi, N. Kamegashira, "Studies on oxygen dissociation pressure of $LnMnO_3$ (Ln = rare earth) with the e.m.f. technique." *J. Alloys Compd.* 238, 35–40, **1996**, doi:10.1016/0925-8388(96)02253-0.

44. S. Hosokawa, "Hexagonal rare earth-iron mixed oxides ($REFeO_3$): Crystal structure, synthesis, and catalytic properties." *Front. Chem.* 7, 8, **2019**, doi:10.3389/FCHEM.2019.00008.

45. A. A. Bosak, C. Dubourdieu, J. P. Sénateur, O. Y. Gorbenko, A. R. Kaul, "Hexagonal rare earth (R = Eu-Dy) manganites: XRD study of epitaxially stabilized films." *Cryst. Eng.* 5, 355–364, **2002**, doi:10.1016/S1463-0184(02)00047-3.

46. I. E. Graboy, A. A. Bosak, O. Y. Gorbenko, A. R. Kaul, C. Dubourdieu, J. P. Sénateur, V. L. Svetchnikov, H. W. Zandbergen, "HREM study of epitaxially stabilized hexagonal rare earth manganites." *Chem. Mater.* 15, 2632–2637, **2003**, doi:10.1021/CM021315B.

47. S. Ishiwata, Y. Tokunaga, Y. Taguchi, Y. Tokura, "High-pressure hydrothermal crystal growth and multiferroic properties of a perovskite $YMnO_3$." *J. Am. Chem. Soc.* 133, 13818–13820, **2011**, doi:10.1021/ja205408m.

48. M. Počuča-Nešić, Z. Marinković Stanojević, Z. Branković, P. Cotič, S. Bernik, M. S. Góes, B. A. Marinković, J. A. Varela, G. Branković, "Mechanochemical synthesis of yttrium manganite." *J. Alloys Compd.* Complete, 451–456, **2013**, doi:10.1016/J.JALLCOM.2012.11.031.

49. A. Waintal, J. Chenavas, "Transformation sous haute pression de la forme hexagonale de MnT′O_3 (T′ = Ho, Er, Tm, Yb, Lu) en une forme perovskite." *Mater. Res. Bull.* 2, 819–822, **1967**, doi:10.1016/0025-5408(67)90009-8.

50. K. Uusi-Esko, J. Malm, N. Imamura, H. Yamauchi, M. Karppinen, "Characterization of $RMnO_3$ (R = Sc, Y, Dy-Lu): High-pressure synthesized metastable perovskites and their hexagonal precursor phases." *Mater. Chem. Phys.* 112, 1029–1034, **2008**, doi:10.1016/J.MATCHEMPHYS.2008.07.009.

51. C. Lin, J. Liu, X. Li, Y. Li, S. Chu, L. Xiong, R. Li, "Phase transformation in hexagonal $ErMnO_3$ under high pressure." *J. Appl. Phys.* 112, 113512-1, **2012**, doi:10.1063/1.4768285.

52. Y. Kawazoe, T. Kanomata, R. Note, "o-$HoMnO_3$ (synthesized under pressure)", High Pressure Materials Properties: Magnetic Properties of Oxides, *Springer*, 661–663, **2023**, doi: 10.1007/978-3-662-64593-2_177.

53. G. Szabo, "Thèse Doctorat ès Sciences," Lyon, **1969**.

54. H. W. Brinks, H. Fjellvåg, A. Kjekshus, "Synthesis of metastable perovskite-type $YMnO_3$ and $HoMnO_3$." *J. Solid State Chem.* 129, 334–340, **1997**, doi:10.1006/JSSC.1996.7261.

55. H. W. Brinks, J. Rodríguez-Carvajal, H. Fjellvåg, A. Kjekshus, B. C. Hauback, "Crystal and magnetic structure of orthorhombic $HoMnO_3$." *Phys. Rev. B - Condens. Matter Mater. Phys.* 63, 944111–9441112, **2001**, doi:10.1103/PhysRevB.63.094411.

56. P. A. Salvador, T. D. Doan, B. Mercey, B. Raveau, "Stabilization of $YMnO_3$ in a perovskite structure as a thin film." *Chem. Mater.* 10, 2592–2595, **1998**, doi:10.1021/cm9802797.

57. A. A. Bosak, A. Kamenev, I. E. Graboy, S. V. Antonov, O. Y. Gorbenko, A. R. Kaul, C. Dubourdieu, J. P. Senateur, V. L. Svechnikov, H. W. Zandbergen, B. Holländer, "Epitaxial phase stabilization phenomena in rare-earth manganites." *Thin Solid Films*. 400, 149–153, **2001**, doi:10.1016/S0040-6090(01)01501-2.

58. R. Wunderlich, C. Chiliotte, G. Bridoux, T. Maity, Ö. Kocabiyik, A. Setzer, M. Ziese, P. Esquinazi, "Structural, magnetic and electric properties of $HoMnO_3$ films on $SrTiO_3$(001)." *J. Magn. Magn. Mater.* 324, 460–465, **2012**, doi:10.1016/J.JMMM.2011.08.021.

59. Y. W. Windsor, S. W. Huang, Y. Hu, L. Rettig, A. Alberca, K. Shimamoto, V. Scagnoli, T. Lippert, C. W. Schneider, U. Staub, "Multiferroic properties of o-$LuMnO_3$ controlled by *b*-axis strain." *Phys.*

Rev. Lett. 113, 167202, **2014**, doi:10.1103/PhysRevLett.113.167202.

60. A. A. Bosak, C. Dubourdieu, J. P. Sénateur, O. Y. Gorbenko, A. R. Kaul, "Epitaxial stabilization of hexagonal $RMnO_3$ (R = Eu–Dy) manganites." *J. Mater. Chem.* 12, 800–801, **2002**, doi:10.1039/B110870K.

61. B. B. Van Aken, T. T. M. Palstra, A. Filippetti, N. A. Spaldin, "The origin of ferroelectricity in magnetoelectric $YMnO_3$." *Nat. Mater.* 3, 164–170, **2004**, doi:10.1038/nmat1080.

62. S. W. Cheong, M. Mostovoy, "Multiferroics: a magnetic twist for ferroelectricity." *Nat. Mater. 2007 61*. 6, 13–20, **2007**, doi:10.1038/nmat1804.

63. I. Kizhaev, S. Kizhaev, "Determination of the curie point of the ferroelectrics $YMnO_3$ and $YbMnO_3$ (High temperature X-ray examination of yttrium manganate and ytterbium manganate to determine Curie point)." *Sov. Physics-Solid State*. 7, 236–238, **1965**.

64. H. L. Yakel, W. C. Koehler, E. F. Bertaut, E. F. Forrat, "On the crystal structure of the manganese(III) trioxides of the heavy lanthanides and yttrium." *Acta Cryst.* 16, 957–962, **1963**, doi:10.1107/S0365110X63002589.

65. L. J. Wang, S. M. Feng, J. L. Zhu, R. C. Yu, C. Q. Jin, W. Yu, X. H. Wang, L. T. Li, "Ferroelectricity of multiferroic hexagonal $TmMnO_3$ ceramics synthesized under high pressure." *Appl. Phys. Lett.* 91, 172502, **2007**, doi:10.1063/1.2800816/334190.

66. A. Ghosh, J. R. Sahu, S. V. Bhat, C. N. R. Rao, "A Raman study of multiferroic $LuMnO_3$." *Solid State Sci.* 11, 1639–1642, **2009**, doi:10.1016/J.SOLIDSTATESCIENCES.2009.06.002.

67. N. Fujimura, T. Ishida, T. Yoshimura, T. Ito, "Epitaxially grown $YMnO_3$ film: New candidate for nonvolatile memory devices." *Appl. Phys. Lett.* 69, 1011–1013, **1996**, doi:10.1063/1.117969.

68. B. B. Van Aken, T. T. M. Palstra, A. Filippetti, N. A. Spaldin, "The origin of ferroelectricity in magnetoelectric $YMnO_3$." *Nat. Mater.* 3, 164–170, **2004**, doi:10.1038/nmat1080.

69. C. Y. Ren, "Atomic, electronic, and ferroelectric properties of manganite $RMnO_3$ (R = Ho, Er, Tm, Lu) in hexagonal and orthorhombic phases." *Phys. Rev. B - Condens. Matter Mater. Phys.* 79, 125113, **2009**, doi:10.1103/PhysRevB.79.125113.

70. T. Choi, Y. Horibe, H. T. Yi, Y. J. Choi, W. Wu, S. W. Cheong, "Insulating interlocked ferroelectric and structural antiphase domain walls in multiferroic $YMnO_3$." *Nat. Mater.* 9, 253–258, **2010**, doi:10.1038/nmat2632.

71. Q. Zhang, G. Tan, L. Gu, Y. Yao, C. Jin, Y. Wang, X. Duan, R. Yu, "Direct observation of multiferroic vortex domains in $YMnO_3$." *Sci. Rep.* 3, 1–5, **2013**, doi:10.1038/srep02741.

72. O. W. Sandvik, A. M. Mü, H. W. Ånes, M. Zahn, J. He, M. Fiebig, T. Lottermoser, T. Rojac, D. Meier, J. Schultheiß, "Pressure control of nonferroelastic ferroelectric domains in $ErMnO_3$." *Nano Lett.* 23, 6994–7000, **2023**, doi:10.1021/acs.nanolett.3c01638.

73. M. Lilienblum, E. Soergel, M. Fiebig, "Manipulation of ferroelectric vortex domains in hexagonal manganites." *J. Appl. Phys.* 110, **2011**, 052007-1, doi:10.1063/1.3623777.

74. E. Ruff, S. Krohns, M. Lilienblum, D. Meier, M. Fiebig, P. Lunkenheimer, A. Loidl, "Conductivity contrast and tunneling charge transport in the vortexlike ferroelectric domain patterns of multiferroic hexagonal $YMnO_3$." *Phys. Rev. Lett.* 118, 1–5, **2017**, doi:10.1103/PhysRevLett.118.036803.

75. J. A. Mundy, J. Schaab, Y. Kumagai, A. Cano, M. Stengel, I. P. Krug, D. M. Gottlob, H. Doğanay, M. E. Holtz, R. Held, Z. Yan, E. Bourret, C. M. Schneider, D. G. Schlom, D. A. Muller, R. Ramesh, N. A. Spaldin, D. Meier, H. Doğanay, *et al.*, "Functional electronic inversion layers at ferroelectric domain walls." *Nat. Mater.* 16, 622–627, **2017**, doi:10.1038/NMAT4878.

76. A. B. Mosberg, E. D. Roede, D. M. Evans, T. S. Holstad, E. Bourret, Z. Yan, A. T. J. Van Helvoort, D. Meier, "FIB lift-out of conducting ferroelectric domain walls in hexagonal manganites." *Appl. Phys. Lett.* 115, 1–5, **2019**, doi:10.1063/1.5115465.

77. J. Schultheiß, E. Lysne, L. Puntigam, J. Schaab, E. Bourret, Z. Yan, S. Krohns, D. Meier, "Charged ferroelectric domain walls for deterministic ac signal control at the nanoscale." *Nano Lett.* 21, 9560–9566, 2400091, **2021**, doi:10.1021/acs.nanolett.1c03182.

78. J. Schultheiß, T. Rojac, D. Meier, J. Schultheiß, D. Meier, "Unveiling alternating current electronic properties at ferroelectric domain walls." *Adv. Electron. Mater.* 8, 2100996, **2021**, doi:10.1002/aelm.202100996.

79. J. McCartan, P. W. Turner, J. P. V. McConville, K. Holsgrove, C. Cochard, A. Kumar, R. G. P. McQuaid, D. Meier, J. M. Gregg, "Fundamental aspects of conduction in charged $ErMnO_3$ domain walls." *Adv. Electron. Mater.*, 2400091, **2024**, doi:10.1002/aelm.202400091.

80. H. Pang, F. Zhang, M. Zeng, X. Gao, M. Qin, X. Lu, J. Gao, J. Dai, Q. Li, "Preparation of epitaxial hexagonal $YMnO_3$ thin films and observation of ferroelectric vortex domains." *npj Quantum Mater.* 1, 1–6, **2016**, doi:10.1038/npjquantmats.2016.15.

81. Z. Yan, D. Meier, J. Schaab, R. Ramesh, E. Samulon, E. Bourret, "Growth of high-quality hexagonal $ErMnO_3$ single crystals by the pressurized floating-zone method." *J. Cryst. Growth*. 409, 75–79, **2015**, doi:10.1016/J.JCRYSGRO.2014.10.006.

82. K. Yamauchi, F. Freimuth, S. Blügel, S. Picozzi, "Magnetically induced ferroelectricity in orthorhombic manganites: Microscopic origin and chemical trends." *Phys. Rev. B - Condens. Matter*

Mater. Phys. 78, 014403, **2008**, doi:10.1103/PhysRevB.78.014403.

83. D. Okuyama, S. Ishiwata, Y. Takahashi, K. Yamauchi, S. Picozzi, K. Sugimoto, H. Sakai, M. Takata, R. Shimano, Y. Taguchi, T. Arima, Y. Tokura, "Magnetically driven ferroelectric atomic displacements in orthorhombic $YMnO_3$." *Phys. Rev. B - Condens. Matter Mater. Phys.* 84, 054440, **2011**, doi:10.1103/PhysRevB.84.054440.

84. E. M. Choi, T. Maity, A. Kursumovic, P. Lu, Z. Bi, S. Yu, Y. Park, B. Zhu, R. Wu, V. Gopalan, H. Wang, J. L. MacManus-Driscoll, "Nanoengineering room temperature ferroelectricity into orthorhombic $SmMnO_3$ films." *Nat. Commun*. 11, 1–9, **2020**, doi:10.1038/s41467-020-16101-2.

85. T. Kimura, T. Goto, H. Shintani, K. Ishizaka, T. Arima, Y. Tokura, "Magnetic control of ferroelectric polarization." *Nature*. 426, 55–58, **2003**, doi:10.1038/nature02018.

86. T. Kimura, G. Lawes, T. Goto, Y. Tokura, A. P. Ramirez, "Magnetoelectric phase diagrams of orthorhombic $RMnO_3$ (R = Gd, Tb, and Dy)." *Phys. Rev. B - Condens. Matter Mater. Phys.* 71, 224425, **2005**, doi:10.1103/PhysRevB.71.224425.

87. H. Han, S. Song, J. H. Lee, K. J. Kim, G.-W. Kim, T. Park, H. M. Jang, "Switchable photovoltaic effects in hexagonal manganite thin films having narrow band gaps." *Chem. Mater.* 27, 7425–7432, **2015**, doi:10.1021/acs.chemmater.5b03408.

88. A. M. Kalashnikova, R. V. Pisarev, "Electronic structure of hexagonal rare-earth manganites RMnO3." *J. Exp. Theor. Phys. Lett.* 78, 143–147, **2003**, doi:10.1134/1.1618880.

89. S. Ying, Z. Ma, Z. Zhou, R. Tao, K. Yan, M. Xin, Y. Li, L. Pan, Y. Shi, "Device based on polymer schottky junctions and their applications: A review." *IEEE Access*. 8, 189646–189660, **2020**, doi:10.1109/ACCESS.2020.3030644.

90. F.-C. Chiu, "A review on conduction mechanisms in dielectric films." *Adv. Mater. Sci. Eng*. 2014, **2014**, doi:10.1155/2014/578168.

91. S. M. Sze, K. K. Ng, "Physics of Semiconductor Devices", *John Wiley & Sons*, **2007**, doi: 10.1002/0470068329.

92. S. Cheng, C. Xu, S. Deng, M. G. Han, S. Bao, J. Ma, C. Nan, W. Duan, L. Bellaiche, Y. Zhu, J. Zhu, "Interface reconstruction with emerging charge ordering in hexagonal manganite." *Sci. Adv.* 4, 1–6, **2018**, doi:10.1126/sciadv.aar4298.

93. J. L. Ortiz-Quiñonez, L. García-González, F. E. Cancino-Gordillo, U. Pal, "Particle dispersion and lattice distortion induced magnetic behavior of $La_{1-x}Sr_xMnO_3$ perovskite nanoparticles grown by salt-assisted solid-state synthesis." *Mater. Chem. Phys.* 246, 122834, **2020**, doi:10.1016/J.MATCHEMPHYS.2020.122834.

94. B. B. Van Aken, J.-W. G. Bos, R. A. De Groot, T. T. M. Palstra, "Asymmetry of electron and hole doping in $YMnO_3$." *Phys. Rev. B*. 63, 125127, **2000**, doi:10.1103/PhysRevB.63.125127.

95. W. J. Kim, M. A. Smeaton, C. Jia, B. H. Goodge, B. G. Cho, K. Lee, M. Osada, D. Jost, A. V. Ievlev, B. Moritz, L. F. Kourkoutis, T. P. Devereaux, H. Y. Hwang, "Geometric frustration of Jahn–Teller order in the infinite-layer lattice." *Nature*. 615, 237–243, **2023**, doi:10.1038/s41586-022-05681-2.

96. F. Wan, X. Bai, Y. Wang, Z. Hao, L. Gao, J. Li, N. S. Perov, C. Cao, "Effect of Zr-doping on the structure and magnetic properties of $YMnO_3$ ceramics." *J. Mater. Sci. Mater. Electron.* 34, 926, **2023**, doi:10.1007/S10854-023-10259-3.

97. T. S. Holstad, D. M. Evans, A. Ruff, D. R. Småbråten, J. Schaab, C. Tzschaschel, Z. Yan, E. Bourret, S. M. Selbach, S. Krohns, D. Meier, "Electronic bulk and domain wall properties in B-site doped hexagonal $ErMnO_3$." *Phys. Rev. B*. 97, 085143, **2018**, doi:10.1103/PhysRevB.97.085143.

98. L. Jeuvrey, O. Peña, A. Moure, C. Moure, "Synthesis and magnetic properties of hexagonal $Y(Mn,Cu)O_3$ multiferroic materials." *J. Magn. Magn. Mater.* 324, 717–722, **2012**, doi:10.1016/J.JMMM.2011.09.002.

99. A. J. Overton, J. L. Best, I. Saratovsky, M. A. Hayward, "Influence of topotactic reduction on the structure and magnetism of the multiferroic $YMnO_3$." *Chem. Mater.* 21, 4940–4948, **2009**, doi:10.1021/cm9021276.

100. Y. Du, X. Wang, D. Chen, Y. Yu, W. Hao, Z. Cheng, S. X. Dou, "Manipulation of domain wall mobility by oxygen vacancy ordering in multiferroic $YMnO_3$." *Phys. Chem. Chem. Phys.* 15, 20010–20015, **2013**, doi:10.1039/C3CP52892H.

101. S. Cheng, S. Q. Deng, Y. G. Zhao, X. F. Sun, J. Zhu, "Correlation between oxygen vacancies and sites of Mn ions in $YMnO_3$." *Appl. Phys. Lett.* 106, 062905, **2015**, doi:10.1063/1.4909547/29148.

102. S. Remsen, B. Dabrowski, "Synthesis and oxygen storage capacities of hexagonal $Dy_{1-x}Y_xMnO_{3+\delta}$." *Chem. Mater.* 23, 3818–3827, **2011**, doi:10.1021/cm2006956.

103. P. Ren, H. Fan, X. Wang, "Bulk conduction and nonlinear behaviour in multiferroic $YMnO_3$." *Appl. Phys. Lett.* 103, 152905, **2013**, doi:10.1063/1.4824916/25241.

104. J. A. Alonso, M. T. Casais, M. J. Martínez-Lope, I. Rasines, "High oxygen pressure preparation, structural refinement, and thermal behavior of RMn_2O_5 (R = La, Pr, Nd, Sm, Eu)." *J. Solid State Chem.* 129, 105–112, **1997**, doi:10.1006/JSSC.1996.7237.

105. O. Parkkima, S. Malo, M. Hervieu, E. L. Rautama, M. Karppinen, "New $RMnO_{3+\delta}$ (R=Y, Ho; $\delta \approx 0.35$) phases with modulated structure." *J. Solid State Chem.* 221, 109–115, **2015**, doi:10.1016/J.JSSC.2014.09.012.

106. J. A. M. van Roosmalen, E. H. P. Cordfunke, "The defect chemistry of $LaMnO_{3\pm\delta}$: 4. Defect model for $LaMnO_{3+\delta}$." *J. Solid State Chem.* 110, 109–112, **1994**, doi:10.1006/JSSC.1994.1143.

107. J. A. M. Van Roosmalen, E. H. P. Cordfunke, "The defect chemistry of $LaMnO_{3\pm\delta}$: 3. The density of (La,A)$MnO_{3+\delta}$ (A = Ca, Sr, Ba)." *J. Solid State Chem.* 110, 106–108, **1994**, doi:10.1006/JSSC.1994.1142.

108. J. A. M. van Roosmalen, E. H. P. Cordfunke, "The defect chemistry of $LaMnO_{3+\delta}$: 5. Thermodynamics." *J. Solid State Chem.* 110, 113–117, **1994**, doi:10.1006/JSSC.1994.1144.

109. J. A. M. Van Roosmalen, E. H. P. Cordfunke, R. B. Helmholdt, H. W. Zandbergen, "The defect chemistry of $LaMnO_{3\pm\delta}$: 2. Structural aspects of $LaMnO_{3+\delta}$." *J. Solid State Chem.* 110, 100–105, **1994**, doi:10.1006/JSSC.1994.1141.

110. J. Töpfer, J. B. Goodenough, "$LaMnO_{3+\delta}$ revisited." *J. Solid State Chem.* 130, 117–128, **1997**, doi:10.1006/JSSC.1997.7287.

111. A. Bosak, C. Dubourdieu, M. Audier, J. P. Sénateur, J. Pierre, "Compositional effects on the structure and magnetotransport properties of lacunar $La_{1-x}MnO_{3-\delta}$ films (x > 0) grown by MOCVD." *Appl. Phys. A Mater. Sci. Process.* 79, 1979–1984, **2004**, doi:10.1007/S00339-003-2179-4.

112. K. Bergum, H. Okamoto, H. Fjellvåg, T. Grande, M.-A. Einarsrud, S. M. Selbach, "Synthesis, structure and magnetic properties of nanocrystalline $YMnO_3$." *Dalt. Trans.* 40, 7583, **2011**, doi:10.1039/c1dt10536a.

113. J. A. Alonso, M. J. Martínez-Lope, M. T. Casais, M. T. Fernández-Díaz, "Evolution of the Jahn-Teller distortion of MnO_6 octahedra in $RMnO_3$ perovskites (R = Pr, Nd, Dy, Tb, Ho, Er, Y): A neutron diffraction study." *Inorg. Chem.* 39, 917–923, **2000**, doi:10.1021/ic990921e.

114. P. K. Todd, A. Wustrow, R. D. McAuliffe, M. J. McDermott, G. T. Tran, B. C. McBride, E. D. Boeding, D. O'Nolan, C. H. Liu, S. S. Dwaraknath, K. W. Chapman, S. J. L. Billinge, K. A. Persson, A. Huq, G. M. Veith, J. R. Neilson, "Defect-accommodating intermediates yield selective low-temperature synthesis of $YMnO_3$ polymorphs." *Inorg. Chem.* 59, 13639–13650, **2020**, doi:10.1021/acs.inorgchem.0c02023.

115. Z. A. Elsiddig, H. Xu, D. Wang, W. Zhang, X. Guo, Y. Zhang, Z. Sun, J. Chen, "Modulating Mn^{4+} ions and oxygen vacancies in nonstoichiometric $LaMnO_3$ perovskite by a facile sol-gel method as high-performance supercapacitor electrodes." *Electrochim. Acta*. 253, 422–429, **2017**, doi:10.1016/J.ELECTACTA.2017.09.076.

116. S. H. Skjærvø, E. T. Wefring, S. K. Nesdal, N. H. Gaukås, G. H. Olsen, J. Glaum, T. Tybell, S. M. Selbach, "Interstitial oxygen as a source of p-type conductivity in hexagonal manganites." *Nat.*

Commun. 7, 13745–13745, **2016**, doi:10.1038/NCOMMS13745.

117. K. Kamata, T. Nakajima, T. Nakamura, "Thermogravimetric study of rare earth manganites $AMnO_3$ (A = Sm, Dy,Y, Er, Yb) at 1200 °C." *Mater. Res. Bull.* 14, 1007–1012, **1979**, doi:10.1016/0025-5408(79)90065-5.

118. D. Varshney, P. Sharma, I. Mansuri, "Electrical resistivity and thermopower of La/Nd/$PrMnO_3$ manganites: Role of small polaron conduction." *AIP Conf. Proc.* 1349, 941–942, **2011**, doi:10.1063/1.3606168.

119. N. E. Massa, L. Del Campo, D. De Sousa Meneses, P. Echegut, M. J. Martínez-Lope, J. A. Alonso, "High temperature far-infrared dynamics of orthorhombic $NdMnO_3$: emissivity and reflectivity." *J. Phys. Condens. Matter*. 25, 235603, **2013**, doi:10.1088/0953-8984/25/23/235603.

120. A. Kumar, P. Sharma, Q. Fujun, H. Jiang, C. Jin, "Electrical resistivity behavior and small polaron conduction transport mechanism in semiconducting $RMnO_3$ manganites." *Adv. Mater.* 13, 16–19, **2024**, doi:10.11648/J.AM.20241301.13.

121. B. Wang, J. Yao, J. Wang, A. Chang, "Valence-induced distortion controls the resistivity and thermal stability of $Co_{2.77}Mn_{1.71}Fe_{1.10}Zn_{0.42}O_8$ ceramics." *Mater. Des.* 192, 108736, **2020**, doi:10.1016/J.MATDES.2020.108736.

122. S. R. Sehlin, H. U. Anderson, D. M. Sparlin, "Semiempirical model for the electrical properties of $La_{1-x}Ca_xCoO_3$." *Phys. Rev. B*. 52, 11681–11689, **1995**, doi:10.1103/PhysRevB.52.11681.

123. C. Moure, J. F. Fernandez, M. Villegas, P. Duran, "Non-ohmic behaviour and switching phenomena in $YMnO_3$-based ceramic materials." *J. Eur. Ceram. Soc.* 19, 131–137, **1999**, doi:10.1016/S0955-2219(98)00180-0.

124. D. M. Evans, T. S. Holstad, A. B. Mosberg, D. R. Småbråten, P. E. Vullum, A. L. Dadlani, K. Shapovalov, Z. Yan, E. Bourret, D. Gao, J. Akola, J. Torgersen, A. T. J. van Helvoort, S. M. Selbach, D. Meier, "Conductivity control via minimally invasive anti-Frenkel defects in a functional oxide." *Nat. Mater.* 19, 1254, **2020**, doi:10.1038/S41563-020-00823-1.

125. W. Wang, Y. Sun, D. Yuan, L. Zhang, Y. Zhao, Z. Dai, "Thermionic and Frenkel-Poole emission effects in orthorhombic $HoMnO_3$/Nb-doped $SrTiO_3$ epitaxial heterojunctions." *J. Appl. Phys.* 109, 073723, **2011**, doi:10.1063/1.3569849/919920.

126. D. Emin, "Generalized adiabatic polaron hopping: Meyer-neldel compensation and Poole-Frenkel behavior." *Phys. Rev. Lett.* 100, 166602, **2008**, doi:10.1103/PhysRevLett.100.166602.

127. Z. Wang, H. Yu, X. A. Tran, Z. Fang, J. Wang, H. Su, "Transport properties of HfO_{2-x} based resistive-switching memories." *Phys. Rev. B - Condens. Matter Mater. Phys.* 85, 195322, **2012**,

doi:10.1103/PhysRevB.85.195322.

128. N. Fujimura, S. I. Azuma, N. Aoki, T. Yoshimura, T. Ito, "Growth mechanism of $YMnO_3$ film as a new candidate for nonvolatile memory devices." *J. Appl. Phys.* 80, 7084–7088, **1996**, doi:10.1063/1.363719.

129. I. Ǵlard, C. Dubourdieu, S. Pailh̀s, S. Petit, C. Simon, "Neutron diffraction study of hexagonal manganite $YMnO_3$, $HoMnO_3$, and $ErMnO_3$ epitaxial films." *Appl. Phys. Lett.* 92, 90–93, **2008**, doi:10.1063/1.2943276.

130. T. Kordel, C. Wehrenfennig, D. Meier, T. Lottermoser, M. Fiebig, I. Gélard, C. Dubourdieu, J. W. Kim, L. Schultz, K. Dörr, "Nanodomains in multiferroic hexagonal $RMnO_3$ films (R = Y, Dy, Ho, Er)." *Phys. Rev. B - Condens. Matter Mater. Phys.* 80, 1–8, **2009**, doi:10.1103/PhysRevB.80.045409.

131. C. Dubourdieu, I. Gélard, O. Salicio, G. Saint-Girons, B. Vilquin, G. Hollinger, "Oxides heterostructures for nanoelectronics." *Int. J. Nanotechnol.* 7, 320–347, **2010**, doi:10.1504/IJNT.2010.031723.

132. I. Gélard, N. Jehanathan, H. Roussel, S. Gariglio, O. I. Lebedev, G. Van Tendeloo, C. Dubourdieu, "Off-stoichiometry effects on the crystalline and defect structure of hexagonal manganite $REMnO_3$ films (RE = Y, Er, Dy)." *Chem. Mater.* 23, 1232–1238, **2011**, doi:10.1021/cm1029358.

133. N. Aoki, N. Fujimura, T. Yoshimura, T. Ito, "Formation of $YMnO_3$ films directly on Si substrate." *J. Cryst. Growth*. 174, 796–800, **1997**, doi:10.1016/S0022-0248(97)00016-X.

134. H. Kitahata, K. Tadanaga, T. Minami, N. Fujimura, T. Ito, "Microstructure and dielectric properties of $YMnO_3$ thin films prepared by dip-coating." *J. Am. Ceram. Soc.* 81, 1357–1360, **1998**, doi:10.1111/J.1151-2916.1998.TB02491.X.

135. T. Yoshimura, N. Fujimura, T. Ito, "Ferroelectric properties of c-oriented $YMnO_3$ films deposited on Si substrates." *Appl. Phys. Lett.* 73, 414–416, **1998**, doi:10.1063/1.122269.

136. W. C. Shin, K. J. Choi, C. H. Yang, J. B. Park, S. G. Yoon, "Preparation of ferroelectric $YMnO_3$ thin films for nonvolatile memory devices by metalorganic chemical vapor deposition." *Integr. Ferroelectr.* 21, 319–329, **2006**, doi:10.1080/10584589808202073.

137. W. C. Yi, J. S. Choe, C. R. Moon, S. Il Kwun, J. G. Yoon, "Ferroelectric characterization of highly (0001)-oriented $YMnO_3$ thin films grown by chemical solution deposition." *Appl. Phys. Lett.* 73, 903–905, **1998**, doi:10.1063/1.122443.

138. D. C. Yoo, J. Y. Lee, I. S. Kim, Y. T. Kim, "Effects of post-annealing on the microstructure and ferroelectric properties of $YMnO_3$ thin films on Si." *J. Cryst. Growth*. 233, 243–247, **2001**, doi:10.1016/S0022-0248(01)01563-9.

139. D. C. Yoo, J. Y. Lee, I. S. Kim, Y. T. Kim, "Microstructure control of $YMnO_3$ thin films on Si (100) substrates." *Thin Solid Films*. 416, 62–65, **2002**, doi:10.1016/S0040-6090(02)00703-4.

140. H. Kitahata, K. Tadanaga, T. Minami, N. Fujimura, T. Ito, "Ferroelectricity of $YMnO_3$ thin films prepared via solution." *Appl. Phys. Lett.* 75, 719–721, **1999**, doi:10.1063/1.124493.

141. H. Nyung Lee, Y. Tae Kim, Y. K. Park, "Memory window of highly c-axis oriented ferroelectric thin films." *Appl. Phys. Lett.* 74, 3887–3889, **1999**, doi:10.1063/1.124213.

142. S. Imada, T. Kuraoka, E. Tokumitsu, H. Ishiwara, "Ferroelectricity of $YMnO_3$ thin films on Pt(111)/Al_2O_3(0001) and Pt(111)/Y_2O_3(111)/Si(111) structures grown by molecular beam epitaxy." *Jpn. J. Appl. Phys.* 40, 666–671, **2001**, doi:10.1143/JJAP.40.666.

143. K. J. Choi, W. C. Shin, S. G. Yoon, "Ferroelectric $YMnO_3$ thin films grown by metal-organic chemical vapor deposition for metal/ferroelectric/semiconductor field-effect transistors." *Thin Solid Films*. 384, 146–150, **2001**, doi:10.1016/S0040-6090(00)01803-4.

144. K. Suzuki, K. Nishizawa, T. Miki, K. Kato, "Low-temperature synthesis in vacuum of *c*-axis oriented ferroelectric $YMnO_3$ thin films using alkoxy-derived precursors." *Integr. Ferroelectr.* 40, 155–162, **2001**, doi:10.1080/10584580108010838.

145. Y. Chen, Y. Li, D. Zheng, L. Li, M. Zeng, M. Qin, Z. Hou, Z. Fan, X. Gao, X. Lu, Q. Li, J. M. Liu, "Domain structure and multiferroic properties of epitaxial hexagonal $ErMnO_3$ films." *J. Alloys Compd.* 821, 3–8, **2020**, doi:10.1016/j.jallcom.2019.153529.

146. N. Fujimura, H. Tanaka, H. Kitahata, K. Tadanaga, T. Yoshimura, T. I. T. Ito, T. M. T. Minami, T. I. Taichiro Ito, T. M. Tsutomu Minami, "$YMnO_3$ thin films prepared from solutions for non volatile memory devices." *Jpn. J. Appl. Phys.* 36, L1601, **1997**, doi:10.1143/JJAP.36.L1601.

147. C. I. Cheon, K. Y. Yun, J. S. Kim, J. H. Kim, "Ferroelectric properties of $YMnO_3$ thin films prepared by chemical solution deposition." *Integr. Ferroelectr.* 34, 73–80, **2001**, doi:10.1080/10584580108012876.

148. L. Zhou, Y. P. Wang, Z. G. Liu, W. Q. Zou, Y. W. Du, "Structure and ferroelectric properties of ferroelectromagnetic $YMnO_3$ thin films prepared by pulsed laser depositon." *Phys. Status Solidi Appl. Res.* 201, 497–501, **2004**, doi:10.1002/pssa.200306747.

149. D. Kim, D. Killingensmith, D. Dalton, V. Olariu, F. Gnadinger, M. Rahman, A. Mahmud, T. S. Kalkur, "Ferroelectric properties of $YMnO_3$ films deposited by metalorganic chemical vapor deposition on Pt/Ti/SiO2/Si substrates." *Mater. Lett.* 60, 295–297, **2006**, doi:10.1016/J.MATLET.2005.08.045.

150. Y. Romaguera-Barcelay, J. A. Moreira, A. Almeida, P. B. Tavares, L. Fernandes, J. Pérez de la Cruz,

"Persistence of the orthorhombic phase in $YMnO_3$ hexagonal thin films." *Ferroelectrics*. 498, 80–84, **2016**, doi:10.1080/00150193.2016.1168211.

151. H. Y. Guol, L. H. Wilson, J. B. Xul, W. Y. Cheung, N. Ke, B. Sundaral, E. Z. Luo, J. Lin, J. Yu, "Preparation and characterization of ferroelectric $YMnO_3$ thin film." *IEEE*, 657–659, **2002**, doi:10.1109/ISAF.2000.942406.

152. K. Uusi-Esko, J. Malm, M. Karppinen, "Atomic layer deposition of hexagonal and orthorhombic $YMnO_3$ thin films." *Chem. Mater.* 21, 5691–5694, **2009**, doi:10.1021/cm9020172.

153. J. H. Choi, C. Pham, J. Dorman, T. Kim, J. P. Chang, "Atomic layer deposition of $YMnO_3$ thin films." *J. Magn. Magn. Mater.* 498, 166146, **2020**, doi:10.1016/J.JMMM.2019.166146.

154. I. Iliescu, M. Boudard, L. Rapenne, O. Chaix-Pluchery, H. Roussel, "MOCVD selective growth of orthorhombic or hexagonal $YMnO_3$ phase on Si(100) substrate." *Appl. Surf. Sci.* 306, 27–32, **2014**, doi:10.1016/j.apsusc.2014.01.090.

155. J. Nordlander, M. D. Rossell, M. Campanini, M. Fiebig, M. Trassin, "Epitaxial integration of improper ferroelectric hexagonal $YMnO_3$ thin films in heterostructures." *Phys. Rev. Mater.* 4, 1–6, **2020**, doi:10.1103/PhysRevMaterials.4.124403.

156. K. N. Rathod, K. Gadani, D. Dhruv, V. G. Shrimali, S. Solanki, A. D. Joshi, J. P. Singh, K. H. Chae, K. Asokan, P. S. Solanki, N. A. Shah, " Effect of oxygen vacancy gradient on ion-irradiated Ca-doped $YMnO_3$ thin films ." *J. Vac. Sci. Technol. B*. 38, 062208, **2020**, doi:10.1116/6.0000507/588885.

157. K. Gadani, K. N. Rathod, D. Dhruv, V. G. Shrimali, B. Rajyaguru, J. Joseph, A. D. Joshi, D. D. Pandya, K. Asokan, P. S. Solanki, N. A. Shah, "Defects induced resistive switching behavior in Ca doped $YMnO_3$–based non–volatile memory devices through electronic excitations." *Mater. Sci. Semicond. Process.* 121, **2021**, doi:10.1016/j.mssp.2020.105347.

158. S. K. Lai, "Flash memories: Successes and challenges." *IBM J. Res. Dev.* 52, 529–535, **2008**, doi:10.1147/RD.524.0529.

159. A. S. Sokolov, H. Abbas, Y. Abbas, C. Choi, A. S. Sokolov, H. Abbas, Y. Abbas, C. Choi, "Towards engineering in memristors for emerging memory and neuromorphic computing: A review." *J. Semicond.* 42, 013101-013101–29, **2021**, doi:10.1088/1674-4926/42/1/013101.

160. A. Sawa, "Resistive switching in transition metal oxides." *Mater. Today*. 11, 28–36, **2008**, doi:10.1016/S1369-7021(08)70119-6.

161. G. Molas, E. Nowak, "Advances in emerging memory technologies: From data storage to artificial intelligence." *Appl. Sci.* 11, 11254, **2021**, doi:10.3390/APP112311254.

162. F. Masuoka, M. Asano, H. Iwahashi, T. Komuro, S. Tanaka, “A new flash E2PROM cell using triple polysilicon technology.” *1984 Int. Electron Devices Meet.*, 464–467, **1984**, doi:10.1109/IEDM.1984.190752.

163. T. Cho, Y. T. Lee, E. C. Kim, J. W. Lee, S. Choi, S. Lee, D. H. Kim, W. G. Han, Y. H. Lim, J. D. Lee, J. D. Choi, K. D. Suh, “A dual-mode NAND flash memory: 1-Gb multilevel and high-performance 512-Mb single-level modes.” *IEEE J. Solid-State Circuits*. 36, 1700–1706, **2001**, doi:10.1109/4.962291.

164. H. Tanaka, M. Kido, K. Yahashi, M. Oomura, R. Katsumata, M. Kito, Y. Fukuzumi, M. Sato, Y. Nagata, Y. Matsuoka, Y. Iwata, H. Aochi, A. Nitayama, “Bit Cost Scalable technology with and plug process for ultra high density flash memory.” *2007 IEEE Symp. VLSI Technol.*, 14–15, **2007**, doi:10.1109/VLSIT.2007.4339708.

165. “Renesas Electronics develops industry’s first 28nm embedded flash memory technology for microcontrollers,” *Renesas*, https://www.renesas.com/us/en/about/press-room/renesas-electronics-develops-industrys-first-28nm-embedded-flash-memory-technology-microcontrollers (accessed May 26, **2024**).

166. K. Moon, S. Lim, J. Park, C. Sung, S. Oh, J. Woo, J. Lee, H. Hwang, “RRAM-based synapse devices for neuromorphic systems.” *Faraday Discuss.* 213, 421–451, **2019**, doi:10.1039/C8FD00127H.

167. J. H. Byrne, R. Heidelberger, M. N. Waxham, “From molecules to networks: an introduction to cellular and molecular”, *Academic Press*, **2014**.

168. C. Bäumer, R. Dittmann, “Redox-based memristive metal-oxide devices”, Metal Oxide-Based Thin Film Structures, Elsevier, 2018, doi: 10.1016/B978-0-12-811166-6.00020-0.

169. M. Darwish, L. Pohl, “Insulator metal transition-based selector in crossbar memory arrays.” *Electron. Mater.* 5, 17–29, **2024**, doi:10.3390/ELECTRONICMAT5010002.

170. X. Cui, Y. Ma, F. Wei, X. Cui, “The synthesis method of logic circuits based on the NMOS-like RRAM gates.” *IEEE Access*. 9, 54466–54477, **2021**, doi:10.1109/ACCESS.2020.2967080.

171. F. Pan, S. Gao, C. Chen, C. Song, F. Zeng, “Recent progress in resistive random access memories: Materials, switching mechanisms, and performance.” *Mater. Sci. Eng. R Reports*. 83, 1–59, **2014**, doi:10.1016/J.MSER.2014.06.002.

172. G. Liu, Y. Chen, S. Gao, B. Zhang, R. W. Li, X. Zhuang, “Recent advances in resistive switching materials and devices: From memories to memristors.” *Eng. Sci.* 4, 4–43, **2018**, doi:10.30919/ES8D779.

173. S. Slesazeck, T. Mikolajick, “Nanoscale resistive switching memory devices: a review.”

Nanotechnology. 30, 352003, **2019**, doi:10.1088/1361-6528/AB2084.

174. G. S. Park, X. S. Li, D. C. Kim, R. J. Jung, M. J. Lee, S. Seo, "Observation of electric-field induced Ni filament channels in polycrystalline NiO_x film." *Appl. Phys. Lett.* 91, 222103, **2007**, doi:10.1063/1.2813617/334512.

175. K. Bejtka, G. Milano, C. Ricciardi, C. F. Pirri, S. Porro, "TEM nanostructural investigation of Ag-conductive filaments in polycrystalline ZnO-based resistive switching devices." *ACS Appl. Mater. Interfaces*. 12, 29451–29460, **2020**, doi:10.1021/ACSAMI.0C05038.

176. K. H. Son, H. S. Lee, "Grain boundary effect on the resistive switching characteristics of $SrTi_{1-x}Fe_xO_3$ directly patterned via photochemical organic-metal deposition." *Appl. Surf. Sci.* 575, 151754, **2022**, doi:10.1016/J.APSUSC.2021.151754.

177. M. N. Kozicki, M. Yun, L. Hilt, A. Singh, E. Society, "Applications of programmable resistance changes in metal-doped chalcogenides." *Electrochem. Soc.* 99, 298–309, **1999**.

178. M. Balakrishnan, T. Mikolajick, M. Mitkova, R. Symanczyk, M. Balakrishnan, C. Gopalan, T. Happ, M. Kozicki, M. Kund, M. Mitkova, M. Park, C.-U. Pinnow, J. Robertson, K.-D. Ufert, "Electrical characterization of solid state ionic memory elements." *Proc. Non-Volatile Mem. Technol. Symp.*, 17, **2003**.

179. I. Valov, R. Waser, J. R. Jameson, M. N. Kozicki, "Electrochemical metallization memories—fundamentals, applications, prospects." *Nanotechnology*. 22, 254003, **2011**, doi:10.1088/0957-4484/22/25/254003.

180. M. N. Kozicki, M. Balakrishnan, C. Gopalan, C. Ratnakumar, M. Mitkova, "Programmable metallization cell memory based on Ag-Ge-S and Cu-Ge-S solid electrolytes." *2005 Non-Volatile Mem. Technol. Symp. NVMTS05*, 83–89, **2005**, doi:10.1109/NVMT.2005.1541405.

181. K. Tsunoda, Y. Fukuzumi, J. R. Jameson, Z. Wang, P. B. Griffin, Y. Nishi, "Bipolar resistive switching in polycrystalline TiO_2 films." *Appl. Phys. Lett.* 90, 113501, **2007**, doi:10.1063/1.2712777/912990.

182. C.-J. Kim, S.-G. Yoon, K.-J. Choi, S.-O. Ryu, S.-M. Yoon, N.-Y. Lee, B.-G. Yu, "Characterization of silver-saturated Ge–Te chalcogenide thin films for nonvolatile random access memory." *J. Vac. Sci. Technol. B Microelectron. Nanom. Struct. Process. Meas. Phenom.* 24, 721–724, **2006**, doi:10.1116/1.2180260.

183. J. Van Den Hurk, V. Havel, E. Linn, R. Waser, I. Valov, "Ag/GeS_x/Pt-based complementary resistive switches for hybrid CMOS/Nanoelectronic logic and memory architectures." *Sci. Rep.* 3, 1–5, **2013**, doi:10.1038/srep02856.

184. Y. Yang, P. Gao, L. Li, X. Pan, S. Tappertzhofen, S. Choi, R. Waser, I. Valov, W. D. Lu, “Electrochemical dynamics of nanoscale metallic inclusions in dielectrics.” 5, 1–9, **2014**, doi: 10.1038/ncomms5232.

185. R. Bruchhaus, M. Honal, R. Symanczyk, M. Kund, “Selection of optimized materials for CBRAM based on HT-XRD and electrical test results.” *J. Electrochem. Soc.* 156, H729, **2009**, doi:10.1149/1.3160570/XML.

186. T. Sakamoto, K. Lister, N. Banno, T. Hasegawa, K. Terabe, M. Aono, “Electronic transport in Ta_2O_5 resistive switch.” *Appl. Phys. Lett.* 91, 092110–1, **2007**, doi:10.1063/1.2777170/144301.

187. F. Maudet, A. Hammud, M. Wollgarten, V. Deshpande, C. Dubourdieu, “Insights on the variability of Cu filament formation in the SiO_2 electrolyte of quantized-conductance conductive bridge random access memory devices.” *Nanotechnology*. 34, 245203, **2023**, doi:10.1088/1361-6528/ACBCD7.

188. S. Tappertzhofen, S. Menzel, I. Valov, R. Waser, “Redox processes in silicon dioxide thin films using copper microelectrodes.” *Appl. Phys. Lett.* 99, 1–4, **2011**, doi:10.1063/1.3662013/385396.

189. S. Tappertzhofen, H. Mündelein, I. Valov, R. Waser, “Nanoionic transport and electrochemical reactions in resistively switching silicon dioxide.” *Nanoscale*. 4, 3040–3043, **2012**, doi:10.1039/C2NR30413A.

190. S. Tappertzhofen, M. Hempel, I. Valov, R. Waser, “Proton mobility in SiO_2 thin films and impact of hydrogen and humidity on the resistive switching effect.” *Mater. Res. Soc. Symp. Proc.* 1330, 1–6, **2011**, doi: 10.1557/opl.2011.1198.

191. J. Zhou, “Resistive switching characteristics of PECVD-deposited porous SiO_2-based electrochemical metallisation memory cells.” *Electron. Lett.* 52, 965–966, **2016**, doi:10.1049/EL.2015.4058.

192. S. R. Nandakumar, M. Minvielle, S. Nagar, C. Dubourdieu, B. Rajendran, “A 250 mV Cu/SiO_2/W memristor with half-integer quantum conductance states.” *Nano Lett.* 16, 1602–1608, **2016**, doi:10.1021/acs.nanolett.5b04296.

193. B. Cheng, A. Emboras, Y. Salamin, F. Ducry, P. Ma, Y. Fedoryshyn, S. Andermatt, M. Luisier, J. Leuthold, “Ultra compact electrochemical metallization cells offering reproducible atomic scale memristive switching.” *Commun. Phys.* 2, 1–9, **2019**, doi:10.1038/s42005-019-0125-9.

194. K. Terabe, T. Hasegawa, T. Nakayama, M. Aono, “Quantized conductance atomic switch.” *Nature*. 433, 47–50, **2005**, doi:10.1038/nature03190.

195. J. J. Yang, I. H. Inoue, T. Mikolajick, C. S. Hwang, “Metal oxide memories based on

thermochemical and valence change mechanisms." *MRS Bull.* 37, 131–137, **2012**, doi:10.1557/mrs.2011.356.

196. R. Waser, R. Dittmann, C. Staikov, K. Szot, "Redox-based resistive switching memories nanoionic mechanisms, prospects, and challenges." *Adv. Mater.* 21, 2632–2663, **2009**, doi:10.1002/adma.200900375.

197. R. Waser, "Redox-based resistive switching memories." *J. Nanosci. Nanotechnol.* 12, 7628–7640, **2012**, doi:10.1166/JNN.2012.6652.

198. A. Padovani, L. Larcher, P. Padovani, C. Cagli, B. De Salvo, "Understanding the role of the Ti metal electrode on the forming of HfO 2-based RRAMs", *2012 4th IEEE International Memory Workshop, IMW,* 2012, 1–4, doi: 10.1109/IMW.2012.6213667.

199. B. Traore, P. Blaise, B. Sklenard, E. Vianello, B. Magyari-Kope, Y. Nishi, "HfO_2/Ti Interface Mediated Conductive Filament Formation in RRAM: An Ab Initio Study." *IEEE Trans. Electron Devices*. 65, 507–513, **2018**, doi:10.1109/TED.2017.2785352.

200. S. U. Sharath, S. Vogel, L. Molina-Luna, E. Hildebrandt, C. Wenger, J. Kurian, M. Duerrschnabel, T. Niermann, G. Niu, P. Calka, M. Lehmann, H. J. Kleebe, T. Schroeder, L. Alff, "Control of switching modes and conductance quantization in oxygen engineered HfO_x based memristive devices." *Adv. Funct. Mater.* 27, 1700432, **2017**, doi:10.1002/ADFM.201700432.

201. S. Petzold, E. Piros, R. Eilhardt, A. Zintler, T. Vogel, N. Kaiser, A. Radetinac, P. Komissinskiy, E. Jalaguier, E. Nolot, C. Charpin-Nicolle, C. Wenger, L. Molina-Luna, E. Miranda, L. Alff, "Tailoring the switching dynamics in yttrium oxide-based RRAM devices by oxygen engineering: From digital to multi-level quantization toward analog switching." *Adv. Electron. Mater.* 6, **2020**, doi:10.1002/aelm.202000439.

202. M. Hellenbrand, J. MacManus-Driscoll, "Multi-level resistive switching in hafnium-oxide-based devices for neuromorphic computing." *Nano Converg.* 10, 1–20, **2023**, doi:10.1186/S40580-023-00392-4.

203. Z. Chen, F. Zhang, B. Chen, Y. Zheng, B. Gao, L. Liu, X. Liu, J. Kang, "High-performance HfOx/AlOy-based resistive switching memory cross-point array fabricated by atomic layer deposition." *Nanoscale Res. Lett.* 10, 1–7, **2015**, doi:10.1186/S11671-015-0738-1/FIGURES/7.

204. S. K. Vishwanath, H. Woo, S. Jeon, "Enhancement of resistive switching properties in Al_2O_3 bilayer-based atomic switches: multilevel resistive switching." *Nanotechnology*. 29, 235202, **2018**, doi:10.1088/1361-6528/AAB6A3.

205. U. Böttger, M. von Witzleben, V. Havel, K. Fleck, V. Rana, R. Waser, S. Menzel, "Picosecond

multilevel resistive switching in tantalum oxide thin films." *Sci. Rep.* 10, 1–9, **2020**, doi:10.1038/s41598-020-73254-2.

206. T. Gao, J. Feng, H. Ma, X. Zhu, "The ovonic threshold switching characteristics in Si_xTe_{1-x} based selector devices." *Appl. Phys. A Mater. Sci. Process.* 124, 1–8, **2018**, doi:10.1007/S00339-018-2153-9/FIGURES/2.

207. R. Midya, Z. Wang, J. Zhang, S. E. Savel, C. Li, M. Rao, M. Hyung Jang, S. Joshi, H. Jiang, P. Lin, K. Norris, N. Ge, Q. Wu, M. Barnell, Z. Li, H. L. Xin, R. Stanley Williams, Q. Xia, J. Joshua Yang, *et al.*, "Anatomy of Ag/hafnia-based selectors with 1010 nonlinearity." *Adv. Mater.* 29, 1604457, **2017**, doi:10.1002/ADMA.201604457.

208. M. D. Pickett, S. Williams, "Sub-100 fJ and sub-nanosecond thermally driven threshold switching in niobium oxide crosspoint nanodevices." *IOP Publ. Nanotechnol. Nanotechnol.* 23, 215202–215211, **2012**, doi:10.1088/0957-4484/23/21/215202.

209. S. Li, X. Liu, S. K. Nandi, R. G. Elliman, "Anatomy of filamentary threshold switching in amorphous niobium oxide." *Nanotechnology*. 29, 375705, **2018**, doi:10.1088/1361-6528/AACEE4.

210. G. A. Gibson, S. Musunuru, J. Zhang, K. Vandenberghe, J. Lee, C. C. Hsieh, W. Jackson, Y. Jeon, D. Henze, Z. Li, R. Stanley Williams, "An accurate locally active memristor model for S-type negative differential resistance in NbO_x." *Appl. Phys. Lett.* 108, 23505, **2016**, doi:10.1063/1.4939913/566101.

211. M. Herzig, M. Weiher, A. Ascoli, R. Tetzlaff, T. Mikolajick, S. Slesazeck, "Improvement of NbO_x-based threshold switching devices by implementing multilayer stacks." *Semicond. Sci. Technol.* 34, 075005, **2019**, doi:10.1088/1361-6641/AB1DA3.

212. Z. Wang, S. Kumar, Y. Nishi, H. S. P. Wong, "Transient dynamics of NbO_x threshold switches explained by Poole-Frenkel based thermal feedback mechanism." *Appl. Phys. Lett.* 112, 193503, **2018**, doi:10.1063/1.5027152.

213. Z. Wang, S. Kumar, H. S. P. Wong, Y. Nishi, "Effect of thermal insulation on the electrical characteristics of NbO_x threshold switches." *Appl. Phys. Lett.* 112, 73102, **2018**, doi:10.1063/1.5015941/36277.

214. X. Liu, S. Md. Sadaf, M. Son, J. Park, J. Shin, W. Lee, K. Seo, D. Lee, H. Hwang, "Co-occurrence of threshold switching and memory switching in $Pt/NbO_x/Pt$ cells for crosspoint memory applications." *IEEE Electron Device Lett.* 33, 236–238, **2012**, doi:10.1109/LED.2011.2174452.

215. S. Kumar, M. D. Pickett, J. P. Strachan, G. Gibson, Y. Nishi, R. S. Williams, "Local temperature redistribution and structural transition during Joule-heating-driven conductance switching in VO_2."

Adv. Mater. 25, 6128–6132, **2013**, doi:10.1002/ADMA.201302046.

216. A. S. Alexandrov, A. M. Bratkovsky, B. Bridle, S. E. Savel'Ev, D. B. Strukov, R. Stanley Williams, "Current-controlled negative differential resistance due to Joule heating in TiO_2." *Appl. Phys. Lett.* 99, 202104, **2011**, doi:10.1063/1.3660229/384963.

217. J. M. Goodwill, A. A. Sharma, D. Li, J. A. Bain, M. Skowronski, "Electro-thermal model of threshold switching in TaO_x-based devices." *ACS Appl. Mater. Interfaces*. 9, 11704–11710, **2017**, doi:10.1021/acsami.6b16559.

218. S. Lashkare, A. Bhat, U. Ganguly, "Temperature dependence of volatile current shoot-up in $PrMnO_3$ based selector-less RRAM." *ArXiv*, **2019**, doi:10.48550/arXiv.2002.00703.

219. S. Slesazeck, H. Mähne, H. Wylezich, A. Wachowiak, J. Radhakrishnan, A. Ascoli, R. Tetzlaff, T. Mikolajick, "Physical model of threshold switching in NbO_2 based memristors." *RSC Adv.* 5, 102318–102322, **2015**, doi:10.1039/C5RA19300A.

220. A. Ascoli, S. Slesazeck, H. Mähne, R. Tetzlaff, T. Mikolajick, "Nonlinear dynamics of a locally-active memristor." *IEEE Trans. Circuits Syst. I Regul. Pap.* 62, 1165–1174, **2015**, doi:10.1109/TCSI.2015.2413152.

221. Z. Wang, S. Kumar, R. S. Williams, Y. Nishi, H. S. P. Wong, "Intrinsic limits of leakage current in self-heating-triggered threshold switches." *Appl. Phys. Lett.* 114, **2019**, doi:10.1063/1.5089261, doi:10.1063/1.5089261.

222. S. Kumar, J. P. Strachan, R. S. Williams, "Chaotic dynamics in nanoscale NbO_2 Mott memristors for analogue computing." *Nature*. 548, 318–321, **2017**, doi:10.1038/NATURE23307.

223. S. Li, X. Liu, S. K. Nandi, S. K. Nath, R. G. Elliman, "Origin of current-controlled negative differential resistance modes and the emergence of composite characteristics with high complexity." *Adv. Funct. Mater.* 29, 1905060, **2019**, doi:10.1002/ADFM.201905060.

224. M. Zhu, K. Ren, Z. Song, "Ovonic threshold switching selectors for three-dimensional stackable phase-change memory." *MRS Bull.* 44, 715–720, **2019**, doi:10.1557/MRS.2019.206.

225. J. M. Goodwill, G. Ramer, D. Li, B. D. Hoskins, G. Pavlidis, J. J. Mcclelland, A. Centrone, J. A. Bain, M. Skowronski, "Spontaneous current constriction in threshold switching devices." *Nat. Commun.* 10, 1628, **2019**, doi:10.1038/s41467-019-09679-9.

226. T. Hennen, D. Bedau, J. A. J. Rupp, C. Funck, S. Menzel, M. Grobis, R. Waser, D. J. Wouters, "Forming-free Mott-oxide threshold selector nanodevice showing s-type NDR with high endurance (> 10 12 cycles), excellent Vth stability (5%), fast (< 10 ns) switching, and promising scaling properties", 2018 IEEE International Electron Devices Meeting (IEDM), San Francisco, CA, USA,

2018, 37.5.1-37.5.4, doi: 10.1109/IEDM.2018.8614618.

227. M. Steyaert, A. Sarafianos, N. Butzen, E. De Pelecijn, "Fully integrated power management: The missing link?" *2017 Eur. Conf. Circuit Theory Des. ECCTD*. 10, **2017**, doi:10.1109/ECCTD.2017.8093304.

228. N. Rouger, "Challenges and benefits of microelectronics for power electronics: From integrated optical driving to optimized power semiconductor switches." *Conf. Proc. - 10th Conf. Ph. D. Res. Microelectron. Electron. PRIME 2014*, **2014**, doi:10.1109/PRIME.2014.6872675.

229. K. Wasa, I. Kanno, H. Kotera, H. Adachi, T. HAta, T. Matsushima, T. Motohiro, K. Tominaga, "Sputter Deposition Technology", *Elsevier*, **2012**, doi: 10.1016/C2010-0-67037-4.

230. D. M. Mattox, "Handbook of Physical Vapor Deposition (PVD) Processing", *Elsevier*, **2010**, doi: 10.1016/C2009-0-18800-1.

231. "Maskless Laser Lithography", *Heidelberg Instruments*, https://heidelberg-instruments.com/core-technologies/maskless-laser-lithography (accessed May 26, **2024**).

232. "LOR Lift-off Resists", *MICROCHEM*,. https://amolf.nl/wp-content/uploads/2016/09/datasheets_LOR_datasheet.pdf (accessed May 26, **2024**).

233. M. Birkholz, "Thin film analysis by X-ray scattering", *Viley-VCH*, **2005**, doi: 10.1002/3527607595.

234. W. C. Marra, P. Eisenberger, A. Y. Cho, "X-ray total-external-reflection–Bragg diffraction: A structural study of the GaAs-Al interface." *J. Appl. Phys.* 50, 6927–6933, **1979**, doi:10.1063/1.325845.

235. H. Fujiwara, "Spectroscopic ellipsometry for photovoltaics", *Springer*, **2018**, doi: 10.1007/978-3-319-75377-5.

236. R. M. A. Azzam, N. M. Bashara, "Instrumentation and techniques for ellipsometry." *Ellipsom. Polariz. Light*, 269–363, **1977**.

237. H. Fujiwara, "Spectroscopic ellipsometry: Principles and applications", *John Wiley & Sons*, **2007**, doi:10.1002/9780470060193.

238. C. Xu, B. Min, R. Reineke-Koch, "Extended Tauc-Lorentz model (XTL) with log-normal distributed bandgap energies for optical permittivity in polycrystalline semiconductors." *AIP Adv.* 12, 115007, **2022**, doi:10.1063/5.0119256/2819709.

239. "Multi75-G AFM Probe", *BudgetSensors*, https://www.budgetsensors.com/force-modulation-afm-probe-multi75, (accessed May 26, **2024**).

240. "PPP-EFM", *NANOSENSORSTM*, https://www.nanosensors.com/pointprobe-plus-electrostatic-

force-microscopy-ptir5-coating-afm-tip-PPP-EFM, (accessed May 26, **2024**).

241. "HQ:NSC14/Pt Conductive Soft Tapping Mode AFM Probe", *MikroMasch*, https://www.spmtips.com/afm-tip-hq-nsc14-pt, (accessed May 26, **2024**).

242. G. Schitter, P. Menold, H. F. Knapp, F. Allgöwer, A. Stemmer, "High performance feedback for fast scanning atomic force microscopes." *Rev. Sci. Instrum.* 72, 3320–3327, **2001**, doi:10.1063/1.1387253.

243. G. Meyer, N. M. Amer, "Novel optical approach to atomic force microscopy." *Appl. Phys. Lett.* 53, 1045–1047, **1988**, doi:10.1063/1.100061.

244. F. J. Giessibl, "AFM's path to atomic resolution." *Materialstoday*, 32–41, **2005**, doi:10.1016/S1369-7021(05)00844-8.

245. A. Buldum, S. Ciraci, C. Y. Fong, J. S. Nelson, "Interpretation of long-range interatomic force." *Phys. Rev. B*. 59, 5120–5125, **1999**, doi:10.1103/PhysRevB.59.5120.

246. P. Eyben, M. Xu, N. Duhayon, T. Clarysse, S. Callewaert, W. Vandervorst, "Scanning spreading resistance microscopy and spectroscopy for routine and quantitative two-dimensional carrier profiling." *J. Vac. Sci. Technol. B*. 20, 471–478, **2002**, doi:10.1116/1.1424280.

247. L. Jiang, J. Weber, F. M. Puglisi, P. Pavan, L. Larcher, W. Frammelsberger, G. Benstetter, M. Lanza, "Understanding current instabilities in conductive atomic force microscopy." *Materials (Basel).* 12, 1–10, **2019**, doi:10.3390/MA12030459.

248. S. A. Sumaiya, A. Martini, M. Z. Baykara, "Improving the reliability of conductive atomic force microscopy-based electrical contact resistance measurements." *Nano Express*. 1, 030023, **2020**, doi:10.1088/2632-959X/ABCAE0.

249. E. Soergel, "Piezoresponse force microscopy (PFM)." *J. Phys. D. Appl. Phys.* 44, 464003, **2011**, doi:10.1088/0022-3727/44/46/464003.

250. D. Seol, B. Kim, Y. Kim, "Non-piezoelectric effects in piezoresponse force microscopy." *Curr. Appl. Phys.* 17, 661–674, **2017**, doi:10.1016/J.CAP.2016.12.012.

251. A. Gruverman, M. Alexe, D. Meier, "Piezoresponse force microscopy and nanoferroic phenomena." *Nat. Commun.* 10, 1–9, **2019**, doi:10.1038/s41467-019-09650-8.

252. K. Akhtar, S. A. Khan, S. B. Khan, A. M. Asiri, "Scanning electron microscopy: Principle and applications in nanomaterials characterization", Handbook of materials characterization, *Springer,* **2018**, doi: 10.1007/978-3-319-92955-2_4.

253. I. Müllerová, I. Konvalina, "Collection of secondary electrons in scanning electron microscopes."

J. Microsc. 236, 203–210, **2009**, doi:10.1111/J.1365-2818.2009.03189.X.

254. G. S. Bumbrah, R. M. Sharma, "Raman spectroscopy – Basic principle, instrumentation and selected applications for the characterization of drugs of abuse." *Egypt. J. Forensic Sci.* 6, 209–215, **2016**, doi:10.1016/J.EJFS.2015.06.001.

255. T. Dey, "Microplastic pollutant detection by Surface Enhanced Raman Spectroscopy (SERS): a mini-review." *Nanotechnol. Environ. Eng.* 8, 41–48, **2023**, doi:10.1007/S41204-022-00223-7/FIGURES/5.

256. N. Altangerel, B. W. Neuman, P. R. Hemmer, V. V. Yakovlev, N. Rajil, Z. Yi, A. V. Sokolov, M. O. Scully, "Label-free drug interaction screening via Raman microscopy." *Appl. Phys. Sci.* 120, 2218826120, **2023**, doi:10.1073/pnas.2218826120.

257. F. A. Stevie, C. L. Donley, "Introduction to X-ray photoelectron spectroscopy." *J. Vac. Sci. Technol. A*. 38, 63204, **2020**, doi:10.1116/6.0000412.

258. W. H. Doh, V. Papaefthimiou, S. Zafeiratos, "Applications of synchrotron-based X-ray photoelectron spectroscopy in the characterization of nanomaterials", Surface Science Tools for Nanomaterials Characterization, *Springer*, **2015**, doi: 10.1007/978-3-662-44551-8_9.

259. "Main Vision Manual." *Radiant Technologies*, https://download.ferroelectricdevices.com/MainVisionManualHTML/index.htm, (accessed May 26, **2024**).

260. M. Lallart, "Ferroelectrics - physical effects", *InTech*, **2011**, doi: 10.5772/942.

261. H. Y. Kuo, Y. H. Cheng, H. Chang, J. S. Shaw, R. Lee, "Design of electrodes on gold test strips for enhanced accuracy in glucose measurement." *J. Sensors*. 2019, 1–10, **2019**, doi:10.1155/2019/8627198.

262. M. Rossle, W. Leitenberger, M. Reinhardt, A. Koc, J. Pudell, C. Kwamen, M. Bargheer, "The time-resolved hard X-ray diffraction endstation KMC-3 XPP at BESSY II." *J. Synchrotron Radiat.* 28, 948–960, **2021**, doi:10.1107/S1600577521002484.

263. C. L. T. Kwamen, "Investigating the Dynamics of Polarization Reversal in Ferroelectric Thin Films by Time-Resolved X-ray Diffraction," Doctoral dissertation, Uni Potsdam, **2018**.

264. "B1500A Semiconductor Device Analyzer" *Keysight*, https://www.keysight.com/in/en/assets/7018-03960/technical-overviews/5991-2443.pdf, (accessed May 26, **2024**).

265. J. Schultheiß, F. Xue, E. Roede, H. W. Ånes, F. H. Danmo, S. M. Selbach, L.-Q. Chen, D. Meier, J. Schultheiß, E. Roede, H. W. Ånes, F. H. Danmo, S. M. Selbach, D. Meier, F. Xue, L.-Q. Chen,

"Confinement-driven inverse domain scaling in polycrystalline $ErMnO_3$." *Adv. Mater.* 34, 2203449, **2022**, doi:10.1002/adma.202203449.

266. R. Wu, S. Schmitt, F. Maudet, D. J. Kim, V. Deshpande, C. Dubourdieu, "Electrochemical metallization memristive devices with Al active electrode using engineered mixed hexagonal/orthorhombic polycrystalline $YMnO_3$." *Small Struct.* 5, 2300494, **2024**, doi:10.1002/sstr.202300494.

267. N. Bishop, J. Walker, C. T. Deroo, T. Liu, M. Tendulkar, V. Cotroneo, E. N. Hertz, V. Kradinov, E. D. Schwartz, P. B. Reid, T. N. Jackson, S. Trolier-Mckinstry, S. Trolier, "Thickness distribution of sputtered films on curved substrates for adjustable X-ray optics." *J. Astron. Telesc. INSTRUMENTS, Syst.* 5, 21005, **2019**, doi:10.1117/1.JATIS.5.2.021005.

268. E. Gebhardt, W. Köster, "Das System Platin-Kobalt mit besonderer Berücksichtigung der Phase CoPt." *Int. J. Mater. Res.* 32, 253–261, **1940**, doi:10.1515/IJMR-1940-320801.

269. D. P. Kozlenko, S. E. Kichanov, S. Lee, J. G. Park, V. P. Glazkov, B. N. Savenko, "High-pressure effect on the crystal and magnetic structures of the frustrated antiferromagnet $YMnO_3$." *J. Exp. Theor. Phys. Lett. 2005 824*. 82, 193–197, **2005**, doi:10.1134/1.2121813.

270. V. E. Wood, A. E. Austin, E. W. Collings, K. C. Brog, "Magnetic properties of heavy-rare-earth orthomanganites." *J. Phys. Chem. Solids*. 34, 859–868, **1973**, doi:10.1016/S0022-3697(73)80088-5.

271. S. Hirai, A. M. Dos Santos, M. C. Shapiro, J. J. Molaison, N. Pradhan, M. Guthrie, C. A. Tulk, I. R. Fisher, W. L. Mao, "Giant atomic displacement at a magnetic phase transition in metastable Mn_3O_4." *Phys. Rev. B - Condens. Matter Mater. Phys.* 87, 014417, **2013**, doi:10.1103/PhysRevB.87.014417.

272. S. A. Prokudina, Y. S. Rubinchik, M. M. Pavlyuchenko, "Solid-phase reactions in system Y_2O_3-Mn_2O_3." *Inorg. Mater.* 12, 598–603, **1976**.

273. R. K. Kirby, "Platinum - a thermal expansion reference material." *Int. J. Thermophys.* 12, 679–685, **1991**, doi:10.1007/BF00534223.

274. A. Prikockyt˙, D. Bilc, P. Hermet, C. Dubourdieu, P. Ghosez, "First-principles calculations of the structural and dynamical properties of ferroelectric $YMnO_3$." *Phys. Rev. B*. 84, 214301, **2011**, doi:10.1103/PhysRevB.84.214301.

275. M. Iliev, H. Lee, V. Popov, "Raman- and infrared-active phonons in hexagonal: Experiment and lattice-dynamical calculations." *Phys. Rev. B - Condens. Matter Mater. Phys.* 56, 2488–2494, **1997**, doi:10.1103/PhysRevB.56.2488.

276. M. N. Iliev, M. V. Abrashev, H. G. Lee, V. N. Popov, Y. Y. Sun, C. Thomsen, R. L. Meng, C. W.

Chu, “Raman active phonons in orthorhombic $YMnO_3$ and $LaMnO_3$.” *J. Phys. Chem. Solids*. 59, 1982–1984, **1998**, doi:10.1016/S0022-3697(98)00161-9.

277. M. Iliev, M. Abrashev, “Raman spectroscopy of orthorhombic perovskitelike $YMnO_3$ and $LaMnO_3$.” *Phys. Rev. B - Condens. Matter Mater. Phys.* 57, 2872–2877, **1998**, doi:10.1103/PhysRevB.57.2872.

278. M. Sánchez-Pérez, O. J. Dura, J. P. Andrés, R. López Antón, J. A. Gonzalez, M. A. López De La Torre, “Influence of the orthorhombic phase content on the dielectric and magnetic properties of $YMnO_3$.” *J. Appl. Phys.* 126, 224103, **2019**, doi:10.1063/1.5125217.

279. Q. Zhang, G. Tan, L. Gu, Y. Yao, C. Jin, Y. Wang, X. Duan, R. Yu, “Direct observation of multiferroic vortex domains in $YMnO_3$.” *Sci. Reports*. 3, 1–5, **2013**, doi:10.1038/srep02741.

280. L. Kuerten, S. Krohns, P. Schoenherr, K. Holeczek, E. Pomjakushina, T. Lottermoser, M. Trassin, D. Meier, M. Fiebig, “Local control of improper ferroelectric domains in $YMnO_3$.” *Phys. Rev. B*. 102, 94108, **2020**, doi:10.1103/PhysRevB.102.094108.

281. V. R. Rayapati, D. Bürger, N. Du, C. Kowol, D. Blaschke, H. Stöcker, P. Matthes, R. Patra, I. Skorupa, S. E. Schulz, H. Schmidt, “Charged domains in ferroelectric, polycrystalline yttrium manganite thin films resolved with scanning electron microscopy.” *Nanotechnology*. 31, 31–32, **2020**, doi:10.1088/1361-6528/ab8b09.

282. H. Lu, C. W. Bark, D. Esque De Los Ojos, J. Alcala, C. B. Eom, G. Catalan, A. Gruverman, “Mechanical writing of ferroelectric polarization.” *Science (80-.).* 335, 59–61, **2012**, doi:10.1126/science.1218693.

283. Y. Gu, Z. Hong, J. Britson, L. Q. Chen, “Nanoscale mechanical switching of ferroelectric polarization via flexoelectricity.” *Appl. Phys. Lett.* 106, 22904, **2015**, doi:10.1063/1.4905837.

284. D. J. Kim, T. R. Paudel, H. Lu, J. D. Burton, J. G. Connell, E. Y. Tsymbal, S. S. A. Seo, A. Gruverman, “Room-temperature ferroelectricity in hexagonal $TbMnO_3$ thin films.” *Adv. Mater.* 26, 7660–7665, **2014**, doi:10.1002/adma.201403301.

285. G. Sassine, S. La Barbera, N. Najjari, M. Minvielle, C. Dubourdieu, F. Alibart, “Interfacial versus filamentary resistive switching in TiO_2 and HfO_2 devices.” *J. Vac. Sci. Technol. B*. 34, 012202, **2016**, doi:10.1116/1.4940129.

286. W. M. Haynes, D. R. Lide, T. J. Bruno, “CRC handbook of chemistry and physics : a ready-reference book of chemical and physical data.”, *CRC Press*, Boca Raton, **2012**.

287. M. Lübben, I. Valov, M. Lübben, I. Valov, “Active electrode redox reactions and device behavior in ECM type resistive switching memories.” *Adv. Electron. Mater.* 5, 1800933, **2019**, doi:10.1002/AELM.201800933.

288. S. Tappertzhofen, H. Mündelein, I. Valov, R. Waser, "Nanoionic transport and electrochemical reactions in resistively switching silicon dioxide." *Nanoscale*. 4, 3040–3043, **2012**, doi:10.1039/c2nr30413a.

289. I. Valov, M. N. Kozicki, "Cation-based resistance change memory." *J. Phys. D. Appl. Phys.* 46, 074005, **2013**, doi:10.1088/0022-3727/46/7/074005.

290. I. Valov, E. Linn, S. Tappertzhofen, S. Schmelzer, J. Van Den Hurk, F. Lentz, R. Waser, "Nanobatteries in redox-based resistive switches require extension of memristor theory." *Nat. Commun. 2013 41*. 4, 1–9, **2013**, doi:10.1038/ncomms2784.

291. A. Mehonic, A. L. Shluger, D. Gao, I. Valov, E. Miranda, D. Ielmini, A. Bricalli, E. Ambrosi, J. J. Yang, Q. Xia, A. J. Kenyon, "Silicon oxide (SiO_x): A promising material for resistance switching?" *Adv. Mater.* 30, 1801187, **2018**, doi:10.1002/adma.201801187.

292. Z. Hu, F. Cao, T. Yan, L. Su, X. Fang, "In situ vulcanization synthesis of $CuInS_2$ nanosheet arrays for a memristor with a high on–off ratio and low power consumption." *J. Mater. Chem. C*. 11, 244–251, **2022**, doi:10.1039/D2TC04003D.

293. F. Cao, Z. Hu, T. Yan, E. Hong, X. Deng, L. Wu, X. Fang, "A dual-functional perovskite-based photodetector and memristor for visual memory." *Adv. Mater.* 35, 2304550, **2023**, doi:10.1002/ADMA.202304550.

294. H. S. Lee, H. H. Park, "Band structure analysis of $La_{0.7}Sr_{0.3}MnO_3$ perovskite manganite using a synchrotron." *Adv. Condens. Matter Phys.* 2015, 746475, **2015**, doi:10.1155/2015/746475.

295. A. Bogusz, D. Bürger, I. Skorupa, O. G. Schmidt, H. Schmidt, "Bipolar resistive switching in $YMnO_3$/Nb:$SrTiO_3$ pn-heterojunctions." *Nanotechnology*. 27, 455201, **2016**, doi:10.1088/0957-4484/27/45/455201.

296. A. Turut, M. Coşkun, F. M. Coşkun, O. Polat, Z. Durmuş, M. Çağlar, H. Efeoğlu, "The current-voltage characteristics of the ferroelectric p-$YMnO_3$ thin film/bulk p-Si heterojunction over a broad measurement temperature range." *J. Alloys Compd.* 782, 566–575, **2019**, doi:10.1016/j.jallcom.2018.12.246.

297. B. Ofuonye, J. Lee, M. Yan, C. Sun, J. M. Zuo, I. Adesida, "Electrical and microstructural properties of thermally annealed Ni/Au and Ni/Pt/Au Schottky contacts on AlGaN/GaN heterostructures." *Semicond. Sci. Technol.* 29, 095005, **2014**, doi:10.1088/0268-1242/29/9/095005.

298. M. J. Lee, S. Lee, S. Lee, K. Balamurugan, C. Yoon, J. T. Jang, S. H. Kim, D. H. Kwon, M. Kim, J. P. Ahn, D. H. Kim, J. G. Park, B. H. Park, "Synaptic devices based on two-dimensional layered single-crystal chromium thiophosphate ($CrPS_4$)." *NPG Asia Mater.* 10, 23–30, **2018**,

doi:10.1038/s41427-018-0016-7.

299. Y. Li, "What Is a Control System and How to Design a Control Loop for a DC-to-DC Converter", *Analog Devices*, https://www.analog.com/en/resources/technical-articles/how-to-design-a-control-loop-for-a-dc-dc-converter.html, (accessed May 26, **2024**).

300. K. Tadanaga, H. Kitahata, T. Minami, N. Fujimura, T. Ito, "Preparation and dielectric properties of $YMnO_3$ ferroelectric thin films by the sol-gel method." *J. Sol-Gel Sci. Technol.* 13, 903–908, **1998**, doi:10.1023/A:1008675307600.

301. S. Parashar, A. R. Raju, C. N. R. Rao, P. Victor, S. B. Krupanidhi, "Electrical properties of ferroelectric $YMnO_3$ films deposited on n-type Si(111) substrates." *J. Phys. D. Appl. Phys.* 36, 2134–2140, **2003**, doi:10.1088/0022-3727/36/17/317.

302. H. Bommer, "Die Gitterkonstanten der C-Formen der Oxyde der seltenen Erdmetalle." *Zeitschrift für Anorg. und Allg. Chemie*. 241, 273–280, **1939**, doi:10.1002/ZAAC.19392410215.

303. F. Ye, B. Lorenz, Q. Huang, Y. Q. Wang, Y. Y. Sun, C. W. Chu, J. A. Fernandez-Baca, P. Dai, H. A. Mook, "Incommensurate magnetic structure in the orthorhombic perovskite $ErMnO_3$." *Phys. Rev. B - Condens. Matter Mater. Phys.* 76, 060402-1, **2007**, doi:10.1103/PHYSREVB.76.060402.

304. N. Curetti, M. Merli, S. Capella, P. Benna, A. Pavese, "Low-pressure ferroelastic phase transition in rutile-type AX2 minerals: cassiterite (SnO_2), pyrolusite (MnO_2) and sellaite (MgF_2)." *Phys. Chem. Miner.* 46, 987–1002, **2019**, doi:10.1007/S00269-019-01057-7.

305. R. R. Phiri, O. Philip Oladijo, E. T. Akinlabi, "Defect formation and surface evolution of thin film materials", *International conference on industrial engineering and operations management*, Pretoria, South Africa, **2018**, 1087–1093.

306. K. A. Hunnestad, E. D. Roede, A. T. J. J. Van Helvoort, D. Meier, "Characterization of ferroelectric domain walls by scanning electron microscopy." *J. Appl. Phys.* 128, 191102-1, **2020**, doi:10.1063/5.0029284.

307. E. D. Roede, A. B. Mosberg, D. M. Evans, E. Bourret, Z. Yan, A. T. J. Van Helvoort, D. Meier, "Contact-free reversible switching of improper ferroelectric domains by electron and ion irradiation." *APL Mater.* 9, 021105-1, **2021**, doi:10.1063/5.0038909.

308. J. Vermette, S. Jandl, M. M. Gospodinov, "Raman study of spin–phonon coupling in $ErMnO_3$." *J. Phys. Condens. Matter*. 20, 425219, **2008**, doi:10.1088/0953-8984/20/42/425219.

309. L. Martín-Carrón, A. De Andrés, M. J. Martínez-Lope, M. T. Casais, J. A. Alonso, "Raman phonons as a probe of disorder, fluctuations, and local structure in doped and undoped orthorhombic and rhombohedral manganites." *Phys. Rev. B*. 66, 174303, **2002**, doi:10.1103/PhysRevB.66.174303.

310. A. Ruff, Z. Li, A. Loidl, J. Schaab, M. Fiebig, A. Cano, Z. Yan, E. Bourret, J. Glaum, D. Meier, S. Krohns, “Frequency dependent polarisation switching in h-$ErMnO_3$.” *Appl. Phys. Lett.* 112, 182908-1, **2018**, doi:10.1063/1.5026732.

311. I. A. Kalinin, I. V. Roslyakov, D. N. Khmelenin, K. S. Napolskii, “Long-term operational stability of Ta/Pt thin-film microheaters: Impact of the Ta adhesion layer.” *Nanomaterials*. 13, 94, **2023**, doi:10.3390/NANO13010094/S1.

312. N. Strkalj, C. Gattinoni, A. Vogel, M. Campanini, R. Haerdi, A. Rossi, M. D. Rossell, N. A. Spaldin, M. Fiebig, M. Trassin, “In-situ monitoring of interface proximity effects in ultrathin ferroelectrics.” *Nat. Commun.* 11, 5815, **2020**, doi:10.1038/s41467-020-19635-7.

313. M. Rössle, O. Thomas, C. Mocuta, R. Rousset, M. Texier, S. Escoubas, C. Dubourdieu, E. B. Araújo, T. W. Cornelius, “Time-resolved piezoelectric response in relaxor ferroelectric $(Pb_{0.88}La_{0.12})(Zr_{0.52}Ti_{0.48})O_3$ thin films.” *J. Appl. Phys.* 131, 064102, **2022**, doi:10.1063/5.0077785.

314. M. Lilienblum, “Ferroelectric order in multiferroic hexagonal manganites.” Doctoral dissertation, ETH Zurich, **2016**.

315. F. C. Chiu, “Conduction mechanisms in resistance switching memory devices using transparent boron doped zinc oxide films.” *Materials (Basel).* 7, 7339–7348, **2014**, doi:10.3390/MA7117339.

316. K. E. González-Flores, P. Horley, S. A. Cabañas-Tay, S. A. Pérez-García, L. Licea-Jiménez, L. Palacios-Huerta, M. Aceves-Mijares, M. Moreno-Moreno, A. Morales-Sánchez, “Analysis of the conduction mechanisms responsible for multilevel bipolar resistive switching of SiO_2/Si multilayer structures.” *Superlattices Microstruct.* 137, 106347, **2020**, doi:10.1016/J.SPMI.2019.106347.

317. A. Kosinova, O. Kovalenko, L. Klinger, E. Rabkin, “Mechanisms of solid-state dewetting of thin Au films in different annealing atmospheres.” *Acta Mater.* 83, 91–101, **2015**, doi:10.1016/J.ACTAMAT.2014.09.049.

318. K. Nagashima, T. Yanagida, K. Oka, T. Kawai, “Unipolar resistive switching characteristics of room temperature grown SnO2 thin films.” *Appl. Phys. Lett.* 94, **2009**, doi:10.1063/1.3156863/337128.

319. Y. Sharma, P. Misra, S. P. Pavunny, R. S. Katiyar, “Multilevel unipolar resistive memory switching in amorphous $SmGdO_3$ thin film.” *Appl. Phys. Lett.* 104, **2014**, doi:10.1063/1.4865802/27952.

320. Y. Sharma, P. Misra, S. P. Pavunny, R. S. Katiyar, “Unipolar resistive switching behavior of high-k ternary rare-earth oxide $LaHoO_3$ thin films for non-volatile memory applications.” *Mater. Res. Soc. Symp. Proc.* 1729, 23–28, **2015**, doi:10.1557/OPL.2015.92.

321. A. Moure, T. Hungría, A. Castro, J. Galy, O. Peña, J. Tartaj, C. Moure, “Mechanosynthesis of the orthorhombic perovskites $ErMn_{1-x}Ni_xO_3$ (x = 0, 0.1). Processing and characterization of

nanostructured ceramics." *Chem. Mater.* 22, 2908–2915, **2010**, doi:10.1021/cm100236q.

322. S. H. Skjærvø, E. T. Wefring, S. K. Nesdal, N. H. Gaukås, G. H. Olsen, J. Glaum, T. Tybell, S. M. Selbach, "Interstitial oxygen as a source of p-type conductivity in hexagonal manganites." *Nat. Commun. 2016 71.* 7, 1–8, **2016**, doi:10.1038/ncomms13745.

323. Y. T. Tsai, T. C. Chang, C. C. Lin, L. S. Chiang, S. C. Chen, S. M. Sze, T. Y. Tseng, "Effect of top electrode material on resistive switching characteristics in MnO_2 nonvolatile memory devices." *ECS Trans.* 41, 475–482, **2011**, doi:10.1149/1.3633064/XML.

324. C. Y. Lin, C. Y. Wu, C. Y. C. Y. Wu, T. C. Lee, F. L. Yang, C. Hu, T. Y. Tseng, "Effect of top electrode material on resistive switching properties of ZrO_2 film memory devices." *IEEE Electron Device Lett.* 28, 366–368, **2007**, doi:10.1109/LED.2007.894652.

325. C. Liu, G. Ma, J. Zeng, Q. Tan, Z. Zhang, A. Chen, N. Liu, H. Wan, B. Wang, L. Tao, Y. Rao, L. Shen, H. Wang, J. Zhang, H. Wang, "Research on improving the working current of NbO_x-based selector by inserting a Ti layer." *Front. Mater.* 8, 716065, **2021**, doi:10.3389/fmats.2021.716065.

326. J. Kim, J. Lee, M. Kang, H. Sohn, "Threshold switching of Ag-Ga_2Te_3 selector with high endurance for applications to cross-point arrays." *Nanoscale Res. Lett.* 16, 128, **2021**, doi:10.1186/s11671-021-03585-0.

327. X. Zhang, Y. Zhuo, Q. Luo, Z. Wu, R. Midya, Z. Wang, W. Song, R. Wang, N. K. Upadhyay, Y. Fang, F. Kiani, M. Rao, Y. Yang, Q. Xia, Q. Liu, M. Liu, J. J. Yang, "An artificial spiking afferent nerve based on Mott memristors for neurorobotics." *Nat. Commun.* 11, 1–9, **2020**, doi:10.1038/s41467-019-13827-6.

328. X. Zhang, W. Wang, Q. Liu, X. Zhao, J. Wei, R. Cao, Z. Yao, X. Zhu, F. Zhang, H. Lv, S. Long, M. Liu, "An artificial neuron based on a threshold switching memristor." *IEEE Electron Device Lett.* 39, 308–311, **2018**, doi:10.1109/LED.2017.2782752.

329. T. Driscoll, Y. V. Pershin, D. N. Basov, M. Di Ventra, "Chaotic memristor." *Appl. Phys. A*. 102, 885–889, **2011**, doi:10.1007/s00339-011-6318-z.

330. S. Kumar, J. P. Strachan, R. S. Williams, "Chaotic dynamics in nanoscale NbO_2 Mott memristors for analogue computing." *Nature*. 548, 318–321, **2017**, doi:10.1038/nature23307.

331. H. Du, J. Chen, M. Tu, S. Luo, S. Li, S. Yuan, T. Gong, W. Huang, W. Jie, J. Hao, "Transition from nonvolatile bipolar memory switching to bidirectional threshold switching in layered MoO_3 nanobelts." *J. Mater. Chem. C*. 7, 12160–12169, **2019**, doi:10.1039/C9TC03842F.

332. J. Song, A. Prakash, D. Lee, J. Woo, E. Cha, S. Lee, H. Hwang, "Bidirectional threshold switching in engineered multilayer (Cu_2O/Ag:Cu_2O/Cu_2O) stack for cross-point selector application." *Appl.*

Phys. Lett. 107, 113504-1, **2015**, doi:10.1063/1.4931136/28276.

333. G. A. Gibson, "Designing negative differential resistance devices based on self-heating." *Adv. Funct. Mater.* 28, 1704175, **2018**, doi:10.1002/ADFM.201704175.

334. B. Raneesh, H. Soumya, J. Philip, N. Kalarikkal, "Size-dependent thermal properties of multiferroic $ErMnO_3$ nanoparticles using photopyroelectric technique." *J. Alloys Compd.* 579, 243–248, **2013**, doi:10.1016/J.JALLCOM.2013.06.018.

335. S. M. Selbach, A. N. Løvik, K. Bergum, J. R. Tolchard, M. A. Einarsrud, T. Grande, "Crystal structure, chemical expansion and phase stability of $HoMnO_3$ at high temperature." *J. Solid State Chem.* 196, 528–535, **2012**, doi:10.1016/j.jssc.2012.07.024.

336. S. H. Skjærvø, D. R. Småbråten, N. A. Spaldin, T. Tybell, S. M. Selbach, "Oxygen vacancies in the bulk and at neutral domain walls in hexagonal $YMnO_3$." *Phys. Rev. B*. 98, 184102, **2018**, doi:10.1103/PhysRevB.98.184102.

337. M. M. Frydenlund, "Development of a new class of oxygen ion mixed conductors." Master thesis, NTNU, **2014**.

338. S. K. Nath, S. K. Nandi, S. Li, R. G. Elliman, "Metal-oxide interface reactions and their effect on integrated resistive/threshold switching in NbO_x." *Nanotechnology*. 31, 235701, **2020**, doi:10.1088/1361-6528/ab7889.

339. I. Messaris, R. Tetzlaff, A. Ascoli, R. S. Williams, S. Kumar, L. Chua, "A simplified model for a NbO_2 Mott memristor physical realization,"*2020 IEEE International Symposium on Circuits and Systems (*ISCAS), Seville, Spain, **2020**, 1-5, doi: 10.1109/ISCAS45731.2020.9181036.

340. A. Ascoli, A. S. Demirkol, R. Tetzlaff, S. Slesazeck, T. Mikolajick, L. O. Chua, "On local activity and edge of Chaos in a NaMLab memristor." *Front. Neurosci.* 15, 651452, **2021**, doi:10.3389/fnins.2021.651452.

341. A. S. Demirkol, A. Ascoli, I. Messaris, R. Tetzlaff, "Pattern formation in a RD-MCNN with locally active memristors." Memristor - An Emerging Device for Post-Moore's Computing and Applications, *IntechOpen*, **2021**, doi: 10.5772/intechopen.100463.

List of publications

1. R. Wu, S. Schmitt, F. Maudet, D. J. Kim, V. Deshpande, C. Dubourdieu, "Electrochemical metallization memristive devices with Al active electrode using engineered mixed hexagonal/orthorhombic polycrystalline $YMnO_3$." *Small Struct.* 5, 2300494, **2024**, doi:10.1002/sstr.202300494.
2. R. Wu, F. Maudet, T. L. Phan, S. Schmitt, V. Deshpande, C. Dubourdieu, "Study of crystalline phase dependent bipolar resistive switching performance in polycrystalline $ErMnO_3$." In preparation.
3. R. Wu, F. Maudet, T. L. Phan, W. Hamouda, V. Deshpande, C. Dubourdieu, "Tunable threshold switching and negative differential resistance in polycrystalline $ErMnO_3$ based memristive devices." In preparation.